LBL-20204
UC-13

Lawrence Berkeley Laboratory
UNIVERSITY OF CALIFORNIA

APPLIED SCIENCE DIVISION

FY 1985 Annual Report
ENVIRONMENTAL RESEARCH PROGRAM

August 1986

APPLIED SCIENCE DIVISION

Prepared for the U.S. Department of Energy under Contract DE-AC03-76SF00098

DISCLAIMER

LBL-20204

APPLIED SCIENCE DIVISION ANNUAL REPORT

ENVIRONMENTAL RESEARCH PROGRAM

FY 1985

Elton J. Cairns
Head, Applied Science Division
and
Associate Director, LBL

Tihomir Novakov
Program Leader, Environmental Research Program

Applied Science Division
Lawrence Berkeley Laboratory
University of California
Berkeley, California 94720

Prepared for the U.S. Department of Energy under Contract No. DE-AC03-76SF00098

CONTENTS

ENVIRONMENTAL RESEARCH PROGRAM STAFF

Tihomir Novakov, Program Leader
Nancy Brown, Deputy Program Leader

ATMOSPHERIC AEROSOL RESEARCH

William Benner
Mirke Bizjak*
Ray Dod
Lara Gundel
Anthony Hansen
Vida Hudnik*
Samuel Markowitz
Fred Mowrer
Tihomir Novakov†
Roland Otto
Cass Parker
Carolyn Pryor
Hal Rosen
Richard Schmidt
Wenzhi Song*
Wei-Han Su*
Linda Wroth
Quipeng Zhang*

APPLIED PHYSICS AND LASER SPECTROSCOPY RESEARCH

Nabil Amer†
Helmut Dersch
Robert Gerlach
William Imler
Marjorie Olmstead
Andrew Skumanich

OIL SHALE RESEARCH

Ernest Blatchley
Christian Daughton‡
Gloria Harris
Joseph Healy, Jr.
Leon Hunter
Bonnie Jones
Gregg Langlois
Frank Mandola
Carl Martin
Peter Persoff
Rick Sakaji
Robert Selleck‡
Jerome Thomas†

COMBUSTION RESEARCH

James Ang
Diana Brehob
Mark Brosmer
Nancy Brown†
John Cavolowsky
Robert Cheng
Peck Cho§
Derek Dunn-Rankin
Christopher Edwards
Janet Ellzey
Michael Forsha
Iskander Gokalp*
Ralph Greif
Jean Hertzberg
Kenneth Hom
Wei-Ming Huang
Gary Hubbard
Frank Hurlbut
Eileen Javar
Chung Lau§
Kwi Lee
Russell Lewis
Trudy Lionel
Donald Lucas
Richard Martin
Mehdi Namazian‡
Clement Okoh
Antoni Oppenheim
Patrick Pagni
Terry Parker
Richard Peterson
Maciej Pindera
Ahmed Rashed
Ola Rashed
Frank Robben
Robert Sawyer
Ian Shepherd‡
Pauline Sherman*
Horton Stewart‡
Lawrence Talbot
R. Brady Williamson

SCRUBBER CHEMISTRY RESEARCH

Kevin Brodbeck‡
Shih-Ger Chang†
Elizabeth Griffiths
Ke-Yuan Hu*
David Littlejohn
David Liu
Minduan Tu*
Abbey Wizansky
Steven Wolfgang

*Participating guest, †Group Leader, ‡University of California Berkeley,
§University of California Davis.

TOXICOLOGY STUDIES OF BIOLOGICAL SYSTEMS

Charles Blanchard	Johanna Lang	Rolf Mehlhorn	Lester Packer
Ian Fry	John Maguire	Harvey Michaels	Richard Schneider
John Harte			

TRACE ELEMENT ANALYSIS

Frank Asaro	Helen Michel	Lina Sindelar	Rafael Zamora
Robert Giauque	Amos Newton	Fred Stross*	

ADMINISTRATIVE SUPPORT

Rachelle Edmond	Gloria Gill

*Participating guest.

ENVIRONMENTAL RESEARCH PROGRAM

INTRODUCTION

The objective of the Environmental Research Program is to understand the formation, transformation, transport, and effects of energy-related pollutants on the environment. This multidisciplinary research program includes fundamental and applied research in physics, chemistry, engineering, and biology, as well as research on the development of advanced methods of measurement and analysis. The Program's Annual Report contains summaries of research performed during FY 1985 in the areas of Atmospheric Aerosol Research, Applied Physics and Laser Spectroscopy, Oil Shale Research, Combustion, Flue Gas Chemistry, Toxicological Effects on Biological Systems, and Trace Element Analysis.

The Atmospheric Aerosol Research group focused its studies on the formation, transformation, characterization, and effects of atmospheric aerosols. At present, the main research interests of the group concern the chemical processes that occur in haze, clouds, and fogs, and the role of particulate carbon in global climate modification. For their studies, the group developed novel analytical and research methods for characterizing particles, fog, and aerosol species. Aerosol research is performed in the laboratory and in the field. National and international cooperative studies constitute the principal emphasis of the field studies.

The Applied Physics and Laser Spectroscopy Research group applies advanced laser spectroscopy and condensed-matter physics to energy and environmental problems. Emphasis is on the development of physical methods, as opposed to conventional chemical analysis techniques. The ultrahigh sensitivity, narrow linewidth, and tunability of lasers and the minimal sample preparation required make it possible for group members to apply these techniques to the studies of surfaces and interfaces, amorphous photovoltaic semiconductors, and liquid crystals.

The Oil Shale project studies the environmental and waste-treatment problems that would arise from the tremendously large quantities of solid and liquid wastes that a commercial-scale shale oil industry would generate. A major task of the project is to delineate the potential problems of process wastewater and spent-shale codisposal, in particular the estimation of the types and quantities of uncontrollable air emissions that may result from such use of wastewaters (raw or treated). Its second major task is the development of economical approaches to the treatment of process wastewaters. Because of their high concentrations of organic and inorganic solutes, they present tremendous difficulties to any water management scheme that entails reuse or discharge. This research effort is conducted with the Sanitary Engineering and Environmental Health Research Laboratory of the University of California.

The Combustion Research group studies complex combustion processes by acquiring a fundamental understanding of the chemical and physical processes that determine combustion efficiency, emissions, and safety. Development of suitable analytical techniques for measuring intermediate and product species formed during the oxidation of fossil fuels and for characterizing turbulence has been a major effort. The characterization and understanding of turbulence and high-temperature chemistry are of high priority in this program. Areas of application that dominate these studies are engine research, pollutant abatement in utilities, fire control, and ignition phenomena.

The Scrubber Chemistry group is investigating the chemical character of pollutants generated by the combustion of fossil fuels to develop new, efficient strategies for pollutant emission control. Current research is directed toward understanding the kinetics and mechanisms of homogeneous and heterogeneous catalysis of the interactions of sulfur dioxide and nitrogen oxides, both among themselves and with other compounds. When this fundamental chemistry is understood, it will be applied to the development of an efficient, cost-effective scrubber for simultaneous desulfurization and denitrification of flue gases.

In Toxicological Effects on Biological Systems, the study of strongly chemically reactive compounds generated within cells during aerobic metabolism is of particular interest in attempting to understand cellular damage and repair. In particular, "active oxygen" species (including free radicals) that are

generated during the normal life span of cells have been implicated in many processes that result in altered cellular metabolism. The study of free radicals in mitochondrial membranes focuses primarily on oxygen radicals generated by mitochondria (the energy-generating organelles within cells) during respiration and their effects on biological membranes.

The main emphasis of the Trace Element Analysis group is the study of the relationship between massive repetitive life extinctions on the earth and asteroid (or other extraterrestrial) impacts. Studies of this relationship have concentrated on searches for unusually high iridium abundances in geochemical samples from rock layers known or expected to mark life-extinction horizons. Geochemical and other tests are made to determine if the iridium-rich rocks are of extraterrestrial origin and hence related to impacts. The nature of the sedimentation of the rocks, the worldwide extent of the extinction horizons, and the extent to which the extinctions are related to impacts are also studied.

The short reports that follow describe the program activities in FY 1985. For most of these reports, more detailed papers have been or will be published in appropriate scientific journals.

Estimates of Springtime Soot and Sulfur Fluxes Into the Arctic Troposphere: Implications to Source Regions*†

H. Rosen and A.D.A. Hansen

During winter and spring, the Arctic atmosphere contains significant concentrations of sulfur-[1] and carbon-containing[2] particles that may have been transported long distances from combustion sources at midlatitudes in Eurasia. The 1983 Arctic Gas and Aerosol Sampling Project (AGASP) explored the horizontal and vertical distributions of the haze throughout the western Arctic. (See Special Issue of *Geophysical Research Letters*, v. 11, 1984, for details.) One of the instruments on these flights was an aethalometer,[3] which can measure graphitic carbon concentrations on a real-time basis and which determined vertical profiles of graphitic particles in the Arctic troposphere.[4] In this report, we use these vertical profiles in conjunction with a box model calculation to make a first estimate of the fluxes of graphitic carbon, total carbon, and sulfur particles into the Arctic troposphere. These fluxes are compared with the fluxes of carbon and sulfur produced from fossil fuel combustion on a regional and global basis.

ACCOMPLISHMENTS DURING FY 1985

For the purposes of a box model calculation, we view the Arctic troposphere as a cylindrical volume with a radius extending from the North Pole to 70°N latitude and a height of 7 km, corresponding to the approximate level of the tropopause. For a conserved species like graphitic carbon that is not produced or destroyed in the atmosphere, the rate of change of the mass of particles within this box is equal to the flux of particles entering minus the flux leaving. This equation can be written as

$$\frac{dM(t)}{dt} = F_M - \frac{M(t)}{\tau}, \qquad (1)$$

where M(t) is the mass of the component with the box at time t; dM(t)/dt its rate of change; F_M is the input flux through all surfaces of the box; and $M(t)/\tau$ is the loss of mass, represented by an exponential decay with an effective residence time τ. This residence time includes both losses by deposition and by transport of air masses out of the Arctic basin. At equilibrium dM/dt = 0, and the input flux equals the decay rate:

$$F_M = \frac{M(t)}{\tau}. \qquad (2)$$

For nonequilibrium situations, the input flux can be greater or less than the decay rate. If the input flux at time t is less than $M(t)/\tau$, it had to be at least as large as this decay rate at some previous time. In other words, even for a nonequilibrium situation, Eq. (2) can be used to get a lower limit on the maximum input flux.

If one can estimate the mass of graphitic particles in the Arctic troposphere, then using Eq. (2), the input flux as a function of residence time can be determined. The mass of graphitic particles G is given by integrating the concentration as a function of altitude over the considered volume. The profiles of graphitic particles obtained during AGASP can be used to make an estimate of the concentrations during March and April, 1983. In this analysis we neglect the dependence of the graphitic concentrations on latitude and longitude and use an average vertical distribution obtained from the nine tropospheric AGASP flights to characterize the whole Arctic region. These flights were in the western Arctic, and therefore probably underrepresent the Arctic as a whole because the primary source regions appear to be in the eastern sector.[1] With these assumptions, we determine the average mass of graphitic particles in the Arctic troposphere during AGASP to be G = 2.4×10^{10} g = 2.4×10^4 metric tons. Reliable total carbon determinations could not be obtained from the airborne filters on these flights. However, ground-level determinations have been made at the

*This work was supported by the Director, Office of Energy Research, Office of Basic Energy Sciences, Carbon Dioxide Research Division of the U.S. Department of Energy under Contract No. DE-AC03-76SF00098.

†Summary of paper published in *Atmospheric Environment 19*, pp. 2203–2207 (1985).

NOAA-GMCC station at Barrow, Alaska, and indicate that during March-April approximately 20% of the total carbon is graphitic.[5] Therefore, we assume that we can make an estimate of the total carbon in the Arctic from the ground-level measurements at Barrow by multiplying the graphitic component by 5, i.e., the estimated total particulate carbon mass is 1.2×10^5 tons. It is also possible to make an estimate of the total sulfur in the Arctic because we collected 20 airborne filters during AGASP, which we analyzed for sulfur and graphitic carbon contents. The sulfur-to-graphitic-carbon ratio for these filters is 3.3 ± 0.75. If we assume that the vertical profiles of sulfur and graphitic carbon are similar, then the total amount of particulate sulfur in the Arctic can be estimated by multiplying the graphitic mass by 3.3, i.e., the estimated particulate sulfur mass = 8×10^4 tons. This represents a lower limit on the total amount of sulfur in the Arctic because it does not include the gas-phase contribution.

These estimates of the mass of graphitic carbon, total carbon, and sulfur can be used in conjunction with Eq. (2) to estimate the input fluxes of each of these components into the Arctic troposphere. These estimates as a function of residence time are shown for total carbon and sulfur in Figs. 1 and 2. The shaded region in the figures represents a reasonable range of values for the residence time of particles in the Arctic atmosphere, from 1 week to 1 month.[1,6] This effective residence time includes the effects of deposition as well as transport of air out of the Arctic basin.

For comparing the fluxes shown in Figs. 1 and 2 with fluxes from source regions, we chose a residence time of 2 weeks, which will give fluxes within a factor of 2 of the extreme values of residence time. Recently, Marland *et al.*[7] have made estimates of fossil fuel burned as a function of latitude in 5° latitude bands. In Table 1 we compare the fluxes of graphitic carbon (F_G), total carbon (F_C), and sulfur (F_S) entering the Arctic to the carbon burned in various latitude ranges. It becomes immediately obvious from this table that sources between 70–90°N cannot account for these fluxes because the amount of carbon burned in this region is less than the flux of emitted particulate carbon. In other words, sources in the Arctic cannot account for the Arctic haze. In the latitude range 65–70°N, the fluxes are less than the carbon burned but are too large a fraction of it to be reasonable. Typical emission factors for soot as a fraction of the mass of carbonaceous fuel burned range from zero for complete combustion to ~4% for very dirty burning of soft coal. Significant source contributions in the 60–65°N latitude range are more

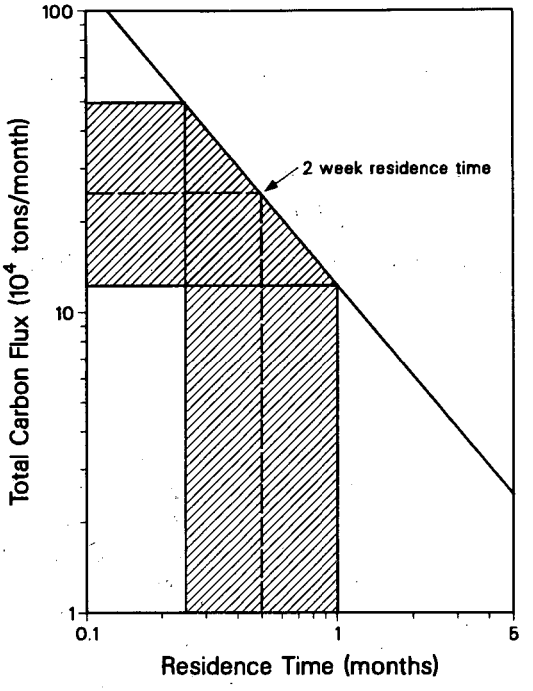

Figure 1. Estimated flux of total particulate carbon entering the Arctic troposphere as a function of residence time. The shaded area represents a range of residence times of 1 week to 4 weeks. (XCG 8410-13400)

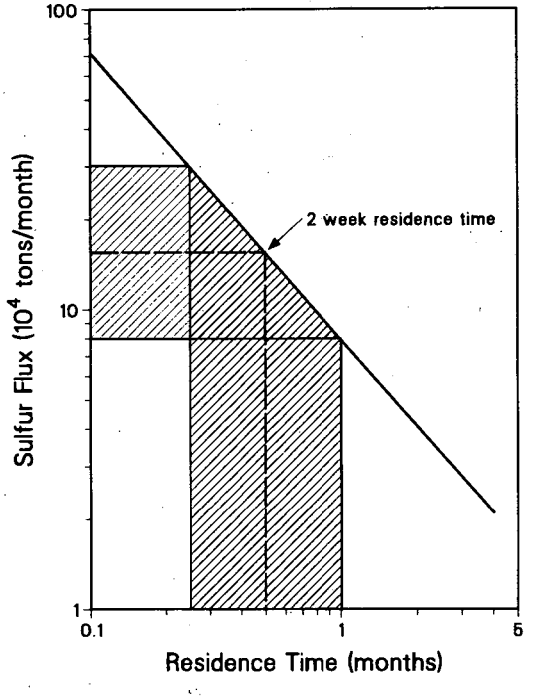

Figure 2. Estimated flux of sulfur entering the Arctic troposphere as a function of residence time. The shaded area represents a range of residence times of 1 week to 4 weeks. (XCG 8410-13402)

Table 1. Comparison of graphitic carbon total carbon, and sulfur fluxes to the amount of fuel burned at various latitudes.

Latitude	Carbon burned (tons month^{-1})	F_G as % of carbon burned	F_C as % of carbon burned	F_S as % carbon burned
75–90°N	1.5×10^3	3,200	16,300	10,600
70–75°N	5×10^4	98	490	320
65–70°N	7.6×10^5	6.4	32	21
60–65°N	3.3×10^6	1.5	7.4	4.8
55–60°N	2.5×10^7	0.2	1	0.6
50–55°N	7.1×10^7	0.07	0.35	0.2
45–50°N	5.3×10^7	0.09	0.45	0.3
0–45°N	2.3×10^8	0.02	0.1	0.07
Global	4.4×10^8	0.01	0.05	0.04

reasonable; however, it would still require extremely poor combustion of very high sulfur content fuels to fully account for the fluxes into the Arctic. Furthermore, it would require almost all the emissions from this region to be transported only in a northerly direction toward the Arctic with minimal deposition along the transport path. Major contributors to the Arctic haze in the 55–60° latitude band become more reasonable, but even here it would require very effective transport of source emissions to the Arctic. As one goes below 55°N latitude, the fluxes become a very reasonable fraction of the fuel burned, which is consistent with the midlatitude sources proposed on the basis of trace element analyses.[1]

The flux of sulfur, F_S, entering the Arctic can be compared with estimated sulfur emissions in various source regions.[8] These estimates are based on the sulfur content of the fuels and represent a maximum possible aerosol sulfur input into the atmosphere assuming complete conversion of SO_2 to particulate sulfur. Table 2 shows this comparison, with the Arctic sulfur flux shown as a percentage of the sulfur emissions from potential source regions. Individually, these fractions are large and could indicate that the Arctic haze is due to the combined input of several major source regions. On a global scale, these calculations estimate that 2.5% of the global sulfur emissions enter the Arctic, despite the fact that the Arctic is remote from major source regions and accounts for only ~6% of the northern hemisphere's surface area. These conclusions are preliminary because of uncertainties in the vertical and horizontal distribution of the Arctic haze and its residence time. However, they do indicate that the fluxes entering the Arctic are large, must be due to major combustion source regions, and have to be taken into account in the global sulfur and carbon budget.

PLANNED ACTIVITIES FOR FY 1986

During FY 1985 we also designed and constructed the second-generation aethalometer, incorporating greatly increased sensitivity as well as real-time data analysis and display. This instrument is scheduled for deployment on two major aircraft programs in FY 1986—AGASP-2, a more detailed study of Arctic haze, and WATOX 86 (Western Atlantic Ocean Experiment), which is part of an ongoing research program studying the flux of pollutants from the North American continent to the Atlantic ocean.

Table 2. Comparison of Arctic sulfur fluxes to sulfur emissions in various regions.[a]

Region	Sulfur emissions (tons month^{-1})	Arctic sulfur flux as % of emissions
Europe	2.5×10^6	6.4
Capitalist Europe	1.1×10^6	14.5
Socialist Europe	1.4×10^6	11.4
U.S.S.R.	1.1×10^6	14.5
U.S.A.	1.3×10^6	12.3
Canada	2.5×10^5	64.0
Global	6.6×10^6	2.4

[a]Sulfur emission data obtained from Moller (1984).

REFERENCES

1. Rahn, K.A. and McCaffrey, R.J. (1980), "On the Origin and Transport of the Winter Arctic Aerosol," *Ann. N.Y. Acad. Sci. 338*, p. 486.
2. Rosen, H. and Novakov, T. (1983), "Combustion-Generated Carbon Particles in the Arctic Atmosphere," *Nature 306*, p. 768.
3. Hansen, A.D.A., Rosen, H., and Novakov, T. (1982), "Real-Time Measurement of the Absorption Coefficient of Aerosol Particles," *Appl. Opt. 21*, p. 3060.
4. Hansen, A.D.A. and Rosen, H. (1984), "Vertical Distributions of Particulate Carbon, Sulfur, and Bromine in the Arctic Haze and Comparison with Ground-Level Measurements at Barrow, Alaska," *Geophys. Res. Lett. 11*, p. 381.
5. Rosen, H., Novakov, T., and Bodhaine, B.A. (1981), "Soot in the Arctic," *Atmospheric Environment 15*, p. 1371.
6. Raatz, W.E. and Shaw, G.E. (1983), "Long Range Tropospheric Transport of Pollution into the Alaskan Arctic," submitted to *J. Climate and Appl. Meteor.*
7. Marland, G., Rotty, R.M., and Treat, N.L. (1984), "CO_2 from Fossil Fuel Burning: Global Distributions of Emissions," submitted to *Tellus.*
8. Moller, D. (1984), "Estimation of the Global Man-Made Sulphur Emission," *Atmospheric Environment 18*, p. 19.

Horizontal Inhomogeneities in the Particulate Carbon Component of the Arctic Haze*†

A.D.A. Hansen and H. Rosen

The Arctic haze has been found to have a large carbonaceous component with submicron particles containing both organic compounds and microcrystalline graphitic forms.[1] This latter species is often termed "black carbon" due to its large optical absorption cross section. It can only be produced during incomplete combustion and is inert to transformation in the atmosphere. There are therefore no sources of black carbon within the atmosphere, making this material a good tracer for the evolution of a polluted air mass. Particulate black carbon was found through the Arctic troposphere during the Arctic Gas and Aerosol Sampling Project (AGASP) 1983 program in sufficient concentrations that its optical absorption may lead to a significant perturbation of the solar radiation balance.[2-4] We have previously reported results on the vertical distributions of aerosol black carbon in the Arctic haze, showing strong layering structure as well as significant concentrations at all altitudes in the troposphere.[5] In this report we present results from detailed analyses of portions of the flight tracks showing substantial horizontal variations of black carbon concentration, often (but not always) in conjunction with meteorological features.

ACCOMPLISHMENTS DURING FY 1985

Our installation aboard the AGASP WP-3D aircraft included the aethalometer, an instrument developed at Lawrence Berkeley Laboratory that measures the concentration of aerosol black carbon in real time.[6] We obtained a data set of black carbon concentrations averaged over 1-minute intervals and expressed in units of nanograms per geometric cubic meter. The estimated error on the measurements presented here is ± 0.09 $\mu g/m^3$. We then meshed these aethalometer data with the aircraft systems tape to give a data base containing average readings every minute for black carbon concentration, position and altitude, wind speed and direction, air temperature and relative humidity, etc. The periods of time during which all the above measurements were valid add to a total of approximately 70 hours of flying time north of 70° latitude. The flight patterns employed during the AGASP 1983 program included both rapid and gradual descents and ascents, as well as portions of level flight paths at various altitudes down to 30 m ASL. We scanned the data base to search for flight track portions that indicated a horizontal pass through a varying black carbon concentration. Details from three suitable events are presented in this report.

*This work was supported by the Director, Office of Energy Research, Office of Basic Energy Sciences, Carbon Dioxide Research Division of the U.S. Department of Energy under Contract No. DE-AC03-76SF00098.

†Summary of paper published in *Atmospheric Environment 19*, pp. 2175–2180 (1985).

Figure 1 shows data obtained during AGASP flight 9 over a period of approximately 35 minutes during which the aircraft flew in a constant northerly track at altitudes between 83 m and 91 m ASL. The track covered a distance of approximately 250 km from 75.5°N, 26.2°E to 78.2°N, 27.2°E, i.e., somewhat to the east of Spitzbergen. From 0 to 50 km on the track scale, the aircraft was over ocean with broken ice; from 50 km on, the surface was more or less continuous ice with leads. The air temperature had been steady at around 270 K before the ice was reached; it then gradually decreased to 265 K at the 200-km mark. During this time, the wind direction was steady at 200° to 210°, and the dew point was approximately constant at 261 K; i.e., the relative humidity increased from 60% to 80%. These data suggest that the aircraft was flying in a single moist air mass whose temperature was dropping. Conditions were noted as being overcast and visibly hazy. The black carbon concentration increased from about 0.2 $\mu g/m^3$ to a peak of 1.6 $\mu g/m^3$ at the 200-km mark. At this point, the observer's record states that snow flurries had started and continued for a few minutes until by the 250-km mark the aircraft had flown through a front into clear skies. The wind direction shifted by 55°, the air temperature fell by 5 K, and the dew point fell by 10°. The new air mass was colder and drier, and its black carbon concentration was down to about 0.25 $\mu g/m^3$.

Figure 2 shows 47 minutes of data from AGASP flight 3, encompassing almost a complete loop of length 130 km and height from 30 m to 1800 m altitude. The descent spiral was at 72.7°N, 156.8°W, and the ascent climb was at 71.5°N, 157.4°W. The low-level portion was a southerly track from about 200 km to 50 km north of Barrow. During this portion, the wind speed and direction were steady at 4.3 ±0.4 m/sec and 51 ±8° respectively, and the relative humidity was 75 ±5%. There was no clear evidence of a changing air mass. However, Fig. 2a shows that the average black carbon concentration

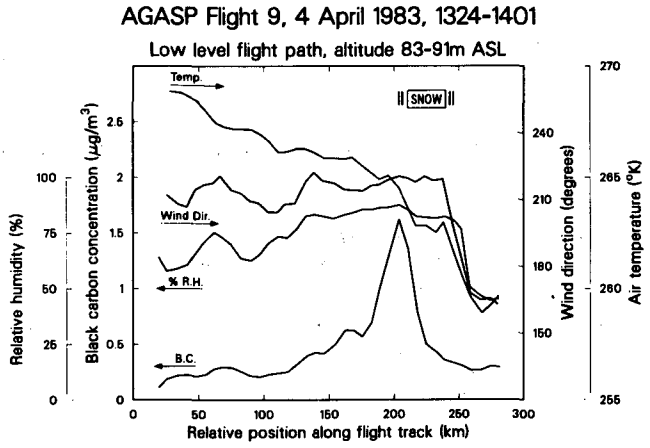

Figure 1. Data taken during low-level flight from 1324 to 1401 UT, 4 April 1983. Air temperature and wind direction scales are on the right-hand axis; relative humidity and aerosol black carbon concentration scales are on the left. The track was straight and northerly with the horizontal origin at 75.5°N, 26.2°E. The bar at upper right indicates the observation of snow flurries. (XCG 8411-13429)

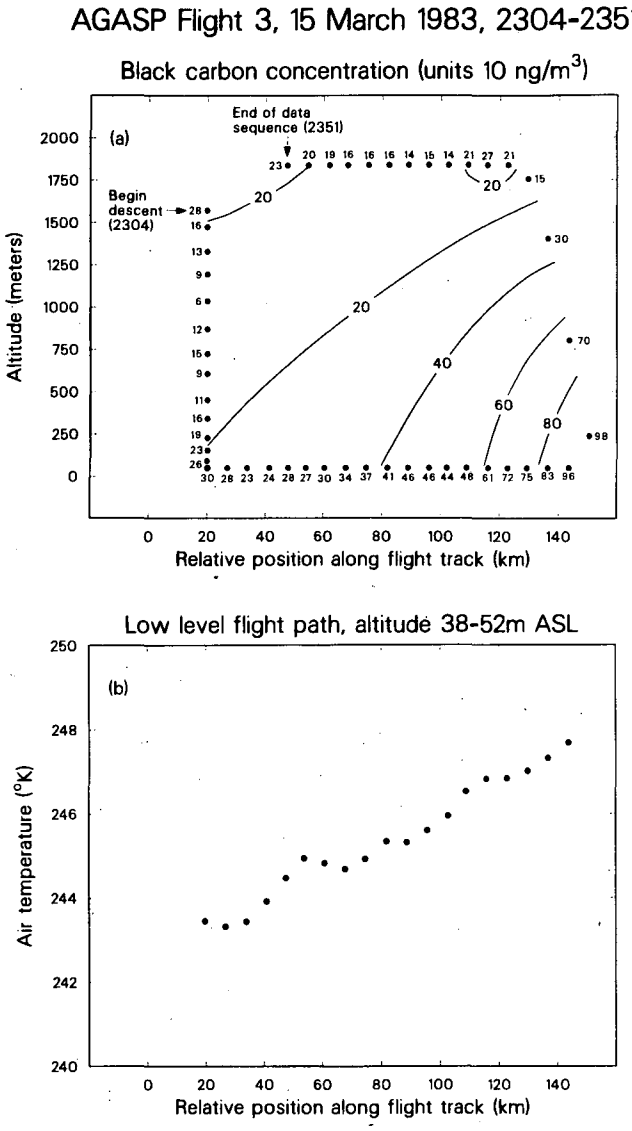

Figure 2. Data taken during loop flight pattern from 2304 to 2351 UT, 15 March 1983. The descent was a spiral at 72.7°N, 156.8°W; the level flight track was southerly. (a) Aerosol black carbon concentration vs. altitude and relative horizontal position. The contours are hypothetical, calculated by interpolation of the perimeter measurements. (b) Air temperature for the low-altitude flight track portion from 2317 to 2335 UT. (XCG 8411-13426A)

increased steadily from about 0.25 $\mu g/m^3$ to almost 1 $\mu g/m^3$ along the low-level track portion; and Fig. 2b shows that the air temperature increased by 4 K in the same period. The aircraft then climbed and essentially retraced its track at 1850 m altitude for altitude for about 100 km distance. We have constructed contours of aerosol black carbon concentration for the purposes of visualization, based on interpolation of the data points around the track perimeter. We emphasize that these are not measured contours; however, because there were neither sources nor sinks of aerosol black carbon within this perimeter, the implied continuity is reasonable. The data suggest a concentration of black carbon at low altitudes, with a maximum at some point beyond the 150-km track point. However, there was no evidence of precipitation nor crossing of an air mass boundary during the flight loop.

Figure 3 shows 51 minutes of data taken during AGASP flight 5. This track portion was a straight path from 71.8°N, 141.4°W to 74.0°N, 137.3°W over the Beaufort Sea during the flight from Anchorage, Alaska, to Thule Air Base, Greenland. The Canadian coast was from 100 to 400 km distant during this time. The flight profile was a descent to 30 m altitude followed by about 17 minutes of flying at low altitudes, after which the aircraft climbed to 1550 m ASL altitude. Figure 3b shows the air temperature and wind direction. There was a strong temperature inversion, with a 10 K fall between 700 m altitude and sea level. The wind direction shifted very little along the first 250 km of the track but then rapidly turned by 50° soon after the climb-out. At this time, although the air temperature showed little change, the dew point rose from 237 K to 252 K, indicating that the aircraft had entered a different air mass. The black carbon concentration was of the order of 0.2 $\mu g/m^3$ at high altitudes at the start of the sequence. This increased to 0.73 $\mu g/m^3$ at about 800 m altitude on the descent and then fell off rapidly to low values at low altitudes when the aircraft was within the surface temperature inversion air layer. Upon climbing, the black carbon concentration increased again to almost 1 $\mu g/m^3$ but then rapidly disappeared at the start of the level flight portion at the same time as the changing meteorological measurements indicated an air mass boundary. The constructed contours shown in the figure suggest a concentration maximum close to this point.

The data presented in Fig. 1 suggest the following situation, similar to one described by Raatz and Schnell[7] for another AGASP flight in the Norwegian Arctic. The aircraft was flying on a northerly track at a constant low altitude in a moist, polluted air

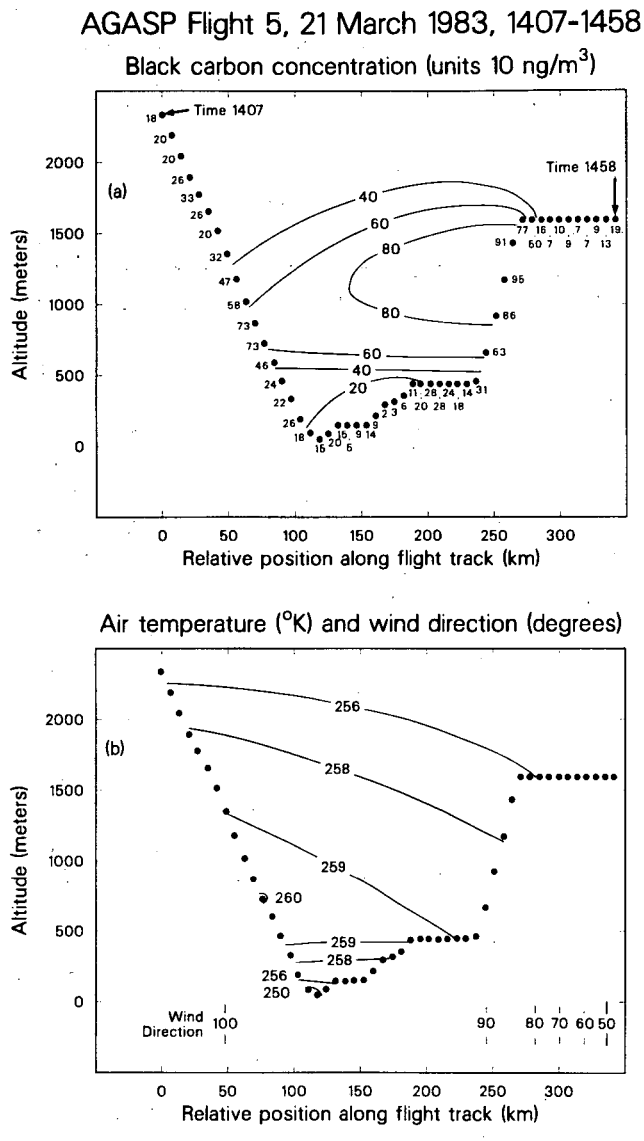

Figure 3. Data taken during descent/ascent flight pattern from 1407 to 1458 UT, 21 March 1983. The track was straight and northeasterly with the horizontal origin at 71.8°N, 141.4°W. (a) Aerosol black carbon concentration vs. altitude and horizontal position. (b) Air temperature and wind direction vs. altitude and position. In both figures the contours are estimated from the perimeter measurements and drawn for visualization purposes only. (XCG 8411-13430A)

mass. The black carbon concentration started increasing substantially at around the 150-km track mark but fell rapidly as soon as precipitation started. Shortly thereafter, the aircraft passed through a front into an air mass whose aerosol black carbon concentration was low. The removal of aerosols by precipitation is expected; however, there was no ongoing

meteorological activity to explain the five-fold change in black carbon concentration between the start of the track and the peak at the 200-km mark. Figure 2a shows a similar situation, in which the aerosol black carbon concentration increased four-fold within the same air mass. Here, the air temperature gradually rose (see Fig. 2b), but there was no clear evidence of recent meteorological activity or the approach of a front.

There may be several explanations for these observations. One is that the air masses were at one time uniformly polluted but that precipitation or other scavenging had occurred at some time in the past over only part of the air mass, removing aerosols from a portion of the flight track. Another is that the injection of carbonaceous aerosol into the air mass had been confined in an area at the source region and that these are plume edge profiles. However, this would require only a small amount of horizontal dispersion over the long transport paths (see Harris[8]) and imply a diffusion coefficient of the order of 10^9 cm^2/sec. At present, we cannot unambiguously identify either these or other possible mechanisms as explanation for the data.

The maximum instantaneous concentration of black carbon observed during the entire AGASP program was approximately 1.5 $\mu g/m^3$, which we shall take as a reasonable value for the maximum concentration likely to be found at the center of an inhomogeneity. If we assume that the flight track of Fig. 2a penetrated the edge of such a patch, we can estimate the size scale of the patch from the spacing of the contours. This suggests a horizontal scale of 50 to 100 km as the characteristic length over which the aerosol black carbon concentration changes by a factor of two. We must strongly emphasize that this distance represents a characteristic length on the basis of partial perimeter measurements, rather than an actual complete mapping. The data shown in Fig. 1 from the start of the track to the onset of precipitation also fit into this scale.

The data shown in Fig. 3 present a more complex situation. Figure 3b indicates a surface temperature inversion layer extending to about 400 m altitude and an air mass boundary at about 280 km on the track. The constructed contours in Fig. 3a show strong aerosol black carbon concentrations in the air above the surface layer but very low levels below the inversion, an observation in agreement with the expected weak coupling of these layers. The effect of the front at 280–300 km track is similar to that shown in Fig. 1: in the new air mass, the black carbon concentrations are low. The constructed contours indicate a very rapid change of aerosol black carbon concentration at the front and also show that the polluted air mass is resting on top of a clean surface temperature inversion layer. This contrasts with the situation often found in urban atmospheres, in which the emissions are trapped in the surface layer beneath the inversion. This observation in the Arctic may imply long-range transport of combustion emissions.[9–10]

PLANNED ACTIVITIES FOR FY 1986

The 1983 AGASP aircraft experiment demonstrated the value of measurements of aerosol black carbon from an airborne platform in real time. However, the instrument used during this program was still at the prototype stage. During FY 1985 we also designed and constructed the second-generation aethalometer, incorporating greatly increased sensitivity as well as real-time data analysis and display. This instrument is scheduled to be deployed on two major aircraft programs in FY 86—WATOX '86 (Western Atlantic Ocean Experiment) and AGASP-2, in which it will be used to indicate the presence of aerosol graphitic carbon as a tracer for combustion emissions in conjunction with airborne measurements of other pollutants.

REFERENCES

1. Rosen, H. and Novakov, T. (1983), "Combustion-Generated Carbon Particles in the Arctic Atmosphere," *Nature 306*, p. 768.
2. Shaw, G.E. and Stamnes, K. (1980), "Arctic Haze: Perturbation of the Polar Radiation Budget," *Ann. N.Y. Acad. Sci. 338*, p. 533.
3. Porch, W.M. and MacCracken, M.C. (1982), "Parametric Study of the Effects of Arctic Soot on Solar Radiation," *Atmos. Environ. 16*, p. 1365.
4. Valero, F.P.J., Ackerman, T.P. and Gore, W.J.Y. (1984), "The Absorption of Solar Radiation by the Arctic Atmosphere During the Haze Season and Its Effects on the Radiation Balance," *Geophys. Res. Lett. 11*, p. 465.
5. Hansen, A.D.A. and Rosen, H. (1984), "Vertical Distributions of Particulate Carbon, Sulfur and Bromine in the Arctic Haze and Comparison with Ground-Level Measurements at Barrow, Alaska," *Geophys. Res. Lett. 11*, p. 381.
6. Hansen, A.D.A., Rosen, H., and Novakov, T. (1982), "Real-Time Measurement of the Absorption Coefficient of Aerosol Particles," *Appl. Opt. 21*, p. 3060.
7. Raatz, W.E. and Schnell, R.C. (1984), Aerosol Distributions and an Arctic Aerosol Front Dur-

ing AGASP: Norwegian Arctic," *Geophys. Res. Lett. 11*, p. 373.
8. Harris, J.M. (1984), "Trajectories During AGASP," *Geophys. Res. Lett. 11*, p. 453.
9. Rahn, K.A. and McCaffrey, R.J. (1980), "On the Origin and Transport of the Winter Arctic Aerosol," *Ann. N.Y. Acad. Sci. 388*, p. 486.
10. Iversen, T. (1984), "On the Atmospheric Transport of Pollution to the Arctic," *Geophys. Res. Lett. 11*, p. 457.

Primary Oxidants—Results from Laboratory and Field Experiments*

W.H. Benner and T. Novakov

Chemical reactions that oxidize SO_2 dissolved in fog and rain droplets or in a layer of water that covers many particles in the troposphere are called heterogeneous-type reactions and are considered to be important in the formation of tropospheric sulfate. Because some of the reported[1] SO_2 oxidation reactions[2] are relatively slow at the concentrations of reactants found in the troposphere, long-range transport of pollutants is invoked to explain the concentrations of sulfate observed. Long-range transport supplies the reaction time necessary for the relatively slow reactions to produce the observed sulfate concentrations. In contrast, reactions that are much faster require respectively less reaction time to produce the same observed sulfate concentrations. The oxidation of dissolved SO_2 by dissolved H_2O_2 can be one of the fastest heterogeneous SO_2 oxidation reactions when enough H_2O_2 is available. In a recent publication,[1] we reported that incomplete combustion is a source of H_2O_2. Prior to this, it was generally assumed that gas-phase photochemical reactions produced all of the H_2O_2 found in the troposphere.

This report describes our continuing investigation of heterogeneous SO_2 oxidation reactions and focuses on the oxidation of SO_2 by gaseous oxidants produced during combustion of hydrocarbon fuels. It builds on work reported in previous annual reports[3,4] and summarizes experiments we conducted to determine how closely the heterogeneous oxidation of SO_2 is coupled to combustion emissions. The results presented here were also presented at a recent symposium on heterogeneous chemistry.[5]

*This work was supported by the Director, Office of Energy Research, Office of Health and Environmental Research, Physical and Technological Research Division of the U.S. Department of Energy under Contract No. DE-AC03-76SF00098 and by the National Science Foundation under Contract ATM 83-15442.

ACCOMPLISHMENTS DURING FY 1985

Filtered combustion gases from a laboratory diesel fuel burner and from two diesel-powered cars were individually sampled into several different aqueous solutions, using a technique described previously.[3] The solutions were H_2O, 1 mM H_2CO (pH = 5), 5 mM $CO_3^=$ (pH = 10), and a suspension of activated carbon in water. The H_2CO solution was used to quench the reactions between oxidants and S(IV) by converting the S(IV) to hydroxymethane sulfonate ion. The carbonate solution was used to quench the reaction between H_2O_2 and S(IV) by application of the fact that the rate constant for this reaction is 10^4 times slower at pH = 10 than at pH = 4.[1] The percent oxidized S, $SO_4^= \times 100\%/[S_{TOT}]$, in the samples was determined by ion chromatography, and the $[H_2O]$ was determined by a colorimetric technique.[6] No attempt was made to measure the amount of combustion water collected during sampling because the condensation of combustion water in the bubbler contributed a negligible dilution factor.

In a small diesel fuel burner, fuel and air were premixed and heated to $\approx$150°C before combustion. The fuel was introduced into the burner at $\approx$5 ml/min and, by adjusting the air flow rate, the air to fuel (A/F) ratio could be varied between 2 and 10. Optionally, a flame quencher (a water-cooled stainless steel surface) could be placed in the flame. The emissions from this burner were diluted with a large excess of air and only a small fraction of the diluted mixture was sampled through a bubbler. Exhaust gases from the diesel-powered cars were sampled directly without dilution. This sampling system was constructed from stainless steel and glass and was heated to preclude condensation of H_2O in the sampling tubes. Control experiments in which SO_2 and CO_2 from a cylinder were sampled simultaneously at concentrations and conditions similar to those present in the combustion streams and immediately analyzed showed the percent oxidized sulfur always to be less than 0.5% for samples collected in H_2CO, H_2O, and $CO_3^=$.

A set of field experiments was conducted by collaborators in Ljubljana, Yugoslavia, to see if detectable concentrations of primary oxidants could be detected in ambient air. The Ljubljana site was chosen because of an ongoing joint aerosol sampling project and because high levels of air pollution are commonly observed in winter due to poorly controlled coal burning. Filtered ambient air was bubbled through water for 3 hours, and H_2CO was then added to prevent oxidation of dissolved SO_2 by air (O_2). Later the samples were analyzed for percent oxidized sulfur.

Diesel Fuel Burner Experiments

The results of analysis of samples prepared by absorbing filtered diesel burner combustion gases into the three collection solutions is shown in the top half of Table 1. In these fuel burner experiments, a decrease in the A/F ratio increased the percent oxidized S. Thermal quenching of the flame also increased the percent oxidized S over that amount of S oxidized in nonquenched flame samples (Table 1).

Sampling filtered combustion gases into a suspension of an activated carbon (RB-1), suspension of which can catalytically oxidize dissolved SO_2, greatly increased the percent of oxidized SO_2. In these suspension experiments, a decrease in the A/F ratio from 10 to 2 also decreased the percent oxidized S, a finding that is opposite to that observed for unfiltered combustion gases collected in H_2O. The effect can be explained by the conversion of the normally hydrophilic RB-1 particles to hydrophobic ones as evidenced by their floating out of suspension. An A/F ratio of 2 caused more particles to become hydrophobic than did combustion gases from a flame having an A/F ratio of 10.

Combustion gas samples collected in H_2CO solutions showed a reproducible percent oxidized S, regardless of flame A/F ratio and thermal quenching. However, the 2% values observed for all samples of diesel fuel burner gases collected in H_2CO is above the 0.5% control value. This demonstrates that H_2CO chemically quenches the oxidation but not completely. Since H_2CO reduced the percent oxidized S, gas-phase oxidation of SO_2 before it is absorbed into water in these experiments can probably be discounted.

Much higher percentages of oxidized S were observed in filtered combustion gas samples collected in $CO_3^=$ solution. The cause for this can only be speculated at this time. The reaction between H_2O_2 and dissolved SO_2 at pH = 10 is many times slower than at the pH of the H_2O samples (pH = 3–4), so this increased oxidation can't be attributed to H_2O_2. NO_2^- is present in these samples, but the rate of reaction of NO_2^- with dissolved SO_2 also slows with increasing pH.[2] It suggests that a different oxidant may be involved. This finding could be of interest in materials damage studies of marble.

Diesel Car Experiments

The results of the analysis of samples prepared by absorbing filtered diesel car exhaust into the three collection solutions is shown in the bottom half of Table 1. In these experiments combustion conditions (i.e., A/F ratios) could not be varied; however, each car was made by a different manufacturer and maintained by separate owners.

The percent oxidized S in the H_2O samples was as large as 13 (diesel-2). H_2CO did not quench the oxidation of dissolved SO_2 in these samples as well as it did in the diesel fuel burner experiments.

Table 1.

	% S oxidized		
Conditions	H_2O	H_2CO	$CO_3^=$
Burner flame, not quenched, A/F = 2	4	2	27
Burner flame, not quenched, A/F = 10	2	2	
Burner flame, quenched, A/F = 2	9	2	
Burner flame, quenched, A/F = 10	3	2	
Diesel car 1	6	7	72
Diesel car 1 + 0.1 g/l RB-1	13		
Diesel car 2	13	9	40
Diesel car 2 + 0.1 g/l RB-1	25		

Again, samples collected in $CO_3^=$ solution showed much more oxidized S than did samples collected in H_2O. The speculation is also the same, i.e., an oxidant other than H_2O_2 was activated at this pH.

Repeated analysis of the samples over several hours showed that the percent S oxidized initially reflects only part of the chemistry that occurs in these samples. From Fig. 1, it can be seen that the exhaust gases from these two cars were very different in composition with respect to SO_2 oxidants. Starting first with the samples collected in H_2CO solution, little change in percent of oxidized S occurred with time. Although each car exhaust sample showed different initial percentages of oxidized S, the H_2CO allows only negligible S to be oxidized over the ensuing 2–3 hours. The same was observed for samples collected in $CO_3^=$ solution.

Samples that were not chemically quenched with H_2CO or $CO_3^=$ show large differences when diesel-1 and diesel-2 samples are compared. Exhaust from diesel-1 produced substances that continued to oxidize dissolved SO_2 while diesel-2 did not. By comparing H_2O samples of filtered combustion gases, diesel-1 produced a solution that continued to oxidize S, but this was not observed for diesel-2. In the water sample for diesel-1, 45% of the S was oxidized after 2 hours. Only differences in combustion for the two car engines can be invoked to explain these observations.

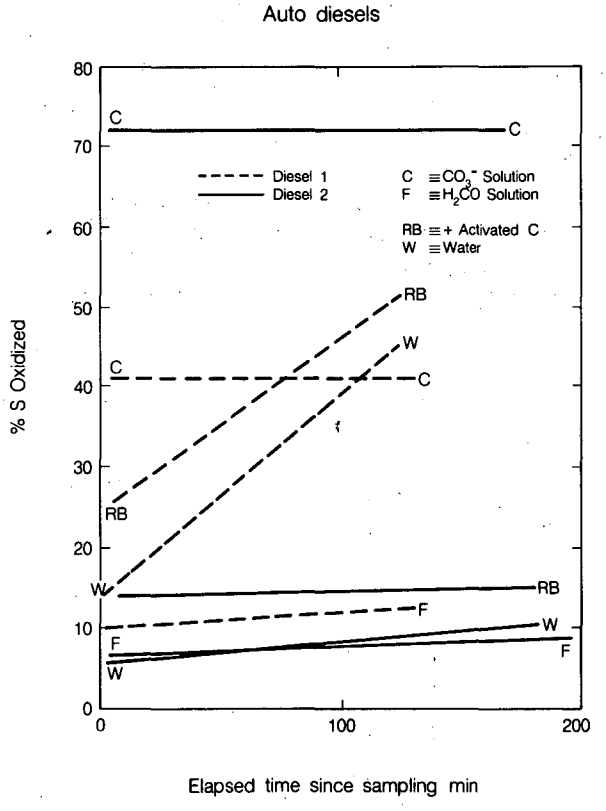

Figure 1. Oxidation of sulfur in bubbler samples. (XBL 859-11696)

Hydrogen Peroxide Sampling

Filtered exhaust samples collected from the laboratory diesel burner into H_2O, H_2CO, and $CO_3^=$ contained no detectable concentrations of H_2O_2 (H_2O_2 detection limit 10^{-8} M). All the filtered exhaust samples from the diesel cars, however, contained H_2O_2. The maximum H_2O_2 concentration was 5×10^{-6} M as compared to 1×10^{-4} M dissolved S. Comparison of collection solutions showed the highest H_2O_2 concentrations in the $CO_3^=$ solutions.

Field Experiments

Twenty samples of filtered ambient air were bubbled through H_2O and chemically quenched with H_2CO immediately after collection. Approximately 3 weeks later, these samples were analyzed at Technical University in Vienna and then reanalyzed 5 weeks later at LBL. Comparison of TUV and LBL analyses showed that a large increase in the percent S oxidized occurred between analyses. In some samples, no residual S(IV) was detected at LBL. Control experiments in which SO_2 alone was collected in H_2O and similarly quenched with H_2CO showed only 6% of the dissolved SO_2 to be oxidized after 3 months. Clearly the H_2CO quenching was not adequate for these samples. Extrapolation of the data backwards in time to sampling time indicated that as much as 20% of the dissolved S could have been oxidized initially; but because several of the extrapolations yielded negative percents, the results are questionable for assaying the presence of primary oxidants in this source-dominated air mass.

PLANNED ACTIVITIES FOR FY 1986

This work has demonstrated that the oxidation of SO_2 in tropospheric droplets can be closely connected with combustion efficiency. We have started to construct a fog chamber in which combustion H_2O in the presence of combustion gases is condensed on the combustion particles. Experiments will be conducted to determine the importance of rapid heterogeneous reactions in plumes. Studies at several field locations will be repeated.

REFERENCES

1. Benner, W.H. and Novakov, T. (1985), "Oxidation of SO_2 in Fog Droplets by Primary Oxidants," *Atmos. Environ. 19,* p. 1377.
2. Martin, L.R. (1984), "Kinetic Studies of Sulfite Oxidation in Aqueous Solution," in *SO_2, NO and NO_2 Oxidation Mechanisms,* J. Calvert, Ed., Butterworth, Boston, p. 63.
3. Benner, W.H., McKinney, P.M., and Novakov, T. (1983), "Evidence for Primary Oxidants of SO_2," in *Energy and Environment Division Annual Report, FY 1982,* LBL-15298, p. 3.
4. Benner, W.H. and Novakov, T. (1985), "Oxidation of SO_2 in Fog Droplets by Primary Oxidants," in *Applied Science Division Annual Report, FY 1984,* LBL-18754, p. 3.
5. Benner, W.H. and Novakov, T. (1985), "Primary Oxidants—Results from Field and Laboratory Studies," in *Proc. Symp. on Heterogeneous Processes in Source-Dominated Atmospheres,* p. 26, LBL-20261.
6. Madsen, B.C. and Kromis, M.S. (1984), "Flow Injection and Photometric Determination of Hydrogen Peroxide in Rainwater with N-Ethyl-N-(sulfopropyl)aniline Sodium Salt," *Anal. Chem. 56,* p. 2849.

Empirical Evidence for Heterogeneous SO_2 Oxidation in Ljubljana, Yugoslavia*

M. Bizjak,† V. Hudnik,† A.D.A. Hansen, and T. Novakov

Most previous work on sulfate aerosols was devoted either to SO_2 conversion during long-range transport or to sulfate formation in urban atmospheres where, because of the high degree of environmental regulations and controls, the pollutant concentrations are relatively low. Much less is known about sulfate chemistry in highly polluted source-dominated urban atmospheres, where scattered and usually inefficient small combustion furnaces are major sources of pollutants. Such atmospheres, because of high concentrations of both particles and gases, are more likely to provide conditions for heterogeneous reactions and therefore a greater probability for demonstrating their occurrence and inferring the contributions of local sources to aerosol sulfates. The research described in this report deals with certain aspects of heterogeneous formation of aerosol sulfate in Ljubljana, Yugoslavia. This location is well suited for such a study because of high pollutant concentrations, especially during the winter. Because relatively low-grade coal is burned in inefficient combustors, large soot concentrations are observed in the winter. During the relatively cold winters, inversions with characteristic pollution-induced urban fog occur almost daily.

*The portion of this work done at LBL was supported by the Director, Office of Energy Research, Office of Health and Environmental Research, Physical and Technological Research Division of the U.S. Department of Energy under Contract No. DE-AC03-76SF00098 and by the National Science Foundation under Contract No. ATM-8315442. This work is a summary of LBL-20953, accepted for publication by *Atmospheric Enviroment.*

†Boris Kidrich Institute of Chemistry, Ljubljana, Yugoslavia.

ACCOMPLISHMENTS DURING FY 1985

Two kinds of 24-hour ground-level aerosol samples were collected in Ljubljana on two filters in parallel for different analyses. The filter materials used were quartz fiber (Pallflex type 2500 QAO, prefired for 6 hours at 700°C to remove combustible carbon) and cellulose membrane (Millipore type RATF, 1.2-μm pore size). Total samples, i.e., without size segregation, were collected during the 1981/82 sampling period. During the 1983/84 period, size-segregated 24-hour filter samples corresponding to cutoffs of < 0.3 μm and 2.0 μm were collected on the quartz afterfilters of two single-stage impactors. Two such units were used, producing one filter sample from which all particles of effective diameter greater than 0.3 μm have been excluded and another representing particles smaller than 2 μm. The impaction surfaces were greased to minimize particle bounce. The sampling was performed at the Hydrometeorological Institute in central Ljubljana. Meteorological data consisting of wind speed and direction, temperature, and relative humidity were collected at the site, as well as 24-hour average SO_2 concentrations by a conventional titration method.

The exposed quartz filters were analyzed for total carbon and sulfur by combustion followed by relative conductometric determination of SO_2 and CO_2

at the B. Kidric Institute in Ljubljana. Portions of the same filters were also analyzed for total carbon at Lawrence Berkeley Laboratory by a combustion technique, and the Millipore filters were analyzed for sulfur and trace elements by x-ray fluorescence.

The seasonal pattern of pollutants in Ljubljana is illustrated in Fig. 1a and b, where biweekly SO_2 and particulate sulfur, S_p, concentrations are plotted as a function of time during the 1981/82 sampling season. The particulate sulfur to gaseous sulfur ratios, S_p/S_g, for this period are shown in Fig. 1c. This ratio, which can be viewed as a measure of SO_2-to-sulfate conversion, is about four times higher in the summer (~0.4) than in the winter (~0.1), indicating a different chemistry during the two seasons.

In the analysis of the data, we will also make use of another ratio: particulate sulfur to particulate carbon, S_p/C_p. In Ljubljana, as previously demonstrated,[1] total particulate carbon and soot concentrations are approximately equivalent. As a primary combustion-generated particulate pollutant, soot can be used as a conservative tracer for the products of incomplete combustion.[2] The S_p/C_p ratio can therefore be used to infer the relationship between secondary sulfates and primary source emissions. The S_p/C_p ratios for the 1981/82 sampling period are shown in Fig. 1d. The variations of these ratios are qualitatively similar to the variations of S_p/S_g ratios but with less pronounced maxima. Furthermore, there seems to be a clear difference in these ratios between Nov./Dec. and Jan./Feb., with the latter period having higher values.

The average 24-hour relative humidity was high, usually exceeding 80%, and the wind speed was generally low (< 1 m sec^{-1}) during both the Nov.-Dec. and Jan.-Feb. periods. The only drastic difference in meteorology corresponding to low and high S_p/C_p ratios was the ambient temperature. This is seen from Fig. 2, where S_p/C_p ratios, average daily relative humidity, and temperature are plotted for December 1981 and January 1982. This figure shows that the high S_p/C_p ratios during January correspond to periods with high humidity and persistent subzero temperatures. In our view, this observation represents the manifestation of a heterogeneous liquid-phase mechanism of SO_2 oxidation. Under conditions of high humidity and low wind speed, subzero temperatures would enhance condensation of water droplets on combustion nuclei and increase the solubility of SO_2. Such conditions are known to

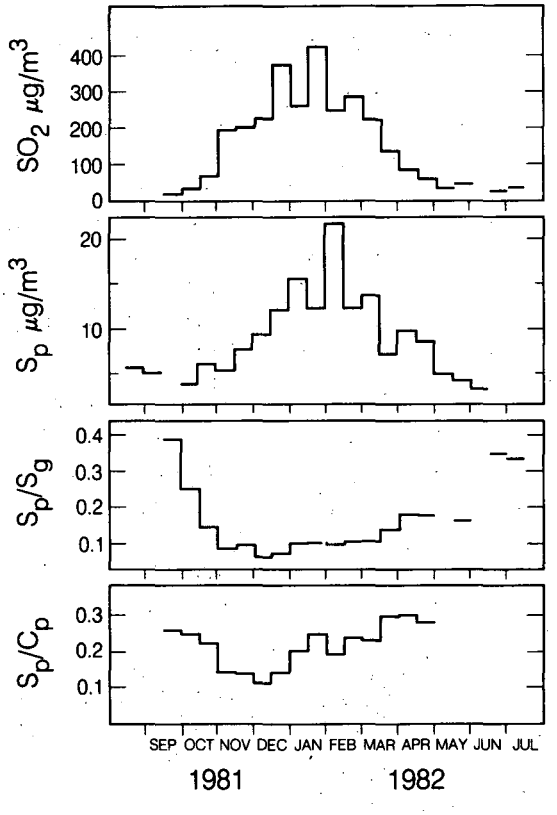

Figure 1. Biweekly concentrations of SO_2, particulate sulfur (S_p), particulate to gaseous sulfur ratios (S_p/S_g), and particulate sulfur to particulate carbon ratios (S_p/C_p) for the 1981–1982 sampling season. (XBL 8411-8924A)

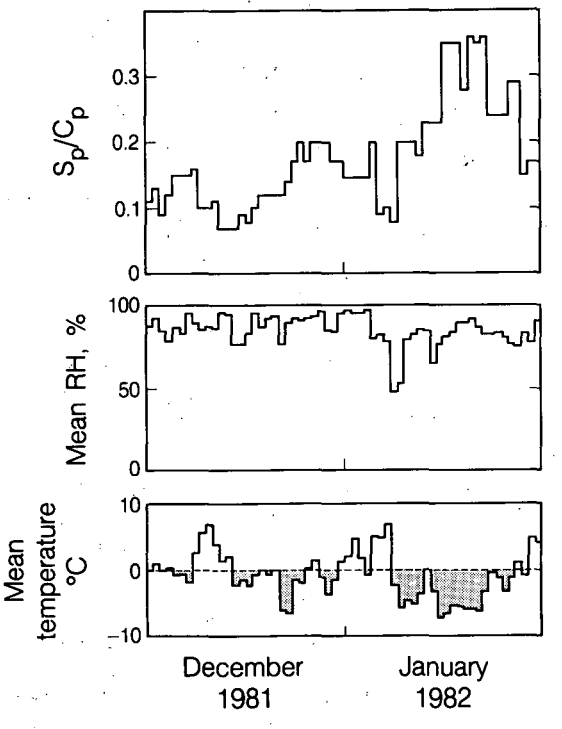

Figure 2. Dependence of the particulate sulfur to carbon ratio on mean relative humidity and ambient temperature. (XBL 859-12125)

favor the formation of urban fog, consisting of supercooled droplets.

The effect of high humidity and low ambient temperatures on enchanced sulfur formation observed from 1981/82 data has been confirmed during the winter of 1983/84 with size-segregated sampling. This is illustrated in Fig. 3, where S_p/C_p, and S_p/S_g ratios (for particle diameters < 2 μm), average temperature, relative humidity, and SO_2 concentrations for February 1984 are shown. The second half of the month showed a pronounced increase in the S_p/C_p and S_p/S_g ratios. It is clear from the figure that during this period the average daily temperatures were consistently below 0°C and that the increase in the S_p/C_p and S_p/S_g ratios occurred after the relative humidity exceeded approximately 65%. Such dependence on relative humidity has been shown to be characteristic of heterogeneous reactions.[3] It should be noted that during this period, the SO_2 concentration remained approximately constant, and therefore the apparent increase of the sulfate production is related entirely to the physical changes in the atmosphere, i.e., the liquid water content.

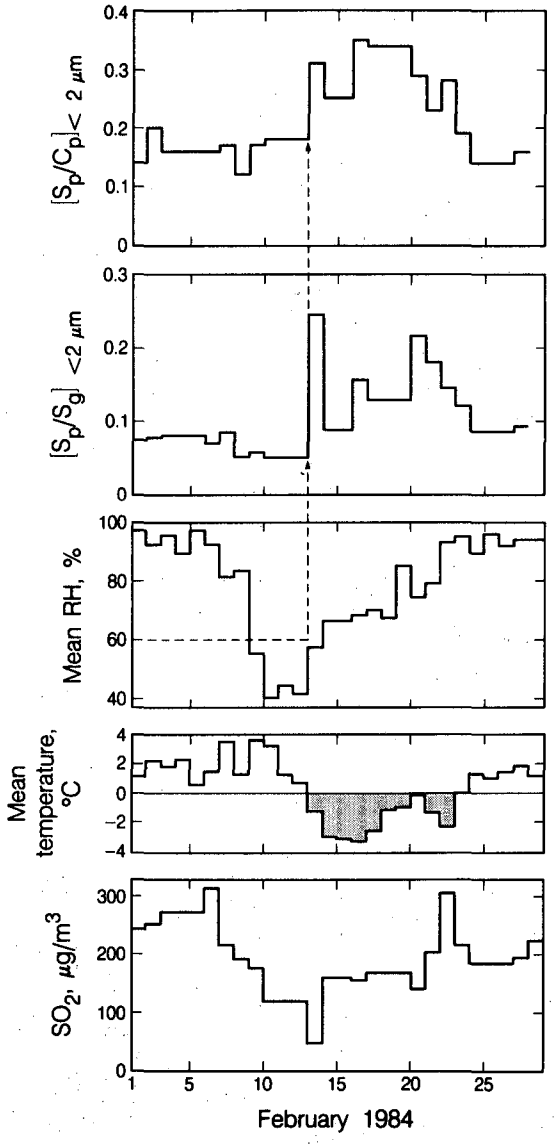

Figure 3. Dependence of particulate sulfur (S_p) to particulate carbon (C_p) and gaseous sulfur (S_g) ratios on mean daily relative humidity, temperature, and SO_2 concentration for February 1984. The data are for the < 2-μm size cut. An increase in S/C_p and S_p/S_g ratios is seen when the temperature is below 0°C and the relative humidity exceeds 60%. (XBL 859-12124)

The observations described thus far can be qualitatively explained as follows: Water may condense on soot (or other) particles in a plume, forming a layer of liquid water on the particle. The SO_2 in the plume will be dissolved in this layer and oxidized to sulfate by one or more oxidation mechanisms. If the ambient conditions, such as relative humidity and temperature, do not favor additional water condensation during transport to the receptor site, the entire oxidation would possibly occur in the first phases of plume development. The resulting sulfate concentration would be related to the volume of the original layer of condensed water and hence to soot concentration. However, if conditions favor additional condensation (e.g., high relative humidity and low temperature), particle-associated liquid water and its S(IV) content would continue to exist both in the plume and during transport, resulting in a S_p/C_p ratio greater than in conditions of low humidity.

PLANNED ACTIVITIES FOR FY 1986

We plan to continue aerosol sampling in Ljubljana using LBL-fabricated samplers that collect filters over preset time intervals of as little as 1/2 hour. These samples will allow a time-resolved analysis of the interrelationship of aerosol species and meteorological changes. In parallel with the aerosol sampling, we plan to collect bubbler samples to study oxidants that may be present in the gas phase.

REFERENCES

1. Bizjak, M., Hudnik, V., Gomiscek, S., Hansen, A. D. A., and Novakov, T. (1984), "Aerosol Studies in Ljubljana Under Conditions of Combustion-Derived Winter Pollution," *Sci. Total Environ. 336*, p. 377.
2. Novakov, T. (1981), "Microchemical Characterization of Aerosols," in *Nature, Aim and Methods of Microchemistry*, H. Malissa, M.

Grasserbauer, and R. Belcher, Eds., Springer-Verlag, New York, p. 141.
3. McMurry, P.H. and Wilson, J.C. (1983), "Droplet Phase (Heterogeneous) and Gas Phase (Homogeneous) Contributions to Secondary Ambient Aerosol Formation as a Function of Relative Humidity," *J. Geophys. Research 88*, p. 5101.

Kinetics of Soot-Catalyzed SO_2 Oxidation in Aqueous Systems*

L.A. Gundel, W.H. Benner, and T. Novakov

Because of its potential significance for atmospheric chemistry, oxidation of sulfur dioxide by carbon particles has received considerable attention, and assessments of its importance range from significant (under nonphotochemical conditions)[1] to negligible.[2] A recent review[3] using rate data obtained at LBL[4] concludes that this reaction can compete with H_2O_2 at pH < 6, only when the concentration of carbon exceeds 0.1 g l^{-1}. Such conditions frequently occur in polluted urban atmospheres.[5,6] Our earlier work[7] has shown that the differences in catalytic activity for different carbons could be ascribed to the capability of carbon surfaces to adsorb oxygen and that this adsorbed oxygen is the actual oxidant of dissolved SO_2. Fresh combustion carbon particles may therefore be more reactive than aged particles.

This report describes measurements of the reaction rate for two carbons that differ greatly in reactivity. The kinetic data are interpreted by a proposed mechanism for carbon-catalyzed oxidation. This complete kinetic information should help in assessing the importance of the conversion of SO_2 to $SO_4^=$. The results are used to estimate conversion rates for dissolved S(IV) under polluted atmospheric conditions.

ACCOMPLISHMENTS DURING FY 1985

Commercially available activated carbons Nuchar-SN (Westvaco) and RB1 (Norit) were used in this study. A sample of each carbon was ground overnight in an agate ball mill, washed in boiling de-ionized water, filtered, and dried at 100°C. Portions of each washed carbon were heated at 1000°C in N_2 for 15 minutes, cooled to room temperature, and exposed to room air for about half an hour before reaction. Earlier work[7] showed that this treatment cleaned the surface, decreased total oxygen content, and enhanced the catalytic reactivity. The purpose of heating in this experiment was preparation of carbons with reproducible oxidation behavior that would be more like freshly generated soot particles.

The oxidation rate of S(IV) was measured in aqueous slurries of these carbons. The S(IV) was prepared from $Na_2S_2O_5$ that hydrolyzes to HSO_3^- in solution. Before reaction, slurries of carbons were sonicated for 15 minutes to disperse and equilibrate the particles with dissolved air. The reaction began when 1.0 μl of the S(IV) solution was added from a syringe to 9.0 ml of suspended particles with continuous stirring. After mixing, the initial S(IV) concentration, $[S(IV)]_o$, was 3.8×10^{-4} M for all experiments; and the concentration of carbon particles was 1.0 g l^{-1}. To quench the reaction, 5.0 μl of formaldehyde was injected into the reaction mixture before filtration. The HCHO reacted with S(IV) to form hydroxymethane sulfonate, a stable adduct. The filtrate was analyzed by ion chromatography for S(IV) and $SO_4^=$. The filtered particles were dried, weighed, and extracted with water to measure levels of adsorbed $SO_4^=$. With this procedure we were able to study reaction times as short as 5 seconds; results obtained for times $\geq$ 1 minute were indistinguishable from those obtained using filtration (i.e., without adding HCHO) to stop the reaction, as had been done in earlier studies.[7,8]

Figure 1 shows S(IV) and $SO_4^=$ concentrations as a function of time for Nuchar-SN. Figure 2 shows the data for RB1. The reaction has the same features as reported earlier[7,8]: an initial rapid drop in [S(IV)] followed by a slower step whose rate is constant and independent of [S(IV)]. For RB1, the first step accounts for the whole reaction. No second step was observed for the experimental conditions used.

The decrease in [S(IV)] was accompanied by a simultaneous increase in $[SO_4^=]$ concentration. For Nuchar, after 20 minutes the $[SO_4^=]$ in solution was about 40% of the decrease in [S(IV)] concentration. About half of this missing $[SO_4^=]$ was extracted with water from the filtered particles. After 20 minutes in contact with RB1, the [S(IV)] had dropped to zero,

*This work was supported by the Director, Office of Energy Research, Office of Health and Environmental Research, Physical and Technological Research Division of the U.S. Department of Energy, under Contract No. DE-AC03-76SF00098 and by the National Science Foundation under Contract No. ATM 83-15442.

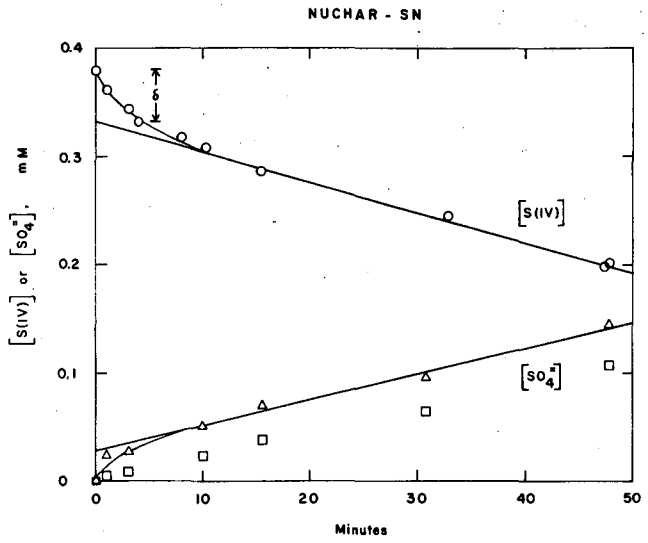

Figure 1. Kinetic data for Nuchar-SN. The circles represent [S(IV)] vs. time. The squares represent $[SO_4^=]$ in solution; the triangles correspond to the sum of $[SO_4^=]$ in solution and $[SO_4^=]$ extracted from the dried particles after reaction. The straight lines represent linear regression lines for $t \geq 10$ minutes. (XBL 863-775)

and the $[SO_4^=]$ in solution was about 70% of the initial [S(IV)]. Here, about one-third of the missing sulfate was extracted from the particles. At this point we have no further data to indicate whether the missing sulfur was entirely adsorbed on the particles or partially present in solution as a species other than S(IV) or $SO_4^=$. These mass balance considerations are not taken into account in the subsequent discussion.

To interpret the kinetic data, we are extending the mechanism proposed by Brodzinsky *et al.*[8] These authors found that the slow part of the reaction could be explained as a sequence of three adsorption steps followed by the decomposition of the adsorbate to $SO_4^=$. These adsorption steps are formation of a surface oxygen species $Cx \cdot O_2$, which is in equilibrium with dissolved oxygen, and sequential adsorption of two S(IV) ions at the same site to form $Cx \cdot O_2 \cdot (S(IV))_2$. Two $SO_4^=$ ions diffuse away from the surface. The decomposition of $Cx \cdot O_2 \cdot (S(IV))_2$ is the rate-determining step. At equilibrium and at sufficiently high [S(IV)] the rate will be zero order in [S(IV)]. As the [S(IV)] drops, the rate will change to first order and then second order in [S(IV)].

For Nuchar-SN, when the initial concentration $[S(IV)]_o = 3.8 \times 10^{-4}$ M, the slow step has zero order dependence on [S(IV)]. The straight line in Fig. 1 can be represented by

$$[S(IV)]_z = [S(IV)]_o - \delta + k_z t, \qquad (1)$$

where $[S(IV)]_z$ is the S(IV) concentration attributable to this step and k_z is its rate constant.

The first step causes the decrease in [S(IV)] from $[S(IV)]_o$ to $[S(IV)]_z$. δ is the decrease in [S(IV)] due to the first step, defined as:

$$\delta + [S(IV)]_o - [S(IV)]_z \quad \text{at } t = 0. \qquad (2)$$

To investigate the first step, we have subtracted the contribution of the second, zero order step and plotted the logarithm of the difference ($[S(IV)] - [S(IV)]_z$) vs. time in Fig. 3. The straight line indicates that the first step has first order dependence on the difference between [S(IV)] and $[S(IV)]_z$. This means that the concentration of $Cx \cdot O_2 \cdot (S(IV))_2$ is higher during the rapid first step than it will be after the adsorption steps have reached equilibrium. This high $[Cx \cdot O_2 \cdot (S(IV))_2]$ could be due to either or both of these effects:

(a) The first step uses $Cx \cdot O_2$ that was formed from the gas-phase adsorption of oxygen before reactants mixed, and the initial $[Cx \cdot O_2]$ is higher than the equilibrium value.

(b) During the first step, the concentration of $Cx \cdot O_2 \cdot (S(IV))_2$ has not built up high enough to cause significant dissociation without reaction; i.e., before equilibrium is

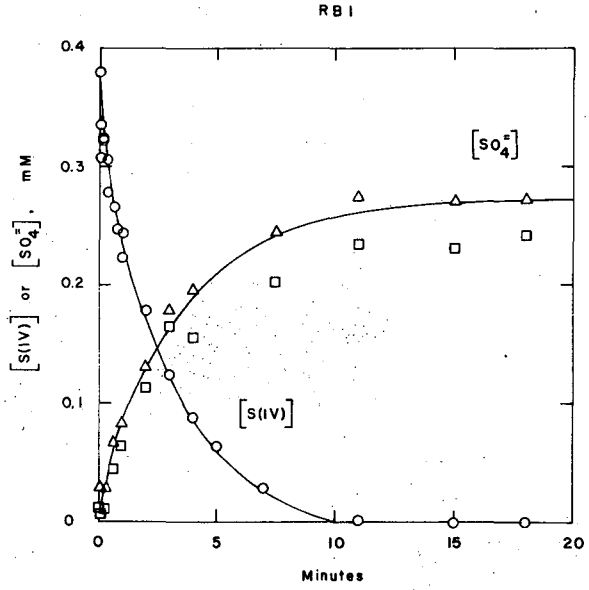

Figure 2. Kinetic data for RB1. The circles, squares, and triangles correspond to those in Fig. 1. (XBL 863-772)

established, the forward rate of the adsorption step to form $Cx \cdot O_2 \cdot (S(IV))_2$ is faster than the reverse rate to $Cx \cdot O_2 \cdot S(IV)$ and S(IV).

For RB1, Figs. 2 and 4 show that the reaction is first order in [S(IV)] throughout its course; i.e., there is no differentiation between the first and second step. This may mean that the third adsorption step never reaches equilibrium or that the reaction is so fast that the dissociation of $CxO_2 \cdot (S(IV))_2$ without reaction is unimportant. Either of these interpretations is consistent with first order dependence of the rate on [S(IV)].

Table 1 provides a summary of the rate data. The initial rate of reaction R_i, the first order rate constant k_1, and the zero order rate constant k_2 are given.

If carbon particles in polluted atmospheres have the range of activity represented by these two activated carbons, can this heterogeneous mechanism play an important role in atmospheric oxidation of SO_2 in water droplets containing soot? Using conditions representative of highly polluted urban atmospheres,[5] we have estimated the conversion time for [S(IV)] in two ways. First, $t_{0.95}$ represents the time necessary to reduce [S(IV)] from 3.80×10^{-4} M to 5% of this value, using

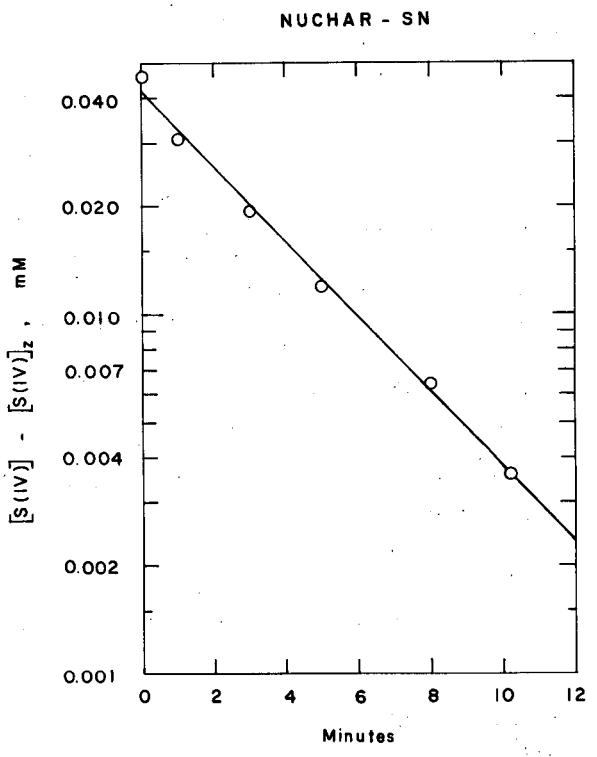

Figure 3. Semilogarithmic plot of the first step of the reaction for Nuchar-SN. (XBL 863-774)

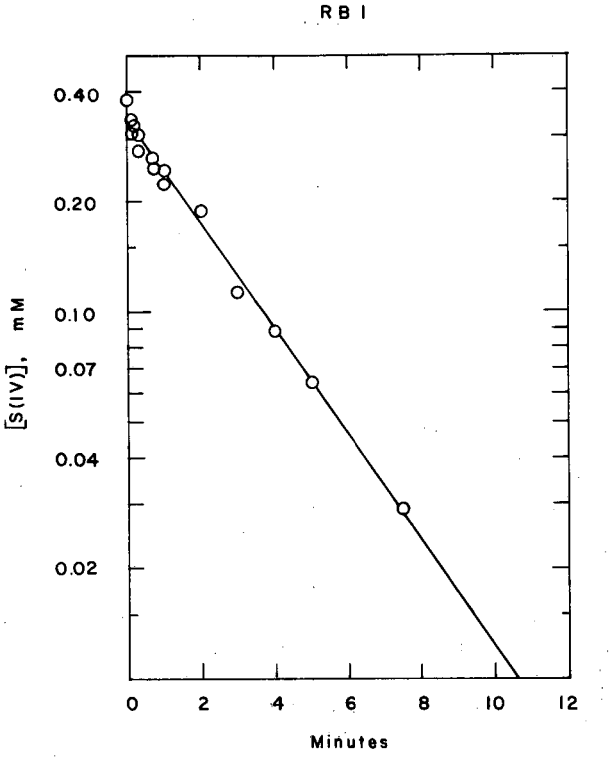

Figure 4. Semilogarithmic plot of the concentration of [S(IV)] vs. time for RB1. (XBL 863-773)

$$[S(IV)] = [S(IV)]_o - \delta(1 - \exp(-k_1 t)) + k_z t \quad (4)$$

for Nuchar-SN and RB1. For RB1 we used

$$[S(IV)] = [S(IV)]_o \exp(-k_1 t). \quad (5)$$

We also calculated the conversion time using the initial reaction rate R_i, the tangent to the curves of Figs. 1 and 2 at t = 0. This corresponds to the rate of reaction when the concentration of [S(IV)] is constant at its initial value, as occurs in water droplets that are in equilibrium with gaseous SO_2. The atmospheric conditions chosen are $[SO_2(g)] = 400\ \mu g\ m^{-3}$; $[C] = 100\ \mu g\ m^{-3}$; liquid water content (LWC) = $0.1\ g\ m^{-3}$; particulate sulfur to gaseous sulfur ratio, $S_p/S_g = 0.1$; and $[SO_4^{=}] = 6.25 \times 10^{-3}$ M. $[S(IV)] = 3.8 \times 10^{-4}$ M corresponds to the expected concentration at pH = 5 in equilibrium with $[SO_2(g)] = 400\ \mu g\ m^{-3}$.[9] R_i, $t_{0.95}$, and t_i are given in Table 1. For Nuchar-SN these times vary from 2 to 6 hours. For RB1 they are between 10 minutes and 1 hour. These results indicate that carbon could play a significant role in aqueous oxidation of SO_2 under such conditions.

Table 1. Rate data for oxidation of S(IV) in aqueous slurries of two activated carbons.

Carbon	R_i ($M\ g^{-1}s^{-1}$)	k_1 ($g^{-1}s^{-1}$)	k_z ($M\ g^{-1}s^{-1}$)	$\frac{[SO_4^=]^a}{[S(IV)]_o-[S(IV)]}$	$t_{0.95}{}^b$	$t_i{}^c$
Nuchar-SN (1000°)	2.85×10^{-7}	4.00×10^{-3}	4.70×10^{-8}	0.44	1.9 hr	6.1 hr
RB1 (1000°)	1.85×10^{-6}	4.87×10^{-3}	—	0.62	10 min	56 min

[a] $[SO_4^=]/([S(IV)]_o - [S(IV)])$ is the fraction of the decrease in [S(IV)] that appears as $[SO_4^=]$ in solution for a reaction time of 20 minutes, when $[S(IV)] = 3.80 \times 10^{-4}$ M.

[b] $t_{0.95}$ is the time necessary to reduce [S(IV)] from its initial value of 3.80×10^{-4} M to 1.90×10^{-5} M, a reduction of 95%.

[c] t_i is the time necessary to produce $[SO_4^=] = 6.25 \times 10^{-3}$ M using the *initial* reaction rate. This assumes $[S(IV)] = 3.8 \times 10^{-4}$ M throughout the reaction, using ambient conditions reported in the text.

PLANNED ACTIVITIES FOR FY 1986

We will complete rate studies directed toward a better understanding of the reaction mechanism. The rate measurement will be extended to higher and lower initial concentrations of S(IV) · (10^{-3} to 10^{-5} M).

REFERENCES

1. Middleton, P. and Kiang, C.S. (1979), "The Relative Importance of Nitrate and Sulfate Aerosol Production Mechanisms in Urban Atmospheres," in *Nitrogenous Air Pollutants: Chemical and Biological Implications,* p. 269, D. Grosjean, Ed., Ann Arbor Science, Ann Arbor.
2. Harrison, R.M. and Pio, C.A. (1983), "Kinetics of SO_2 Oxidation over Carbonaceous Particles in the Presence of H_2O, NO_2, NH_3 and O_3<" *Atmos. Environ. 17,* p. 1261.
3. Calvert, J.G., *et al.* (1985), "Chemical Mechanisms of Acid Generation in the Troposphere," *Nature 317,* p. 27.
4. Chang, S.G., Toossi, R., and Novakov, T. (1981), "The Importance of Soot Particles and Nitrous Acid in Oxidizing SO_2 in Atmospheric Aqueous Droplets," *Atmos. Environ. 15,* p. 1287.
5. Bizjak, M., Hudnik, V., Hansen, A.D.A., and Novakov, T. (1986), *Evidence for Heterogeneous SO_2 Oxidation in Ljubljana, Yugoslavia,* LBL-20953 (submitted to *Atmospheric Environment*).
6. Dod, R.L., *et al.* (1986), *Sulfate and Carbonaceous Aerosols in Beijing, China,* LBL-20954 (submitted to *Atmospheric Environment*).
7. Gundel, L.A., Benner, W.H., and Novakov, T. (1985), "The Role of Surface Oxygen in S(IV) Oxidation by Different Carbons," in *Applied Science Division, Annual Report, FY 1984* (1985), LBL-18754, p. 8.
8. Brodzinsky, R., Chang, S.G., Markowitz, S.S., and Novakov, T. (1980), "Kinetics and Mechanism for the Catalytic Oxidation of Sulfur Dioxide on Carbon in Aqueous Suspensions," *J. Phys. Chem. 84,* p. 3354.
9. Martin, L.M. (1984), "Kinetic Studies of Sulfate Oxidation in Aqueous Solution," in *SO_2, NO and NO_2 Oxidation Mechanisms: Atmospheric Considerations,* p. 63, J.G. Calvert, Ed., Butterworth, Boston.

Sulfate and Carbonaceous Aerosols in Beijing, China*

R.L. Dod, R.D. Giauque, T. Novakov, W.H. Su,† Q.P. Zhang,†, and W.Z. Song†

Beijing air pollution is due principally to coal combustion with a relatively minor contribution from automotive sources. Coal is burned in a large number of individual furnaces and stoves as well as in a number of industrial plants. Because of the low height and large number of chimneys and stacks, the Beijing atmosphere, especially during cold periods, is dominated by local sources. Therefore, studies of pollutant chemistry at such a location may lead to a better understanding of the relation between secondary species such as aerosol sulfate and primary source emissions. Large urban centers such as Beijing, because of the lack of sufficient environmental controls and inefficient combustion technology, may contribute to atmospheric pollution disproportionately more than their per-capita energy consumption may suggest. Chemical characterization of such source-dominated atmospheres may also be useful in assessing their potential impact on the global environment.

ACCOMPLISHMENTS DURING FY 1985

Daily 24-hour filter samples of ambient aerosol particles (<12 μm diameter) were collected in a densely populated part of Beijing, using a sampler constructed at Lawrence Berkeley Laboratory. The sampling program was arranged to cover approximately three seasons—spring, summer, and winter. The spring samples were collected from March through the beginning of May, 1983. Summer samples were gathered during July, 1983; the winter samples, from the end of October, 1983, through February, 1984.

SO_2 measurements were made for a period each morning near the aerosol sampling site using a ThermoElectron Series 43 pulsed fluorescence monitor. In the absence of 24-hour averages, these were taken as estimates of the daily average SO_2 concentration.

Total carbon was determined on the quartz filters by a combustion technique.[1] Temperature-programmed evolved gas analysis (EGA) was used to determine the primary carbon content.[2,3] Particulate sulfur and other trace element concentrations were measured on the cellulose ester filters by energy-dispersive x-ray fluorescence (XRF) spectrometry.[4]

A subset composed of 20% of the samples was analyzed by ion chromatography. Pieces of known area were taken from the quartz filters and extracted in water with sonication for 10 minutes. The extract was filtered and analyzed for anions using a Dionex System 12 ion chromatograph.

The agreement between sulfur concentrations determined by XRF on Millipore filters and sulfate on quartz filters determined by ion chromatography is shown in Fig. 1. The slope of the line is not significantly different from unity, with a correlation coefficient (r^2) of 0.98. This establishes not only that the sulfur in the aerosol particles is practically all in the form of sulfate but also that the parallel filter samples (on quartz and cellulose ester) do contain equivalent particle loadings and that artifact sulfate formation is not significant.

We have previously reported[5] that sulfate behavior in summer is different from that in winter. The summertime sulfate formation mechanism is more efficient, as evidenced by particulate to gaseous

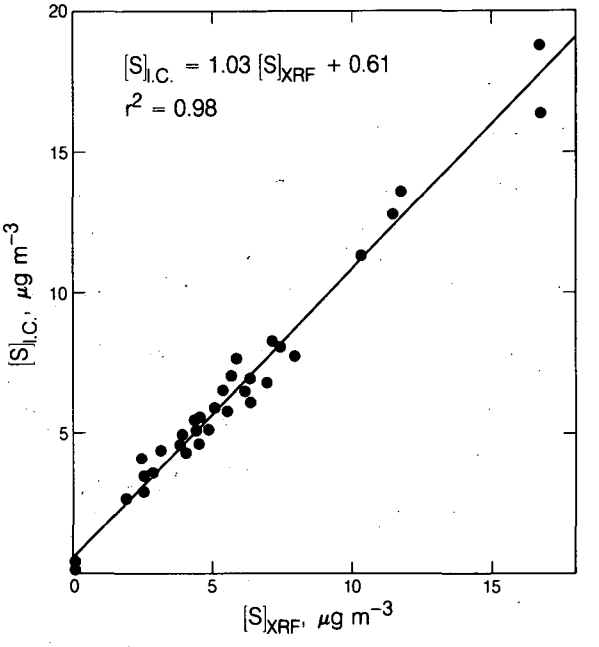

Figure 1. Particulate sulfate (as sulfur) determined by ion chromatography vs. total particulate sulfur determined by x-ray fluorescence for a representative set of samples—Beijing 1983/84. (XBL 859-8982)

*This work was supported by the Office of Energy Research, Office of Health and Environmental Research, Physical and Technological Research Division of the U.S. Department of Energy under Contract No. DE-AC03-76SF00098 and by the National Science Foundation under Contract No. ATM-8315442 and is a summary of a report submitted to *Atmospheric Environment* as LBL-20953.
†Institute of Environmental Chemistry, Academia Sinica, Beijing, People's Republic of China.

sulfur ratios twice those seen in winter. Nevertheless, the maximum absolute concentrations of sulfate are lower during the summer because the concentration of SO_2 available for oxidation is also low. Conversely, a relatively inefficient wintertime mechanism can produce high sulfate concentrations because the SO_2 concentrations are high.

An examination of supplementary meteorological information indicates that there may be a substantial increase in the S/C ratio when relative humidity exceeds 60%, suggesting that a heterogeneous aqueous process (or processes) is involved in the oxidation of SO_2. This finding is illustrated in Fig. 2, where the S/C ratios for the entire sampling period are plotted against the average 24-hour relative humidity. Qualitatively similar behavior has been observed in the United States by McMurry and Wilson.[6]

In Beijing during 1983/84, the relative humidities were markedly higher during summer than in winter or spring. Because high S/C ratios were also observed during summer, we conclude that the summertime SO_2 conversion mechanism could involve liquid water droplets as the medium in which the oxidation reaction takes place. During winter, low ambient humidity will limit both the aqueous-phase reaction time and the liquid water content. Such an explanation, although speculative, could explain the "quasi-primary" wintertime sulfate behavior.

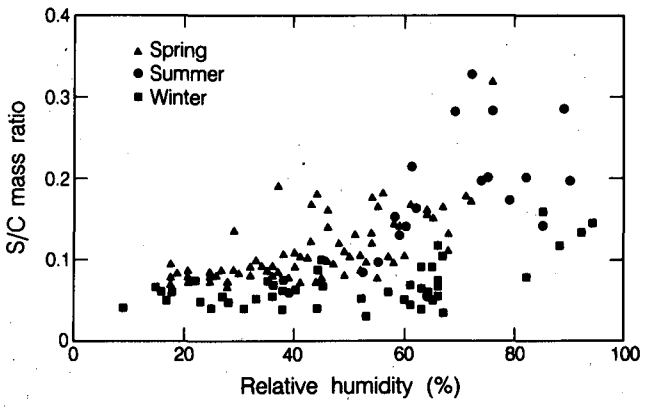

Figure 2. Particulate sulfur to carbon ratios as a function of daily mean relative humidity. (XBL 859-8983)

PLANNED ACTIVITIES FOR FY 1986

A new series of field experiments will be initiated to verify and expand on the results to date, collecting filter samples with better time resolution and with more complete meteorological and pollutant gas measurements.

REFERENCES

1. Huffman, E.W.D., Jr. (1977), "Performance of a New Automatic Carbon Dioxide Coulometer," *Microchem. J. 22*, p. 567.
2. Dod, R.L. and Novakov, T. (1982), "Application of Thermal Analysis and Photoelectron Spectroscopy for the Characterization of Particulate Matter," in *Industrial Applications of Surface Analysis,* L.A. Casper and C.J. Powell, Eds., American Chemical Society, Washington, DC, p. 397.
3. Novakov, T. (1981), "Microchemical Characterization of Aerosols," in *Nature, Aim and Methods of Microchemistry,* H. Malissa, M. Grasserbauer, and R. Belcher, Eds., Springer-Verlag, Vienna, p. 141.
4. Giauque, R.D., Garrett, R.B., and Goda, L.Y. (1979), "Determination of Trace Elements in Light Element Matrices by X-Ray Fluorescence Spectrometry with Incoherent Scattered Radiation as an Internal Standard," *Anal. Chem. 51*, p. 511.
5. Dod, R.L., Giauque, R.D., Novakov, T., and Su, W.H. (1985), "Aerosol Characterization in Beijing, China, 1983-1984," in *Applied Science Division Annual Report, FY 1984*, LBL-18754, p. 12.
6. McMurry, P.H. and Wilson, J.C. (1983), "Droplet Phase (Heterogeneous) and Gas Phase (Homogeneous) Contributions to Secondary Aerosol Formation," *J. Geophys. Res. 88*, p. 5101.

Size Fractionation of Black and Organic Particulate Carbon from Fires*

R.L. Dod, F. Mowrer, L.A. Gundel, R.B. Williamson, and T. Novakov

The concept of "nuclear winter" has been postulated with a number of assumptions regarding the smoke produced by post-nuclear secondary fires.[1] The general premise is that sufficient smoke may be generated and deposited in the stratosphere to cause a decrease in the incident solar energy reaching the earth's surface. Such a change in the net energy balance could potentially cause global cooling. Whether nuclear winter would occur in the aftermath of a nuclear exchange depends largely on the quantity of smoke generated, its distribution in the atmosphere, and the optical characteristics of the smoke produced.

Chemical kinetics during combustion are not understood in the detail necessary to predict smoke production. It has therefore been necessary to develop and use empirical methods to measure smoke generation.[2] Most of these methods have used optical techniques to quantify smoke production, with attenuation of light the principal measured parameter. None of the methods measured directly the size distribution or optical characteristics of smoke particles. A set of measurements of the black ("elemental") and organic carbon content of smoke particles from model forest fires has been reported.[3] The fuels were largely limited to pine needles, and no size segregation of the smoke particles was carried out.

We report here on a series of small-scale fire experiments that were conducted to measure as a function of particle size the black carbon, total carbon, and total mass of smoke particles produced in the burning of building materials such as those found in urban environments.

*This work was supported by the United States Department of Energy, Lawrence Berkeley Laboratory, under Contract No. DE-AC03-76SF00098 and Lawrence Livermore National Laboratory Director's Funds, under Contract No. W-7405-ENG-48.

ACCOMPLISHMENTS DURING FY 1985

Experimental Procedures

Sample Holders

Samples were tested in one of two orientations, depending on the nature of the product. The rigid building materials, including the Douglas fir, birch, and plywood samples, were tested in the parallel plate geometry; the flexible polyurethane samples were burned in the upward facing horizontal geometry.

The sample holder for the parallel plate geometry was adapted from the sample holder used for the proposed ASTM "Ease of Ignition" test apparatus.[4] The sample holders, constructed of brass bar stock, hold samples approximately 15 cm × 15 cm in face area. Two sample holders face each other across a 25.4-mm (1-in.) gap. Samples of varying thicknesses are accommodated and secured in the apparatus by four set screws at the back face of each holder that is used to hold test specimens in place. The specimen holders are bolted to the load cell platform.

Specimens tested in the horizontal orientation had their edges and bottom face wrapped in aluminum foil. These specimens were then placed on the load cell platform.

Burner

The source of ignition used for these experiments varied with the geometry being considered. The horizontal samples, which consisted solely of flexible polyurethane foam, were readily ignited by a match touched to the center of the exposed top sample face. The wood-based building materials tested in the parallel plate geometry were more difficult to ignite so a more severe ignition source, a methane burner, was used.

The methane burner consisted of a 13-mm (1/2-in.) stainless steel tube, which had 21 1.5-mm diameter holes bored along its length at intervals of about 6.5 mm. Methane from a gas cylinder was introduced into the tube at both ends to provide a flow rate of approximately 200 cm^3/s (25-SCFH). The burner tube was located centrally between the two sample holders at a distance of about 25-mm below the bottom of the two samples. The burner ports were located in the top of the tube so that the ignition flame extended up between the two samples. Smoke particle sampling was not conducted during the ignition phase.

Weight Loss Measurement Instrumentation

Mass loss measurements were made during each experiment. The samples and sample holders were placed on top of a weighing cell (Automatic Timing and Controls, Model 6005C, 1-lb dynamic range), which transmits a signal proportional to load to a chart recorder.

Exhaust System Assembly

The sample holder/weighing cell assembly was mounted on a platform, which was placed within a three-sided enclosure. This enclosure, constructed of sheet metal and measuring 0.91 m × 0.91 m × 1.22 m high (3 ft × 3 ft × 4 ft high), was topped by a pyramid-shaped reducer that terminated at the exhaust stack.

The exhaust stack was 100-mm (4-in.) diameter aluminum pipe. The length of the aluminum stack was 2.1 m. A 1.9-m length of 100-mm flexible duct connected the exhaust stack to the exhaust fan. This centrifugal blower produced flow rates of approximately 5.38 m^3/min (190 cfm) under test conditions, as determined by an orifice plate located in the aluminum stack.

Smoke Sampling Equipment

Smoke samples were taken from the exhaust duct approximately 3 m above the flame position. These samples were taken isokinetically through stainless steel probes at a rate of 14.2 liters/min (0.50 cfm).

One probe was connected to a 10-stage impactor for size fractionation of the smoke particles. The impactor (Pilat Mark 5 Source Test Cascade Impactor) (University of Washington) was fitted with aluminum foil collection plate inserts on the impaction plates. These inserts were cleaned before use by sonication in reagent grade acetone, followed by two rinses in the same solvent. The foils were then allowed to dry and equilibrate in a humidity-controlled atmosphere (51% R.H.) before their tare weights were determined. The afterfilter was quartz fiber (Pallflex 2500QAO) that had been fired in air at 800°C for 4 hours to remove all combustible carbon. The filters were humidity equilibrated as the foils before tare weights were determined. Following collection of a sample, the collection plate insert foils and afterfilter were removed from the impactor and returned to the humidity-controlled chamber. They were allowed to equilibrate for 24 hours before the weights were measured. The quartz and aluminum substrates used in this study are not optimum for mass determinations, but both are suitable for combustion carbon analyses. Replicate weighings showed that sample masses on the foils could be determined with a 1 σ error of 12 μg, and those on quartz with a 1 σ error of 20 μg.

The second sampling port was fitted with a filter stack unit composed of two stainless steel in-line 47-mm filter holders (Gelman Sciences Inc.). Each filter holder was loaded with a quartz fiber filter that had been treated as had the impactor afterfilter. Since we have shown that under ambient conditions the second (back-up) filter can contain carbon loadings equal to 10% of the loading (total) filter,[5] presumptively from adsorbed gaseous hydrocarbons, it was decided that this technique would allow a realistic correction for nonparticulate organic carbon in the filter samples.

Sample Analyses

The samples were analyzed by CO_2 evolved gas analysis, a thermal technique that has been shown to quantitatively determine the total carbon content of ambient aerosol particles. Additionally, the blackness of the sample was monitored for samples on quartz filters using the transmitted laser light intensity. This information was used to confirm the temperature at which CO_2 from the combustion of black carbon is evolved. We have further shown that for ambient and combustion source samples on quartz filters, black carbon can be determined by measurement of the change in laser light transmission as the sample is burned.[6] Black carbon from combustion sources has an extinction coefficient for visible light large enough to totally absorb incident light in less than 1 μm. To the extent that particles of black carbon exceed this physical (not aerodynamic) particle size, the content reported by this technique will be less than that actually present.

For each of the impactor and filter samples, total carbon was measured from the integrated area of the CO_2 thermogram, and black carbon was estimated from the area of the high temperature peak (Fig. 2). The high temperature peaks for these samples were identified as black carbon for the total filter and impactor afterfilter samples by the laser optical technique. For each of the thermograms, blank values were subtracted equal to either the CO_2 thermogram of a blank aluminum foil or the thermogram for the backup filter in the filter stack as appropriate. Solvent extraction followed by evolved gas analysis was carried out on some of the filter samples to confirm the black carbon determination.

The black carbon content of each of the filter samples was also calculated from the change in

transmission of incident laser light during the analysis. We applied an empirically determined relationship that we have determined for aerosol particles collected in ambient air and from combustion sources.[6]

Results

The summarized results from four test materials are shown in Figs. 1–4. For each particle size fraction, the total mass of collected smoke particles, as well as the total carbon and black carbon content of those particles, is shown. Organic carbon is in each example equal to the difference between total and black carbon. For each of the wood fuels, the preponderance of black carbon is present among the smallest size fraction collected, although organic carbon and noncarbon mass in the smoke particles may have a broader size distribution. Polyurethane foam also produced the majority of its black carbon smoke particles in the smallest size fractions, although it does show a broader size range for particles containing black carbon.

Agreement of the laser optical determined black carbon content with that determined by CO_2 evolved gas analysis is generally within 15% for the wood samples but differs by a factor of 2 for the polyurethane foam. The source of this relatively large disagreement may lie in the black carbon particle size distribution or in particle morphology. Assumptions regarding particle size and shape were made in the development of the laser transmission method; while these assumptions have proven valid for ambient particles and many combustion sources,

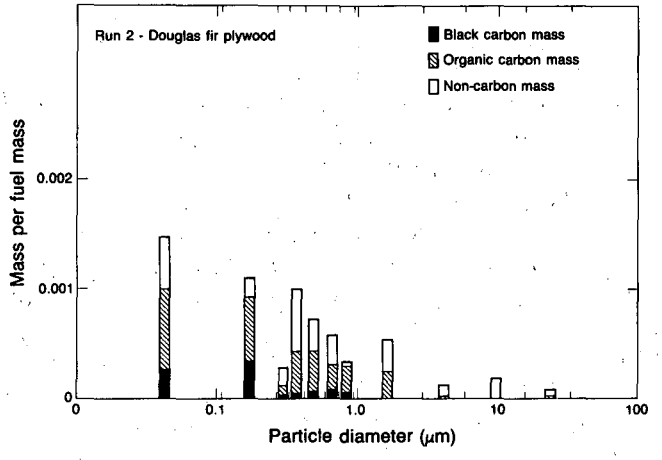

Figure 1. Smoke particle composition as a function of size. (XBL 8512-12819)

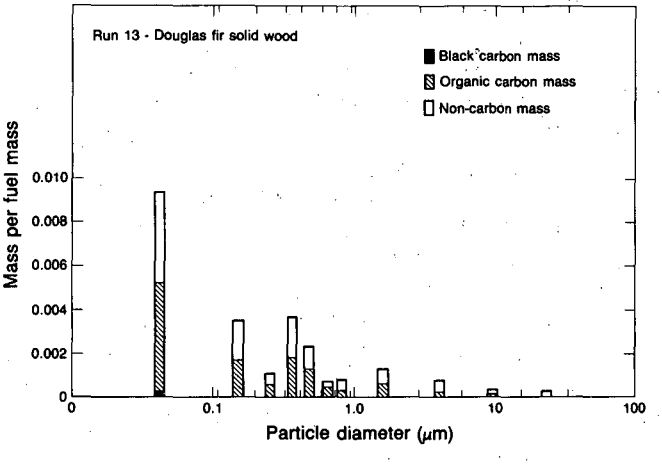

Figure 2. Smoke particle composition as a function of size. (XBL 8512-12820)

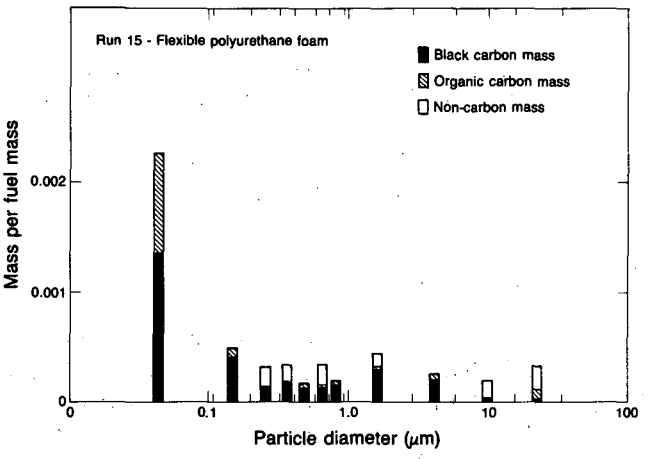

Figure 3. Smoke particle composition as a function of size. (XBL 8512-12821)

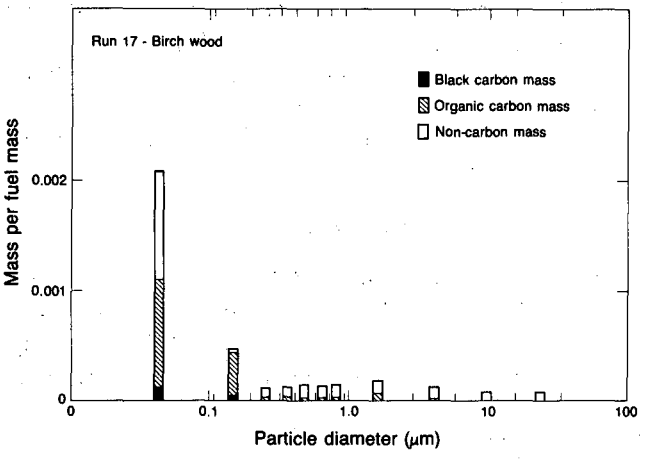

Figure 4. Smoke particle composition as a function of size. (XBL 8512-12822)

they may not hold for fuels such as polyurethane. Observation during individual tests are listed in Table 1.

Replicate combustion tests were carried out on all materials reported here, for a total of 18 test fires. Visual observations and weighings indicate that the results of these four tests are typical.

PLANNED ACTIVITIES FOR FY 1986

We intend to increase the size of our fires to test the transferability of our laboratory-scale results to larger conflagrations. We plan to control heat and oxygen at the fires to study smoke produced under conditions that might be found in a firestorm.

REFERENCES

1. Turco, R.P., *et al.* (1983), "Nuclear Winter: Global Consequences of Multiple Nuclear Explosions," *Science 222*, p. 1283.
2. Bard, S. and Pagni, P.J. (1981), "Carbon Particulate in Small Pool Fire Flames," *J. Heat Trans. 103*, p. 357.
3. Patterson, E.M. and McMahon, C.K. (1984), "Absorption Characteristics of Forest Fire Particulate Matter," *Atmos. Environ. 18*, p. 2541.
4. ASTM Committee E5. (1980), *Draft Standard Method of Test for Time to Ignition of Solid Materials by Flame Exposure.*
5. Dod, R., *et al.* (1980), "Investigation of Sampling Artifacts in Filtration Collection of Carbonaceous Aerosol Particles," LBL-10735, p. 8-35.
6. Gundel, L.A., Dod, R.L., Rosen, H., and Novakov, T. (1984), "The Relationship Between Optical Attenuation and Black Carbon Concentration for Ambient and Source Particles," *Sci. Total Environ. 36*, p. 197.

Table 1. Observations during individual tests.

Run 2 – Douglas fir plywood. The wood was ignited with a methane flame for 2 minutes prior to sampling. The wood burned with flaming for 4 minutes, followed by 2 minutes of smoldering combustion before sampling was terminated.

Run 13 – Douglas fir solid wood. After ignition with a methane flame, we found it difficult to maintain flaming combustion. Sampling was carried out for 4 minutes, followed by reignition using the methane burner. Sampling was then resumed for another 6 minutes. The particles were brown in appearance with evidence of liquid nature.

Run 15 – Flexible polyurethane foam. The foam ignited easily with a match at the center of the top surface of the sample. Flames then moved out in a circular pattern, melting and burning the foam. Sampling was for 6 minutes, the time required to completely burn the fuel.

Run 17 – Birch solid wood. Ignition was with methane and was repeated twice as the flame died. Sampling was not conducted during ignition periods. Total sampling period was 9 minutes, exclusively while wood flames were present.

APPLIED PHYSICS AND LASER SPECTROSCOPY RESEARCH*

(This article has been reprinted from the FY 1984 Annual Report.)

N.M. Amer,† S.-H. Chen, H. Dersch, A. Frova, R.W. Gerlach, W. Imler, M. Olmstead, A. Skumanich, D. Wei, and Z. Yasa

The research philosophy of our group is to develop and apply advanced laser spectroscopy and condensed-matter physics to energy-related problems. Lasers, with their high spectral purity and tunability, constitute an excellent probe of matter, and the advanced state of our knowledge of condensed-matter physics makes it possible to apply such knowledge to energy research. Areas of investigation that we are interested in include the development of novel laser spectroscopic techniques, the physics of photovoltaic semiconductors, semiconductor surfaces and interfaces, liquid crystals and their applications, and the detection of molecular and atomic species at the ultratrace level.

ACCOMPLISHMENTS DURING FY 1984

Laser Photothermal Measurements and Characterization

Laser photothermal spectroscopy employs the heating concomitant with the absorption of electromagnetic radiation to measure minute optical absorption coefficients (10^{-8}), to characterize nonradiative processes quantitatively, and to measure thermal properties of matter. This type of spectroscopy has been developed largely by our group here at LBL.

Spatially Resolved Photothermal Technique for the Investigation of Transport and Recombination in Semiconductors‡

The development of spatially resolved probes for the investigation of transport processes in semiconductors is of increasing interest. In principle, these methods should enable the study of such important phenomena as the interaction between macroscopic defects (e.g., dislocations) and carrier transport, as well as the fate of these carriers near interfaces. Typically, conventional methods integrate the measurement over the entire distance between the electrodes. Furthermore, the electrodes themselves may influence the results unless care is taken in configuring the experimental setup.

These limitations have motivated us to develop a noncontact, spatially resolved *in situ* probe of transport properties in semiconductors. The basic premise of the technique is the use of the heat associated with nonradiative processes (e.g., recombination of carriers) to deflect a focused laser probe beam (subgap energy) propagating *through* the semiconductor. The deflection of the probe beam is caused by a change in the refractive index of the sample, which is in turn governed by carrier diffusion and recombination (Fig. 1). A quantitative theory was developed to account for the observed signal.

The experimental setup employs the method of transverse photothermal deflection shown in Fig. 2. The sample used for our experiment was a *p*-doped Si ($\rho \approx 6\Omega$·cm). One face of the crystal was mechanically polished and its surface treated with methanol to minimize surface recombination. The photocarriers were generated by an Ar^+ ion laser beam (5145

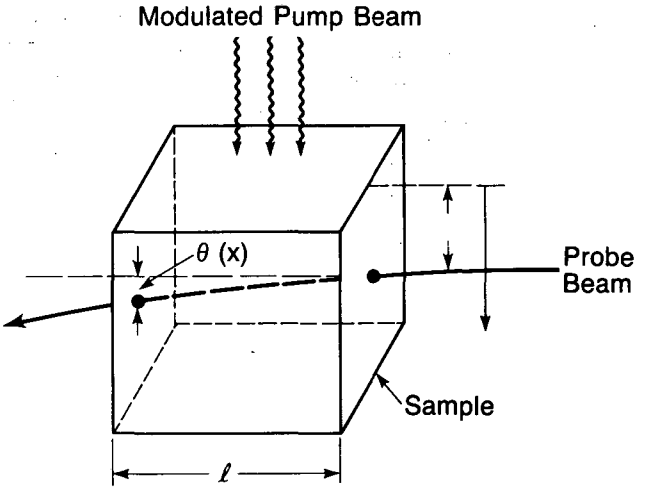

Figure 1. Principle of the scheme for spatially resolved photothermal detection of carrier transport and recombination in semiconductors. Such carrier processes govern the refractive index of semiconductors. A focused laser probe passing through a semiconductor sample will therefore be deflected by an angle, $\theta(x)$, that is governed by these processes. (XBL 8410-10944)

*Supported by the Director, Office of Energy Research, Office of Basic Energy Sciences, Materials Sciences Division of the U.S. Department of Energy under Contract No. DE-AC03-76SF00098, and by the Defense Advanced Research Projects Agency, Department of Defense under DARPA Contract No. 3343.

†Group Leader.

‡Complete version submitted to *Journal of Applied Physics.*

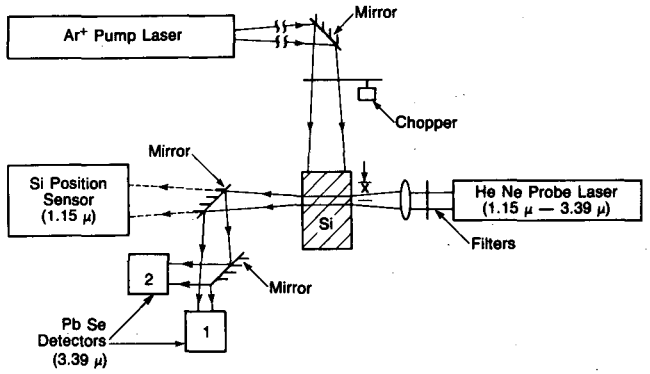

Figure 2. Experimental arrangement for deflection measurements. Two detection schemes are shown: for the 1.15 μ wavelength, a silicon position sensor was used; for the 3.39 μ wavelength, a mirror cutting the beam in two equal parts and two well-matched PbSe detectors were used. The signal was processed by a differential-phase-sensitive detector. (XBL 8410-10945)

Å), the maximum power density on the sample being ~500 mW/cm^2. This corresponds to a minority carrier density one order of magnitude smaller than that of the majority carriers. To probe the index of refraction gradient within the crystal, we used two different wavelengths (1.15 μ and 3.39 μ) from a HeNe laser focused to 30 μ. In the case of the 1.15 μ probe beam, the deflection was measured with a position-sensitive detector, while for the 3.39 μ beam two PbSe detectors were used, as shown in the figure. It should be pointed out that it is important to use an actual position-sensitive detector that gives good rejection of probe-beam intensity fluctuations. This is crucial for the 3.39 μ case where free-carrier absorption is significant.

The measurements were made at two probe-beam wavelengths: 1.15 μ and 3.39 μ. Before proceeding to describe the results, we note that the power dependence of the signal in the range of 30–500 mW/cm^2 was found to be linear within the experimental error.

Figure 3 shows the results obtained when the polished, methanol-treated face of the Si crystal was illuminated and the carrier transport probed at 1.15 μ. At this wavelength, the free-carrier dispersion is negligible, and one expects the $\partial T/\partial n$ term to be dominant. As can be seen, the two regions predicted by the theory are evident, and agreement with the theory is satisfactory.

It is interesting to note that by using the same set of parameters and varying the surface conditions of the Ar$^+$-illuminated surface (i.e., varying the surface recombination velocity s), we obtain good agreement between the theoretical predictions and the experimental results when the opposite unpolished and untreated face was illuminated (Fig. 4).

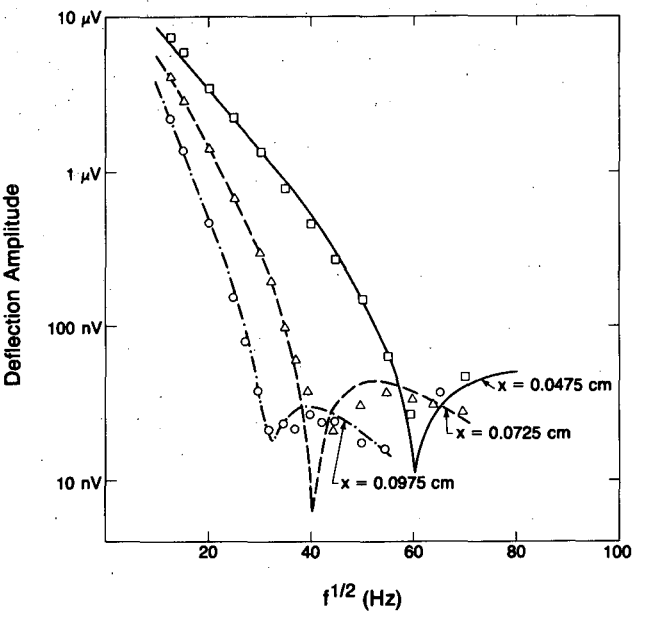

Figure 3. Comparison of the experimental measurements (points) with the theory (lines) for a well-polished treated surface of silicon crystal and a laser probe of 1.15 μ wavelength. (XBL 8410-10927)

To further test the theory, we probed the carrier transport with a 3.39 μ beam. At this wavelength,

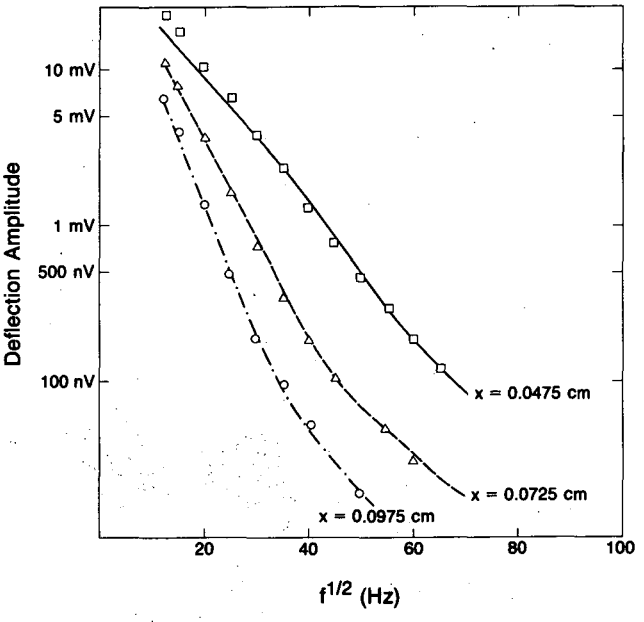

Figure 4. Comparison of the experimental measurements (points) with the theory (lines) for the unpolished surface of the Si crystal and a 1.15 μ laser probe. (XBL 8410-10924)

the free-carrier dispersion is not negligible. The free-carrier contribution (high frequency range) and the thermal contribution (low frequency range) are observed simultaneously. By using the preceding set of parameters to characterize the bulk and the illuminated surface, we obtain good agreement, as shown in Fig. 5.

*Photothermal Spectroscopy and Imaging of Gallium Arsenide**

The small rise in temperature associated with the absorption of electromagnetic radiation has provided the basis for a new spectroscopic tool generally known as photothermal spectroscopy. The advantages of this type of spectroscopy are its sensitivity and the relative ease with which it can be implemented.

The heating causes a change in the index of refraction of the medium surrounding the sample. This change is probed with a weak laser beam that is deflected as the index of refraction changes. Using phase-sensitive methods, the amplitude and the phase of the deflection can be readily measured with a position-sensitive detector (Fig. 6). Thus, by varying the wavelength of the optically exciting (pump) beam, the deflection of the probe beam is a measure

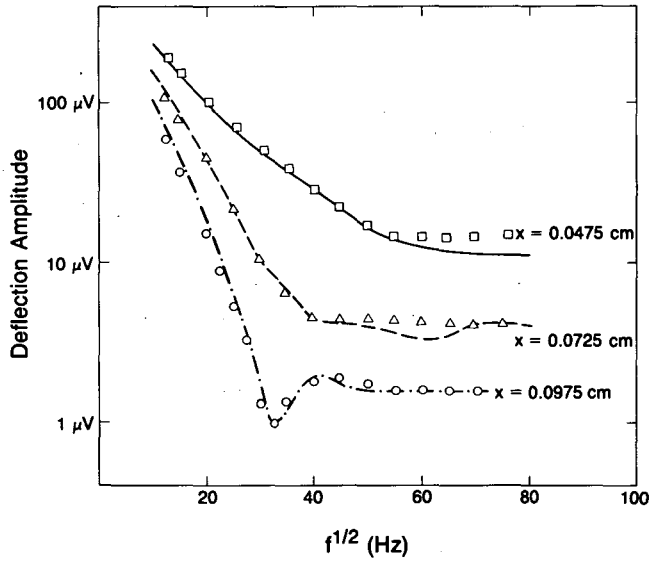

Figure 5. Comparison of the experimental measurements (points) with the theory (lines) for a well-polished treated surface and a 3.39 μ probe. (XBL 8410-10942)

*Complete version appeared in the *Proceedings of Third Conference on Semi-Insulating III–V Materials*, 1984.

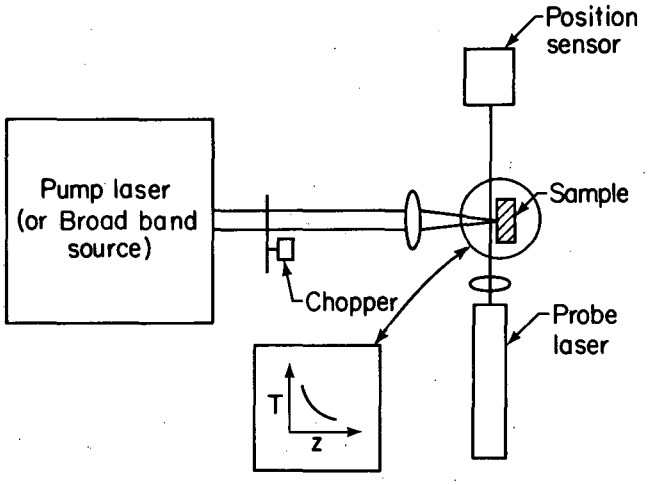

Figure 6. Schematic of experimental setup for photothermal deflection spectroscopy. (XBL 836-2666)

of the optical absorption. This type of spectroscopy is known as *photothermal deflection spectroscopy.*

The photothermal signal S is quantitatively related to the optical absorption coefficient in the following manner:

$$S = A[1 - \exp(-\alpha\ell)] \quad , \qquad (1)$$

where A is a constant that can be determined empirically, α is the optical absorption coefficient, and ℓ is the sample thickness.

Sensitivities of $\alpha\ell \approx 10^{-7}$ have been achieved, and the superiority of this technique in terms of sensitivity and flexibility has been demonstrated in a recent study of the optical properties of defects in amorphous semiconductors.

There exists a class of experimental conditions, however, for which photothermal deflection techniques are not suited in studying the optical and thermal properties of matter. Examples of such experiments are those that require vacuum and/or cryogenic temperatures. Such conditions are encountered in the study of surfaces and interfaces. Similar requirements exist for *in situ* and real-time characterization of thin-film semiconductors. These conditions motivated the use of optical heating in yet another manner. Since heating results in the expansion and buckling of the illuminated surface, a measurement of the surface displacement is a means of determining the optical and thermal properties of the illuminated solid. This small displacement can be detected in a variety of ways, the simplest of which is by reflecting a weak laser beam off the illuminated surface. As the surface is displaced upon being optically heated, the probe beam will be deflected from

its original reflection direction. This deflection is then detected with a position-sensitive detector (Fig. 7). Typically, $\alpha\ell$ of 10^{-6} are readily achievable. This version of photothermal spectroscopy is called *photothermal displacement spectroscopy.*

An important and characteristic parameter in photothermal spectroscopy is the thermal diffusion length L_{th}, which defines the depth from which the photothermal signal originates. L_{th}, which is also called the thermal wavelength, is given by:

$$L_{th} = (K_{th}/\omega\rho\, C)^{1/2} \quad , \qquad (2)$$

where K_{th} is the thermal conductivity of the sample, ω is the modulation frequency of the light, ρ is the density, and C is the heat capacity.

The modulation dependence of the thermal diffusion length is what is exploited to perform nondestructive depth profiling and imaging of solids. The higher the modulation frequency, the shorter the thermal length, and the closer to the surface the information is derived from. On the other hand, for low modulation frequencies, the photothermal signal is a probe of the bulk. Furthermore, by focusing the pump and probe beams, scanning microscopy can be performed. The achieved spatial resolution is a function of the size of the focal spot of the pump beam as well as the thermal diffusion length. Resolution to 1 micrometer has been attained.

We have performed scanning photothermal microscopy of semi-insulating LEC undoped GaAs wafers. The pump beam was an argon-ion laser focused to 1 micron on the wafer. The probe beam was a 0.5 mW HeNe laser. Both the deflection and the displacement schemes were used and yielded identical results. As can be seen (Fig. 8), both the phase and the amplitude of the photothermal signal exhibit small features that are due to the scattering of the thermal wave by thermal inhomogeneities in the wafer. By varying the modulation frequency, we were able to determine that these features lie on and near the surface. By analyzing the photothermal signal, using the theory we developed earlier, we were able to deduce that the inhomogeneities are arsenic-high inclusions. Our preliminary estimate of the degree of arsenic enhancement in these inclusions is approximately 14%, averaged over the 1-micron pump-beam diameter. To test the validity of our conclusion, scanned Auger spectroscopy (2-micron resolution) was performed on these inclusions. The Auger spectra verified our conclusion and gave an arsenic enhancement of 12%. Upon heating the wafers in a nitrogen atmosphere at 250°C, the arsenic-rich inclusions were no longer observed in the photothermal scans. This could be due to the arsenic diffusing into the matrix or evaporating out of the wafer.

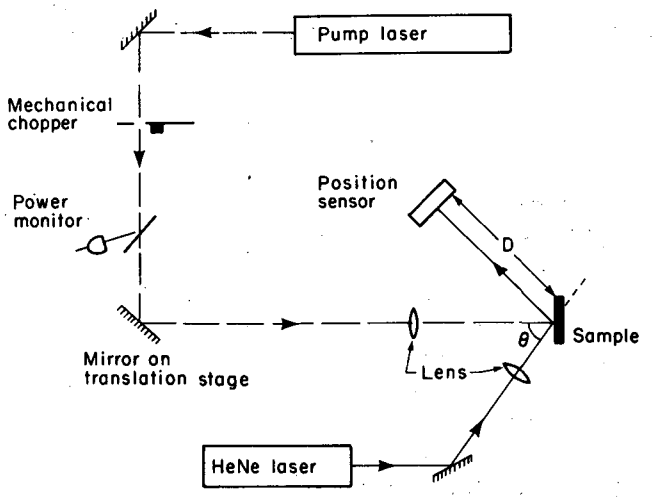

Figure 7. Schematic of experimental arrangement for photothermal displacement spectroscopy. (XBL 831-22)

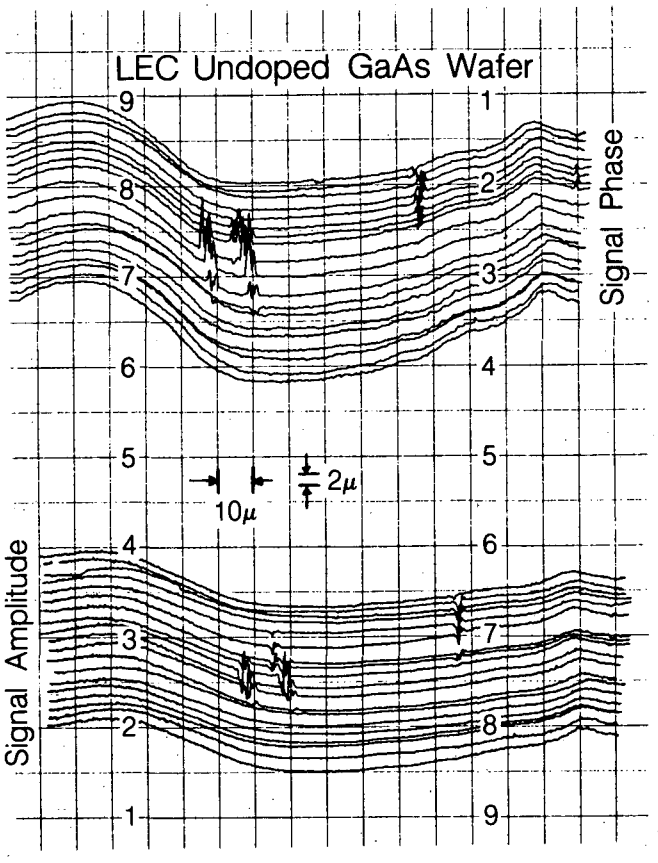

Figure 8. Spatially resolved photothermal scans of LEC undoped GaAs wafer. (XBL 845-1701)

We have also investigated the optical absorption spectra of undoped, chromium-doped, and silicon-doped GaAs crystals in the 0.5–1.5 eV range. In Fig. 9, we compare the photothermal deflection spectra of Cr- and Si-doped materials. As can be seen, the semi-insulating Cr-doped sample reproduces the main features obtained using conventional techniques. In addition, we observe a small peak at 0.5–0.6 eV, which we tentatively attribute to Fe impurities. The Si-doped sample exhibits a qualitatively different spectrum. The absorption coefficient does not drop at photon energies lower than 0.9 eV as is the case for the Cr-doped material. The spectra of two Si-doped n-GaAs samples are shown in Fig. 9. While both are from the same boule, sample A is from near the top of the boule, and sample B is from near the center. The larger thermal gradients and stresses expected near the top of the boule may account for the increased defect density in sample A.

In Fig. 10, we show the spectra of semi-insulating LEC GaAs and of the same material after being plastically deformed at 400°C. It is clear that the deformation increases the deep-level defect density. This is in agreement with results obtained by other methods such as electron spin resonance (ESR) and conventional infrared absorption.

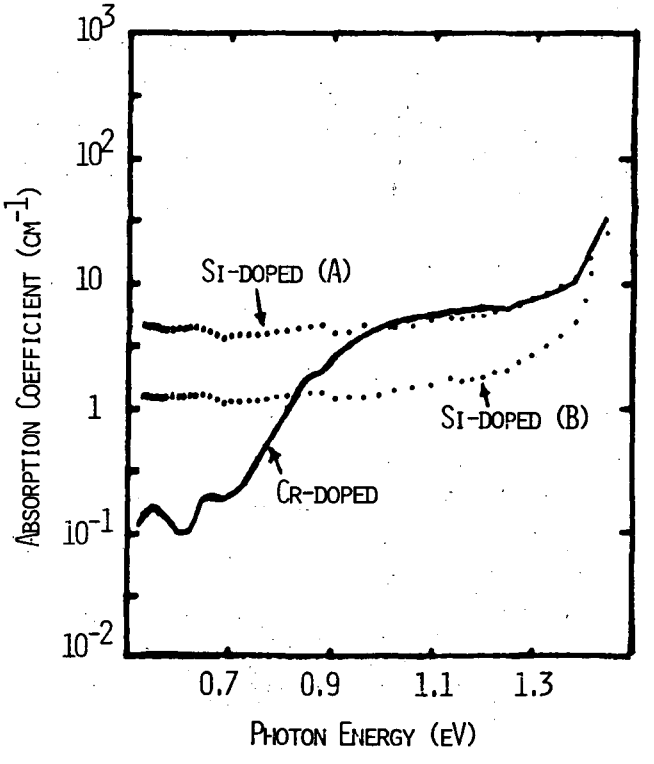

Figure 9. Photothermal absorption spectra of Cr- and Si-doped GaAs. (XBL 845-1702)

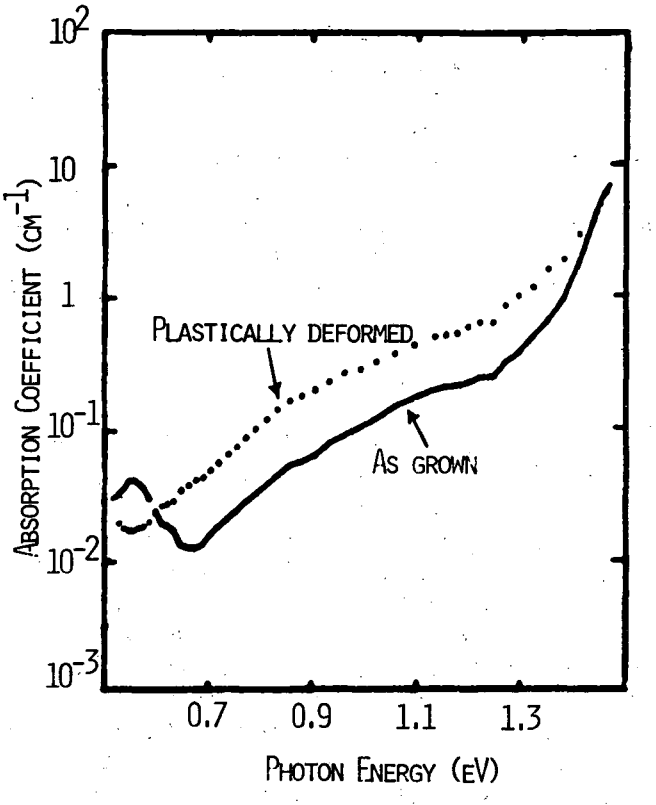

Figure 10. Photothermal absorption spectra of LEC semi-insulating as-grown and plastically deformed (at 400°C) GaAs. (XBL 845-1703)

*An Optical Approach to Thermopower and Conductivity Measurements in Thin-Film Semiconductors**

Conductivity and thermopower measurements are widely used to study the transport properties of semiconductors. The thermopower S is related to the Peltier coefficient Π, which, for conduction above a mobility edge E_c, may be written as:

$$ST = \Pi = \frac{kT}{e}\left[A + \ln\frac{N_0}{n}\right] . \qquad (3)$$

Since the quantities A and N_0 do not contain the mobility μ, the thermopower provides a measure of the carrier density n alone and is often applied to separate the product $n\mu$ in the conductivity $\sigma = en\mu$. Moreover, the sign of S directly gives the charge of the majority carriers.

A common problem with transport experiments is that properties of the metal contacts may influence the results. A current-voltage measurement reflects the conductivity only if the contact resistance is

*Complete version appeared in *Appl. Phys. Lett. 45*, p. 272 (1984).

much lower than the sample resistance. In the thermopower experiment, the metal contacts serve as reference for the thermovoltage, and contact properties are generally not considered to be a problem in the thermal equilibrium case, i.e., dark transport. In studying photoconductivity, however, thermopower measurements are much more difficult to perform because of the photovoltage, which may exceed the small thermovoltage. To understand the steady-state photoconductivity, it is essential to be able to distinguish between the effects due to change in carrier density and those due to changes in mobility. Photothermopower measurements are of particular importance in the case of hydrogenated amorphous silicon, since Hall effect data fail to give even the correct sign of the charge carriers. We have developed a technique to study transport properties that is based on the photothermal detection of Joule and Peltier heat generated by electrical currents. The method gives a spatially resolved profile of the conductivity along the film surface, thus allowing the detection of σ away from any metal contacts. The measurement of the Peltier heat rather than the thermovoltage avoids the influence of photovoltages on the signal. Preliminary results for the photo-Peltier coefficient of doped *a*-Si:H are presented.

All measurements were done on 1-micron-thick *a*-Si:H films deposited onto quartz substrates. An oscillating voltage, $U = U_0 \cos\omega t$ with frequency $f = 5$ to 10 Hz, is applied between two evaporated Al contacts in gap configuration with a spacing of 1 to 1.5 mm (Fig. 11). The heat generated by the current creates a temperature gradient perpendicular to the sample surface, which changes the index of refraction in the surrounding medium. This change is probed by a laser beam skimming the surface of the sample perpendicular to the current direction. To prevent changes in conductivity caused by the probe laser, an IR-laser (λ = 3.39 μ) is used, and the deflection is measured by a position-sensitive PbSe-detector. Both signals appearing at the reference frequency ($1f$ signal) and at twice the reference frequency ($2f$ signal) are monitored as the probe beam is scanned along the direction of the electric current (x direction). It has been demonstrated that the deflection is directly proportional to the heat generated within the interaction region between the probe laser and the sample. The Joule heat U^2/R (R = sample resistance) has a component oscillating at twice the reference frequency with amplitude $U_0^2/2R$. The differential Joule heat per unit length in the x direction is given by:

$$\frac{1}{\sigma}\left(\frac{U_0^2}{2R^2Q}\right),$$

where Q is a cross section of the sample. The $2f$ signal, therefore, provides a profile of the resistivity $1/\sigma$ along the x direction with a resolution determined by the beam diameter and the thermal diffusion length. Both quantities are on the order of 0.2 mm. The Peltier heat Π oscillates at the reference frequency with amplitude $\Pi \frac{U_0}{R}$ and appears centered and with opposite sign at each of the contacts.

In Fig. 12(a), the $2f$ signal, plotted as a function of x, is shown for a heavily phosphorous-doped sample. Both amplitude and phase are nearly constant, indicating that the conductivity is uniform throughout the sample. The strong decrease of the signal at both contacts shows that the contact resistance is negligible compared to the sample resistance. Furthermore, the time delay of the signal at the contacts, exhibited as a decreasing phase angle, indicates that the tail of the signal is caused by diffusing heat from the gap region rather than by contact properties. We found that the $2f$ signal is linear in the Joule heat over more than 3 orders of magnitude. This was verified both by varying the voltage at fixed resistance and by varying the resistance in photoconductive samples illuminated with different light intensities at fixed voltages. The minimum detectable signal corresponds to a total Joule heat of 10^{-5} W, which, for the given geometry and an electric field of 10^3 V/cm, corresponds to a lower limit of $10^{-6}\ \Omega^{-1}\text{cm}^{-1}$ for the conductivity.

The flat conductivity profile shown in Fig. 12(a) is not obtained in all samples. In Fig. 13, results for a sample with lower doping concentration are shown. It can be clearly seen that the major part of the Joule heat is generated at the contacts. It follows that the resistance of the film is much lower than indicated by a current-voltage measurement.

The magnitude and phase of the $1f$ signal of the heavily phosphorus-doped sample are plotted in Fig.

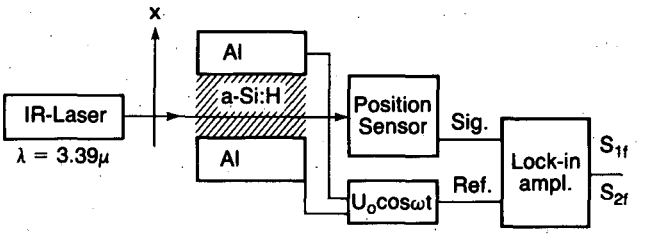

Figure 11. Experimental setup for thermopower and conductivity measurements on *a*-Si:H semiconducting thin film. (XBL 843-10190)

12(b). The signal has the predicted shape for the Peltier heat, with approximately symmetric peaks appearing at the contacts. The phase of the signal at the peak positions differs by 180°, indicating that the deposited heat has opposite signs at the contacts. Also shown is the phase of the $1f$ signal measured in a boron-doped sample, which at each contact is shifted by 180° with respect to the phosphorus-doped

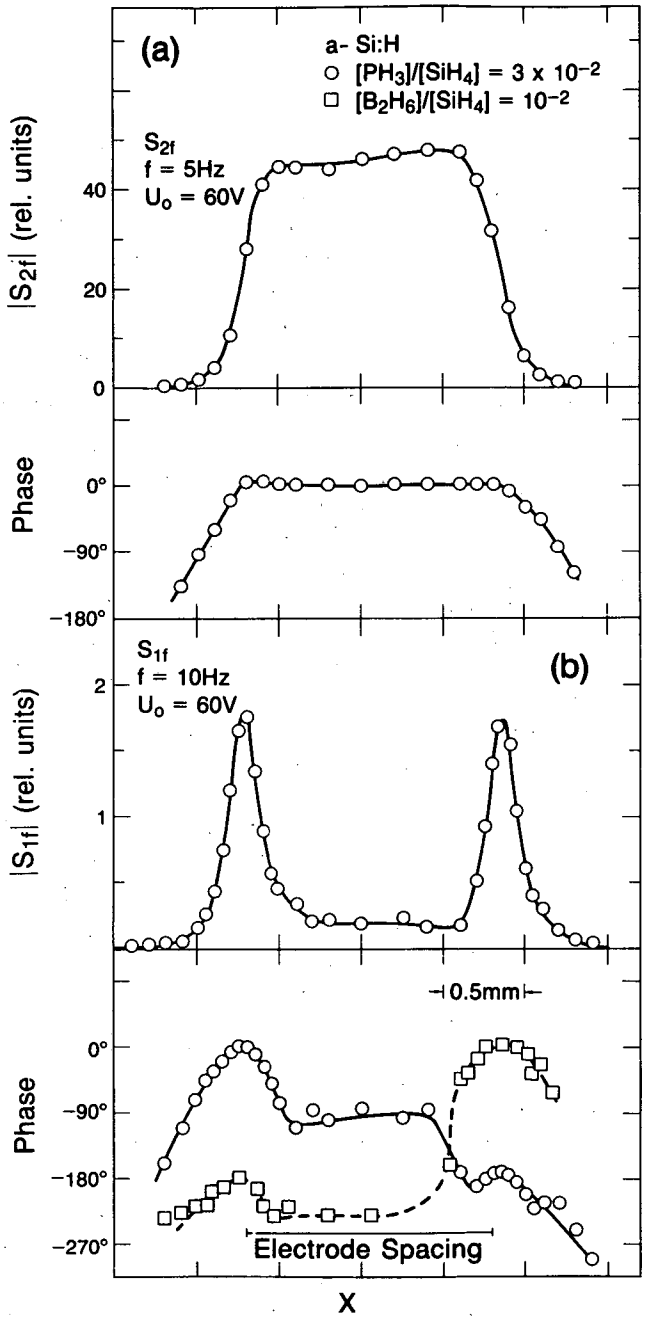

Figure 12. Magnitude and relative phase angle of (a) the $2f$ and (b) $1f$ signals for a heavily phosphorus-doped sample.
(XBL 843-10187)

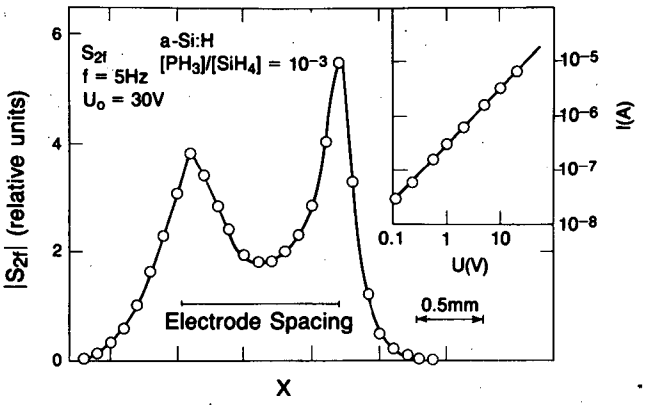

Figure 13. The $2f$ signal for a sample with non-ohmic contacts. Inset shows current-voltage characteristics.
(XBL 843-10184)

sample. This behavior reflects the change in sign of the Peltier coefficient as the conductivity is changed from n to p type. As in the case of the $2f$ signal, the phase decreases in the tails, which is attributed to heat diffusing from the peak position, leading to a time delay in the signal. The Peltier heat was found to be proportional to the current through the sample over more than 2 orders of magnitude. The Peltier coefficient Π can be calculated directly from the integrated $2f$ and $1f$ signals (S_{2f} and S_{1f}). These quantities are proportional to the total Joule heat $\left(\frac{U_0^2}{2R}\right)$ and Peltier heat $\left(\Pi \frac{U_0}{R}\right)$, respectively. To compare the signals quantitatively, we have chosen twice the frequency for S_{1f} than in the case of S_{2f} making sure that both quantities experience the same thermal relaxation. Dividing S_{1f} through S_{2f} and solving the equation for Π, we are left with:

$$\Pi = \frac{U_0}{2} \times \frac{S_{1f}}{S_{2f}} \quad . \tag{4}$$

Determining the sign of Π is equivalent to determining the phase angle, which corresponds to heating in phase with the applied voltage. This can easily be done by adding a dc-offset U_1 to the oscillating voltage $U_0 \cos\omega t$. Then, besides the signal from the Peltier heat, a second $1f$ signal due to the Joule heat appears with amplitude proportional to $(2U_1U_0)/R$. Comparing the phases of these two signals allows the determination of the sign of Π.

We have shown that the photothermal detection of electronic transport yields information about contact influences, macroscopic sample homogeneity, and Peltier coefficients of thin-film samples. Possible extensions of the method that are currently under

investigation include an ability to provide two-dimensional conductivity images of device structures and the separation of surface from bulk contributions to the conductivity.

*Heat Diffusion Solutions for the Nonresonant Spectrophone**

Most theoretical treatments of the nonresonant spectrophone have used as their starting point the standard inhomogeneous heat diffusion equation:

$$\rho_0 C_v \frac{\partial T'}{\partial t} = \kappa \nabla^2 T' + H \qquad (5)$$

where T' is the temperature disturbance, H is the heat released due to collisional deactivation of the optically excited molecules, ρ_0 is the density, C_v is the specific heat per unit mass at constant volume, and κ is the thermal conductivity. This equation neglects the work done on or by the gas in compression or expansion, respectively, and treats it as if it were a solid. A more proper equation of energy conservation for a gas, taking expansion and compression into account, is given by:

$$\rho_0 C_p \frac{\partial T'}{\partial t} = \kappa \nabla^2 T' + H + \frac{\partial p'}{\partial t} \qquad (6)$$

where p' is the pressure disturbance. When the cell dimensions are small compared to the acoustical wavelength, p' is constant throughout the cell, and, if one uses the ideal gas equation of state and the fact that the total mass of gas is conserved, one finds that p' is proportional to the volume integral of the temperature disturbance T'; if one assumes an $e^{-i\omega t}$ time dependence, one obtains the equation

$$\nabla^2 T' + \frac{i\omega\rho_0 C_p}{\kappa} T' - \frac{i\omega(\gamma - 1)\rho_0 C_p}{\gamma\kappa\pi R^2} \times \int_0^R T'(r')\, 2\pi r'\, dr' = -\frac{H}{\kappa} \quad , \qquad (7)$$

where we have assumed an infinitely long cylindrical cell of radius R and assumed that H depends only on r, the radical coordinate, and neglected the microphone impedance correction.

*Complete version submitted for publication in *Journal of Applied Physics.*

We present here a general solution by a Green's function method and show that the pressure amplitude one obtains by integrating the temperature solution is:

$$p' = \frac{i(\gamma - 1)}{\pi R^2 \omega} \times \frac{\int_0^R H(r')\left[1 - \frac{I_0(kr')}{I_0(kR)}\right] 2\pi r'\, dr'}{1 + \left[\frac{2(\gamma - 1)}{\gamma kR}\right]\left[\frac{I_1(kR)}{I_0(kR)}\right]} \quad , \qquad (8)$$

where $k = (-i\,\omega\rho_0 C_p/\kappa)^{1/2}$ and I_0 and I_1 are modified Bessel functions. We have also solved the heat diffusion Eq. (5) in the frequency domain for arbitrary $H(r)$ and obtained for the pressure:

$$p' = \frac{i(\gamma - 1)}{\pi R^2 \omega} \times \int_0^R H(r')\left[1 - \frac{I_0(k'r')}{I_0(k'R)}\right] 2\pi r' dr' \quad , \qquad (9)$$

where $k' = (-i\omega\rho_0 C_v/\kappa)^{1/2} = k/\sqrt{\gamma}$. The heat diffusion Eq. (5) tends to overestimate the temperature disturbance near the center of the cell and underestimate it near the walls, but these effects tend to cancel out in integrating to obtain the pressure, and thus it gives an excellent approximation for the pressure. In particular, both expressions (8) and (9) have identical limiting behavior at high and low frequencies. At low frequencies ($\omega << \kappa/\rho_0 C_p R^2$), both give

$$p' = \frac{p_0}{4\pi\kappa T_0} \int_0^R H(r')\left(1 - \frac{r'^2}{R^2}\right) 2\pi r'\, dr' \quad . (10)$$

At high frequencies ($\kappa/\rho_0 C_p R^2 << \omega << 3.83\ c/R$), both give

$$p' = \frac{i(\gamma - 1)}{\pi R^2 \omega} \int_0^R H(r')\, 2\pi r'\, dr' \quad . \qquad (11)$$

Thus, the use of the heat diffusion equation for the photoacoustic effect in the nonresonant spectrophone is well justified; however, where the temperature and/or density solutions are needed, as in thermal lensing, photothermal deflection, etc., in finite-radius cells, the solution of Eq. (7) may be more appropriate.

*Photothermal Spectroscopy in Turbulent Media**

In the atmosphere, a propagating laser beam wanders due to the effect of turbulence. The larger turbulent eddies deflect the beam as a whole, and the smaller ($<<$ beam diameter) turbulent eddies broaden the beam. Hence, after propagating in the atmosphere over a sufficient distance, a laser beam appears to have a long-term averaged diameter significantly greater than the short-term averaged beam spot that randomly wanders about a mean position with a frequency spectrum $\leq$ 1000 Hz.

In the application of photothermal deflection spectroscopy (PDS) for the measurement of small absorptions in the atmosphere, this turbulence-induced beam wander is the dominant source of noise because of the inherent sensitivity of the technique to variations in the beam position. A modulation scheme that minimizes this component of noise is considered to be the most effective solution. The following pulsed technique proved to be most effective with an $\alpha\ell \sim 10^{-4}$ detection level: In the typical geometry of a PDS experiment, a pulsed pump beam and a cw probe beam are used. The advantage of the high power of pulsed lasers is therefore available. The rapid thermalization following the pump absorption and the consequent stepwise deflection of the probe beam is detected by a lateral position sensor (LPS) with a bandwidth of $\sim$100 Hz. Since the high-frequency signal from the LPS is independent of the low-frequency position of the probe beam, there is negligible influence from beam wandering on the signal detection process. Two samples are detected from the transient signal, at a separation of $\lesssim$10 μsec, one before and one after the pump pulse, and the process is repeated at the rate of the pump pulses for signal averaging. For times less than 100 μsec, turbulence is essentially stationary, so one can assume that there is no noise due to turbulence in the difference signal between the two samples. Note that the samples of the short-term-averaged probe beam are taken as it wanders on the LPS at low frequencies.

After each pump pulse, the imposed thermal gradient decays by heat diffusion. A pump repetition rate of $\leq$10 Hz allows sufficient diffusion. The primary effect of turbulence is to be observed in the overlap of the pump and probe beams. At each repetition of this process, the pump and probe beams have wandered to different positions (depending on the conditions of turbulence along the pathlength to the interaction region). Hence, the signal detected (the difference between the samples) is directly affected. However, the initial sample (before the pump pulse) yields information about the probe-beam position at the interaction region. Correlating this signal to the relative positions of the pump and probe at the interaction region, a normalization can be carried out. Since the pump beam also wanders, full correction is possible only if the pump-beam position is also monitored by a position sensor.

This technique accounts for the turbulence-induced beam wandering *before* the interaction region. The random deflections of the beam *after* the interaction region results in the loss of beam position information. The signal level before the pump pulse can only be correlated to the probe beam position at the interaction region probabilistically. This can be an important source of noise. An additional source of turbulence-induced noise is the variations in the beam diameters, which directly affect the signal. An analysis of these contributions of noise has been carried out in order to determine the smallest absorptions measurable under typical atmospheric conditions. Figure 14 shows a setup for a laboratory simulation. Experimental results have yielded a sensitivity of $\alpha\ell \sim 10^{-4}$.

Surfaces and Interfaces

Surfaces and interfaces play an increasingly important role in various technological applications.

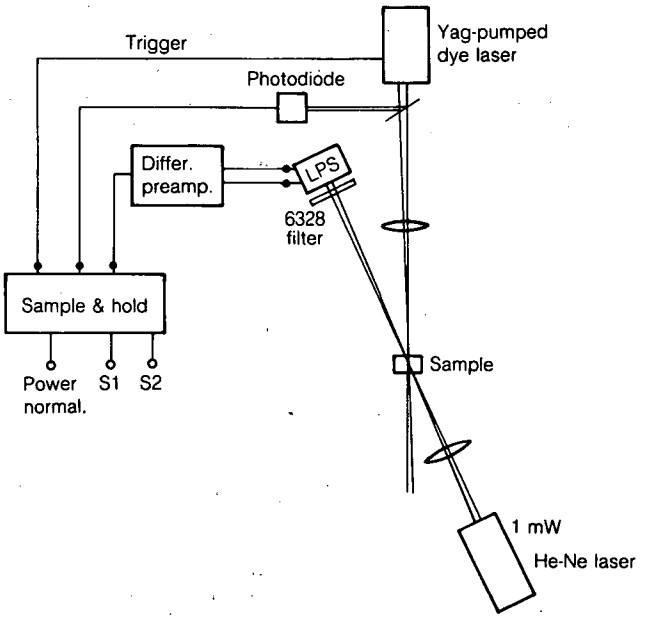

Figure 14. Experimental arrangement for a modulation scheme to minimize "noise" from atmosphere-caused beam wandering in photothermal deflection spectroscopy; LPS, lateral position sensor. (XBL 852-8815)

*Complete version to be submitted to *Applied Optics*.

Although the reactive nature of surfaces has been exploited for some time in processes such as catalysis, the exact nature and mechanisms responsible for their unique behavior remain to be ascertained. In this area of research, we employ photothermal spectroscopy to probe semiconductor surfaces and interfaces. Initially, our emphasis is on gaining a better understanding of the electronic properties of surface states through the investigation of their optical properties.

*Polarization and Temperature Dependence of Surface State Absorption in Si and Ge(111)**

The room temperature (111) cleavage faces of silicon and germanium are known to reconstruct to a metastable 2 × 1 unit cell, with period doubling along one of the three equivalent $<1\bar{1}2>$ directions on the surface. The mechanism behind this doubling of the unit cell has been the subject of much inquiry, with numerous models proposed to explain the various experimental results. The polarization dependence of the surface optical absorption is a consequence of the overall symmetry of the dangling-bond orbitals and does not require exact knowledge of the atomic positions to allow comparison with a class of models. The angular dependence of the dipole matrix element is different for the various models, making the polarization-dependent dangling-bond absorption a crucial test of these models.

We have studied the (111)2×1 surface state absorption of both Si and Ge, using polarization-dependent photothermal displacement spectroscopy. In addition to investigating the room temperature cleaved surface, we have also monitored the temperature dependence of the surface absorption as it is changed during annealing of the Ge(111) surface from the 2×1 to the *c*-2×8 structure.

Polarization Dependence. The polarization-dependent dangling-bond absorption was measured using photothermal displacement spectroscopy. In brief, this involves the optical detection of the thermal expansion of a sample as it is heated by absorption of light. The change in slope of the surface due to local thermal expansion is detected through the deflection of a HeNe probe beam reflected from the sample. Among the advantages of this technique is the ability to measure surface absorption directly, without requiring a difference measurement between a clean and an oxidized surface.

Both Si and Ge (111)2×1 surfaces exhibit ~2% absorption of $[\bar{1}10]$ polarized light, peaked at ~0.46 eV for Si and ~0.50 eV for Ge. The polarization dependence of the absorption peaks for Si and Ge in single-domain regions are shown in Fig. 15. A $\cos^2\theta$ dependence with a maximum along $[\bar{1}10]$ can be seen for both Si and Ge. The silicon results are in agreement with recent polarization-dependent reflectivity measurements. There is no significant rotation of the pattern, with all measurements being within the experimental alignment error of $\sim \pm 5°$. The pattern was observed to change when areas of different or mixed domains were examined. It could always be fitted by:

$$\sum_{\beta_i=-1,0,1} a_i \cos^2\left(\theta + \beta_i \frac{2\pi}{3}\right) ,$$

with the a_i correlating to the observed LEED intensities of the different domains. Of the various models discussed below, this is consistent only with the π-bonded chain model for both materials. The surface absorption disappeared upon oxidation, as can be seen in Fig. 15.

Temperature Dependence. The Ge(111) surface converts from 2×1 to a *c*-2×8 structure upon mild annealing, and preliminary results of observing this phase transition via the polarization-dependent absorption as an order parameter are shown in Fig. 16. This particular cleave was not a single domain, but, by fitting the polarization dependence, it was determined that, at the measurement point, two domains were present in the ratio of ~12:1, with the primary absorption occurring for vertical polarization. The polarization of the incident light ($\kappa\omega$ = 0.48 eV) was alternated between vertical and horizontal during the annealing process, and the photothermal signal at the two polarizations is shown in Fig. 16(a). The spectrum and polarization dependence when half of the signal had been annealed away was indistinguishable from the original except in magnitude. The sample was then heated to 135°C, and as can be seen in Fig. 16, above ~105°C there was no significant polarization dependence. In the first cycle, the sample temperature was greater than 60°C, where the surface signal starts to diminish, for 40 minutes. In the second cycle, the time between the data points at 60°C and 105°C was 37 minutes.

Free carrier absorption can be seen contributing to the signal above room temperature. The surface

*Complete versions of this work appeared in *Phys. Rev. Lett. 52*, p. 1148 (1984); *Phys. Rev. B. 29*, p. 7048 (1984); and the *Proceedings of the 17th International Conference on the Physics of Semiconductors*, J.D. Chadi and W.A. Harrison, Eds. (Springer-Verlag, 1985).

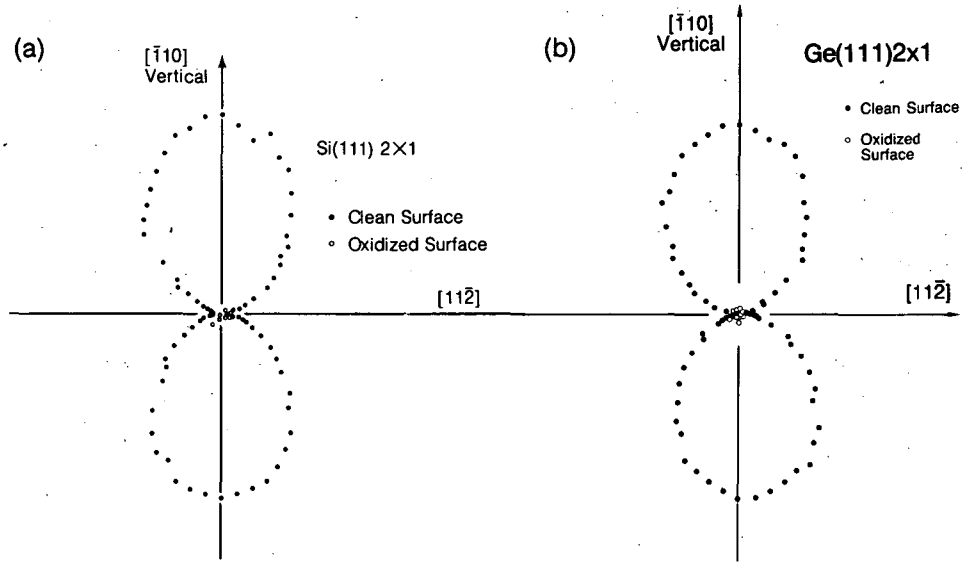

Figure 15. Polarization dependence of (111)2×1 peak absorption for (a) Si (0.46 eV) and (b) Ge (0.50 eV). [(a) XBL 8312-6936; (b) XBL 843-10183]

signal can be extracted as the difference between the absorption of light polarized parallel and perpendicular to $[\bar{1}10]$, since the isotropic free carrier absorption adds equally to both polarizations [Fig. 16(b)]. It is also possible to separate surface and bulk contributions through the phase of the photothermal signal. The phase was observed to change smoothly from that of a surface absorption to the later arrival of the bulk signal between 60°C and 100°C. A vector separation of the two components was found to be consistent with the polarization data in Fig. 16.

The 135°C anneal resulted in a diffuse, "weak 8" LEED superstructure, and a subsequent 210°C anneal resulted in a sharp *c*-2×8 pattern. After the 210°C anneal, a small absorption at room temperature was detected at 0.48 eV. This absorption had a magnitude of ~0.06% and no polarization dependence. Although the signal-to-noise ratio was low, the phase seemed to indicate surface origin. If so, it would indicate that the *c*-2×8 structure has a small absorption at this energy. This is consistent with surface photovoltage (SPV) and photoconductivity (SPC) measurements, which find a signal at similar energies for the *c*-2×8 structure. The precise temperature dependence varies among cleaves, but the signal usually decays between 60°C and 130°C when the sample has been annealed just before cleavage. If the sample is not preannealed, the signal occasionally decays at 35°–60°C, and the resulting LEED pattern is 1×1, probably due to contamination.

The polarization-dependent optical absorption of cleaved Si and Ge (111)2×1 surfaces exhibit similar spectra, peaking at ~0.47 eV in Si and ~0.50 eV in Ge. This peak absorption has a strength of about 2-1/2% on flat, single-domain cleaves and is weaker on less homogeneous surfaces. The absorption is intrinsic to the 2×1 reconstruction and is the same as that previously seen with reflectivity, surface photovoltage, surface photoconductivity, and electron energy loss spectroscopies. The polarization dependence of this absorption was seen to follow $\sin^2\phi$, with maximum absorption parallel to $[1\bar{1}0]$, and no absorption for light polarized along the period doubling $[11\bar{2}]$ direction. This result was found to be consistent with only one of the many models proposed for these surfaces: a rebonded chain exhibiting a $(1\bar{1}0)$ mirror plane. The size of the optical gap indicates a probable buckling of the π-bonded chain. This structural assignment is in agreement with data from a variety of other techniques as reported in the literature.

The polarization-dependent absorption is characteristic of the (111)2×1 surface and was used to probe the extent of the 2×1 phase during annealing and chemisorption. Monitoring of the absorption during a heating cycle similar to that in the stepwise annealing experiments showed additional decay in the 2×1 concentration upon reheating to a lower temperature than previously attained. This leads to the conclusion that the proximity of annealed

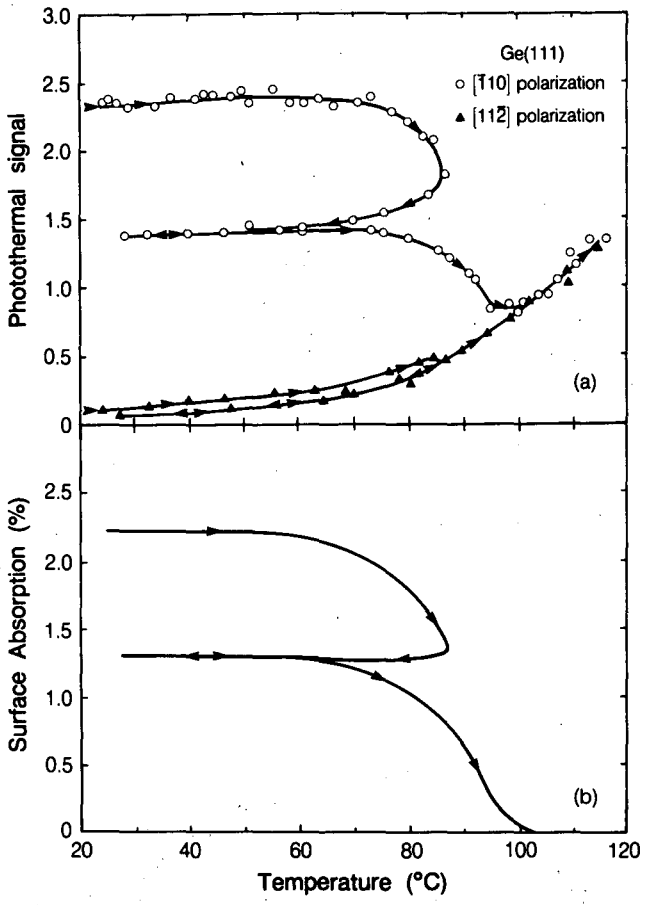

Figure 16. (a) Temperature dependence of photothermal signal from cleaved Ge(111). Sample is heated, cooled, and heated again. (b) Surface absorption. Difference between $[\bar{1}10]$ and $[11\bar{2}]$ signals in (a). (XBL 846-8488)

regions can lower the transition temperature of a given region of the surface. Preliminary experiments probing the temperature dependence of the surface optical energy gap showed little or no temperature dependence in the range of 300–450 K, contrary to the bulk gap dependence. This appears to support the buckled nature of the π-bonded chains, which would result in a strong interaction between the surface phonon and the dangling-bond states. Finally, these results have shown photothermal displacement spectroscopy to be a powerful new tool for surface studies, as well as for other applications that require remote sensing.

Amorphous Photovoltaic Semiconductors

Amorphous photovoltaic semiconductors, such as hydrogenated amorphous silicon (*a*-Si:H), hold promise for meeting Department of Energy cost and efficiency goals for thin-film solar cells prior to 1990. To achieve the higher conservation efficiencies required, it is necessary to better characterize the unique optical and transport properties of these materials. Photothermal spectroscopy can be used to elucidate the optical and electronic properties of *a*-Si:H. Of particular interest is the investigation of the optical properties near the so-called bandgap. By combining luminescence studies, photoconductivity, and optical absorption, a full and accurate characterization of the de-excitation of these photoexcited amorphous semiconductors can be achieved.

*The Effects of Dopants and Defects on Light-Induced Metastable States in Hydrogenated Amorphous Silicon**

An intriguing property of many amorphous semiconductors is that they exhibit metastable defect states. For both the chalcogenide glasses and *a*-Si:H, prolonged illumination creates defect states that disappear upon annealing. In the case of *a*-Si:H, these metastable states (Staebler-Wronski effect) alter various properties such as conductivity and luminescence. Yet, despite extensive research, they are still not well understood. Although silicon dangling-bond defects have been implicated, the question remains whether the apparent increase in the number of these defects is due to a shift in the Fermi level or to the creation of new defects upon illumination. Another significant issue is the connection between already existing (annealed-state) defects and dopants, and those defects induced by illumination. Using photothermal deflection spectroscopy (PDS), we have studied the optical absorption of the light-induced defects in *a*-Si:H. Since the measurement is insensitive to the position of the Fermi level, both the change in defect density due to illumination and the energy level of the defect can be determined.

Figure 17 shows that exposure to light enhances the gap-state absorption, whereas annealing restores the absorption to its original dark value. The enhancement is consistently reproducible when the illumination-anneal cycle is repeated several times. Previous work has demonstrated that the magnitude of gap-state absorption in *a*-Si:H provides a direct measure of the silicon dangling-bond-defect density, N_s. Using the same procedure for the change in optical absorption, we quantitatively determine the change in the defect density between the annealed and illuminated state, ΔN_s. For undoped material, ΔN_s is approximately $10^{16}\,\mathrm{cm}^{-3}$. By comparing the experimental absorption spectra with calculated spectra generated from density-of-states models, the defect energy level is determined to be $\sim$1.25 eV

*Complete version to appear in *Physical Review B.*

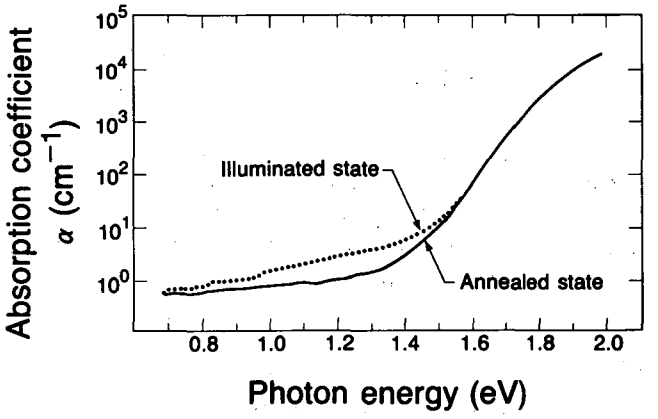

Figure 17. Effect of illumination on gap-state absorption of undoped *a*-Si:H. (XBL 847-10700)

below the conduction band. Since the energy of the defect and its cross section are identical to those measured for silicon dangling-bond defects, we conclude that the change in subgap absorption is due to silicon dangling-bond defects. Little or no change is seen in the exponential absorption (Urbach) edge.

Figure 18 shows that the light-induced defects scale with dopant concentration over a wide range of doping levels. The ratio $\Delta N_s/N_s$ is found to be independent of doping level to within a factor of 2. Thus, the effect is largest for high doping, unlike the case of conductivity changes. The fully compensated sample exhibited the least enhancement, $\lesssim 10^{15}$ cm^{-3} defects, which is an order of magnitude smaller than for the undoped material. For undoped material, the increase in defect density, ΔN_s, is constant to within a factor of 2 or 3, independent of the initial defect density, N_s, as seen in Fig. 19.

The results unambiguously show that the increase in defect density is not due simply to a shift in the Fermi level toward midgap upon illumination. A shift in the Fermi level, without any change in dangling bond defect density, results in less subgap absorption rather than the observed increase. Further, by successively increasing the dopant concentration, the Fermi level moves into the band tails so that after illumination it is still in a region of *smaller* dangling-bond density. Consequently, the effect should increase with increased doping, which is the opposite of what we observe. Since Fermi-level motion alone cannot account for the observed changes, we conclude that illumination creates new dangling-bond defects.

In terms of the mechanism for creating the dangling bonds, the results imply that the light-induced

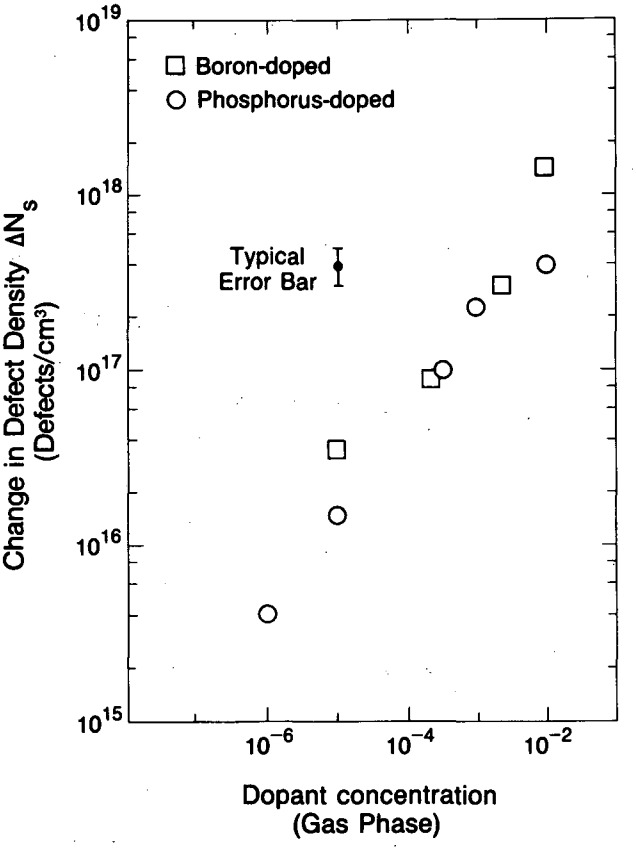

Figure 18. Dependence of the light-induced increase in defect density, ΔN_s, on dopant concentration. (XBL 836-2671)

defects do not result from breaking weak Si-Si bonds. One would expect ΔN_s to be relatively large for high-defect-density undoped material, which has substantial strain disorder (as evidenced by a broad Urbach edge) and consequently a large number of weak Si-Si bonds. Yet, for undoped material, ΔN_s is constant, *independent of disorder.*

Finally, there are several implications for solar cell fabrication. When air is let into the chamber during preparation, the cell exhibits an even larger efficiency drop after prolonged illumination, which again can be annealed away. The conclusion that light-induced defects are impurity-related is consistent with this observation. In addition, for *p-i-n* solar cells, illumination results in a fall-off in the blue response. Here, the doped outer layer will have the largest density of light-induced defects. Consequently, photons with short penetration depths will be strongly affected.

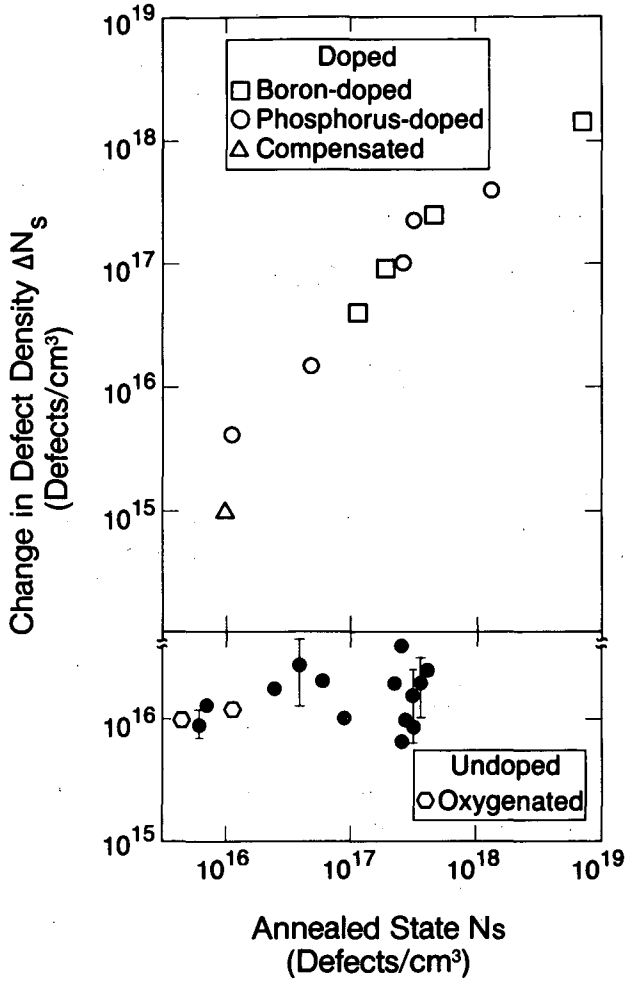

Figure 19. Dependence of the light-induced increase in defect density, ΔN_s on the initial defect density, N_s, for doped and undoped material. (XBL 847-10703)

*Urbach Edge and Gap States in Hydrogenated a-SiC and a-SiGe Alloys**

Considerable interest has developed recently in amorphous alloys based on hydrogenated amorphous silicon. Alloys with gaps smaller than *a*-Si:H—such as *a*-SiGe:H—are of interest in photovoltaic devices since they offer a better match to the solar spectrum (e.g., stacked cells). Alloys with gaps wider than *a*-Si:H—such as *a*-SiC:H or *a*-SiN:H—are also important in the construction of solar cells because they provide suitable window-layer materials. Moreover, *a*-SiC:H is promising for large-area white luminescence devices. Further interest in these alloys has resulted from the development of amorphous superstructures, which are developing into a major field of interest.

*Complete version to appear in *Solid State Communications.*

Most of these alloy phenomena are critically dependent on the spectral distribution of localized states—i.e., band tails and defect levels—inside the pseudogap of the alloy. For instance, the best SiGe alloys available to date have a density of dangling-bond defects that are a few times 10^{17} cm^{-3}. This results in a very poor photoconductive and luminescent behavior. Also, the SiC alloy, although exhibiting good room-temperature luminescence efficiency, shows a rapid drop in photoconductivity as the amount of carbon in the solid is gradually increased. Possible mechanisms behind this behavior include (1) the added compositional disorder of the alloy, which is reflected by a larger localized state density, and (2) the different energies and bond lengths of the elements, differences that can influence the formation of structural defects.

We investigated such effects when undoped *a*-Si:H, produced by glow discharge in silane, is increasingly mixed with either carbon or germanium.

The spectral distribution of the subgap states was determined by photothermal deflection spectroscopy (PDS), which allows detection of very weak optical absorption levels. The above-gap absorption was measured by direct transmission, using a Cary spectrophotometer. Typical absorption curves of the *a*-Si_xC_{1-x}:H alloys are shown in Fig. 20 for values of x between 1 and 0.77.

A remarkable result is that there is no appreciable variation in the density of defect states throughout the concentration range explored. This leads to two important conclusions: first, the presence of carbon has little effect on the existing structural defects, or on the bond passivation due to hydrogen; second, one can rule out the possibility that tail states are involved in the low-energy absorp-

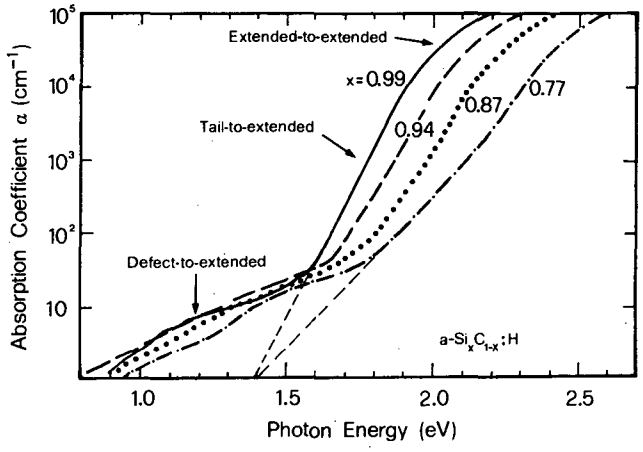

Figure 20. Absorption spectra of *a*-Si_xC_{1-x}:H alloys of different composition. (XBL 851-9704)

tion region because their increased density for larger C content would be reflected in stronger transition rates at those energies. The integrated absorption in the low-energy region is therefore a true measure of defect density.

Corresponding experimental results for the *a*-Si_xGe_{1-x}:H alloy are reported in Fig. 21. We shall stress only the significant differences. (1) The Urbach characteristic energy E_o increases with germanium content, but not as effectively as in *a*-SiC:H. Moreover, the tail is soon ill-defined for the reason discussed in (2) below, so that E_o is almost certainly overestimated. (2) The defect state density is higher than in *a*-SiC:H. It can be measured with some accuracy only for the lowest Ge content sample; its determination is otherwise made difficult by serious overlap with the Urbach tail. The values found are consistent with the silicon dangling-bond density found in the same samples by ESR. However, for $x \lesssim 0.60$, ESR predicts a higher density of Ge-related dangling bonds—10^{18} cm^{-3} and above. These states apparently are not optically active in the same energy range as Si dangling bonds but are closer to the gap. Figure 22 has been obtained by additively superimposing the Si and Ge dangling-bond spectra and the alloy bands. Because of their position in the upper half of the bandgap, above Fermi level, Ge dangling bonds can only be final states for transitions from the valence continuum. The minimum energy for these is about 1.1 eV, which already falls over the Urbach tail. This explains why in *a*-SiGe the latter is ill-defined for $x \leqslant 0.60$.

We now proceed to account for the Urbach tail broadening observed in the alloys in terms of compositional disorder. The appearance of an exponential tail below the fundamental threshold is due to

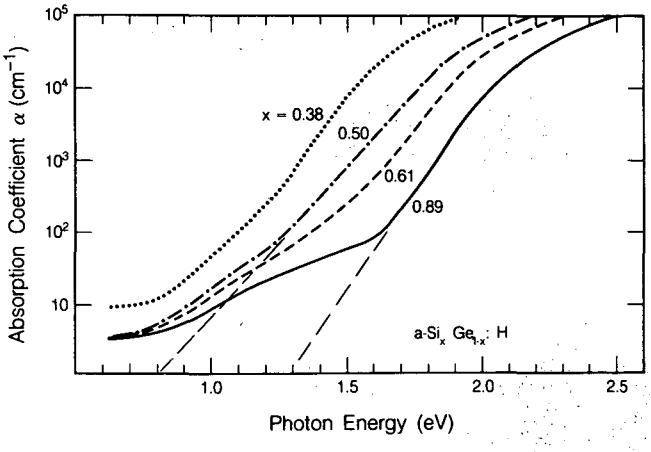

Figure 21. Absorption spectra of *a*-Si_xGe_{1-x}:H alloys.
(XBL 851-9705)

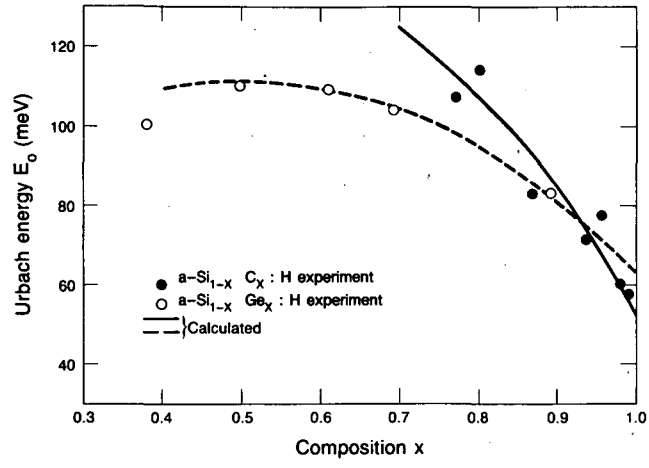

Figure 22. Urbach characteristic energy as deduced from PDS spectra and as calculated by a model assuming a Gaussian bandgap due to compositional disorder.
(XBL 8412-6457A)

the definition of local gap values over regions comparable to the phonon coherence length. The tail states are in a sense "pulled out" of the band continua. We extend the model to the alloys by taking a characteristic Urbach energy E_o that results from the sum of three contributions:

$$E_o = E_T + E_X + E_c$$

$$= K[\langle U^2\rangle_T + \langle U^2\rangle_X] + E_c \quad , \tag{12}$$

where K is an appropriate quadratic deformation potential of the bandgap and the $\langle U^2\rangle$'s are the mean-square deviations of atoms from an ideally ordered configuration, respectively due to thermal and structural disorder. E_c is the added term from compositional disorder, due to potential fluctuations associated with the heterobonds. We take the $\langle U^2\rangle_T$ and $\langle U^2\rangle_X$ terms as constants; in other words, we assume that structural disorder and phonon effects are comparatively unaffected by the inclusion of carbon or germanium. A measure of the third term in Eq. (12) is then given by the gap spreading which stems from local fluctuations in the alloy composition. If these are Gaussian, as in the case of *a*-Si_xC_{1-x}:H, where the Si and C atoms are randomly distributed throughout the film without chemical ordering, Urbach tailing is expected. The probability of finding the local composition y in a cell containing n atoms for an alloy of given x, is:

$$P(y) \propto e^{-\frac{n(y-x)^2}{2x(1-x)}} \quad , \tag{13}$$

whose full width at half maximum is:

$$\Delta = 2\,\frac{2\ln 2x(1-x)^{1/2}}{n} \quad . \qquad (14)$$

A measure of the bandgap spreading around $E_g(x)$ is given by:

$$\Delta E_g = \frac{dE_g}{dx}\,\Delta \quad ,$$

where (dE_g/dx) is the experimental x range. We assume $E \approx f\,\Delta\,E_g$, where f is a suitable coupling factor. We collect the prefactors into a single constant:

$$A = \frac{8\ln 2^{1/2}}{n} \quad ,$$

and try to fit the experimental data (Fig. 22) by means of the equation:

$$E_o = E_T + E_X + A[x(1-x)]^{1/2}\,\frac{dE_g}{dx} \quad . \qquad (15)$$

The best fitting is obtained for $A = 0.106$ for a-SiC and 0.192 for a-SiGe, and $E_T + E_X = 34$ meV in both cases. If we take $f \approx 1$, i.e., the gap spreading does directly add to the Urbach energy, the A value gives $n \approx 150$ for the number of the sampled atoms in SiGe and $n \approx 490$ in SiC, which fit respectively in spheres of radii approximately 8 and 12 Å. These values are probably closer to the average localization length of the tail states than, for instance, to excitonic radii. The agreement of this model with the experimental data is particularly good.

Liquid Crystal Research

The liquid-crystalline state of matter is characterized by a spontaneous anisotropic order and by fluidity. The anisotropic order leads to anisotropy in the physical properties of the medium, and the fluidity makes it easily susceptible to external perturbations in the form of electric or magnetic fields, temperature, or pressure. In addition, we have demonstrated that certain gaseous organic pollutants change the liquid-crystalline structure. This change, which is readily detectable, was the basis for the development of a sensitive (10^{-6}) personal dosimeter for exposure to organic chemicals. Our current research focuses on the basic physics of the liquid-crystalline state to lay the groundwork for further applications of this class of materials.

*Two-Dimensional Phase Transition in Lyotropic Liquid Crystals**

The nature of phase transition in a monolayer of lecithin (DPPC) at the water-oil interface has been investigated using photon correlation spectroscopy (Fig. 23). We observe the following results:

Main Transition (LE/LC). The "main transition" is the large flat region shown in Fig. 24. We believe this region represents either a weak first-order or first-order phase transition. There clearly seems to be only one slope discontinuity, so the weak first-order transition seems more likely. This would be driven by chain melting and should not be of the Halperin-Nelson type because of the large entropy involved in the chain's degrees of freedom. The nearly zero slope is also consistent with a weak first-order transition. Presumably, the difference between air-water and oil-water isotherms is due to the size of the cooperative domains.

Second Phase Transition. We believe that we have also seen evidence of a second phase transition at lower areas. This may be related to the "pretransition" observed in bilayer stacks. This transition could possibly correspond to the elimination of a chain tilt in the region between the two transitions. It is also not likely to be of the Halperin-Nelson type since large viscosities are observed for pressures above the main (LE/LC) transition in lecithin monolayers.

We believe this is a real effect, since the flat region, the increase in transversal viscosity, and the decrease in slope all occur at the same region of the isotherm. Since the photon correlation is a local probe, a leak would not explain the increase in instrumental linewidth. Film collapse is unlikely because the size of the hysteresis indicates collapse did not occur until much later. Also, no evidence of a leak was observed during the course of the experiment. At very high pressures, above the second flat region, the high signal-to-noise ratio allowed rapid measurements, but total times of 5 minutes between points were still maintained since one could easily see that the film took ~3 minutes to "relax" to its final value.

*Complete version to be submitted to *Physical Review Letters.*

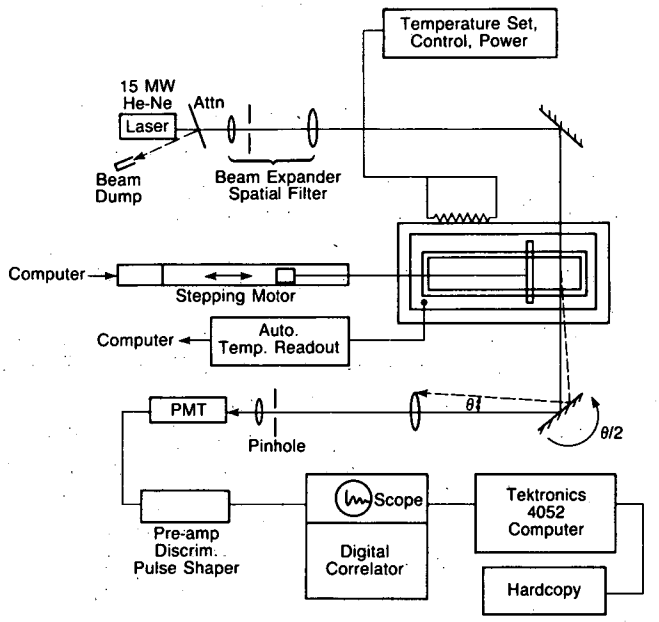

Figure 23. Experimental setup for a investigation of phase transition in a liquid-crystal monolayer (lecithin), using photon correlation spectroscopy. (XBL 846-10616)

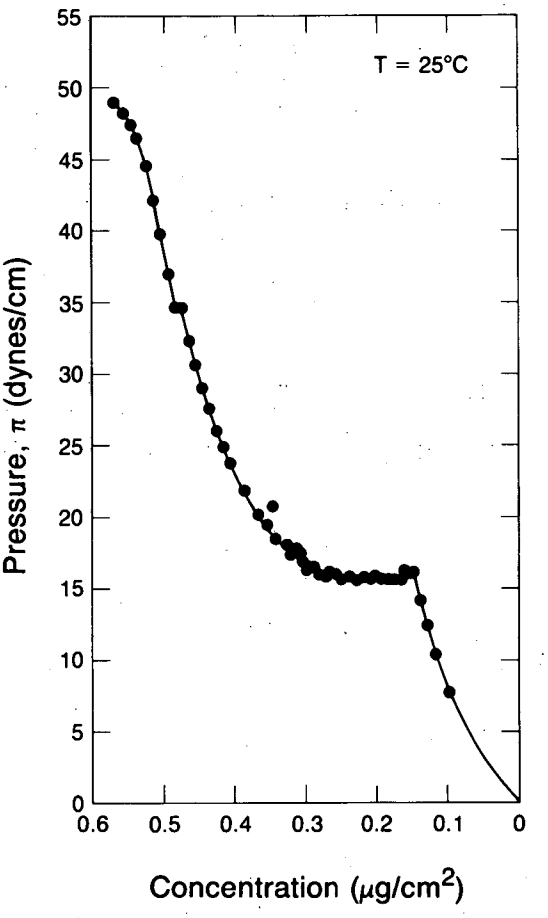

Figure 24. Lecithin (DPPC) isotherm at water-dodecane interface. (XBL 846-10640)

PLANNED ACTIVITIES FOR FY 1985

In laser spectroscopy, our goals will be to develop novel techniques and to exploit advanced applied physics concepts to the ultrasensitive measurements of minute optical absorption and vibrational spectra of gases, liquids, and solids. The emphasis will continue to be on unambiguous remote sensing of atmospheric constituents of laser photothermal spectroscopy and detection. Pulsed photothermal displacement spectroscopy will continue to be studied, and extensions of this technique for the study of liquids will be devised. Nonlinear photoacoustic and photothermal spectroscopy of gases will be initiated.

Research on amorphous semiconductors will focus on the physics of defects in hydrogenated amorphous silicon and germanium. The elucidation of the nature of the metastable photoinduced defects in amorphous silicon will continue to be of interest. A new research direction is the physics of photovoltaic devices.

Another relatively new activity is the investigation of the properties of semiconductor surfaces and interfaces. Processes at the liquid-semiconductor and gas-semiconductor interfaces will also be studied.

Finally, we will continue our research on laser physics and technology, with the goal of achieving widely tunable, high-average-power pulses a few femtoseconds wide. Another goal is to continue exploiting the waveguide laser configuration we have developed.

Treatment of an Oil Shale Retort Water by Stationary Fixed Biofilm*

J.B. Healy, Jr., G.W. Langlois, R.H. Sakaji, J.F. Thomas, and C.G. Daughton†

The process wastewaters from oil shale retorting originate from mineral dehydration, combustion, and input steam during pyrolysis of the embedded polymeric kerogen, a high-molecular-weight heterogeneous polymer. High concentrations of numerous organic and inorganic solutes are typically present. Although many of these compounds have been identified for a few waters (see references cited[1]), most have not. For the waters that have been studied only small portions of the spectrum of organic solutes have been found to be biodegradable during aerobic biological treatment.[1-3] Insufficient acclimated biomass, low individual-substrate concentrations, and chemical inhibition have been proposed as mechanisms responsible for the resistance of dissolved organic carbon (DOC) present in a range of process wastewaters.[1,2,4,5] All of these purported limitations could potentially be overcome by fixed-biofilm treatment (FBT), which has inherent advantages over homogeneous dispersed-growth systems.[6]

Few FBT studies that use small, lab-scale columns have been described in the literature,[7-9] and only two used actual industrial wastewater.[10,11] Several studies, however, were particularly relevant to retort water. With synthetic "wastewater" media, fixed biofilms are reported to be capable of removing low concentrations of aromatic compounds,[7-9] even in the presence of high ammonia concentrations.[10] These results suggest that the refractory aromatic amines present at low concentrations in ammonia-rich oil shale process waters could be removed in FBT reactors, especially when granular activated carbon (GAC) is used as a solid support.[12] We investigated the potential for FBT to remove a greater percentage of the organic solutes in Oxy-6 retort water (Occidental Oil Shale, Inc.) than has been reported for batch, dispersed-phase treatment.[1]

*This work was supported by the Assistant Secretary for Fossil Energy, Office of Oil Shale, Division of Oil, Gas, and Shale Technology of the U.S. Department of Energy under Contract No. DE-AC03-76SF00098.

†Sanitary Engineering and Environmental Health Research Laboratory, University of California (Berkeley), Richmond, CA 94804.

ACCOMPLISHMENTS DURING FY 1985

Removal of DOC from an oil shale retort water by stationary fixed-biofilm treatment was investigated using aerated, lab-scale columns operated on recycle mode.[13] The FBT columns were packed with one of four solid-support materials: (1) Calgon F-400 GAC, (2) spent shale, (3) raw shale, and (4) glass beads.

There are two major mechanisms by which fixed-biofilm columns can remove organic solutes from a wastewater: sorption onto the solid support and biodegradation. In practice it is difficult to determine the relative extents of these two processes for a complex waste because they occur simultaneously. Our initial objective was to pre-saturate the sorptive sites of the solid support so that any further DOC removals could be attributed to biological mechanisms. To ensure that the sorptive capacities of the columns had been exceeded, all columns were operated three times longer than the time estimated for saturation of the GAC, the support having the greatest sorptive capacity of the four packing materials. Removal of DOC by volatilization or sorption onto the pump tubing was less than 10% of the total DOC removed.

Sorption Equilibrium on GAC

A batch equilibrium experiment indicated that only three hours was required to reach 95% of sorptive equilibrium. Greater than 99% sorptive equilibrium was achieved between 15 and 24 hours; therefore the equilibrium time was assumed to be 24 hours. The sorptive equilibrium data were fitted to the Langmuir model for adsorption isotherms, and the sorptive capacity of GAC for the DOC in spent medium was determined to be 0.29 g/g.

Routine Operation of Columns

Hydraulic retention times of the columns after more than one year of operation under recycle mode were: glass beads, 1.4 hours; raw shale, 1.1 hours; GAC (fed raw medium), 0.8 hour. The hydraulic retention time for the GAC column that was fed spent medium and operated under single-pass mode was 0.2 hour. The above retention times appeared to be long enough to allow maximum biodegradation because doubling the retention times did not increase DOC removals.

Microbial growth in all of the columns and respective feed lines was extensive and most likely resulted from the high organic loading rate and presence of readily degradable fatty acids.[3] The development of thick biofilms occasionally caused clogging problems. Usually a simple disruption of the top portion of the column material was sufficient to reestablish flow. Clogging in the spent-shale column could not be remedied because the friable, combusted shale particles broke down into smaller sizes until they permanently clogged the passages. For this reason, the spent-shale column was abandoned.

Treatment of Raw Retort Water Medium

Fixed-biofilm treatment of raw medium effected limited removals of organic solutes. The percentage of DOC removed by the three columns ranged from 59% to 65% after 11 days of recycle operation (Table 1). The removals of DOC external to the fixed-biofilm columns (i.e., within the delivery and collection system) were less than 65 mg/L (5%). It is possible that biological removals were actually higher (approaching the total removal percentages of Table 1) because volatile and adsorbable compounds lost in the abiotic control system may have been biodegraded in the columns before being lost from the system. When external removal percentages were subtracted from total removal percentages in Table 1, the following minimum-biodegradation percentages (means) resulted: GAC/FBT, 60%; raw-shale/FBT, 56%; glass-beads/FBT, 54%; and batch shake flask, 52%. These corrected removals were biologically mediated because they were effected well after physical sorption removals had reached steady state. Although biological removals exceeded the 52% removal by 11-day batch cultures, a large portion of the DOC still resisted biodegradation.

The minimum-biodegradation percentages (means) were used for statistical comparisons. A one-way analysis of variance and subsequent significance testing showed that the GAC and raw-shale FBT columns removed significantly greater amounts of DOC than the batch culture ($P < 0.05$). In addition, the GAC column removed significantly greater amounts of DOC than the glass-beads and raw-shale columns ($P < 0.05$). There was no significant difference between the glass-beads colum and batch culture ($P > 0.05$). Removals by the raw-shale column were not statistically different from the removals by the glass-beads column ($P > 0.05$). DOC removals appeared to be synergistically enhanced when FBT was combined with a sorptive solid support, even when its sorptive sites were saturated (cp. GAC column versus glass-beads column).

As an indirect, rapid measure of organonitrogen compounds in the treated and untreated samples of raw media, headspaces were analyzed for the presence of these compounds. Many of the compounds were tentatively identified as simple alkylpyridines.[13] These were extensively removed by all of the FBT columns. These compounds did not disappear, however, from the headspace above an 11-day batch culture. Although a number of alkylpyridines are at least slowly biodegradable by acclimated cultures,[1] it was possible that some or all of the volatile alkylpyridines in the retort water medium were removed by volatilization or sorption onto the silicone tubing. Abiotic controls lost approximately the same amount of volatile organonitrogen compounds as the active

Table 1. Percentage of DOC removed from the hydrophilic (HpF) and lipophilic (LpF) fractions of raw retort water media by fixed-biofilm columns (operating under 11-day recycle mode) and by batch shake cultures.

Biological treatment conditions[a]	Percent DOC removed (n, rsd%)		
	HpF	LpF	Total
GAC[b]/fixed-biofilm	74 (4, 9.4)	57 (4, 19.8)	65 (14, 3.3)
Raw shale/fixed-biofilm	68 (3, 14.3)	56 (3, 22.6)	61 (11, 6.7)
Glass beads/fixed-biofilm	71 (4, 11.8)	50 (4, 28.0)	59 (14, 5.1)
Batch shake flask	71 (3, 2.9)	33 (3, 8.1)	52 (6, 5.1)

[a]Solid support material for fixed biofilms was previously saturated with organic solutes from raw retort-water media.

[b]GAC, granular activated carbon.

FBT columns. Retort-water medium treated with $HgCl_2$ and recycled for 11 days through an uninoculated glass-beads column produced a headspace (Fig. 1) that was typical of the headspaces obtained both for the FBT samples and for the abiotic control that excluded the glass-beads column. The total peak area for all peaks with retention times greater than 3 minutes decreased about 90% regardless of the type of FBT column or abiotic control conditions. The total removal of DOC by both abiotic controls was 5%.

A simple reverse-phase fractionation technique[1] indicated that raw Oxy-6 retort water contains roughly equal amounts of DOC in the polar (hydrophilic fraction; HpF) and nonpolar (lipophilic fraction; LpF) fractions, and as with batch culture, the majority of the DOC removed resided in the HpF (Table 1). The three FBT columns removed a similar amount of HpF-DOC as did batch culture (ca. 70%) (Table 1). In contrast, the increased total DOC removals by the FBT columns were at the expense of LpF-DOC; the columns removed 1.5 to 1.7 times as much DOC from the LpF (Table 1) as did the batch cultures. The percentage of LpF-DOC removed by the individual FBT columns increased in the same order as the percentage of total DOC removed (glass beads < raw shale < GAC). This same order also held for the relative decrease of the characteristic brownish color of the Oxy-6 retort water and UV absorbances. This color, in a variety of oil shale process wastewaters, is attributed to the presence of refractory aromatic amines in the LpF.[1]

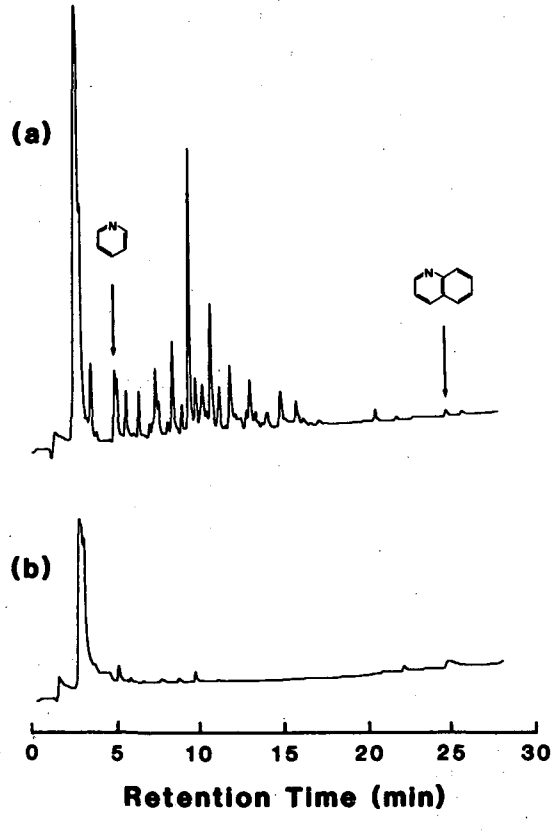

Figure 1. Gas chromatograms (flame thermionic, N-selective detection) of headspace over raw medium (Oxy-6 retort water) treated with 200 mg/L $HgCl_2$. Time 0, (a). After 11 days of recycle through glass-beads column, (b). Arrows mark positions of pyridine and quinoline, used for calculating retention indices. (XBL 8511-4771)

Despite abiotic losses of volatile nitrogenous compounds (Fig. 1), organic nitrogen measurements indicated that many less-volatile nitrogenous compounds (e.g., hydroxylated alkylpyridines and quinolines) remained after all of the biological treatments. Of the initial 88 mg/L of nonpolar organic nitrogen, 53 mg/L remained after treatment with the GAC column; 68 and 64 mg/L remained in the raw-shale and glass-beads columns, respectively. Batch shake cultures removed less than 5% of nonpolar organic nitrogen. Molar carbon-to-nitrogen ratios for the LpF fraction after any of the biotreatments ranged from 6 to 7, a range consistent with the presence of simple alkylpyridines and quinolines.

Even though the GAC-packed FBT column probably selected for a greater diversity of microbial niches, the column only increased the extent of DOC removal to 60% compared with 52% removals achievable in dispersed-phase batch cultures. The incomplete DOC removals and long treatment times in FBT columns suggest that FBT may be unsuitable for economic waste treatment. In addition, the FBT columns treating raw medium had the significant drawback of clogging.

Treatment of Spent Retort Water Medium

To avoid disruptions of the biofilm by clogging or from switching reservoirs in recycle mode, a GAC-packed FBT column was fed spent medium in single-pass mode. Since all of the readily degradable DOC in the spent water had been previously biooxidized during its production,[13] the remaining DOC was not expected to support a biofilm sufficiently thick to cause clogging. The spent medium was amended to 2% (vol/vol) with raw medium to provide about 10 mg/L of readily degradable fatty acids. This would meet the minimum requirements for a sparse biofilm. Bouwer and McCarty[7] supported a biofilm in the same size column with only 1 mg/L of acetate. The fatty acids could also have served as cosubstrates for organisms capable of degrading aromatic amines.

The GAC-packed FBT column fed spent medium was operated under single-pass mode for one year to ensure that the GAC sorptive sites had been completely saturated with spent-medium DOC. The adsorption capacity predicted by the Langmuir equation and a calculated first-order rate constant[13] were used to generate a theoretical breakthrough curve for the GAC spent-medium column. The effluent DOC concentration at breakthrough was defined to be 5% of the influent concentration, and the effluent concentration at exhaustion was defined to be 95% of the influent concentration.

The data collected during the first year of operation and the theoretical breakthrough curve for the GAC/spent-medium column are presented in Fig. 2. The volume of waste treated at exhaustion was 1.2 liters per gram of GAC. If biodegradation indeed were accounting for removal of a portion of the DOC, however, then saturation may have required a much longer time than estimated from the equilibrium data. Discrepancies have been observed[12] between observed saturation times and theoretical estimates. Furthermore, one research group believes that significant biodegradation did not occur in their GAC column until after saturation had first occurred.[9] Under our treatment conditions, 3.3 liters per gram of GAC were treated to ensure that saturation had indeed been achieved before DOC removals were attributed solely to biodegradation.

After one year of treatment under single-pass mode, the GAC-packed FBT column consistently removed, on average, 14% of the DOC from the spent medium (Fig.2). This removal was attributed to biodegradation because the replicate measurements were made well after sorptive removals had presumably reached a steady state. This contrasts with previous attempts to remove additional DOC from spent medium using batch cultures,[1] all of which have failed. Switching the GAC/spent-medium column to 11-day recycle mode after a year of single-pass operation did not significantly increase the DOC removal. Although this FBT column was able to remove some of the refractory material remaining after batch treatment of raw medium, the combined DOC removal (62%) remains as low as the removals by fixed-biofilm treatment in a single treatment step (Table 1).

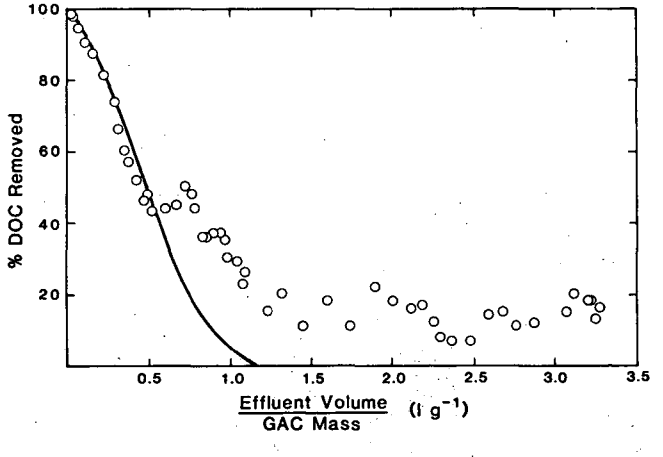

Figure 2. DOC removal from spent medium (Oxy-6 retort water) by a fixed-biofilm/GAC column operated under single-pass mode for one year; total cumulative volume of 150 liters of spent medium was treated by 44.8 grams of GAC. The theoretical removal of DOC by sorption (solid line) onto the GAC solid support was modeled from calculations made with data from adsorption isotherm experiments. (XBL 8511-4770)

REFERENCES

1. Healy, J.B., Jr., Langlois, G.W., and Daughton, C.G. (1985), "Biooxidation of Organic Solutes in Oil Shale Wastewaters," *Water Res. 19*, p. 1429.
2. Dobson, K.R., Stephenson, M., Greenfield, P.F., and Bell, P.R.F. (1985), "Identification and Treatability of Organics in Oil Shale Retort Water," *Water Res. 19*, p. 849.
3. Rogers, J.E., *et al.* (1981), "Microbiological Degradation of Organic Components in Oil Shale Retort Water: Organic Acids," *Appl. Envir. Microbiol. 42*, p. 830.
4. Healy, J.B., Jr., Jones, B.M., Langlois, G.W., and Daughton, C.G. (1983), "Biotreatment of Oil Shale Wastewaters," in *Sixteenth Oil Shale Symposium Proceedings*, J.H. Gary, Ed., Colorado School of Mines Press, Golden, CO, p. 498.
5. Jones, B.M., Sakaji, R.H., and Daughton, C.G. (1982), "Physicochemical Treatment Methods for Oil Shale Wastewater: Evaluation as Aids to Biooxidation," in *Fifteenth Oil Shale Symposium Proceedings*, J.H. Gary, Ed., Colorado School of Mines Press, Golden, CO, p. 581.
6. Stratton, R.G., Namkung, E., and Rittmann, B.E. (1983), "Secondary Utilization of Trace Organics by Biofilms on Porous Media," *J. Am. Water Works Assoc. 75*, p. 463.
7. Bouwer, E.J. and McCarty, P.L. (1982), "Removal of Trace Chlorinated Organic Compounds by Activated Carbon and Fixed-Film Bacteria," *Envir. Sci. Technol. 16*, p. 836.
8. Li, A.Y.L. and DiGiano, F.A. (1983), "Availability of Sorbed Substrate for Microbial Degradation on Granular Activated Carbon," *J. Wat. Pollut. Control Fed. 55*, p. 392.

9. Suidan, M.T., Siekerka, G.L., Kao, S.-W., and Pfeffer, J.T. (1983), "Anaerobic Filters for the Treatment of Coal Gasification Wastewater," *Biotechnol. Bioengng. 25*, p. 1581.
10. Lee, D.D., Scott, C.D., and Hancher, C.W. (1979), "Fluidized-Bed Bioreactor for Coal-Conversion Effluents," *J. Wat. Pollut. Control Fed. 51*, p. 974.
11. Suidan, M.T., Strubler, C.E., Kao, S.-W., and Pfeffer, J.T. (1983), "Treatment of Coal Gasification Wastewater with Anaerobic Filter Technology," *J. Wat. Pollut. Control Fed. 55*, p. 1263.
12. Ying, W.-C. and Weber, W.J., Jr. (1979), "Bio-Physicochemical Adsorption Model Systems for Wastewater Treatment," *J. Wat. Pollut. Control Fed. 51*, p. 2661.
13. Healy, J.B., Jr., Langlois, G.W., Sakaji, R.H., and Daughton, C.G. (1986), "Stationary Fixed-Biofilm Treatment of an Oil Shale Retort Water," LBL-19052.

Effect of Oil Shale Retort Water on Biooxidation of Aromatic Amines*

J.B. Healy, Jr., G.W. Langlois, J.F. Thomas, and C.G. Daughton†

Biooxidation would be one of the most cost-effective means of upgrading oil shale process wastewaters if a sufficient portion of dissolved organic carbon (DOC) were amenable to mineralization. In addition to large quantities of easily degradable aliphatic acids,[1] retort waters have been reported to contain numerous nitrogen heterocycles and other aromatic amines.[2–6] Several previous studies[7,8] have indicated that large numbers of aromatic amines, each present at a low part-per-million concentration, may be responsible for the resistance of a large portion of the DOC to biodegradation.

There is little published literature on simple aromatic amine catabolism. Of the studies, most have reported aromatic amines to be at least slowly biodegradable at relatively high concentrations in single-substrate systems.[9–14] Aromatic amines in retort water, however, may be refractory because of repression or inhibition of enzyme activity by high levels of the easily utilized nitrogen source, ammonia, or because of interactions of the numerous aromatic amine congeners.[7] Although some aromatic amines may be inherently recalcitrant,[12] no published literature exists regarding matrix effects that could cause normally biodegradable aromatic amines to resist biooxidation when present in a mixture.

The purpose of the work reported here was to determine the importance of inherent recalcitrance and inhibitory matrix effects on the resistance of multiple aromatic-amine substrates to biooxidation in retort water. For a simplified model system comprising a defined mixture of biodegradable aromatic amines at low concentrations, biodegradability was evaluated in the absence of high ammonia concentrations, and these results were compared with those obtained after adding a retort water containing ammonia.

ACCOMPLISHMENTS DURING FY 1985

To investigate possible causes of recalcitrance, we followed the disappearance of selected aromatic amines in both single- and mixed-substrate systems to model the more complex arrays found in retort waters. Before selecting individual compounds for the defined mixture, the biodegradability of each of 35 aromatic amines was evaluated in a series of batch, dispersed-phase cultures with each compound (100 mg/L) as the sole source of carbon, nitrogen, and energy. Although more than half of the compounds resisted biodegradation during the one to three months of incubation, we were able to demonstrate biodegradability for a sufficient number of the aromatic amines.

All cultures were incubated in 250-mL Erlenmeyer flasks at 30°C in the dark. Volatilization of aromatic amines was greatly reduced by capping the flasks with aluminum foil and by not agitating the culture fluid. Single-substrate cultures consisted of 33 mL of defined medium[15] containing 100 mg/L of the candidate aromatic amine. An inoculum was pooled from activated sludge (mixed-liquor suspended solids from the municipal sewage treat-

*This work was supported by the Assistant Secretary for Fossil Energy, Office of Oil Shale, Division of Oil, Gas, and Shale Technology of the U.S. Department of Energy under Contract No. DE-AC03-76SF00098.

†Sanitary Engineering and Environmental Health Research Laboratory, University of California (Berkeley), Richmond, CA 94804.

ment plant, Richmond, CA) and from a culture acclimated to nine oil shale wastewater media.[7]

Uninoculated media treated with 200 mg/L of the growth inhibitor, $HgCl_2$, served as the controls for detecting abiotic losses of DOC (e.g., volatilization). Losses of DOC measured in the controls were subtracted from the total removals in active cultures.

Cleavage of the heterocyclic and aromatic rings in single-substrate batch cultures was indicated by a reduction in UV absorbance. Only two to six days were required for original cultures to acclimate to aniline; 2-methylaniline; quinoline; pyridine; and 2- and 3-methyl-, 2- and 3-ethyl-, and 2- and 3-hydroxypyridine. Acclimation to 2-methylquinoline required a lag of 2 weeks before biodegradation began; mineralization occurred over the next 10 days. Excluding lag periods, each of these compounds was biodegraded in less than 2 weeks. Pyridine, quinoline, and aniline compounds substituted in the 4-position or those that contained more than one ring substitution were significantly more refractory than those substituted in the 2- or 3-positions.

Although original acclimation times for 2,4- and 2,6-dimethylpyridine were about one week, 5 weeks was needed for biodegradation of the initial 100 mg/L of substrate. After 3 weeks of acclimation, cultures required an additional 3 weeks to biodegrade 2,4,6-trimethylpyridine and 2-methylpyrazine. After 3 months of incubation in defined media, none of the other 20 aromatic amines was biodegraded. Some of these aromatic amines may be inherently refractory.

Time required for the biodegradation of an additional 100 mg/L of substrate by outgrown, acclimated cultures was much less than the time required for the original substrate dosage. For example, while 5 weeks was required for the biodegradation of more than 90% of the initial dose of 2,6-dimethylpyridine, only a few days were required for a second dose (Fig. 1). This increased rate can be attributed to the increased concentration of acclimated cells. Although greater cell numbers were observed with phase-contrast microscopy, the increase in cell numbers could not be quantified, because of predatory protozoa in the enrichment cultures.

Each of the 15 biodegradable aromatic amines was completely mineralized by the acclimated cultures as evidenced by DOC removals, which correlated with reductions in UV absorbance. These results agreed with those reported in the literature (Table 1). With the exceptions of cyanuric acid, 4-methyl- and 2,3,6-trimethyl-pyridine, and 3-methyl-, 4-methyl-, 2,4-dimethyl-, and *N*-methyl-aniline, the aromatic amines previously reported to be biodegradable were also mineralized in our defined media. In addition, we believe this is the first report of the biodegradability of 3-methyl- and 3-ethyl-pyridine; 2-methylquinoline; and 2-methylpyrazine.

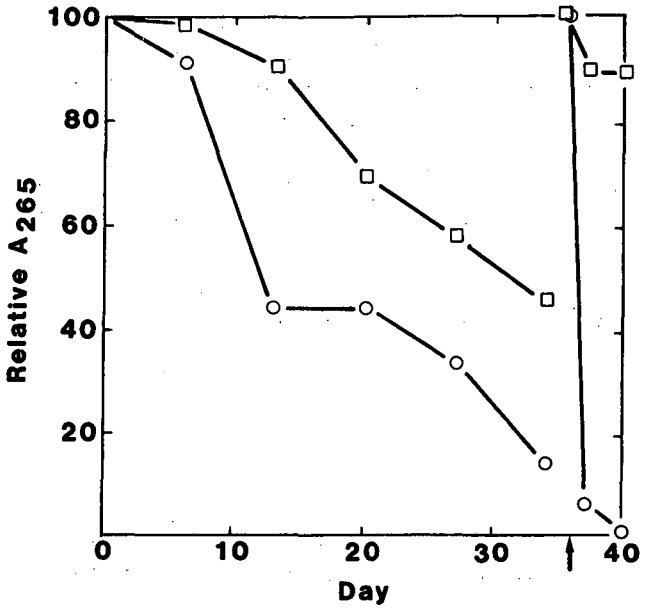

Figure 1. Relative disappearance (reduction in A_{265}) of 100 mg/L of 2,6-dimethylpyridine in an enrichment culture. Comparison of biodegradation (open circle) with abiotic losses from a $HgCl_2$-inhibited control (open square). Arrow indicates time of spike of an additional 100 mg/L of substrate. (XBL 8511-4769)

Of the 15 biodegradable aromatic amines, 12 had been previously studied as part of a defined mixture of 26 N-heterocycles.[16,7] These 12 N-heterocycles were used to make the multiple-substrate media containing the defined-mixture compounds. Acclimated cultures developed from a pool of the 12 individual enrichment cultures completely mineralized the mixture (92 mg/L) in less than a week. This behavior indicated that the individual substrates were degraded simultaneously by the mixed populations and that inhibitory interactions among the 12 component aromatic amines did not appear to be significant.

To determine the importance of inherent recalcitrance and inhibitory matrix effects on the resistance to biooxidation of multiple aromatic amine substrates in retort water, the defined mixture of 12 N-heterocycles was evaluated for its biodegradability in the presence and absence of Oxy-6 retort water. The total concentration of the defined mixture was increased to 332 mg/L so that these N-heterocycles could be easily detected above the endogenous DOC when added to 38% Oxy-6 retort water medium.[15] The behavior of this array of heterocycles in the

Table 1. Occurrence of aromatic amines in retort water and their biodegradability in defined media.

Chemical	Source[b]	Occurrence in retort water (literature reference)	Biodegradability[a]	
			Literature reference	This study
Aniline	1	+ (4)	+ (17,11)	+
2-Methylaniline	1	+ (4)	+ (11)	+
3-Methylaniline	1	+ (4)	+ (11)	−
4-Methylaniline	1	+ (4)	+ (11)	−
N-Methylaniline	1	+ (6)	+ (11)	−
2,4-Dimethylaniline	1	nr[c]	+ (17)	−
N-Ethylaniline	1	nr	nr	−
Pyridine	1	+ (4)	+ (12)	+
2-Methylpyridine	1	+ (4)	+ (12)	+
3-Methylpyridine	1	+ (4)	nr	+
4-Methylpyridine	1	+ (4)	+ (12)	−
2,4-Dimethylpyridine	1	+ (6)	+ (13)	+
2,6-Dimethylpyridine	1	+ (4)	+ (12)	+
2,3,6-Trimethylpyridine	2	nr	+ (12)	−
2,4,6-Trimethylpyridine	1	+ (4)	+ (13)	+
2-Ethylpyridine	2	+ (5)	+ (13)	+
3-Ethylpyridine	2	+ (3)	nr	+
4-Ethylpyridine	2	+ (2)	nr	−
3-Ethyl-4-methylpyridine	2	+ (5)	nr	−
4-Ethyl-3-methylpyridine	2	+ (5)	nr	−
5-Ethyl-2-methylpyridine	3	+ (5)	nr	−
2-*n*-Propylpyridine	2	nr	nr	−
4-tert-Butylpyridine	2	+ (3)	nr	−
2-Hydroxypyridine	4	+ (4)	+ (12)	+
3-Hydroxypyridine	4	+ (4)	+ (10)	+
2-Hydroxy-6-methylpyridine	4	+ (4)	nr	−
Quinoline	1	+ (4)	+ (9)	+
Isoquinoline	1	+ (4)	nr	−
8-Hydroxyquinoline	1	nr	nr	−
2-Methylquinoline	4	+ (4)	nr	+
4-Methylquinoline	4	+ (6)	nr	−
3,5-Dimethylpyrazole	1	+ (5)	nr	−
Benzimidazole	1	nr	nr	−
2-Methylpyrazine	1	nr	nr	+
Cyanuric acid	1	nr	+ (14)	−

[a]Biodegradability defined as the microbial cleavage of the ring structure.

[b]List of chemical suppliers: (1) Chem Service, West Chester, PA; (2) NOAH Chemical, Farmingdale, NY; (3) Fluka AG, Buchs, Switzerland; (4) Aldrich, Milwaukee, WI.

[c]nr, not reported.

absence of high ammonia in defined medium was then compared with its behavior in the retort water matrix.

These cultures were inoculated with 0.2 mL of either culture KY, which had been routinely maintained on 50% Oxy-6 retort-water medium, or culture RW-12, which was preadapted to 50% Oxy-6 retort water medium spiked with the defined mixture-12. Culture RW-12 was originally derived by combining culture KY with individual cultures acclimated to the 12 N-heterocycles.

Culture RW-12 biodegraded over 80% of the N-heterocycle mixture in defined medium (332 mg/L) in 3 weeks. Despite the threefold increase in total N-heterocycle concentration, the mixture was no more resistant to biooxidation than the same mixture at 92 mg/L.

The DOC removal from 38% Oxy-6 retort water by culture RW-12 was compared with the removal from the same retort water with the added (spiked) mixture of N-heterocycles (247 mg/L DOC). The major portion of biooxidation had ceased by day 21. After one week, 48% of the DOC in unspiked retort water was biooxidized. This was the same removal previously reported for culture KY,[7] which normally completes biooxidation of the readily degradable substrates (e.g., aliphatic acids) in 5 days and is incapable of further DOC removal. After three weeks, however, culture RW-12 had removed 55% of the DOC, indicating that these preadapted microorganisms were degrading additional solutes, perhaps aromatic amines to which culture KY was not adapted; in a parallel incubation with 38% Oxy-6 retort water, culture KY removed only 49% of the DOC by day 28.

Assuming that the readily degradable DOC in retort water medium was removed equally in the presence and absence of the N-heterocycle spike, the fate of the spike was isolated from the total removal of DOC by subtracting the DOC remaining for unspiked retort water from DOC remaining for spiked retort water. The resulting values indicated that the N-heterocycle spike was degraded slowly in the presence of retort water until degradation ceased at about 3 weeks. Only 32% of the spike was removed by culture RW-12. In contrast, the same culture removed 81% of the DOC from the spike when incubated in defined medium for the same time period.

Analysis of the N-heterocycle mixtures by high performance liquid chromatography (Fig. 2) allowed the monitoring of the fates of the individual aromatic amines. All 12 N-heterocycles were attacked via ring cleavage as indicated by the reduction in absorbance at 254 nm (cp. Fig. 2a,b). When

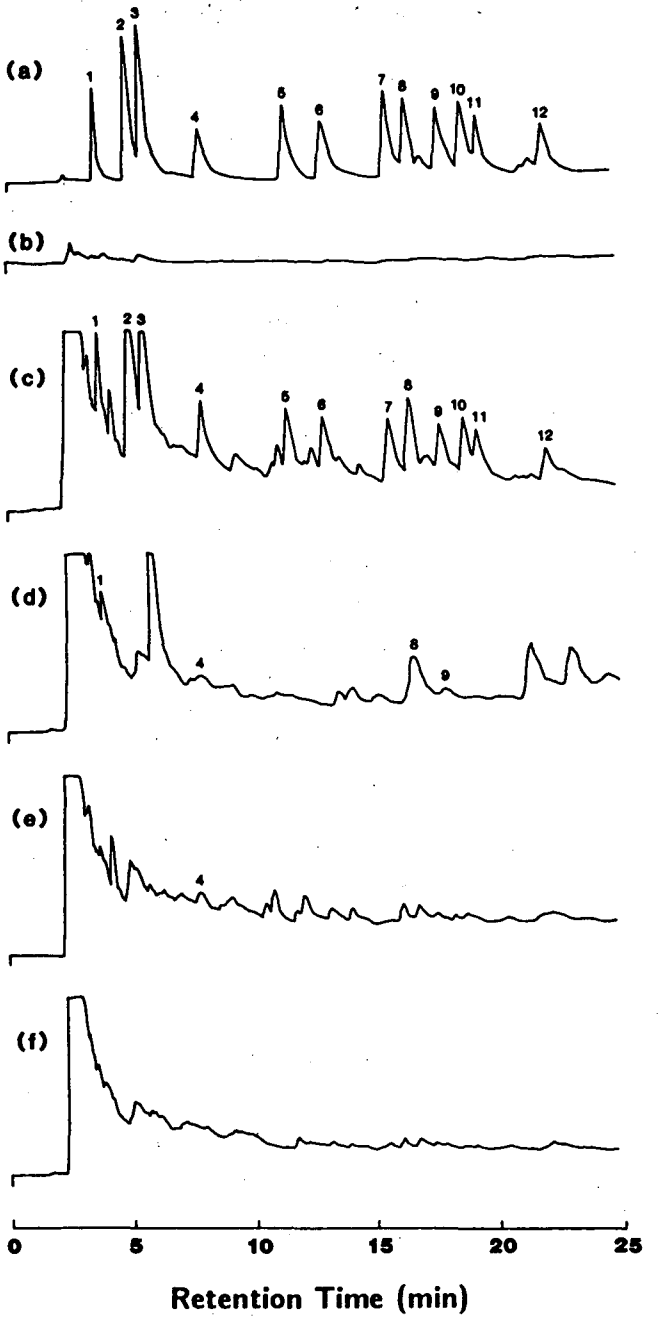

Figure 2. HPLC chromatograms of 12 aromatic amines in the presence and absence of Oxy-6 retort water at day 0 and at day 28 of incubation with culture RW-12. (a) aromatic amines in defined medium at day 0, and (b) day 28; (c) aromatic amines spiked in retort water at day 0, and (d) day 28; (e) unspiked retort water at day 0, and (f) day 28. Numbered-peak identification: (1) 2-hydroxypyridine, (2) 3-hydroxypyridine, (3) 2-methylpyrazine, (4) pyridine, (5) 2-methylpyridine, (6) 3-methylpyridine, (7) 2,6-dimethylpyridine, (8) 2-ethylpyridine, (9) 2,4-dimethylpyridine, (10) 3-ethylpyridine, (11) quinoline, and (12) 2,4,6-trimethylpyridine. (XBL 8511-4768)

spiked into Oxy-6 retort water, these 12 compounds were detectable above the endogenous levels of UV-absorbing compounds in the retort water (Fig. 2c). After 28 days, the majority of the spiked aromatic amines had been attacked (Fig. 2d). Only 2-ethylpyridine (peak 8) clearly remained above background levels. When compared with unspiked retort water (Fig. 2e), several new peaks appeared that may have been metabolites from the initial attack on the substrate spike; this would have accounted for some of the DOC that remained from the spike. Although this model substrate system contained no aromatic amines that were inherently recalcitrant, such compounds are expected to reside in the more complex array of aromatic amines present in retort water. Thus it appears that the retort water environment has inhibitory effects on the rate and extent of mineralization of normally biodegradable aromatic amines, most of which have been identified in retort waters.

Retort water that was not spiked with the N-heterocycle mixture generated numerous peaks (Fig. 2e) that were poorly separated under the HPLC conditions used. Some of these endogenous compounds, however, were definitely attacked (Fig. 2f). Total peak areas were reduced 52%, indicating that almost half of the endogenous aromatic compounds did not experience ring cleavage. The behavior of aromatic amines in spiked and unspiked retort water demonstrates the importance of inherent recalcitrance and inhibitory matrix effects on the resistance of the multiple aromatic-amine substrates to biooxidation in retort water and illustrates limitations likely to be experienced in the management of other complex industrial waste mixtures (e.g., leachates from hazardous waste dumps).

REFERENCES

1. Rogers, J.E., *et al.* (1981), "Microbiological Degradation of Organic Components in Oil Shale Retort Water: Organic Acids," *Appl. Envir. Microbiol. 42*, p. 830.
2. Dobson, K.R., Stephenson, M., Greenfield, P.F., and Bell, P.R.F. (1985), "Identification and Treatability of Organics in Oil Shale Retort Water," *Water Res. 19*, p. 849.
3. Hunter, L., Persoff, P., Thomas, J.F., and Daughton, C.G. (1985), "Identification and Correlation of Volatile Components in Retort Wastewaters," in *Applied Science Division Annual Report, FY 1984*, LBL-18754, p. 4–60.
4. Leenheer, J.A., Noyes, T.I., and Stuber, H.A. (1982), "Determination of Polar Organic Solutes in Oil-Shale Retort Water," *Envir. Sci. Technol. 16*, p. 714.
5. Pellizzari, E.D., *et al.* (1979), "Identification of Organic Components in Aqueous Effluents from Energy-Related Processes," in *Measurement of Organic Pollutants in Water and Wastewater*, C.E. Van Hall, Ed., American Society for Testing and Materials, Philadelphia, PA; ASTM STP 686, p. 256.
6. Raphaelian, L.A. and Harrison, W. (1981), "Organic Constituents in Process Water from the In-Situ Retorting of Oil from Oil-Shale Kerogen," Argonne National Laboratory report ANL/PAG-5.
7. Healy, J.B., Jr., Langlois, G.W., and Daughton, C.G. (1985), "Biooxidation of Organic Solutes in Oil Shale Wastewaters," *Water Res. 19*, p. 1429.
8. Jones, B.M., Sakaji, R.H., and Daughton, C.G. (1982), "Physicochemical Treatment Methods for Oil Shale Wastewater: Evaluation as Aids to Biooxidation," in *Fifteenth Oil Shale Symposium Proceedings*, J.H. Gary, Ed., Colorado School of Mines Press, Golden, CO, p. 581.
9. Grant, D.J.W. and Al-Najjar, T.R. (1976), "Degradation of Quinoline by a Soil Bacterium," *Microbios 15*, p. 177.
10. Khanna, M. and Shukla, O.P. (1977), "Microbial Metabolism of 3-Hydroxypyridine," *Indian J. Biochem. Biophys. 14*, p. 301.
11. Malaney, G.W. (1960), "Oxidative Abilities of Aniline-Acclimated Activated Sludge," *J. Wat. Pollut. Control Fed. 32*, p. 1300.
12. Naik, M.N., Jackson, R.B., Stokes, J., and Swaby, R.J. (1972), "Microbial Degradation and Phytotoxicity of Picloram and Other Substituted Pyridines," *Soil Biol. Biochem. 4*, p. 313.
13. Shukla, O.P. (1975), "Microbial Decomposition of 2-Ethylpyridine, 2,4-Lutidine, and 2,4,6-Collidine," *Indian J. Exp. Biol. 13*, p. 574.
14. Wolf, D.C. and Martin, J.P. (1975), "Microbial Decomposition of Ring-^{14}C Atrazine, Cyanuric Acid, and 2-Chloro-4,6-diamino-s-triazine," *J. Envir. Qual. 4*, p. 134.
15. Healy, J.B., Jr., Langlois, G.W., and Daughton, C.G. (1985), "Effect of Oil Shale Retort Water on Aromatic Amine Biooxidation," LBL-19819.
16. Healy, J.B., Jr., Jones, B.M., Langlois, G.W., and Daughton, C.G. (1983), "Biotreatment of Oil Shale Wastewaters," in *Sixteenth Oil Shale Symposium Proceedings*, J.H. Gary, Ed., Colorado School of Mines Press, Golden, CO, p. 498.
17. Baird, R., Carmona, L., and Jenkins, R.L. (1977), "Behavior of Benzidine and Other Aromatic Amines in Aerobic Wastewater Treatment," *J. Wat. Pollut. Control Fed. 49*, p. 1609.

Sunlight Reactions of Volatile Organonitrogen Emissions from Oil Shale Wastewaters*

E.R. Blatchley III, J.F. Thomas, and C.G. Daughton†

Oil shale developers anticipate the use of minimal upgrading for their process wastewaters (retort waters) prior to disposal. Most disposal schemes also involve temporary storage in ponds prior to disposal. For surface-retort processes, the retort waters would then be codisposed together with the solid wastes (spent shale). Codisposal will take place at elevated temperatures (probably above 65°C) because it will not be economically feasible to store spent shale long enough to allow cooling to ambient temperature. For pond storage and codisposal, the major transport process that will determine the immediate, short-term environmental disposition of organic solutes associated with these wastes will be volatilization.

Of several classes of organic compounds that could be emitted, a major one comprises organonitrogen species including heterocycles, aromatic amines, and nitriles. Nitrogenous compounds are of particular concern because (1) they crosscut the spectrum of compounds produced by most synfuel conversion processes, (2) they are particularly refractory to removal by conventional biotreatment and are therefore likely to undergo uncontrolled emissions and show high persistence, (3) they have extremely low odor thresholds and most are malodorous, (4) phototransformations present the possibility of formation of atmospheric NO_x, a known precursor to photochemical smog, and (5) these compounds are not currently regulated, mainly because they would be unique to the as-yet developed synfuels industry, and little is currently known about them. The problem of nuisance odor could be a major one since many areas of the U.S. are considering air-emission regulations based on smell. The Bay Area Air Quality Management District of San Francisco, for example, now enforces such regulations in the nine Bay Area counties.

*This work was supported by the Assistant Secretary for Fossil Energy, Office of Oil Shale, Division of Oil, Gas, and Shale Technology of the U.S. Department of Energy under Contract No. DE-AC03-76SF00098.

†Sanitary Engineering and Environmental Health Research Laboratory, University of California (Berkeley), Richmond, CA 94804.

The major chemical transformation processes that will determine the environmental fate of those compounds emitted to the atmosphere are all sunlight mediated. This project represents the first investigation of vapor-phase photoreactions of organonitrogen compounds (ONCs) emitted by retort waters. With a thorough understanding of the photochemistry, atmospheric lifetimes could be predicted and management practices could be designed to minimize associated hazards (such as toxic or nuisance photochemical products), or alternatively, to take advantage of reactions that serve to mineralize compounds that may otherwise be hazardous. It is noteworthy that the native air quality in the Western U.S. oil shale region is high. Any anthropogenic introduction of pollutants to the air could be significant. Compounds with sufficiently long lifetimes could be used, however, as tracers or indicators of pollution resulting from oil shale operations since their ambient, baseline concentrations are extremely low.

The photodecomposition of ONCs originating from a retort water was studied in an inert (N_2) atmosphere. The exclusion of molecular oxygen minimized the effects of indirect photoreaction, which could be substantial and will be the focus of future investigation. Only 3 of the 60 major ONCs that volatilized to the headspace were degraded as a result of photoreaction. It was possible that other compounds also photodegraded, but this could not be confirmed because of their relatively low concentrations in the retort water headspace.

ACCOMPLISHMENTS DURING FY 1985

The study was performed on static headspace of retort water samples since the headspace is representative of initial potential emissions. Gas condensate from Occidental Oil Shale Co.'s sixth experimental burn (Oxy-6 GC) was chosen for generation of headspace samples because of its high content of volatile components. Experiments were performed in an inert atmosphere of nitrogen gas to inhibit the formation of oxygen radicals and NO_x. This allowed for an evaluation of direct and photosensitized photoreactions; these would indicate minimum extents of *in-situ* photodecomposition. Future experiments will include the use of a more reactive atmosphere (e.g., air), in which radical induced reactions could also occur.

Headspace samples were generated under conditions that would make the headspace as concentrated as possible and which would also simulate expected codisposal conditions. To a 40-mL sample of Oxy-6 GC, 0.96 g of NaOH was added to increase the pH

from 8.8 to 11. This increased the concentrations of deprotonated (volatile) ONCs and also simulated the effect of alkali salts present in spent shale. This sample was then injected through a Teflon, septum-containing stopper used to seal a 2-L roundbottom flask that had previously been purged with N_2. Two 500-mL Pyrex gas-sampling tubes (GSTs) with Teflon stopcocks were then evacuated to 0.13 Pa and connected through a valved manifold to the 2-L roundbottom flask that had been equilibrated for 1 hour in a 65°C water bath. The valve was opened and the headspace allowed to equilibrate. Experimental samples and controls were produced by flushing the GSTs with N_2 into 2-L Tedlar gas-sampling bags, each equipped with a septum port; parallel experiments were performed in Pyrex GSTs by eliminating this last step. Tedlar is a poly(vinylfluoride) film similar in composition to Teflon. Tedlar was chosen because of its advantages over other container materials. Tedlar transmits tropospheric sunlight better than Pyrex glass, especially in the ultraviolet range, which is more intense at elevations such as those of the Western U.S. oil shale regions; it is less permeable to most gases than other polymeric materials; and the bags are relatively inexpensive and reuseable.

Bags containing the wastewater headspace were randomly divided into two groups: samples (to be exposed to sunlight) and controls (to be submitted to the same conditions, but without sunlight); controls were wrapped in aluminum foil. Both groups were placed on the roof of Building 112 at the U.C. Richmond Field Station from 7–15 May 1985. Time-course analyses of sample and control headspaces were performed using capillary gas chromatography (30-m fused-silica, KOH-deactivated Carbowax 20M column, programmed from 30°C to 220°C at 4°C/min) with flame ionization and flame thermionic (nitrogen/phosphorus) detectors (FID and NPD, respectively); the latter detector is highly selective for nitrogen and phosphorus compounds. Chromatographic data were recorded, stored, and manipulated using a computing integrator.

Chromatographic data (peak areas) from samples and controls at time zero were within approximately 10%, indicating that one headspace had been diluted slightly more than the other in the headspace transfer process. The data for the GSTs also indicated that leakage (presumably through the septum and stopcocks) was a dominant loss mechanism both for samples and controls. From this we concluded that the GSTs were not suitable for headspace containment over the period of irradiation. In contrast, leakage of headspace components through the walls of the Tedlar bags was minimal (Fig. 1). Losses of

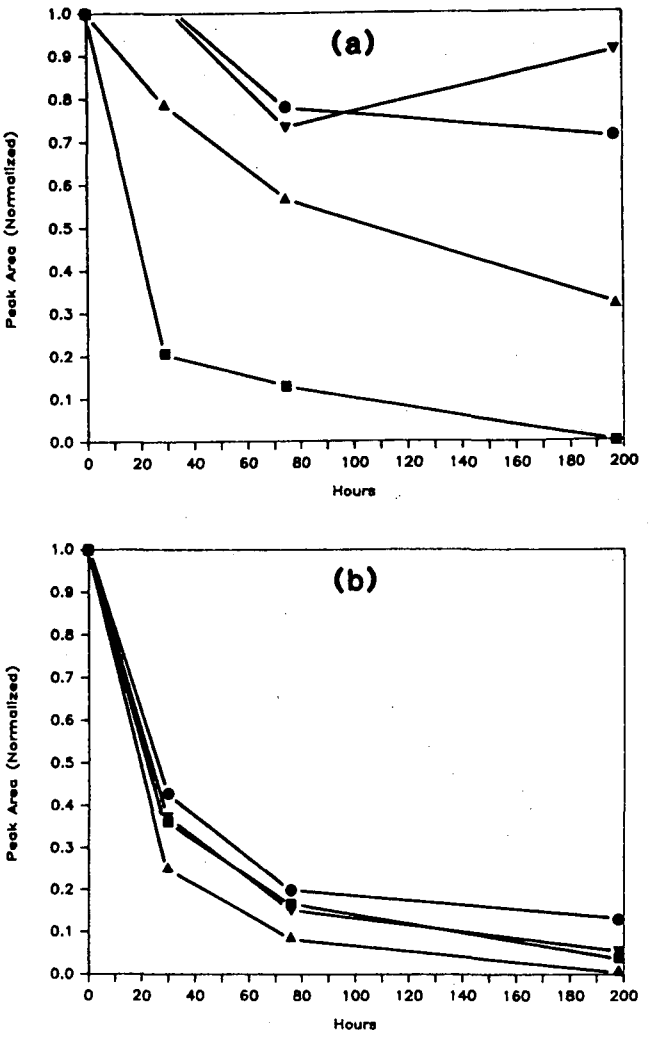

Figure 1. Normalized oil shale wastewater ONC peak areas as a function of time for Tedlar bags (a) and GSTs (b). Time-course headspace samples were analyzed by capillary gas chromatography. Resulting data were normalized with respect to time-zero peak areas. Data for four compounds are shown for each type of chamber: 2,6-dimethylpyridine (inverted triangle), pyridine (circle), C_3-pyridine isomer (triangle), aniline (square). (XBL 8511-4776)

headspace components because of sorption to the walls were found to be more significant but acceptable. Further investigation found these components to readily desorb when the headspace was expelled and replaced with N_2. This demonstrated that sorption was reversible and that cleaning the bags for reuse would be relatively easy.

There were 60 compounds present in the headspace in sufficient quantities to be resolved and detected under our gas chromatographic conditions. Of these, only three showed losses in the samples relative to the controls (Fig. 2). We attributed these losses to photoreactions. Possible mechanisms

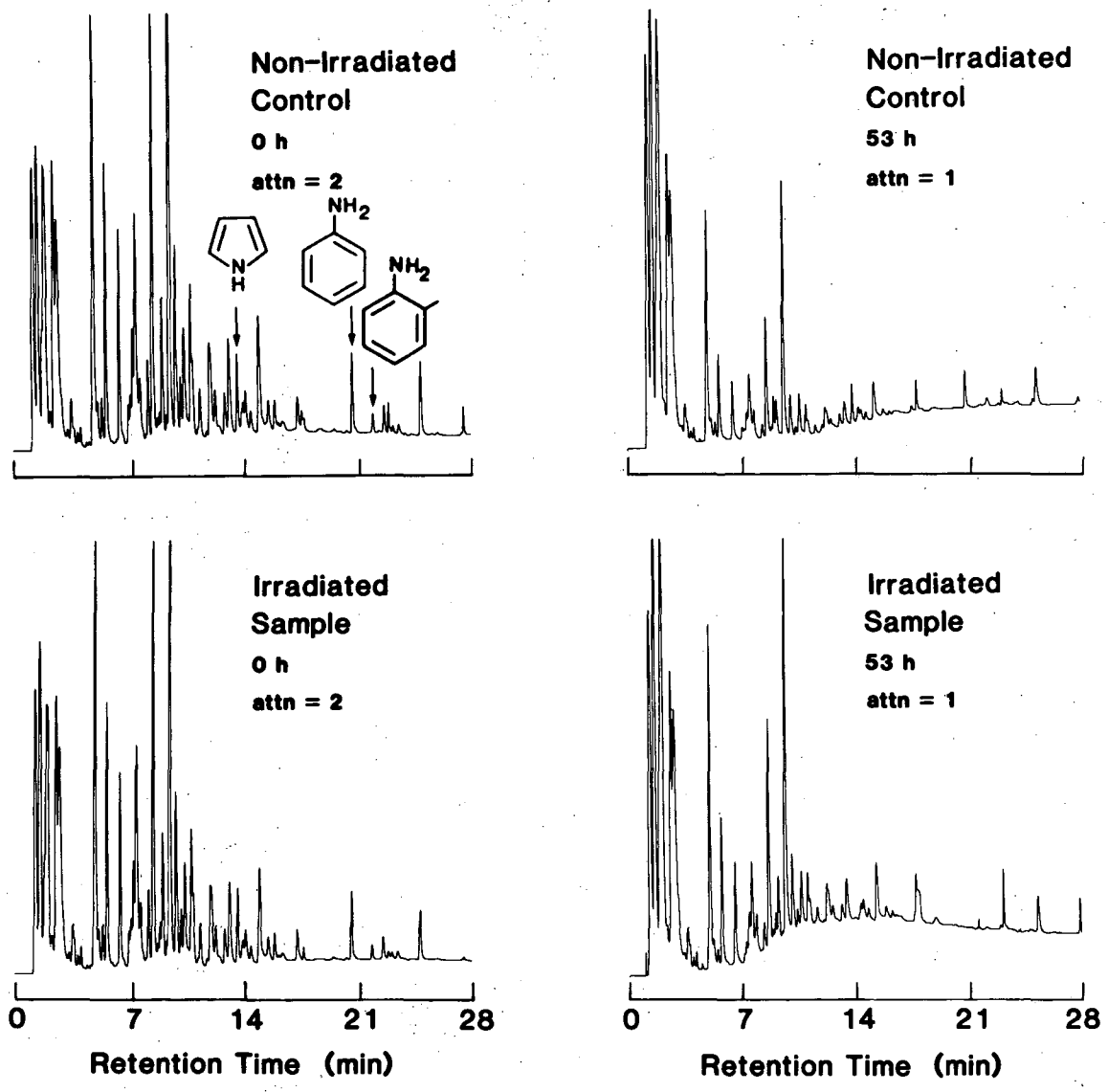

Figure 2. Oxy-6 gas condensate headspace chromatograms (flame ionization detection). Comparison of sunlight irradiated sample and non-irradiated control before and after 53 hours of exposure. Arrows indicate compounds that showed losses in the irradiated sample relative to the non-irradiated control after 53 hours. (XBL 855-2693A)

included reaction via direct absorption of radiation or by collision with other headspace components that had been electronically excited themselves by absorption of radiation. Analysis of Oxy-6 GC by gas chromatography/mass spectrometry indicated that these three compounds were aniline, pyrrole, and *o*-toluidine. These identifications were confirmed using a statistical retention-index matching technique on previously acquired gas chromatographic data from Oxy-6 GC.[1] Other headspace components (e.g., the other toluidine isomers) may have undergone similar reactions but were initially present at such low concentrations that other losses (e.g., sorption, leakage) made this difficult to confirm. No attempt was made to identify reaction products or quantify radiation.

Many of the components present in the retort water headspace are aliphatic pyridines. For example, of the 38 compounds identified in Oxy-6 GC headspace, 22 were alkyl pyridines.[1] None of these compounds underwent sufficient photodegradation to be detected in this experiment. This is significant

because the pyridines represent the majority of the ONCs present in Oxy-6 GC headspace, in part a result of their lower boiling points (higher volatilities) than other ONCs in the headspace. Their concentrations in retort waters are also higher than those of other ONCs.

These experiments were performed in an inert atmosphere. Irradiation in a more reactive atmosphere, such as air, would probably result in degradation of more compounds. Experiments performed on pure compounds in air support this hypothesis. The effects of sunlight exposure on pyridine, 2,4,6-trimethylpyridine, and quinoline in air were studied. A mass of pure compound less than that required to saturate the available headspace was placed in a 100-mL Pyrex volumetric flask. The flask was then stoppered by sliding a Teflon-backed silicone septum into the neck. Eight flasks were prepared for each compound. Four flasks from each group were wrapped in aluminum foil and used as controls. Headspace composition was monitored during the course of irradiation by extracting the headspace with pentane (injected through the septum) and analyzing the extract by gas chromatography. Extractions were performed in order to monitor the production of both volatile and nonvolatile reaction products. One pair of flasks was analyzed daily (one sample and one control). Resulting data indicated that 2,4,6-trimethylpyridine and quinoline photodegraded, while pyridine did not.

Reactions with atmospheric ozone may also prove to be important with respect to air quality. When ozone was injected into samples of Oxy-6 GC headspace, a "fog" formed immediately. Although the concentrations of ozone and organic components were much higher than could ever be expected to occur in the atmosphere, similar reactions could prove to be important in reducing atmospheric visibility.

PLANNED ACTIVITIES FOR FY 1986

To understand the behavior of emissions resulting from oil shale processes in general (not just those of Occidental's modified *in-situ* process), it will be necessary to perform similar experiments on retort water headspace samples from other processes. This work will be expanded to include emissions from wastewaters of other hydrocarbon extraction/conversion processes, such as coal gasification, tar sands extraction, and tertiary oil recovery.

To understand the importance of molecular oxygen on the photodegradation of volatile components, it will be necessary to perform experiments similar to those described, with the addition of air or O_2. Since it is possible that nitrogen oxides will be formed, headspace NO_x concentrations will be monitored using a chemiluminescent nitrogen detector.

REFERENCES

1. Hunter, L., Persoff, P., Thomas, J.F., and Daughton, C.G. (1985), "Identification and Correlation of Volatile Components in Retort Wastewaters," in *Applied Science Division Annual Report, FY 1984,* LBL-18754, p. 4–60.

Diffusivity of Nitrogen Heterocycles in Simulated Codisposed Oil Shale Wastes*

P. Persoff, J.F. Thomas, and C.G. Daughton†

Oil-shale retorting produces large amounts of solid and liquid wastes. For each barrel of shale oil recovered, approximately 0.4 barrels of retort water and 1.4 tons of spent shale are produced, both of which must be disposed of in an environmentally acceptable manner. Both the amounts and characteristics of these waste streams vary, depending on the retorting process and shale grade used. Retort wastewaters vary in quality, but all contain high concentrations of organic nitrogen,[1] largely in the form of nitrogen heterocycles (NHCs).[2,3] These compounds, because of their malodor and toxicity, could present nuisance or worker-health problems at oil shale development sites and environs if significant amounts were released to the atmosphere.

Considering the huge amounts of solid waste to be disposed of, the most feasible disposal option is compaction in landfills with eventual revegetation. Spent shale emerges from the retorting process at an

*This work was supported by the Assistant Secretary for Fossil Energy, Office of Oil Shale, Division of Oil, Gas, and Shale Technology of the U.S. Department of Energy under Contract No. DE-AC03-76SF00098.

†Sanitary Engineering and Environmental Health Research Laboratory, University of California (Berkeley), Richmond, CA 94804.

elevated temperature (typically 150 to 350°C). It must be cooled and then moisturized to promote compaction. Investigation of existing spent shale has shown that the optimum moisture level for compaction (permitting the densest and strongest compacted disposed material for a specified amount of compactive effort) is about 15 L of water per 100 kg of dry spent shale; this optimum level varies according to the process, but the figure cited is typical. This requirement for moisturizing water would be the largest demand for water imposed by a commercial oil shale development. In the semi-arid oil shale region of the western U.S., use of retort wastewater to satisfy the moisturizing-water requirement would be a prudent water conservation practice if it could be done in an environmentally sound manner. An immediate potential problem, however, would be release to the atmosphere of volatile NHCs (and other species) from warm, moisturized spent shale upon delivery to the dumpsite and before, during, and after compaction.

ACCOMPLISHMENTS DURING FY 1985

To estimate the rate at which volatile solutes are released from an oil shale waste codisposal pile, it is necessary to know the effective diffusivity of each compound in the codisposed waste. Effective diffusivity is defined[4] as the negative ratio of diffusive flux to the gradient of bulk concentration; others have used different definitions.[5,6] Under certain assumptions, the effective diffusivity can be calculated from the fractions of solute molecules that distribute to the solid, liquid, and gas phases. Knowing these distribution fractions, in turn, requires that both the Henry's Law constant for each solute and, if the solid phase adsorbs the solute, the adsorption isotherm for each solute be known. An expression to calculate the effective diffusivity has been reported previously,[4,7] as have sorption isotherms (Paraho spent shale and an aqueous solution of five NHCs).[8] This year a method to measure effective diffusivity of NHCs in simulated codisposed oil shale wastes was demonstrated. Effective diffusivity, D_e, was measured simultaneously for five NHCs in three porous media: water-saturated sand, unsaturated sand, and a simulated codisposed oil shale waste.

Apparatus and Methods

The aqueous phase for each of the three runs was the same. An aqueous solution of 5 NHCs (pyridine, pyrrole, and three methylpyridine isomers) was prepared. This solution was then diluted (10 in 11, vol/vol) with a pH 10 buffer (7.72 g boric acid and 6.88 g KOH per L) to produce final concentrations of solutes as shown in Table 1. The pH of the final solution was greater than 8, ensuring that each NHC was in its deprotonated (volatile) form.

The simulated codisposed oil shale waste consisted of Paraho spent shale, moisturized with the aqueous phase. The Paraho spent shale originated from Green River oil shale from the Anvil Points mine in Anvil Points, CO; this particular spent shale was retorted in run C-2, using the Paraho direct process, by Development Engineering, Inc., in the fall of 1979. This material contained 4.1 wt% mineral carbon (undecomposed carbonates) and 1.4 wt% organic carbon.[9] For our work, the −4 +8 mesh size fraction was separated by sieving. To prepare the sample of moisturized spent shale, 50 mL of the NHC aqueous phase was added to 323 g of the dry Paraho spent shale (−4 +8 mesh) in a polyethylene jar. The jar was then rotated on a jar mill for 20 min to uniformly distribute the liquid in the solid; in previous experiments, when water was added to spent shale particles and rotated for various times, the standard deviation of the moisture content (measured as weight loss on evaporation) was found to decrease with longer intervals of rotation up to 20 minutes, but not beyond. The solid/liquid admixture (342 g, assumed to consist of 296 g dry spent shale and 46 mL of the aqueous phase) was transferred to a diffusion cell (Fig. 1), forming a packed bed of moisturized spent-shale particles.

To prepare the sample of unsaturated sand, 50 mL of the buffered NHC solution was added to 606 g of 100-mesh reagent-grade sand in a polyethylene jar. The contents were mixed by rotating, and all of the combined material was transferred to the diffusion cell for sampling of diffusive emissions. For the sample of saturated sand, the diffusion cell was filled to approximately one-third with the buffered NHC solution, and sand was poured into the cell while shaking the cell. As the level of sand approached the liquid level, more liquid was added so that a saturated sand bed completely filled the cell, up to the air inlet holes.

The diffusion cell was a polyethylene jar modified by drilling four holes around its circumference at the level of the top of the sample. Polypropylene tubes (0.25-in. o.d.), which were inserted through these holes forming a gas-tight seal, were used to deliver air to flush the top surface of the sample and maintain the solute concentrations at zero at the top of the sample. The influent air was bubbled through two gas-washing bottles (in series) to saturate it with water and prevent evaporation of pore moisture from the sample. Evaporation would have caused advective solute transport, confounding measure-

Table 1. Effective diffusivity of NHCs in porous media.

NHC compound	Boiling point (°C)	Initial concentration in aqueous phase (mg/L)	Effective diffusivity ($cm^2/sec \times 10^{-7}$)		
			Saturated sand	Unsaturated sand	Moisturized spent shale
Pyridine	115	22.3	100	10.6	0.24
Pyrrole	131	26.4	82	12	0.37
2-Methyl-pyridine	129	25.7	96	8.1	0.10
3-Methyl-pyridine	144	26.1	110	6.9	0.054
4-Methyl-pyridine	143	26.1	120	5.9	0.043
Experimental variables			Associated conditions		
Mass of sand or shale (g)			393	606	296
Volume of aqueous phase (mL)			86	50	46
Volume of air in pore space (mL) (by difference)			0	79	198
Cell volume (mL)			242	362	362
Cell depth (cm)			9	10	10

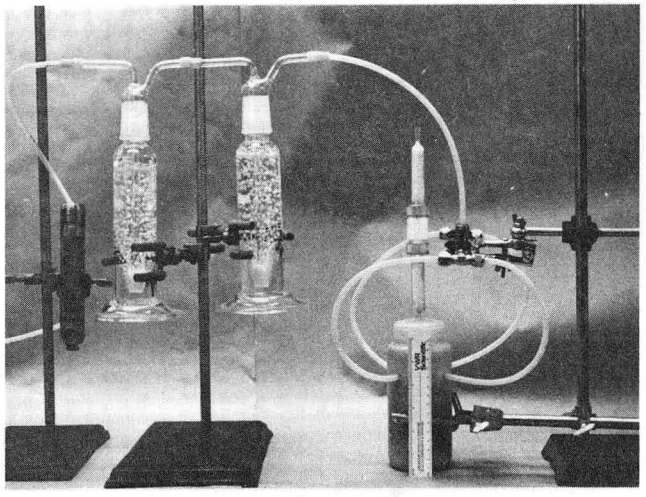

Figure 1. Experimental apparatus for measuring effective diffusivity of compounds in porous media. From left, air passes through a rotameter, two gas-washing bottles in series, then is divided equally into four tubes to sweep the surface of the sample in the diffusion cell. Air leaves the diffusion cell through two Tenax traps in series. (XBB 8511-9691)

ments of diffusive transport. During the runs, the water level dropped in the first bottle but not in the second, indicating that saturation was completed in the first bottle.

The effluent vapor phase, containing all species that volatilized from the packed bed, was passed through two adsorbent traps (Tenax) in series. The traps were 1/2-in. (o.d.) Pyrex tubes containing approximately 0.8 g of −60 +80 mesh Tenax GC (Alltech Associates, Deerfield, IL) retained between Pyrex wool plugs; both the Tenax and the Pyrex wool were pre-cleaned by Soxhlet extraction in methanol and followed by n-pentane and dried *in vacuo* for 4 hours at 110°C before filling the traps. The second trap in series was intended to detect breakthrough from the primary trap; no breakthrough was detected in any experiment. The pairs of Tenax traps were exposed for defined times, after which each trap was flushed with dry N_2 gas at a flow rate of 80 mL/min for 12 min to remove moisture from the traps; Tenax does not adsorb water. After exposure, each trap was placed in a Nutech 320 thermal desorber (Nutech Inc., Research Triangle

Park, NC) to transfer the adsorbed NHCs to a Hewlett-Packard 5840A gas chromatograph (GC) for separation and quantitation.

Each Tenax trap was heated to 280°C in helium (20 mL/min). The gas stream then passed through a cryotrap (a loop of 0.040-in. i.d. stainless steel tubing) maintained at −197°C, where desorbed species were "cryofocused." After 5 min of desorbing, the cryotrap was rapidly heated (<2 min) to 280°C, and the helium (20 mL/min) carried the re-vaporized species through a heated (200°C) 1/16-in. o.d. stainless-steel transfer line into the GC column (10-ft × 2-mm i.d. glass column, packed with 4% Carbowax 20M on 60–80 mesh Carbopack B, deactivated with 0.8% KOH). The transfer line and the glass GC column were connected by a zero-dead-volume reducing union, using a Vespel-and-graphite ferrule on the glass. After 5 min of transferring, the column temperature was increased from 50°C to 200°C at 30°C/min, then increased at 10°C/min to 220°C for isothermal operation for 22 min. Linear correlations ($r^2 > 0.99$) were established between peak-area response from flame ionization detection (FID) and mass of compound for each of the five NHCs by injection of aqueous standards; injection of aqueous standards onto the Tenax traps showed that recovery of spikes from the traps was quantitative.

Diffusivity Calculation

From the mass of each compound trapped during each sampling period, the flux of each species, J, was calculated. These data are plotted for moisturized spent shale (run 3) in Fig. 2, where C_o is the initial uniform bulk concentration of the solute in the diffusion cell and t represents the geometric mean of the starting and ending times of the sampling period. Similar plots (not shown) were drawn for saturated and unsaturated sand (runs 1 and 2, respectively).

A goal of this work was to determine whether diffusion in a packed bed of moisturized, adsorbent particles could be modeled as one-dimensional diffusion in a continuous, uniform medium with a constant or varying effective diffusivity, D_e. Diffusion in a uniform medium is expressed by Fick's second law:

$$\frac{\partial C}{\partial t} = D_e \frac{\partial^2 C}{\partial x^2} \quad , \qquad (1)$$

where

C	=	bulk concentration of solute (g/cm^3)
D_e	=	effective diffusivity (cm^2/sec)
t	=	time (sec)
x	=	distance (cm).

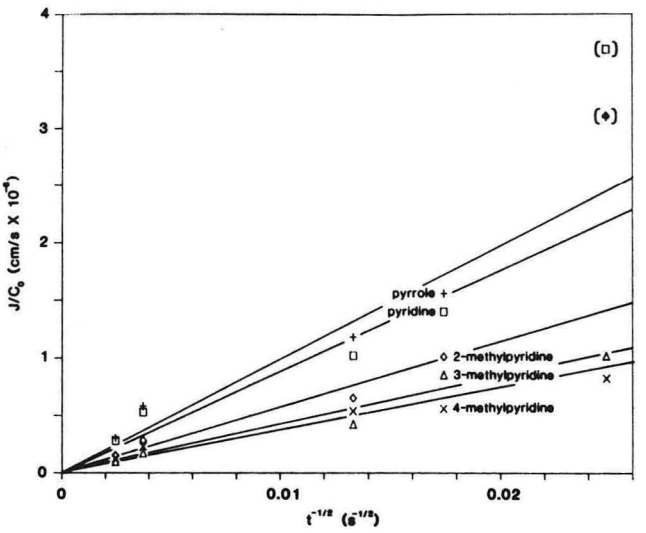

Figure 2. Plot of normalized flux (J/C_o) against inverse square root of time. Points in parentheses were not included in fitting the lines. Slopes of line are $(D_e/\pi)^{1/2}$. (XBL 8511-4777)

The boundary conditions (assuming 100% effective sweeping) are:

$$C = 0 \quad \text{at} \quad x = 0 \quad \text{for} \quad t \geq 0 \quad , \qquad (2)$$

$$\frac{\partial C}{\partial x} = 0 \quad \text{at} \quad x = L \quad , \qquad (3)$$

where L = depth of the diffusion cell (cm), and the initial condition is:

$$C = C_o \quad \text{everywhere at} \quad t = 0 \quad . \qquad (4)$$

For short times, the concentration at the bottom of the diffusion cell (i.e., x = L) remains at C_o. Under these conditions, the cell may be approximated by an infinitely deep cell, and boundary condition (3) is replaced by

$$\frac{\partial C}{\partial x} = 0 \quad \text{at} \quad x = \infty \quad . \qquad (5)$$

Equations (1) through (4) can be solved for C(x,t).[10] Evaluating $D_e \frac{\partial C}{\partial x}$ at x = 0 gives the diffusive flux J at x = 0. This is the flux measured in the experiment. A solution for J/C_o for the infinite-column approximation is:[11]

$$J/C_o = (D_e/\pi)^{1/2} t^{-1/2} \quad . \qquad (6)$$

The data for run 3 in Fig. 2 (and also for runs 1 and 2, not shown) were fitted by straight lines that were forced through the origin, as required by Eq. (6). This tentatively confirmed that all three systems behaved as one-dimensional diffusive systems with constant D_e. Values of effective diffusivity, calculated from the known initial concentrations of the five NHCs and the measured slopes, are shown in Table 1.

Phase Partitioning of Solutes

According to theory presented previously,[4,5] the effective diffusivity of a solute in a porous medium can be predicted from the distribution of solute molecules among the phases and a tortuosity factor for each phase that constitutes a diffusion path. Molecules that partition to the gas or liquid phases are available to transport by diffusion. Although molecules that partition to the solid phase participate in diffusional transport to a negligible degree (because solid-phase diffusion is much slower than diffusion in fluid phases), the solid phase serves as a reservoir of molecules that can replenish the fluid phases as they are depleted. Generally, the greater the proportion of solute molecules that partition to the solid phase, the lower will be the effective diffusivity.

Removal of pyridine and alkylpyridines from aqueous solution by sorption to the solid phase was detected for Paraho C-2 spent shale and for another carbonaceous spent shale, but was not found for two noncarbonaceous spent shales.[8] Sorption was greater for the more highly alkylated species. In control experiments, removal of pyridine and alkylpyridines from aqueous solution by sorption to the solid phase was not detected for either glass or sand.[8] This suggests that sorption from aqueous solution results from the activated-carbon-like char of carbonaceous spent shale. By contrast, in separate experiments, removal of vapor-phase pyridine from air to solid phases was detected for each of glass, sand, and carbonaceous and noncarbonaceous spent shales. This suggests that pyridine molecules can be removed from air either by affinity of the electronegative nitrogen to acid sites on the surface of sand or glass, or by affinity of the molecule to the char of carbonaceous spent shale. In an unsaturated system, where the solid surface is partly wet and partly dry, the water-air and water-solid partitioning coefficients would be insufficient to predict the partitioning of solutes among the three phases.

The values of effective diffusivity shown in Table 1 reflect the partitioning of solute molecules to the solid phase. In run 1 (saturated sand), all the solute molecules remained in the aqueous phase. The effective diffusivity would be expected to be close to the molecular diffusivity in water, reduced by a tortuosity factor; no reduction is required for porosity because the definition of effective diffusivity was based on bulk concentration rather than aqueous-phase concentration. The observed values were all close to 1×10^{-5} cm^2/sec, a typical value for molecular diffusivity in water for these compounds. This implies a tortuosity factor close to unity, which is reasonable for this situation.

In run 2 (unsaturated sand), the sand surface is believed to have been partly dry. Therefore, the pyridine molecules were distributed among all three phases. Distribution of pyridine molecules to the gas phase would increase the effective diffusivity (compared to run 1), while distribution to the solid phase would decrease it. More complex diffusion paths and isolated pockets of air or water would also decrease the effective diffusivity. Values of D_e measured in run 2 were smaller than those measured in run 1 by approximately one order of magnitude.

For run 3 (moisturized spent shale), D_e values were the lowest. This resulted from partitioning of NHCs to the solid phase from both the water and air phases. Higher values of effective diffusivity were associated with greater tendency of the solute to partition to the gas phase (i.e., lower boiling point) and with lesser tendency to sorb to the solid phase (i.e., greater polarity). This agrees with previous hypotheses.[4,7]

Graphical Determination of Diffusivity

The assumption used to calculate D_e—that in all three runs the diffusion cell could be approximated by an infinitely deep column—was confirmed by devising an alternative, graphical technique to find D_e from the experimental data. The method is described here because it is useful when the approximation of an infinitely deep column cannot be made.

This technique is based upon comparison of the experimental emission-rate data with a solution of Eq. (1)–(4) expressed in terms of dimensionless variables. The comparison is made by overlaying a plot of the experimental data on a plot of the dimensionless-variable solution, similar to the Theis method used in geohydrology.[12,13]

The length of the column, L, and the amount of each species originally present in the diffusion cell must be known. Define $f = f(t)$ as the cumulative fraction of material (originally present in the sample) emitted at any time. At time zero, f is zero, and at infinite time, f asymptotically approaches unity; df/dt is the fraction of material emitted per unit time

(sec^{-1}). The observed mass of each species trapped during each sampling interval is converted to an emission rate and expressed as df/dt. For each compound, these data are plotted (df/dt against t) on log-log paper. This plot is referred to as Fig. X. The auxiliary line, t(df/dt) = 1, must also be drawn on Fig. X.

The effective diffusivity, D_e, is found indirectly, by finding the characteristic time of the system, t_c, which is defined as L^2/D_e (sec). Dimensionless time, T, is the ratio t/t_c or tD_e/L^2.

Equations (1)–(4) can be solved[10] for C(x,t), and the solution can be manipulated to give f as a function of T. Differentiating f with respect to T gives df/dT, which is a dimensionless flux; this is plotted against T on log-log paper in Fig. 3. To be used, Fig. 3 must be enlarged so that its log cycles are the same length as those of the user's Fig. X. The auxiliary line, T(df/dT) = 1, is also drawn in Fig. 3. Note that Fig. X contains information about the one-dimensional diffusion cell in the experiment, and Fig. 3 contains information about an ideal one-dimensional diffusion cell. At small values of T (and therefore at small values of t), the curve df/dT versus T is asymptotic to the line $df/dT = (\pi^{-1/2})T^{-1/2}$, which can be shown to be equivalent to Eq. (6). For $T < 0.1$, the curve is quite close to the asymptotic line.

To find t_c, Fig. X must be overlain on the enlarged version of Fig. 3 such that the data points fall along the curve and the two auxiliary lines coincide. If both conditions cannot be met, the data are shown not to fit the model of Eqs. (1)–(4). When the superposition has been made, t_c is the ratio of any pair of values of t and T that correspond to each other. Figure 3 shows that the infinite-column approximation is valid for dimensionless times up to 0.1; therefore it was valid to use it for the experimental data presented here.

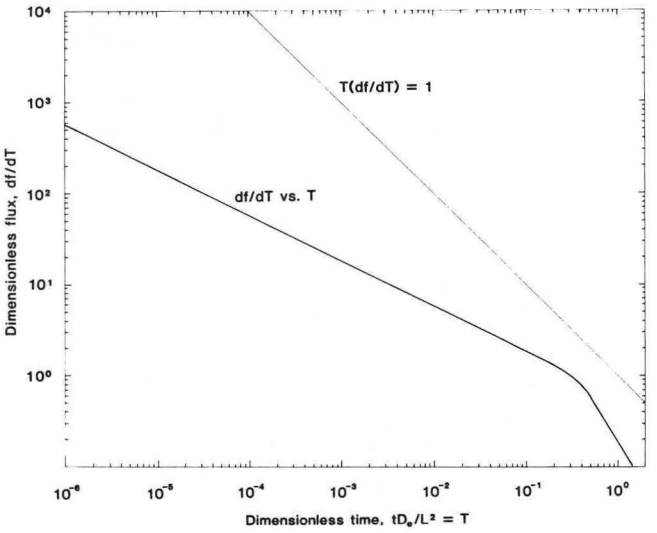

Figure 3. Plot of df/dT (dimensionless flux) against T (dimensionless time). Used for graphical interpretation of experimental data to find D_e. The auxiliary line, (df/dT) = 1, is also shown. (XBL 854-2163)

Conclusions

The results presented here show that sorption to the solid phase strongly influences the rate at which NHCs would be released from a codisposal pile. The moisture content could also be important. Moreover, it appears that the distribution of an NHC among the three phases of a codisposal pile would be determined not only by the amounts of water and air present, but also by the area of shale surface wetted by the water.

The trap-and-desorb technique used here could be applied to the measurement emissions from simulated codisposed wastes under conditions more closely resembling field conditions; by controlling the sample temperature and the humidity of the flushing air, water evaporation could be included in the experiment. A Proctor mold (a metal cylinder in which wastes are compacted to specified densities) fitted with air inlets and Tenax traps could be used as the diffusion cell for simulations of disposal of compacted material.

REFERENCES

1. Daughton, C.G., Jones, B.M., and Sakaji, R.H. (1985), "Organic Nitrogen Determination in Oil Shale Retort Waters," *Anal. Chem. 57*, p. 2326.
2. Hunter, L., Persoff, P., Thomas, J.F., and Daughton, C.G. (1985), "Identification and Correlation of Volatile Components in Retort Wastewaters," in *Applied Science Division Annual Report, FY 1984* , LBL-18754, p. 4–60.
3. Leenheer, J.A., Noyes, T.I., and Stuber H.A. (1982), "Determination of Polar Organic Solutes in Oil Shale Water," *Environ. Sci. Technol. 16*, p. 714.
4. Persoff, P., Hunter, L., and Daughton, C.G. (1984), "Atmospheric Emissions from Codisposed Oil Shale Wastes: a Preliminary Assessment," LBID-890.
5. Jury, W.A., Grover, R., Spencer, W.F., and Farmer, W.J. (1980), "Modelling Vapor Losses of Soil-Incorporated Triallate," *Soil Sci. Soc. Am. J. 44*, p. 445.

6. Thibodeaux, L.J. (1979), *Chemodynamics*, p. 335–341, John Wiley and Sons, New York.
7. Persoff, P., Hunter, L., Daughton, C.G., and Thomas, J.F. (1984), "Prediction of Atmospheric Emissions Resulting from Codisposal of Oil Shale Wastes," in *Applied Science Division Annual Report, FY 1983*, LBL-17073, p. 4–38.
8. Persoff, P., *et al.* (1985), "Removal of Nitrogen Heterocycles from Water by Sorption to Spent Oil Shale," *in Applied Science Division Annual Report, FY 1984*, LBL-18754, p. 4–63.
9. Heistand, R. (1980), letter to J.P. Fox, Development Engineering. Inc., Anvil Points, CO.
10. Crank, J. (1975), *The Mathematics of Diffusion*, 2nd ed., Clarendon Press, Oxford, UK.
11. Mayer, R., Letey, J., and Farmer, W.J. (1974) "Models for Predicting Volatilization of Soil-Incorporated Pesticides," *Soil Sci. Soc. Am. Proc. 38*, p. 563.
12. Freeze, R.A. and Cherry, J.A. (1979), *Groundwater*, p. 343, Prentice-Hall, Englewood Cliffs, NJ.
13. Todd, D.K. (1959), *Ground Water Hydrology*, p. 90, John Wiley and Sons, New York.

Flame Structure in Reacting Turbulent Boundary Layers*

R.K. Cheng, F. Robben, and L. Talbot

Combustion of premixed fuel lean mixtures embedded in a turbulent boundary layer over a strongly heated wall is an experimental configuration which is pertinent to many practical combustion situations. It is also suited for fundamental studies of turbulent combustion interactions since turbulent boundary layer is a classical flow configuration for fluid mechanics studies. Further, the heated turbulent boundary layer is capable of supporting combustion in fuel lean mixtures which otherwise cannot be studied in more conventional burners.

The overall objective of this program is to characterize experimentally the flow field of this reacting turbulent boundary layer using laser diagnostics techniques. The results are used for the development of theoretical turbulent combustion models. To study the changes in the turbulence properties due to combustion, measurements in isothermal and heated non-reacting turbulent boundary layers are also made. Previous investigations include the use of Rayleigh scattering for measuring density fluctuations in heated and reacting turbulent boundary layers[1] and two-component laser Doppler anemometry (LDA) for determining velocity statistics in the isothermal, heated, and reacting layers.[2] In FY 1985, a study of the spatial and temporal structures of the heated and reacting turbulent boundary layers using the two-point Rayleigh scattering technique has been completed.

ACCOMPLISHMENTS DURING FY 1985

The two-point Rayleigh technique[3] measures joint density statistics at two points separated by an adjustable distance. The results are deduced to obtain density spatial correlation coefficient at two points separated in three orthogonal directions, $R(\Delta x)$, $R(\Delta y)$, and $R(\Delta z)$. Here, Δx, Δy, and Δz represent respectively separation distances in the axial direction, x, the transverse direction normal to the heated wall , y, and spanwise direction parallel to the wall, z. Integration of the spatial correlations as functions of the separation distance gives the length scales of the density fluctuations l_x , l_y, and l_z. Also deduced are the space-time double correlations, $R(\Delta t,\Delta x,\Delta y)$, which is the correlation between the data obtained at the two points separated by Δx and Δy with a fixed time delay, Δt. The convection velocities of the thermal or combustion structures are given by correlating the optimum delay time of the space-time correlation with the separation distance. In addition, the orientations of the structures are shown by the locations on the Δx Δy plane where the optimum delay times become zero. The features of the thermal structures in the heated and reacting layers are compared with turbulence structures in isothermal turbulent boundary layer shown on visualization records.

The experimental conditions are free-stream velocity, U_∞, of 19 m/s; wall temperature , T_w, of 1000 K; and ethylene/air equivalence ratio $\phi = 0.35$. The separation distances range from 0.0 to 16.0 mm for Δz, 2.0 to 10.0 mm for Δy, and 2.0 to 50.0 mm for Δx. Figure 1 shows the longitudinal (axial) spatial correlation $R(\Delta x)$ obtained in the reacting layer at four transverse positions. Compared to the spanwise correlation $R(\Delta z)$ shown in FY 1984, the decay of $R(\Delta x)$ is more gradual than that shown for $R(\Delta z)$. The longitudinal length scale l_x is 9.0 mm compared to 4.4 mm for the spanwise length scale l_z. This shows that the thermal structures have a large aspect ratio (i.e., $l_x/l_z > 1$).

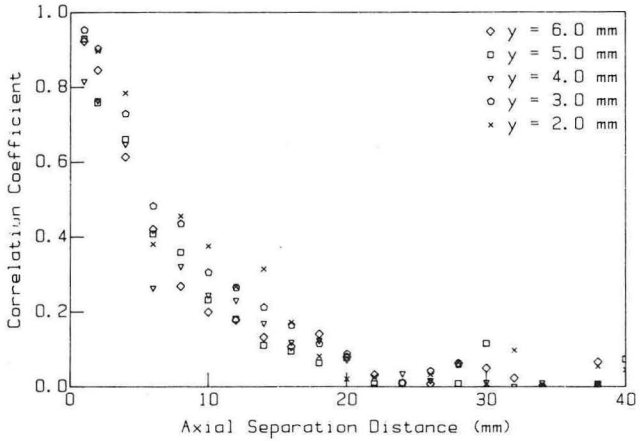

Figure 1. Longitudinal (axial) spatial correlation $R(\Delta x)$ obtained in the reacting layer at y = 2.0, 3.0, 4.0, and 5.0 mm above the heated wall. (XBL 862-455)

*This work was supported by the Director, Office of Energy Research, Office of Basic Energy Sciences, Chemical Sciences Division of the U.S. Department of Energy under Contract No. DE-AC03-76SF00098.

The space-time correlation $R(\Delta t,\Delta x,\Delta y)$ for the reacting layer with Δy fixed at 2.0 mm and various Δx are shown in Fig. 2. The optimum delay time t_0, which is shown by the maximum $R(\Delta t,\Delta x,\Delta y)$ for a fixed Δx and Δy, increases with increasing Δx. The convection velocity U_c for the thermal structures based on $\Delta x/t_0$ is close to the free stream velocity U_∞ . Also note that the optimum delay time for $\Delta x = 1.0$ and $\Delta y = 2.0$ is negative. This indicates that the thermal structures reach position 2 prior to position 1 (Fig. 3a). When Δx and Δy are both at 2.0 mm, t_0 becomes zero. As illustrated in Fig. 3b, this indicates that the thermal structures reach both positions at the same time. Since the two positions are located on an axis at 45° with respect to the wall, our results show that the orientations of the thermal structures are parallel to this 45° axis. Similar conclusions are drawn from the results obtained in the heated layer. Further, the convection velocity and the orientations of the thermal structures observed here are consistent with those observed for the turbulence structures in isothermal layers meaning that the transport of heat and reacting fronts in our flows are dominated by turbulence and with no apparent effects due to heat release.

PLANNED ACTIVITIES IN FY 1986

The diagnostic study of reacting turbulent boundary layer will be extended to include the use of ionization probes. The ionization probe measures the saturation ion current within the reaction fronts and therefore can be used as a flame front detector. One of the shortcomings of the Rayleigh technique for studying the reacting layer is that the measurement cannot distinguish between the heated non-reacting fluids from the reacting fluids. The use of two ionization probes will provide the correlations of the reaction front for comparison with the density correlations.

The technique for measuring velocity at two point separated in space will be developed for studying the reacting turbulent boundary layer. The velocity measurements will complement the density and ion current data. Since velocity space-time correlations in isothermal turbulent boundary layer are only available for the axial velocity component, our investigation will be the first study of transverse space-time correlation. Measurements in the heated and reacting layer will provide a more complete description of the effects of combustion in this flow.

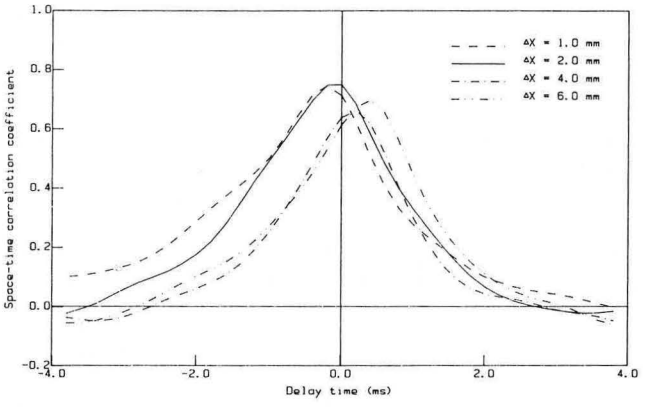

Figure 2. Space-time correlation coefficient $R(\Delta t, \Delta x, \Delta y)$ for the reacting layer with point y fixed at y = 2 mm and point 2 at 2 mm above and at various Δx. (XBL 862-456)

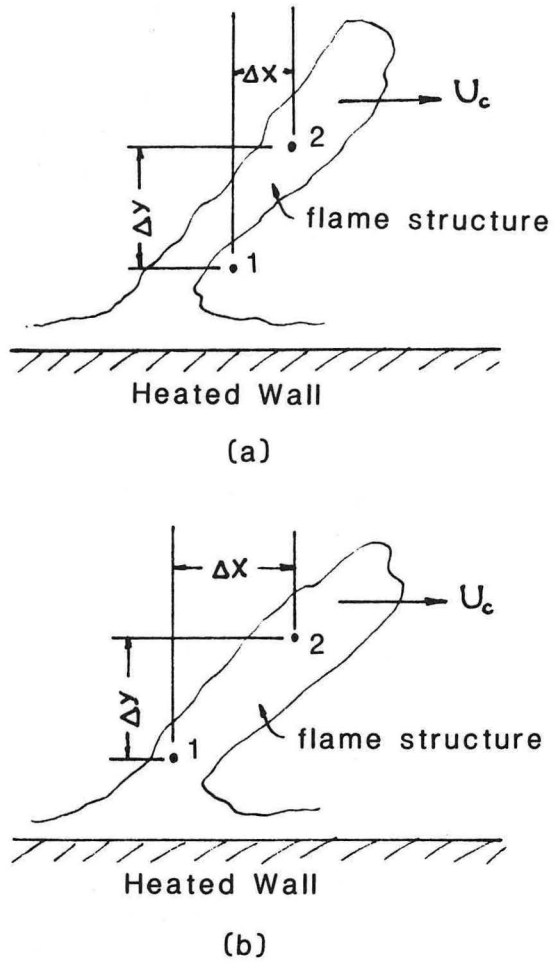

Figure 3. Schematics of the flame structures which would be consistent with the $R(\Delta t, \Delta x, \Delta y)$ results. (XBL 862-457)

REFERENCES

1. Ng, T.T., Cheng, R.K., Robben, F., and Talbot, L. (1982), "Combustion Turbulence Interaction in the Turbulent Boundary Layer Over a Hot Surface," *Nineteenth Symposium (International) on Combustion*, The Combustion Institute, p. 359.
2. Cheng, R.K. and Ng, T.T. (1985), "Conditional Reynolds Stress in a Strongly Heated Turbulent Boundary Layer with Premixed Combustion," to appear in *The Physics of Fluids.*
3. Namazian, M., Talbot, L., Robben, F., and Cheng, R.K. (1982), "Two-Point Rayleigh Scattering Measurements in a V-shaped Turbulent Flame," *Nineteenth Symposium (International) on Combustion,* The Combustion Institute, p. 487.

Intermittency and Conditional Velocity Statistics in Premixed Conical Turbulent Flames*

R.K. Cheng, I.G. Shepherd,† F. Robben, and L. Talbot

The overall goal of this program is to gain better physical understanding of the interaction between turbulence and combustion processes in premixed turbulent flames. The approach is to study the complex turbulent combustion flow field in simplified systems using laser diagnostic techniques. The results are used to compare with predictions of theoretical models. In FY 1985, we have initiated a study of premixed conical turbulent (large Bunsen type) flames. Although this flame configuration has been used in many experimental and theoretical studies the study of conditional velocities has been limited to one velocity component. Our study involves measuring conditional velocity statistics for two velocity components. The results are useful to investigate the difference or similarities between the flame processes in this flame and in the V-flames.

ACCOMPLISHMENTS DURING FY 1985

A schematic of the experimental setup is shown in Fig. 1. The burner is larger than ordinary laboratory model (5.0 cm diameter), and the turbulent flame is stabilized by a ring of pilot flames fitted at the burner exit. Incident turbulence was generated by perforated plate placed 5.0 cm upstream of the exit or at the entrance to the burner cylinder. Conditioned and unconditioned velocity statistics were measured by a two-component laser Doppler anemometry (LDA) system using the sampling technique described in Ref. 1. The intermittency was also obtained by monitoring the Mie scattering from silicon oil aerosol introduced into the flow. The intermittency data are needed to analyze the unconditioned velocity data to obtain the conditioned product velocities. Since intermittency is the probability of encountering the reactants, it can be interpreted as a measure of normalized mean density.

Results were obtained in six flames using either methane/air or ethylene/air mixtures of various concentration ratios. The mean velocity was varied from 3.0 to 8.0 m/s with the incident turbulence intensities ranging from 3 to 15%. Figure 2 shows the contours of the intermittency for a methane/air flame constructed based on three radial profiles at 50, 75, and 100 mm above the exit and a vertical profile along the centerline of the burner axis. As can be seen the flame brush thickness along the centerline is about 90 mm, compared to typical laminar flame thickness of 1 mm.

The conditioned reactant and unconditioned velocities were measured directly by LDA. The unconditioned product velocity was deduced from the unconditioned data using an analysis method described in Ref. 2. This method involves convoluting the velocity probability density functions and is more general than the method used in Ref. 1.

Typical conditioned and unconditioned profiles for the axial and radial velocity components are shown in Fig. 3. The profile of the radial velocity shows that the conditioned product velocities are higher than both the unconditioned and the conditioned reactant velocities. However, the axial velocities show little changes, and significant increases in the unconditioned turbulence intensities within the

*This work was supported by the Director, Office of Energy Research, Office of Basic Energy Sciences, Chemical Sciences Division of the U.S. Department of Energy under Contract No. DE-AC03-76SF00098.

†Department of Mechanical Engineering, University of California, Berkeley.

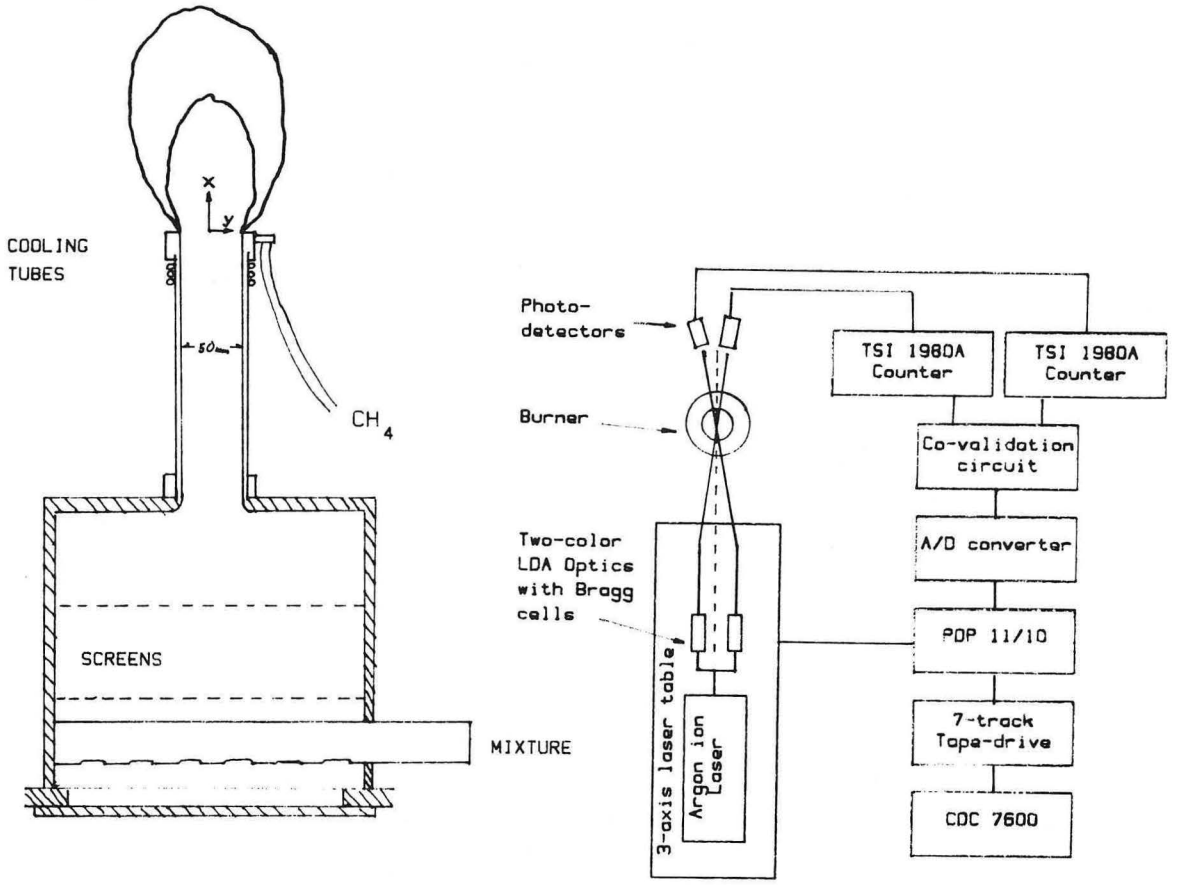

Figure 1. Schematic of the experimental setup. (XBL 862-463)

flame brush were only observed in flames with low incident turbulence (<5%).

The lack of observable increases in the unconditioned turbulence intensities can be explained by the reduction in the relative velocity between the products and the reactants ΔU. The magnitudes of the instantaneous relative velocity for a one-dimensional flame (i.e., the velocity jump across the flame front) Δu is often assumed to be $\Delta u = S_u (\tau - 1)$, where S_u is the local laminar burning velocity and τ is the reactant/product density ratio for the mixture. Since the Bunsen flame flow field is three-dimensional, the relative velocity Δu is reduced due to stream tube divergence. Therefore, the contributions to unconditioned velocity statistics, which are due mostly to the relative velocity, are also reduced.

PLANNED ACTIVITIES FOR FY 1986

Complete analysis of the data is expected to show the changes in ΔU with equivalence ratio and incident turbulence. Though the effect of stream tube divergence provides one of the explanations to the reduction of ΔU in conical flames, further study is needed to fully explain the significant reduction observed along the centerline. In FY 1986, measurement of the orientations of the flame fronts in conical flame will be initiated. Tomographic movies of the conical flame will be obtained and digitized. The distributions of the flame orientations will be correlated with the observed Δu for developing a kinematic model to describe the changes in flame generated turbulence.

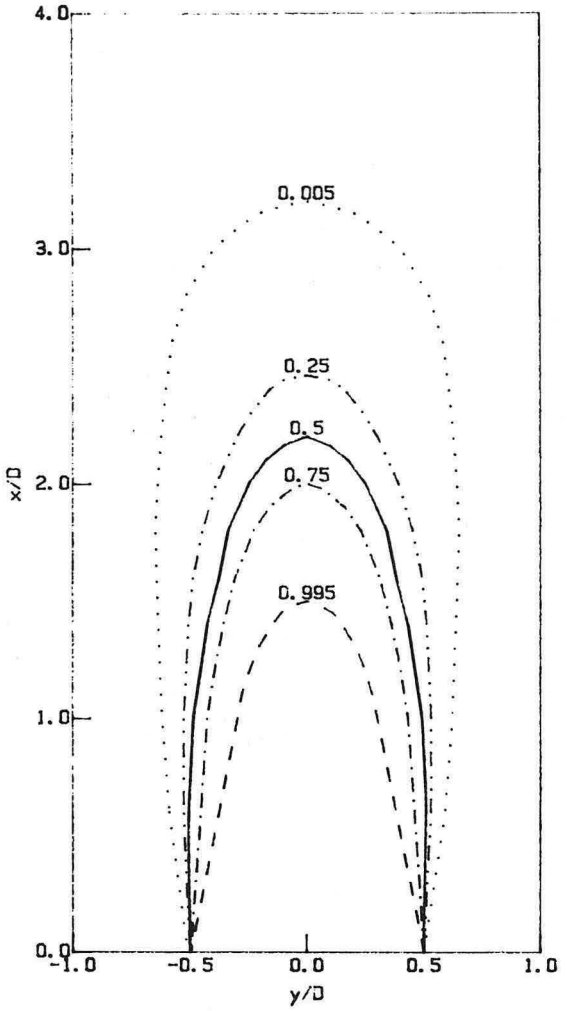

Figure 2. Contours of the intermittency measured in an ethylene/air turbulent conical flame with free stream velocity of 6.6 m/s, equivalence ratio of 0.6, and incident turbulence intensity of 10%. (XBL 862-464)

The initiation of a study in premixed turbulent flame enclosed in a flow channel is also planned. One of the main objectives is to determine whether or not many of the modeling assumptions regarding

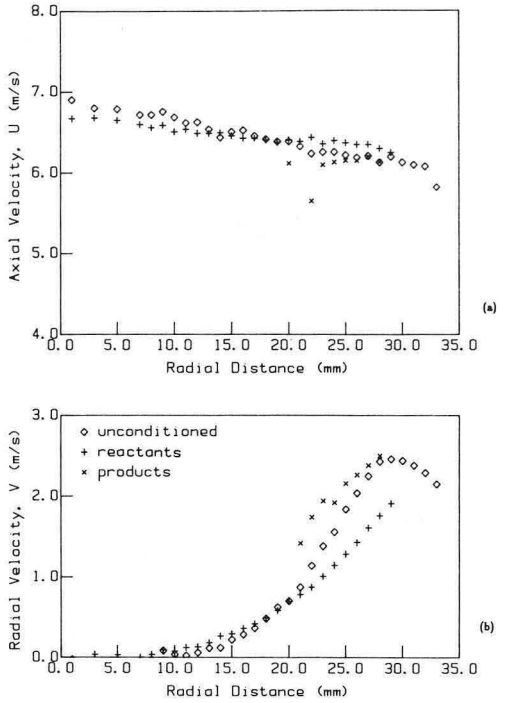

Figure 3. Radial profiles of the conditioned and unconditioned mean velocities for the flame of Fig. 1 at 50 mm above the burner exit. (XBL 862-465)

the behavior of the flame flow field with the constrain of the enclosure are justified. Measurement of the conditional velocities will provide further insight into the turbulence behavior in the enclosed burner.

REFERENCES

1. Cheng, R.K. (1984), "Conditional Sampling of Turbulence Intensities and Reynolds Stress in Premixed Flames," *Combustion Science and Technology 41,* p. 109.
2. Cheng, R.K. and Shepherd, I. G. (1986), "Intermittency and Conditioned Velocity Statistics in Premixed Conical Turbulence Flames," submitted to *Combustion Science and Technology.*

Spectral Behavior of Velocity Fluctuations in Premixed Turbulent Flames*

I. Gokalp,† I.G. Shepherd,‡ and R.K. Cheng

Although spectral analysis has been one of the principal means to to characterize fluid mechanical turbulence in non-reacting flows, experimental spectral information on fluctuating quantities in turbulent flames is scarce. A majority of the investigations of turbulent flames are focused on obtaining the statistical quantities such as the mean, variance, and correlation functions. The lack of spectral data may be due partly to the complexities inherent in the collection of reliable raw data suitable for spectral treatment. Another possible reason is that, at present, most theoretical models of turbulent combustion do not consider temporal scales. Since spectral data provide a great deal more information about the turbulent structures, attempts directed to obtaining them are worth pursuing. With the use of advanced laser optical techniques with sufficient spatial and temporal resolutions and the improved numerical techniques for the spectral analysis of both continuously and randomly sampled turbulent signals, the acquisition of spectral data is greatly facilitated.[1] In addition, development of recent numerical models which consider the length and time scales and the spectra[2-4] have generated more interest in the study of spectral behavior in turbulent flames. In FY 1985 we have initiated a study of the spectral behavior of velocity fluctuations in turbulent premixed V-flames.

ACCOMPLISHMENTS DURING FY 1985

Velocity spectra are calculated for two of the ethylene/air flames investigated in our earlier works. The velocity statistics have been reported in two papers,[5,6] but their spectral behavior has not been investigated. Particular attention is paid to the spectra of the velocity component closest to the normal of the turbulent flame brush. The experimental conditions are: Flame A with $U_\infty = 5.0$ m/s, $\phi = 0.8$, $u' = 5\%$ and Flame B with $U_\infty = 7.0$ m/s, $\phi = 0.75$, $u' = 7\%$. The equivalence ratio for the two flames is close and the main difference is in the turbulence intensities. For Flame B, the incident turbulence is more intense.

The spectral density distributions obtained for Flame A at x = 85 mm are compared in Fig. 1. Three spectra corresponding to the reactants, the flame zone (point of maximum rms fluctuation), and the products are shown. The rms fluctuation velocities are 0.3 m/s in the reactants and 1.2 m/s within the flame. The difference corresponds to an increase in energy level at all frequencies. The "wrinkled laminar flame" concept would predict increase in energy levels in the low frequency range. The spectra obtained at several height above the burner have the same features. The slopes of the reactant spectra are almost constant for different heights above the burner exit and are very close to the classical Komogoroff slope of $-5/3$, which indicates the presence of an inertia subrange. However, the spectra obtained within the flame and the product regions do not exhibit the $-5/3$ slope. The absence of the $-5/3$ slopes suggests that classical velocity spectral interpretation is not appropriate.

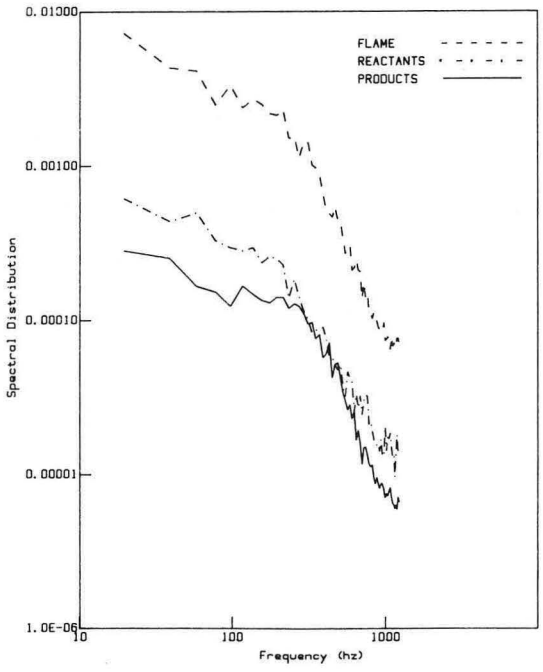

Figure 1. Frequency spectra for an ethylene/air turbulent V-flame with equivalence ratio of 0.8, free stream velocity of 5.0 m/s, and incident turbulent intensity of 5%. (XBL 862-458)

*This work was supported by the Director, Office of Energy Research, Office of Basic Energy Sciences, Chemical Sciences Division of the U.S. Department of Energy under Contract No. DE-AC03-76SF00098.

†Participating guest from CRCCHT-CNRS 45045 Orleans Cedex, France, sponsored by a NATO grant for international collaboration in research.

‡Dept. of Mechanical Engineering, University of California, Berkeley.

One aspect of the turbulent flame, which may provide the key for the interpretation of velocity spectra, is the dynamics of the wrinkled turbulent flame front. Within the flame brush, the stationary LDA probe measures intermittently velocities in the reactant and in the products. Since the two conditioned velocities are different, each passage of flame front across the measurement position results in a sudden jump in velocity. The velocity spectra then contain the effects due to the flame passage. The change in the spectral slopes may be due to this effect. Without the support of additional data, this remains a speculation at best. However, it emphasizes the need to study the analogy between velocity and scalar spectra.

Figure 2 shows the wave-number representation for the velocity spectra shown in Fig. 1. The main feature of the wave-number spectra is the shifting of the most energetic wave number (i.e., the wave number corresponding to the peak of the spectrum) toward a lower value in the flame and in the products. The shifting of the most energetic point of the product spectra to lower wave number is consistent with the dilatation effects and the increased viscosity which smears the small eddies to increase the mean size of the most energetic eddies.

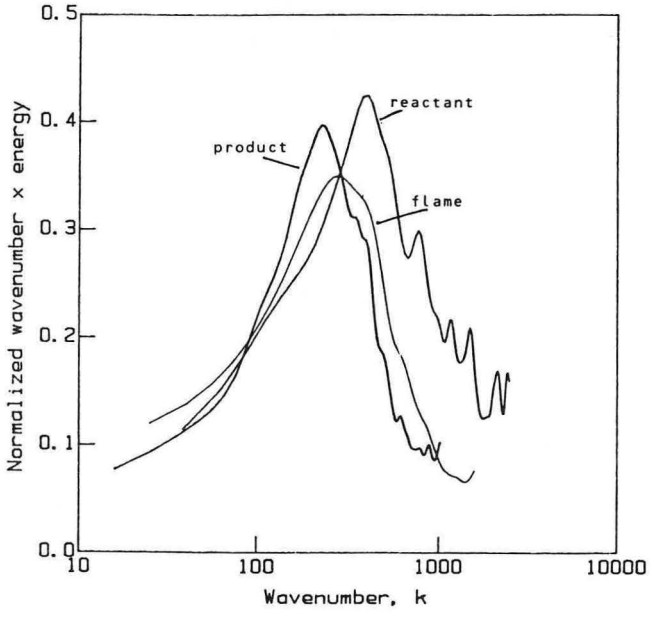

Figure 2. Normalized wave-number spectra corresponding to Fig. 1. (XBL 862-459)

PLANNED ACTIVITIES FOR FY 1986

Velocity spectra will be calculated for the data obtained in the conical flames. Since the velocity measurements for the conical flames are made for two velocity components, the spectra for the component normal to the flame brush will be studied. To further investigate the analogy between velocity and scalar spectra, the spectra for the intermittency will be calculated. Also the spectral dynamics of the flame front which can be deduced form the LARS data will be investigated. The results will be useful to identify the influence of the fluctuating flame on velocity statistics.

REFERENCES

1. Srekantaiah, D.V. and Coleman, H.W. (1984), "Turbulent Spectrum from Individual Realization Laser Velocimetry Data," *Experiments in Fluids 3*, p. 35.
2. Bray, K.N.C., Libby, P.A., and Moss, J.B. (1984), "Scalar Length Scale Variation in Premixed Turbulent Flames," *Twentieth (International) Symposium on Combustion,* The Combustion Institute, p. 421.
3. Bray, K.N.C., Libby, P.A., and Moss, J.B. (1984), "Flamlet Crossing Frequencies and Mean Reaction Rate in Premixed Turbulent Flames," *Combustion Science and Technology 41,* p. 143.
4. Kerstein, A.R. (1985), "Pair Exchange Model of Turbulent Premixed Flame Propagation," paper presented at the 1985 Fall Meeting of the Western States Section of the Combustion Institute, Davis, CA, Oct. 1985.
5. Cheng, R.K. and Ng, T.T. (1983), "Velocity Statistics in Premixed Turbulent Flames," *Combustion and Flame 52,* p. 185.
6. Cheng, R.K. and Ng, T.T. (1984), "On Defining the Turbulent Burning Velocity in Premixed V-Shaped Turbulent Flames," *Combustion and Flame 57,* p. 156.

Structure and Propagation of Turbulent Premixed Flames Stabilized in a Stagnation Flow*

P. Cho,† C.K. Law,† J.R. Hertzberg, and R.K. Cheng

Many configurations and methodologies have been adopted in the fundamental studies of structure and propagation of turbulent premixed flames. The most prevalent configurations for studying open and steady flames are the Bunsen-type conical flames and the V-flames stabilized by a rod. Although the two configurations are relevant to the burner geometries commonly found in practical combustors, comparison of the experimental results with predictions of theoretical turbulent combustion models is not straightforward. This is due in part to the fact that the flame brushs in both configurations are oblique to the approach flow. Since most of the turbulent combustion models (e.g., the model of Bray, Moss, and Libby[1]) are one dimensional, transformation of the results to the "flame coordinate" is necessary.

In view of the above considerations, we have initiated a study of premixed turbulent flame where the flame brush is locally normal to the approach flow and does not involve a recirculation region for stabilization. The methodology involves stabilizing a planar turbulent flame in a stagnation flow with incident turbulence generated by grid or perforated plate. This configuration has been adopted in previous studies of laminar flames,[2] although its application to turbulent flames has not been reported.

ACCOMPLISHMENTS DURING FY 1985

Figure 1 shows a schematic of the experimental setup. A uniform axisymmetrical flow of premixed methane/air mixture is provided by a 50 mm diameter nozzle. The exit velocity is varied from 3 to 6.7 m/s. Incident turbulence is generated by placing at 50 mm upstream of the nozzle exit either a square mesh grid or a perforated plate. The planar turbulent flame is stabilized by a solid brass 200 mm diameter circular stagnation plate. The surface facing the flow is convex (r = 460 mm) to allow LDA access close to the plate surface (Fig. 1). This arrangement enables measurements of the axial velocity component normal to the plate at 3.0 mm from the plate surface. Flow velocities are measured by a four-beam two-color LDA system with a 4.0 watt argon-ion laser. All four beams are shifted by Bragg cells and differential frequency of 5.0 MHz is used for both components for removal of directional ambiguity. The seeding is provided by refractory aluminum oxide particles of 0.3 μm introduced into the flow by a cyclone canister seeder.

The mean and rms centerline axial profiles for two of the thirty methane/air flames studied are compared in Fig. 2. Both mean axial velocity profiles exhibit the characteristic "hump-back" trend previously observed in laminar stagnation flames. The linear decrease of U, with decreasing distance from the wall, is due to the divergence of the stagnation flowfield. Flow acceleration due to combustion gives rise to the "hump." The rms fluctuation profiles show that within the flame zone, u′ increase to a peak of 0.8 m/s for the richer flame while the peak u′ is only slightly higher than the incident turbulence for the leaner flame. The corresponding v′ profiles show that the increase within the flame zone is only shown for the richer flame. But in both cases, v′ increases in the product zone while u′ decreases. The corresponding Reynolds stress profiles (not shown) do not indicate any changes through the flame zone. The same feature is found on all of the Reynolds stress profiles obtained for this study.

The point where the mean axial velocity profile deviates from linearly decay is the boundary of the turbulent flame brush. Since the flame brush is normal to the approach flow, the velocity at this point is by definition the turbulent burning velocity S_t. This concept is similar to that used for the determination of laminar flame speed in stagnation flow[1] and is consistent with the definition proposed by Cheng and Ng[3] for the determination of S_t in V-flames.

In Fig. 3, all of our results are compared with the results of Cheng and Ng[3] for ethylene/air V-flames, Smith and Gouldin[4] and Dandekar and Gouldin[5] for methane/air V-flames, Ballal and Lefebvre[6] for confined propane/air V-flames, and Abdel-Gayed and Bradley[7] for double expanding cylindrical hydrogen/air flames in the form of S_t/S_l versus u'/S_l. Our results are in excellent agreement with the results reported by others using different flame configurations.

*This work was a collaboration effort between U.C. Davis and LBL. The work at LBL was supported by the Director, Office of Energy Research, Office of Basic Energy Sciences, Chemical Sciences Division of the U.S. Department of Energy under Contract No. DE-AC03-76SF00098. The work at Davis was supported by the U.S. Air Force Office of Scientific Research under Grant No. 85-0147.

†Department of Mechanical Engineering, University of California, Davis, CA.

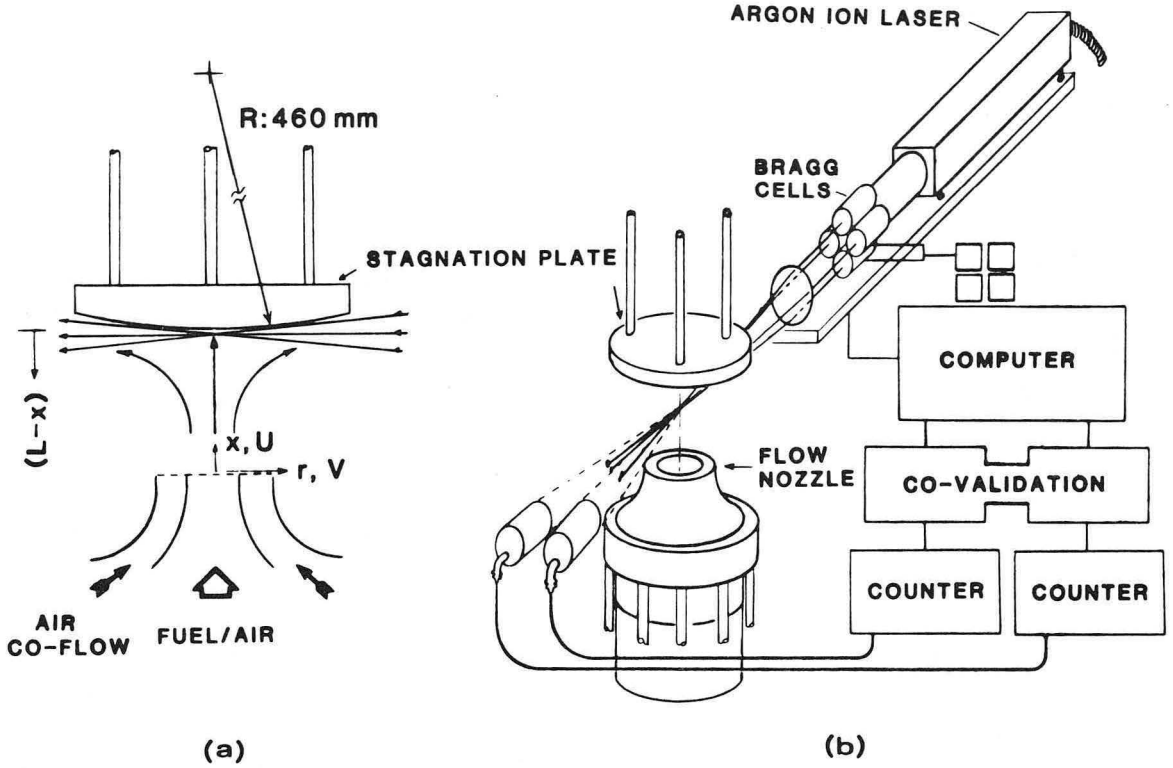

Figure 1. Schematic of the experimental setup. (XBL 862-452)

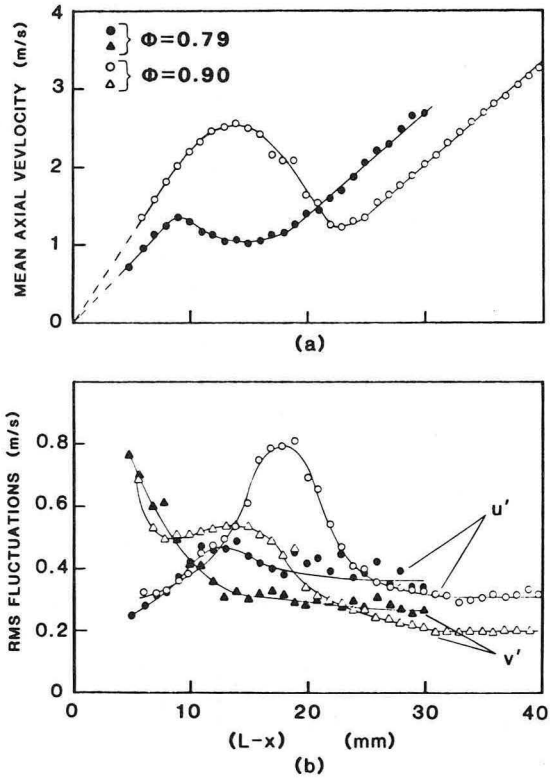

Figure 2. Velocity profiles of reacting flows, centerline traverse. (a) mean velocities; (b) rms fluctuations. (XBL 862-453)

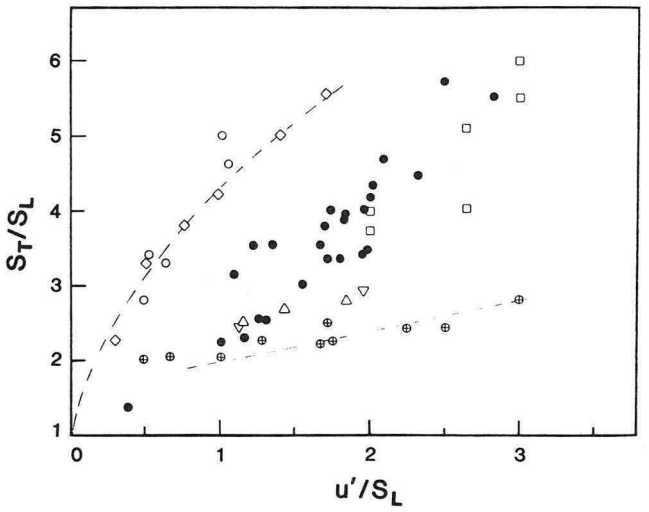

Figure 3. Correlation of turbulent flame speeds: Present work, propane/air, stagnation flow; Abdel-Gayed and Bradley, hydrogen/air bomb; Kleine, methane/air, cone; Ballal and Lefebvre, propane/air, confined V-flame; Cheng and Ng, ethylene/air, open V-flame; Dandekar and Gouldin, methane/air, open V-flame; Smith and Gouldin, ethylene/air, open V-flame. (XBL 862-454)

PLANNED ACTIVITIES FOR FY 1986

The study of turbulent stagnation flame will be extended to measurement of conditional velocities and scalar fluctuations. Ethylene and propane will be used as fuel. The scalar measurements will provide a more concise definition of the flame boundary for the determination of the turbulent flame speeds. The conditional velocities will be useful for studying flame-generated turbulence in this configuration where the flow field in the product zone is divergent.

REFERENCES

1. Bray, K.N.C., Moss, J.B., and Libby, P.A. (1985), "Unified Modeling Approach for Premixed Turbulent Combustion—Part I: General Formulation," *Combustion and Flame 61,* p. 87.
2. Wu, C.K. and Law, C.K. (1985), "On the Determination of Laminar Flame Speeds From Stretched Flames," *Twentieth Symposium (International) on Combustion,* The Combustion Institute, p. 1941.
3. Cheng, R.K. and Ng, T.T. (1984), "On Defining the Turbulence Burning Velocity in Premixed V-Shaped Turbulent Flames," *Combustion and Flame 57*, p. 155.
4. Smith, K.O. and Gouldin, F.C. (1979), "Turbulence Effects on Flame Speed and Flame Structure," *AIAA J. 171*, p. 1243.
5. Dandekar, K.V. and Gouldin, F.C. (1982), "Temperature and Velocity Measurements in Premixed Turbulent Flames," *AIAA J. 20,* p. 642.
6. Ballal, D.R. and Lefebvre, A.H. (1975), "The Structure and Propagation of Turbulent Flames," *Proc. Roy. Soc. London 344A,* p. 217.
7. Abdel-Gayed, R. and Bradley, D. (1977), "Dependence of Turbulent Burning Velocity to R.M.S. Turbulent Velocity," *Sixteenth Symposium (International) on Combustion,* The Combustion Institute, p. 1725.

Premixed Flame Stabilization on a Bluff Body*

J.R. Hertzberg and L. Talbot

In order to study the effects of fluid mechanics on combustion, the structure of a turbulent premixed flame stabilized on a bluff-body flameholder has been observed using Rayleigh scattering for single-point measurements of density. The region near the flame holder is the focus of this work. The intent is to observe the interaction of the recirculation zone and the developing flame in order to better understand the evolution of a flame sheet into a turbulent flame brush.

The combustor configuration for the laminar, premixed V-shaped flame consists of a vertical 5 cm diameter open jet of ethylene-air mixture with a square cross section rod flame holder transverse to the flow. Turbulence is generated by a wire grid of 1 mm elements and 5 mm spacing, placed 50 mm upstream of the flame holder, at the nozzle exit. The fuel-air jet is protected from shear with the stagnant surroundings by an annular air jet. Spatial coordinates are measured from the top center of the flameholder; Z is vertical, X is horizontal. Two conditions have been studied: (1) a very lean flame, close to being blown off the flame holder at 5.5 m/s, equivalence ratio ϕ = 0.54 and (2) a slightly richer, well-stabilized flame at 5.5 m/s, ϕ = 0.63.

ACCOMPLISHMENTS DURING FY 1985

Point measurements of density using laser Rayleigh scattering[1] have been made in a region beginning at 0.5 mm downstream of the flame holder and extending to 80 mm downstream.

Flame brush extent and position can be calculated from time-averaged profiles using the steepest gradient method, and is shown in Figs. 1 and 2. Figure 1 shows the growth of the flame zone with distance downstream. The well-stabilized flame shows a nearly constant rate of brush growth while the very lean case shows a much more rapid growth for the first 25 mm and then slows down for the rest of the observed region. Another important result is that both cases show an initial thickness of 1 mm. This could be due to a nearly laminar flame, moving slightly, or to the thickness of an as yet non-reacting shear flow with a temperature difference. Figure 2 shows the relative positions of the two brushes. It is

*This work was supported by the Air Force Office of Scientific Research under grant AFOSR 84-0124, through the U.S. Department of Energy under Contract No. DE-AC03-76SF00098.

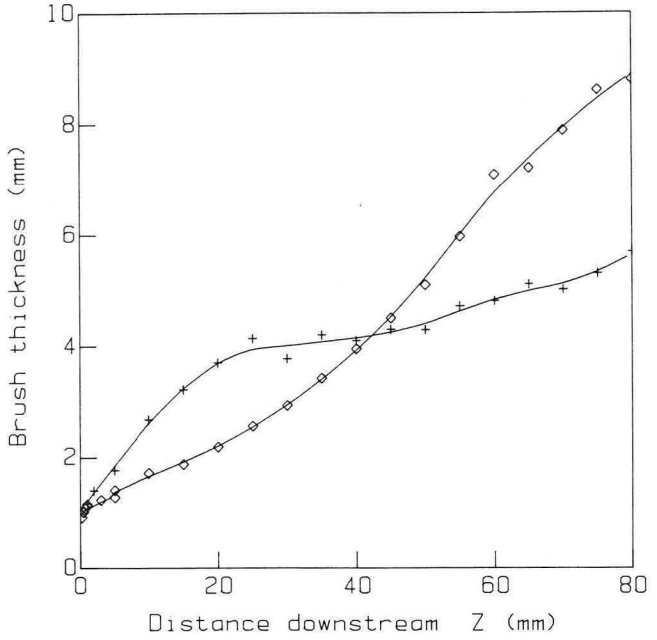

Figure 1. Flame thickness vs. distance downstream of flame holder. Well-stabilized case = diamond; very lean case = plus. (XBL 862-397)

interesting to note that the outer extent of the two coincide until approximately the same distance downstream that the slope of growth of the leaner case slackens. The inner extent of the leaner brush is closer to the centerline of the flow than the well-stabilized case, possibly indicating a narrower recirculation zone.

In order to examine the evolution of the structure of the brush with distance downstream the probability density function (pdf) of gas density at the center of the flame from each profile is shown in Fig. 3 for the richer case and in Fig. 4 for the leaner case. In both cases the pdf at Z = 5 mm is monomodal; that is, the stationary Rayleigh measurement volume sees an even distribution of densities, corresponding to gas temperatures ranging from room temperatures to burned gas temperatures, with nearly equal probability. Staying in the center of the flame and moving downstream, the distribution becomes bimodal: the measurement volume sees mostly burned or unburned, with very little in between. The difference between the two cases is that the well-stabilized case is noticeably bimodal by 20 mm downstream, while the lean case is just beginning to show signs of bimodality. This point, coupled with the fact that the lean case brush is twice as thick as the richer case, seems to indicate that the structure of the lean case at that position may be a thick laminar flame moving slightly, while the well-stabilized case shows a much thinner flame, flapping more rapidly. Unfor-

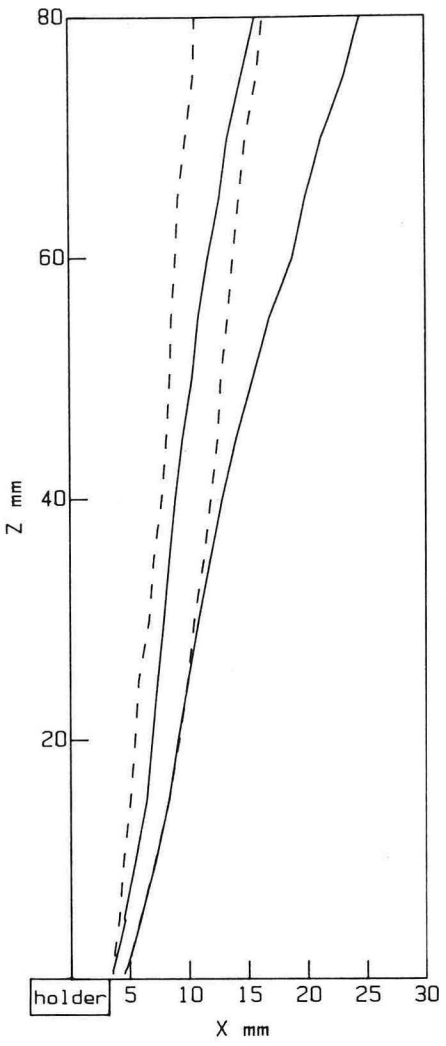

Figure 2. Flame brush position. Well-stabilized case = solid lines; very lean case = dashed line. (XBL 862-398)

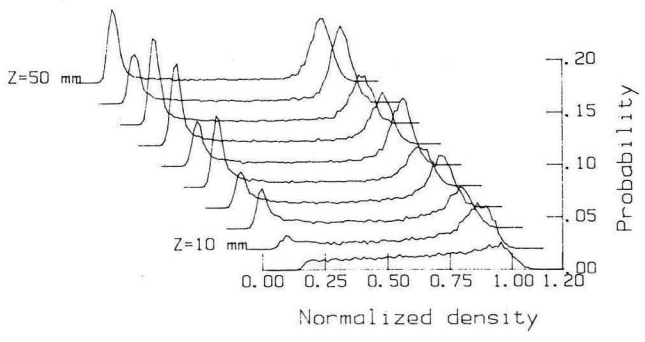

Figure 3. PDF of density at center of flame for well-stabilized case. (XBL 862-399)

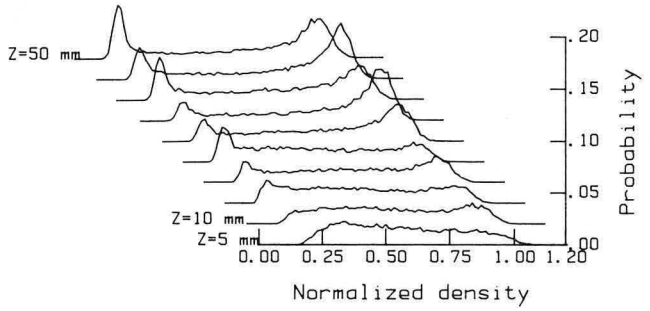

Figure 4. PDF of density at center of flame for very lean case. (XBL 862-400)

tunately, although it is true that the leaner flame will have a slightly thicker laminar flame, the magnitude of that difference is unlikely to be large enough to account for the data.

PLANNED ACTIVITIES FOR FY 1986

Laser doppler velocimetry measurements of reacting flow will be made in order to map the flow characteristics of the flame holder region in the well-stabilized and close to blow off cases. Ionization probe measurements will also be made to determine the flame stand off distance and how it changes with equivalence ratio.

REFERENCES

1. Namazian, M., et al. (1982), "Two-Point Rayleigh Scattering Measurements in a V-Shaped Flame," *Nineteenth Symposium (International) on Combustion,* The Combustion Institute, p. 487.

Fluid Dynamic Considerations in the Numerical Modeling of Flames*

M.Z. Pindera and L. Talbot

The objective of this investigation is to develop a deterministic numerical model of turbulent flame propagation in premixed reactants. The influence of the flame front on fluid dynamics of the surrounding gas is studied both for turbulent and non-turbulent conditions. The model is formulated for continuous flames of finite length such as the V-shaped configuration studied by Cheng[1] or for the stagnation point combustion studied by Wu and Law.[2] Compared to the statistical modeling approach used in many investigations where the change in flame turbulence is often used as input parameters, the present model is capable of predicting the turbulence phenomena.

ACCOMPLISHMENTS DURING FY 1985

The numerical model is based on the concept that the effects of flame exothermicity are manifested only through volumetric expansion which is confined to a narrow (in principle infinitesimally thin) flame region. The flame is thus taken as a collection of sources embedded in a flow of uniform density. The effects of pressure gradients at the flame front (the baroclinic term) are accounted for by adding vorticity to the flow on the burnt side. Magnitude of the vorticity can be found from conservation of momentum. Vorticity then is treated using the Lagrangian method of Chorin.[3] The dynamics of the flame itself are accounted for by computing the flame motion in two steps, as outlined by Ghoniem, *et al.*[4] First it propagates in the direction normal to itself at a specified flame speed, and then is advected by the motion of the gas. The theory and representative calculations have been reported in two papers (Pindera and Talbot[5-6]).

Comparisons of the numerical and experimental results are shown in Figs. 1–3. The experimental flame geometry is the turbulent premixed V-flame.[1] However, the calculations are obtained for a stationary flame without considering the effects of incident turbulence. Since the fluctuating flame is not expected to affect significantly the mean flow velocity, the overall features of the flow field can be compared. Figure 1 shows the mean axial velocity profiles at various axial positions reported by Cheng.[1] Figure 2 shows calculated velocity profiles for the same case when vorticity generation is not considered. As can be seen, the predicted velocity near $y = 0$ is much lower than the experimental value. Figure 3 shows the effects of including vorticity generation in the calculations. The comparison between

*This work was supported by the Director, Office of Energy Research, Office of Basic Energy Sciences, Chemical Sciences Division of the U.S. Department of Energy under Contract No. DE-AC03-76SF00098.

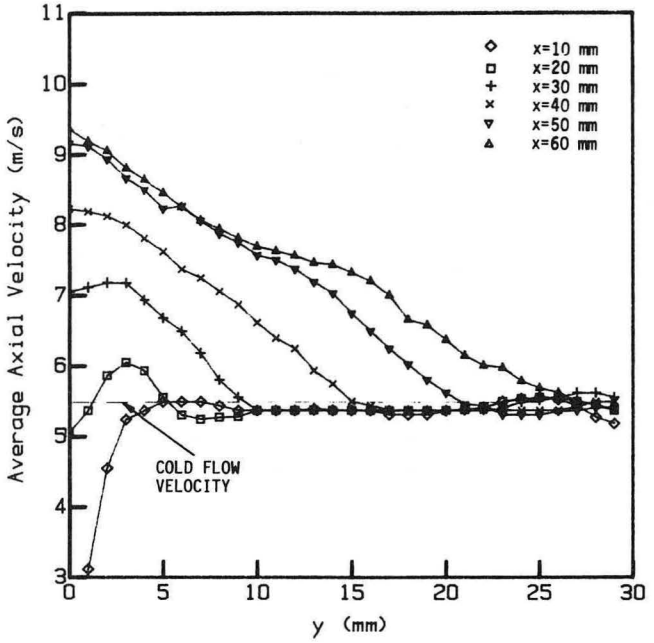

Figure 1. Measured average axial velocities. (XBL 862-421)

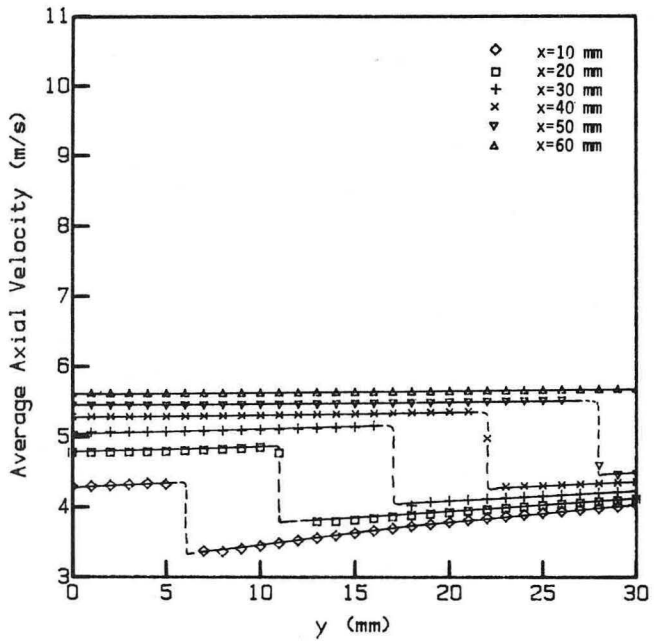

Figure 2. Calculated axial velocities; no vorticity. (XBL 862-422)

the experiments and theory is much improved. Our study shows that when the flame-produced vorticity is not considered in the model, as is common in models of this type (see, for example, Ghoniem, *et al.*,[4] Sethian,[7] Ashurst and Barr[8]), the results may be erroneous, since momentum is not conserved.

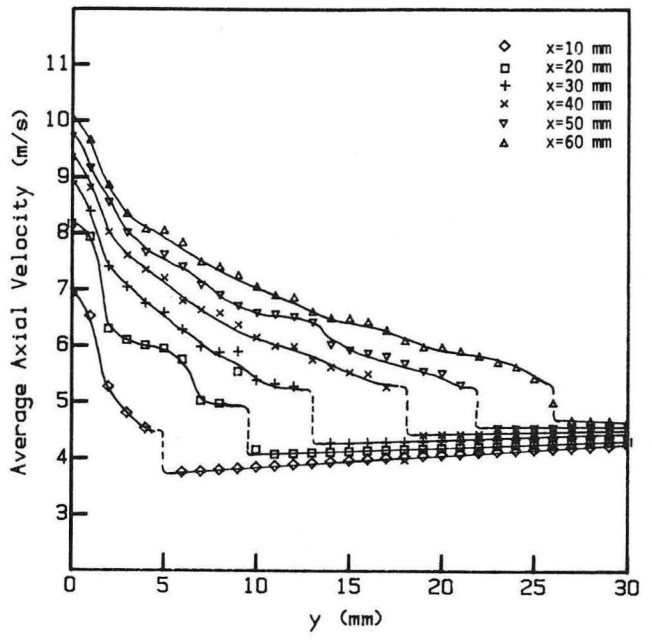

Figure 3. Calculated axial velocities; vorticity added. (XBL 862-423)

PLANNED ACTIVITIES FOR FY 1986

The model will be extended to include the interaction of the flame with the incident turbulent flow field. In particular the experimental work of Cheng[1] for the turbulent V-shaped flame geometry will be modeled. The algorithm will be generalized to consider the effects of nonuniform flame speed on the generation of vorticity. The experimental and predicted values of the mean velocities, the rms fluctuation intensities, and Reynolds stress will be compared.

REFERENCES

1. Cheng, R.K. (1984), "Conditional Sampling of Turbulence Intensities and Reynolds Stress in Premixed Flames," *Comb. Sci. and Tech 25*, p. 109.
2. Wu, C.K. and Law, C.K. (1984), "On the Determination of Laminar Flame Speeds from Stretched Flames," *Twentieth Symposium (International) on Combustion*, The Combustion Institute, p. 1941.
3. Chorin, A. J. (1973), "Numerical Study of Slightly Viscous Flow," *J. of Fluid Mech. 57*, p. 785.
4. Ghoniem, A.F., Chorin, A.J., and Oppenheim, A.K. (1982), "Numerical Modeling of Turbulent Flow in a Combustion Tunnel," *Phil. Trans. R. Soc. A 394*, p. 303.

5. Pindera, M.-Z. and Talbot, L. (1986), "Flame Induced Vorticity: Effects of Stretch," submitted to *Twenty-First Symposium (International) on Combustion*, The Combustion Institute.
6. Pindera, M.-Z. and Talbot, L. (1986), "Some Fluid Dynamic Considerations in the Modelling of Flames," submitted to *Combustion and Flame.*
7. Sethian, J. (1984), "Turbulent Combustion in Open and Closed Vessels," *J. Comp. Phys. 54,* p. 425.
8. Ashurst, W.T. and Barr, P.K. (1983), "Stochastic Calculation of Laminar Wrinkled Flame Propagation Via Vortex Dynamics," *Comb. Sci. and Tech. 34,* p. 227.

Linear Array for Rayleigh Scattering (LARS)*

I.G. Shepherd, G.L. Hubbard, W. Walker, III, F. Robben, and L. Talbot

The award of a Department of Defense Research Equipment Grant has made possible the development of a linear array for Rayleigh scattering system (LARS). This is a new space-time imaging technique which derives the gas density along a segment of a laser beam from the intensity of Rayleigh scattered light.

Previous two-point Rayleigh measurements made by this group[1,2] have been used to investigate the structure of premixed turbulent flame zones. These experiments have been used to develop a model[2,3] which predicts flame statistics from the probability density function of the flame front position. The new technique can determine the instantaneous flame front position directly and hence test some assumptions of the model. In addition it also makes possible the time resolved study of the flame front oscillations and the instantaneous flame profile.

ACCOMPLISHMENTS DURING FY 1985

This year the construction and testing of the LARS system have been completed and preliminary investigations commenced. The Rayleigh light scattered by a segment of a laser beam is imaged by means of collection optics and an image intensifier onto a 512 element Reticon array. The array is driven by a Microtex electronic data transfer system which is capable of a maximum 5 MHz pixel reading rate. The camera is interfaced by direct access memory to a PDP 11/73 computer which can store up to 2560 scan lines, i.e., 1.25 Mbytes of information. In order to deal with such large amounts of data an image processing system of the type used to analyze Landsat images has been incorporated into the computer. This system is manufactured by International Image Systems (I^2S) and is driven by a software package written and developed at U.C. Davis, and provides a sophisticated display as well as performing array computations very quickly. By such means systematic errors in the data, e.g., pixel-to-pixel sensitivity, may be readily removed from the data and carried out online. The camera system has a maximum line scan rate of 10 kHz and at a 1:1 optical magnification has a spatial resolution of 20 pixels/mm, adequate for the resolution of a flame front. A related system has been developed by Rajan, *et al.*[4] using, however, a pulsed laser which severely restricted the laser line sampling rates so that the time evolution of the flame front position could not be followed.

Preliminary experiments have been performed in a lean (ϕ = 0.6), premixed V-shaped flame at 5 m/sec and inlet turbulence of 2%. Figure 1 is an iso-intensity contour in the space-time plane and shows the time history of the flame front position. The linear array was scanned at 3 kHz with a 1:1 magnification. From these data such information as the distribution of the magnitude of flame front excursions and the spectrum of flame front movement, Fig. 2, can be derived. By choosing a different iso-intensity contour, Fig. 3, a measure of the flame front thickness may be obtained. In this case the contour separation represents a 15% difference in light intensity.

PLANNED ACTIVITIES FOR FY 1986

There are two broad areas where the investigation of premixed turbulent flames studied by this

*This work was supported by the Air Force Office of Scientific Research under contract F-44620-76-C-0083, and additional equipment and facilities were provided by the Chemical Sciences Division of the U.S. Department of Energy under Contract No. DE-AC03-76SF00098.

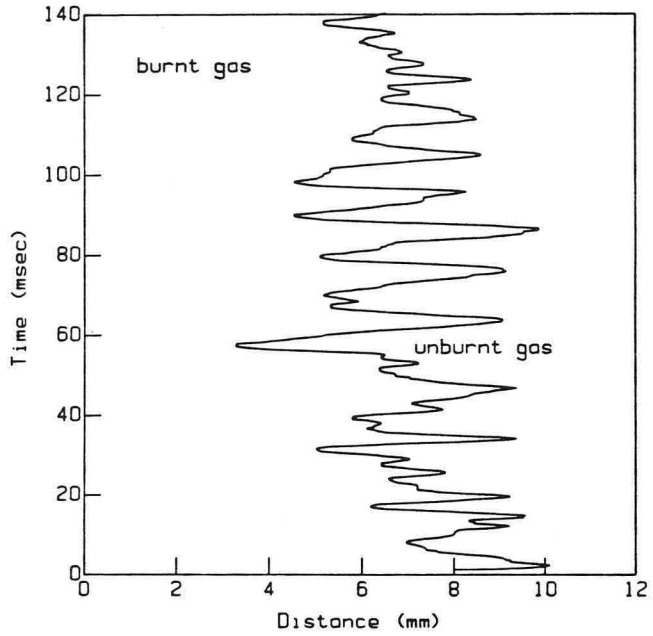

Figure 1. Flame front movement from iso-intensity contour. (XBL 862-460)

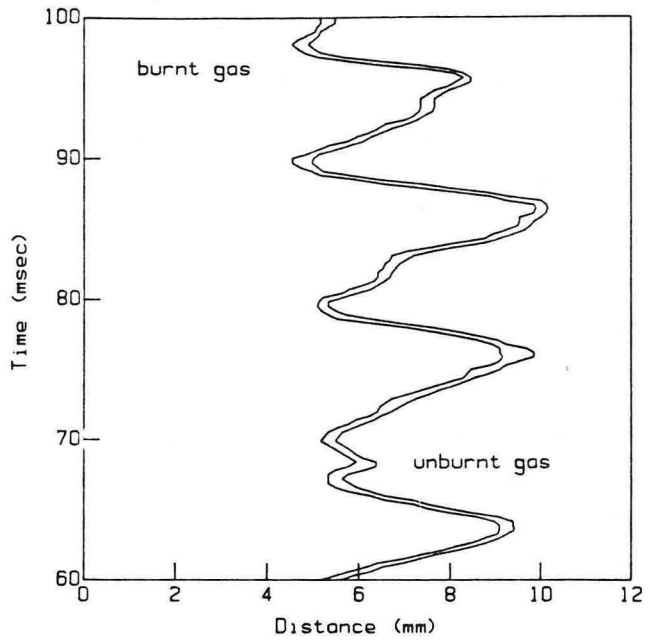

Figure 3. Two iso-intensity contours differing by 15% in light intensity. (XBL 862-462)

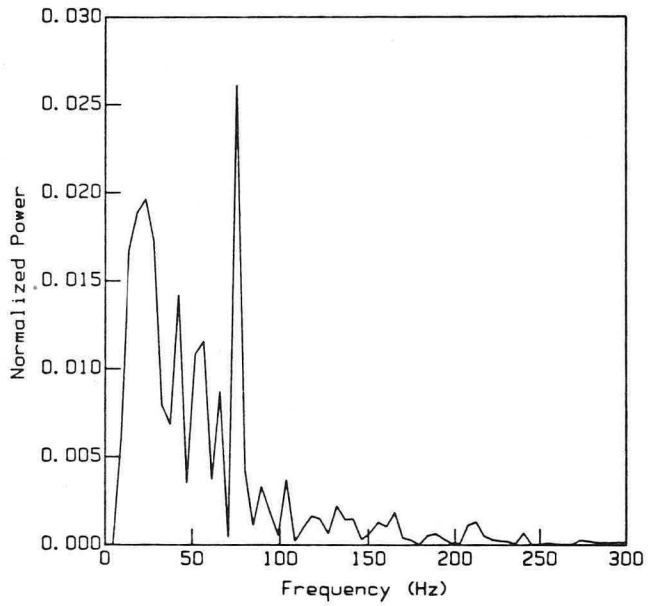

Figure 2. Spectrum of flame front oscillations. (XBL 862-461)

program is necessary: 1) the structure and evolution of the turbulent flame region and 2) the profile of the flame interface within the flame zone. LARS and laser tomography will be used to study these phenomena, and extensive use will be made of image processing techniques, at present under development, to reduce the data.

REFERENCES

1. Namazian, M., Talbot, L., Robben, F., and Cheng, R.K. (1982), "Two-point Rayleigh Scattering Measurements in a V-Shaped Turbulent Flame," *Nineteenth Symposium (International) on Combustion*, The Combustion Institute, p. 487.
2. Namazian, M., Talbot, L., and Robben, F. (1984), "Density Fluctuations in Premixed Turbulent Flames," *Twentieth Symposium (International) on Combustion*, The Combustion Institute, p. 411.
3. Namazian, M., Shepherd, I.G., and Talbot, L. (1986), "Characterization of Density Fluctuations in a Turbulent Premixed V-Shaped Flame," *Combustion and Flame.*
4. Rajan, S., Smith, J.R. and Rambach, G.D. (1984), "Internal Structure of a Turbulent Premixed Flame Using Rayleigh Scattering," *Combustion and Flame 57,* p. 95.

Theoretical Combustion Kinetics and Ignition Chemistry*

Nancy J. Brown, Ola Rashed, and Donald Lucas

Combustion chemistry consists of complex chain mechanisms involving radical species. Radicals occur in small concentrations throughout the flame due to their high reactivity, and as a consequence, are difficult to measure quantitatively. In the majority of flame systems, 100 or more elementary reactions are involved in the oxidation of fuel to CO_2, H_2O, and nitrogen or sulfur-containing pollutant species. The application of theoretical treatments of reactivity has been successful in predicting rate coefficients for several important reactions and for acquiring an understanding of the energetic factors which influence reactivity. Theories of reactivity are classified as being either dynamical or statistical, and our group has pursued the utilization of each of these to investigate reactivity and energy transfer in molecular systems important in high temperature combustion systems.

Understanding ignition phenomena in combustion systems operating over a range of pressures and temperatures, and which utilize a variety of fuel types, is a crucial step in achieving control over the combustion process. Controlling combustion will enable us to burn various fuels under conditions which maximize power output while minimizing pollutant emissions. Our research focusses upon understanding the chemistry of ignition processes. We have initiated combustion with laser photolysis to generate fixed concentrations of radicals to identify limiting requirements for ignition. Our experimental research is complemented by a modelling study which provides results useful for interpreting the experiments.

ACCOMPLISHMENTS DURING FY 1985

We have investigated energy transfer in the He_2 + OH system using the formalism of quasiclassical dynamics. Three basic approximations are employed: 1) the use of the Rashed-Brown[1] modification to the Schatz-Elgersma[2] analytical fit to the Walch-Dunning[3] ab initio potential surface, 2) treatment of the dynamics with classical mechanics, and 3) the use of Monte Carlo averaging techniques to sample the phase space of the system.

*This work was supported by the Director, Office of Basic Energy Sciences, Chemical Sciences Division of the U.S. Department of Energy under Contract No. DE-AC03-76SF00098.

Energy transfer is described in terms of changes in translational energy, and the rotational and vibrational energy in each molecule by subtracting relevant values of the initial energy from the final values. Angular momentum changes are determined in a similar fashion. Average values per collision of the various energy transfer quantities are computed for each ensemble of trajectories. Histograms of the various types of final energies in the system were computed, and state-to-state rotational and vibrational cross sections were determined. Further understanding of the energy transfer mechanism is gained through the use of correlation coefficients, which provide a measure of the relationship between two energy transfer quantities on a single collision basis.

Energy transfer is investigated as a function of translational temperature, the initial rotational energy in each molecule, and initial vibrational energy in each molecule. The translational temperatures considered are 300 to 4000 K, with the majority of the calculations performed at 1200 and 2000 K. The initial value of the rotational quantum number is in the range 0–6 for H_2 and 0–7 for OH. The initial value of the vibrational quantum number for each molecule is in the range 0–4.

The most important finding of our study can be summarized as follows:

1) The energy transfer mechanism is complex with ten types of energy transfer possible. Evidence was found for all types, and this indicates that energy transfer mechanisms in diatom-diatom collisions are far more complicated than those for atom-diatom collisions.

2) There is much more exchange between the translational degrees of freedom and He_2 vibration than OH vibration. Since translational energy is most effective in promoting reactivity in this system, and He_2 vibration couples strongly to it, this accounts for the greater effectiveness of He_2 vibration in promoting reactivity than OH vibration.

3) Translational energy is transferred to the rotational degrees of freedom of each molecule. There is greater propensity for the transfer of translation to OH rotation than He_2 rotation. This is illustrated by examining the rotational cross sections for both molecules as a function of temperature. The rotational cross sections in $bohr^2$ as a function of final rotational quantum number for various values of the translational temperature are plotted for H_2 in Fig. 1 and for OH in Fig. 2. For H_2, as the temperature is increased, the cross sections for lower final rotational states decrease while those for higher final rotational states increase. The OH rotational cross sections exhibit a maximum with respect to final rotational

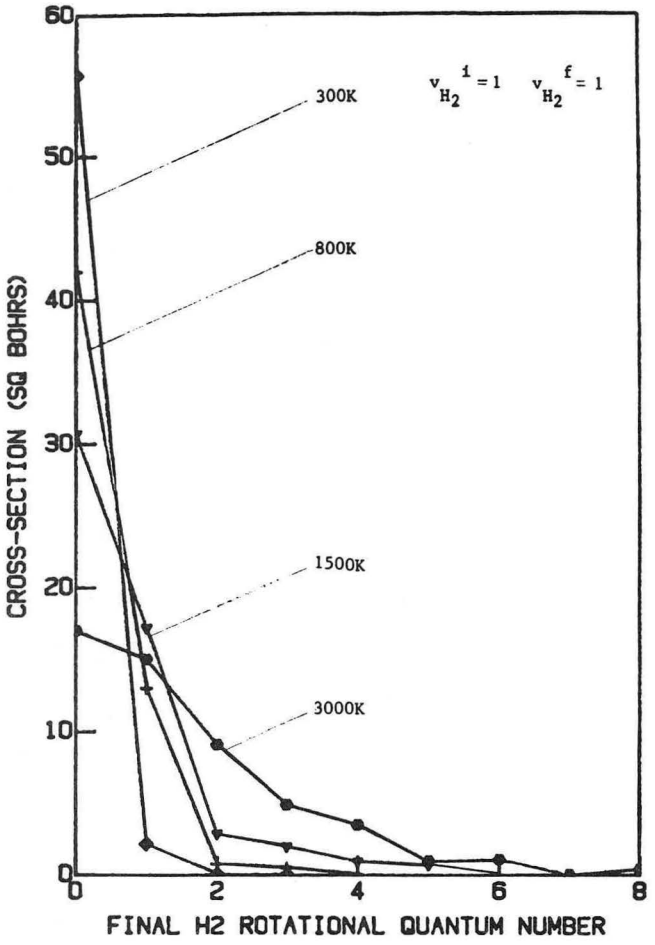

Figure 1. Rotational cross sections in bohr^2 for H_2 for no change in vibrational quantum number, as a function of H_2 final rotational quantum number for various values of the initial translational temperature in Kelvins. (XBL 863-994)

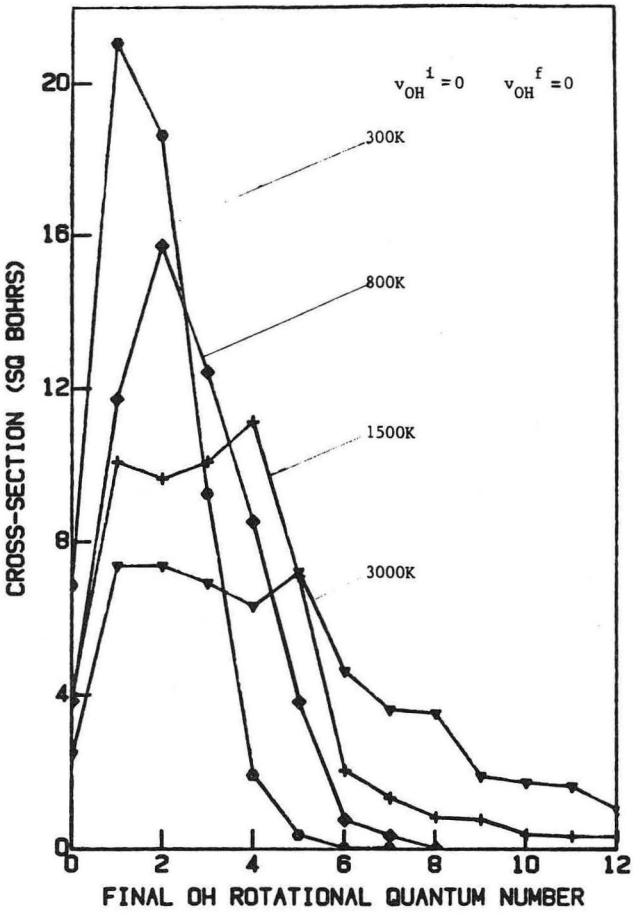

Figure 2. Rotational cross sections in bohr^2 for OH for no change in vibrational quantum number, as a function of OH final rotational quantum number for various values of the initial translational temperature in Kelvins. (XBL 863-993)

quantum number, the particular final rotational state associated with the maximum increases with temperature, and the number of cross sections with values close to the maximum value increases with temperature. The contrasting behavior of the He_2 and OH cross sections is a manifestation of the OH rotational degrees of freedom being more strongly coupled to the translational degree of freedom than H_2, since OH has a more asymmetric force field and is thus more amenable to rotational energy transfer.

4) Energy transfer does not depend strongly on the initial angular momentum in either molecule, which is consistent with our interpretation of the dependence of reactivity on reagent angular momentum.

5) Vibrational energy is transferred to translation, to the rotational degrees of freedom of the same molecule, and to the rotational and vibrational degrees of freedom of the other molecule. The OH molecule does not transfer vibrational energy as effectively as H_2. The H_2 vibrational deactivation associated with the v = 1 to v = 0 transition as a function of temperature follows the Landau-Teller relationship.

In a collaborative study with Dr. James A. Miller and Carmine Parish of Sandia National Laboratory, thermal rate coefficients for the two reactions

$$O + HCN \rightarrow NCO + H \qquad (1)$$

and

$$O + HCN \rightarrow NH + CO \qquad (2)$$

have been predicted. The reactions between O and HCN are the most important reaction steps in the conversion of fuel nitrogen to nitric oxide in

combustion systems. In our study of these reactions, we determined thermal rate coefficients suitable for comparison with experiment for various levels of theoretical approximations. Common to all treatments are the approximations that: 1) the Melius-Binkley calculations of the potential surface parameters using the BAC-MP4 technique provide suitable values of the transition state energies, frequencies, and geometries; 2) the RRKM or strong collision assumption is valid; and 3) the transition state approximation of no recrossing of the transition state dividing surface is valid. The various levels of theoretical approximation employed, each resulting in a thermal rate coefficient, were: 1) canonical theory, CT; 2) canonical theory with a Wigner tunneling correction, CTW; 3) microcanonical theory, MT; 4) microcanonical theory with angular momentum conservation, MJT; and 5) microcanonical theory with angular momentum conservation with one-dimensional tunneling, MJT-T. Barrier heights determined with the BAC-MP4 theory were also varied within the range of the stated error limits.

The reaction path was complex since the net reaction can take place on either of two potential energy surfaces, and both reactions involve the formation and destruction of intermediate complexes. The general formalism developed for obtaining thermal rate coefficients and the branching ratio, ($k_2/k_1 + k_2$), over a range of temperatures should be applicable to several reactive systems. Our theoretical results for the thermal rate coefficients determined using the basic BAC-MP4 parameters and modified parameters are compared with the experimental values of Perry and Melius,[4] Davies and Thrush,[5] and Lohr and Roth.[6] Figure 3 is an Arrhenius plot of the theoretically- and experimentally-determined rate coefficients over a range of temperatures. At high temperatures the available experimental results are predicted accurately by even the crudest theoretical treatment (CT), although the branching ratio predicted by theory is somewhat lower than the 20 to 30% determined experimentally. At lower temperatures the theoretical predictions using the basic BAC-MP4 parameters are too low. Adjustments of the BAC-MP4 barriers to values within their stated error limits lead to satisfactory agreement over the entire temperature range where experimental results are available (500 to 2500 K). The most important results of the investigation concern the dependence of the predictions on the level of approximation. At high temperatures, the rate coefficients calculated for reactions (1) and (2) are independent on the level of approximation. At low temperatures, the total rate coefficient, $k_1 + k_2$, which is dominated by k_1, is also relatively independent of the level of approximation,

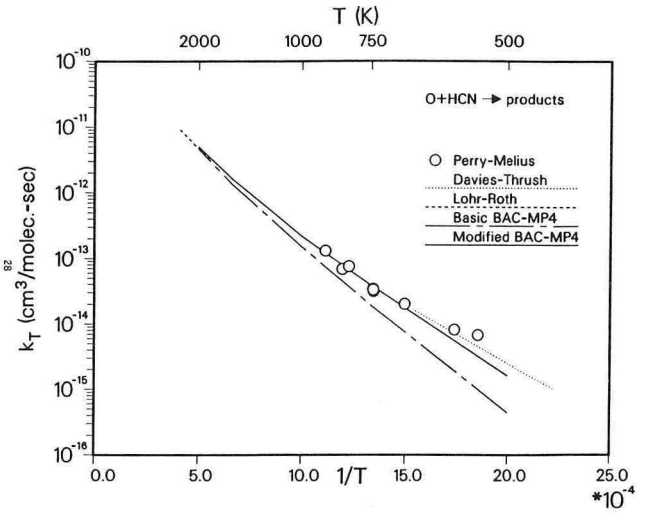

Figure 3. An Arrhenius plot (log k versus 1/T) of the theoretical predictions and experimental values of the thermal rate coefficient for the O + HCN reaction. (XBL 863-991)

and the branching ratio depends strongly on tunneling and on energy and angular momentum conservation. Each successive refinement in the theory produces larger values of k_2. The details of the theoretical treatments and the consequences of these are described in a paper[7] which summarizes the research.

The recent availability of high energy ultraviolet lasers provides new opportunities to study ignition. These lasers produce sufficient photons to initiate combustion by photolysis, and they place reactants in well-defined initial states in a much shorter time (approximately 20 ns) than that required for many chemical reactions important in combustion. We have studied ignition initiated by ozone photolysis at 248 nm using a Lamda Physik 200 EMG KrF excimer laser as a light source.

The ignition of ozone/fuel/oxygen mixtures in a constant volume cell was investigated using H_2, CH_4, and C_3H_8 as fuels. Ozone, the only significant absorber in this system, is photolyzed and produces oxygen atoms which initiate combustion. Light was focussed into heated and unheated aluminum cells with optical windows by MgF_2 or UV grade lenses of various focal lengths. Laser outputs were measured with a Gentec ED-500 joulemeter, and in typical experiments 350 to 400 mJ of light entered the reaction cell. Ozone was produced by passing oxygen through two thermo electron ozinators in series and trapped on silica gel cooled to dry ice-isopropanol mixtures. Ozone concentration in the reaction cell was monitored immediately before laser photolysis

by absorption using a deuterium lamp/monochromator/photomultiplier assembly. Initial gas pressures, measured with an MKS baratron, were in the range of 20 to 200 torr. Transient pressure measurements were made with a Kistler 211B piezotron flush-mounted in the cell wall, and a DEC/CAMAC microcomputer controlled timing and recorded the pressure data as previously described.[8] Spark schlieren photography was used to visualize the absorption and combustion events. Photographs were obtained using two 1.0 m focal length lenses and a knife edge stop, arranged in a U-shape because of space limitations.

A discretized, time-dependent absorption model was used to predict the spatial dependence of oxygen atoms produced by photolysis of ozone by focussed light. Modelling studies of constant volume hydrogen/oxygen/ozone combustion were performed using the CHEMKIN code with an appropriate driver routine. The appropriate conservation equations were solved to determine temperature, pressure, and species concentrations as a function of time. Induction time, defined as the time for the temperature to achieve one-half its total increase, was also computed. The model was verified for reliability by demonstrating concurrence with computational and experimental studies of ignition reported in the literature.[9]

Variation of the ozone partial pressure was the primary method for establishing ignition conditions. Combustion was confirmed by visual observation, pressure rise, and the appearance of water on the cell windows. Figure 4 is a plot of pressure versus time recorded for two ignition events in hydrogen/oxygen/ozone mixtures. Ignition occurs near the lens focus for the top trace and at the cell window for the bottom trace. The laser is fired at the time denoted by the arrow.

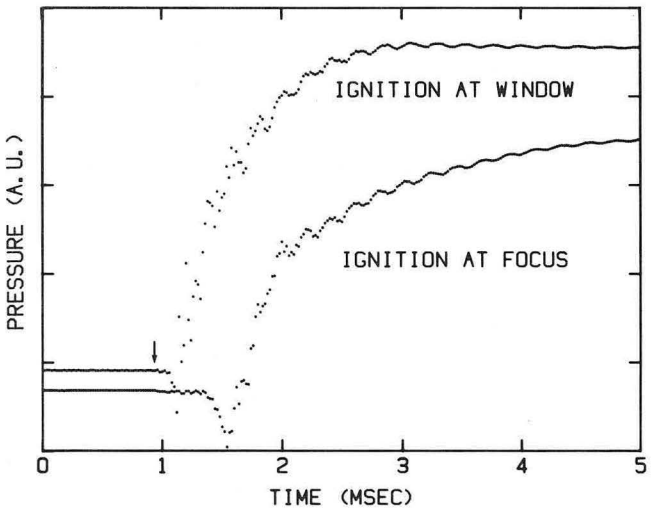

Figure 4. Pressure (arbitrary units) in laser ignited mixtures of hydrogen/oxygen/ozone as a function of time (msec). Ignition occurs near the focus for the top trace and at the window for the bottom trace. The laser is fired at the time denoted by the arrow. (XBL 861-31)

The use of a discretized, time-dependent Beer's Law model showed that photochemical ignition is sensitive to laser power, focal length of the lens, separation distance between the cell and lens, and ozone concentration, and that each of these factors affects the concentration of radicals available to initiate combustion. The system was quite sensitive to changing the initial ozone pressure, with a change of less than 4% in the partial pressure of ozone sufficient to change a no-burn case into a repeatable combustion event. The comparison of spark schlieren photographs, used to visualize ignition events and identify ignition sites with calculated radical concentrations, showed that absorption is a single photon process. The effects of equivalence ratio, pressure, and initial gas temperature were investigated, and temperature was the only variable having a significant effect. The modelling studies showed that ignition is not due entirely to thermal effects but is strongly dependent on the number and type of radicals present initially after photolysis. Hydrogen was the easiest fuel to ignite and methane was the least. The more specific results of the study are described in a paper recently submitted for publication.[10]

PLANNED ACTIVITIES FOR FY 1986

Energy transfer studies of H_2 + OH collisions will be completed. Isotope effects will be considered in both reactive and non-reactive collisions. Rate coefficient calculations for the $H_2 + OH \rightarrow H_2O + H$ reaction using a full Monte Carlo treatment of averaging over initial energy states will be completed and compared with those obtained using statistical theories. Isotope effects on reactivity will also be determined. Modelling studies of ignition will be continued for simple fuels. A new study utilizing and extending a statistical theory for the treatment of unimolecular reactions which occur along a reaction path with no barrier (loose transition state) will be initiated. Fabrication of a new molecular beam-mass spectrometer with a constant volume cell to support homogeneous combustion and a discharge flow reactor will be completed. This system will have the capability of monitoring combustion and reactivity on the microsecond time scale.

REFERENCES

1. Rashed, O. and Brown, N.J. (1985), "A Molecular Dynamics Study of the Reaction H_2 + OH → H_2O + H," *J. Chem. Phys. 82*, p. 5506.
2. Schatz, G.C. and Elgersma, H. (1980), "A Quasi-Classical Trajectory Study of Product Vibrational Distributions in the OH + H_2 → H_2O + H Reaction," *Chem. Phys. Lett. 73*, p. 21.
3. Walch, S.P. and Dunning, T.H. (1980), " A Theoretical Study of the Potential Energy Surface for OH + H_2," *J. Chem. Phys. 72*, p. 1303.
4. Perry, R.A. and Melius, C.F. (1985), "The Rate and Mechanism of the Reaction of HCN with Oxygen Atoms over the Temperature Range 540–900 K," *Twentieth Symposium (Int.) on Combustion,* p. 639.
5. Davies, P.B. and Thrush, B.A. (1968), *Trans. Faraday Soc. 64,*
6. Roth, P., Lohr, R., and Hermanns, H.D. (1980), *Ber. Bunsenges. Phys. Chem. 84*, p. 835.
7. Miller, J.A., Parrish, C., and Brown, N.J. (1985), "A Statistical-Theoretical Rate Coefficient and Branching Ratio for the Reaction O + HCN → Products," accepted for publication in *J. Phys. Chem.*
8. Lucas, D., Peterson, R., Brown, N.J., and Oppenheim, A.K. (1985), "Molecular Beam Mass Spectrometer Sampling of Flash Ignited Combustion," *Twentieth Symposium (Int.) on Combustion,* p. 1205.
9. Dixon-Lewis, G. and Williams, D.J. (1977), "The Oxidation of Hydrogen and Carbon Monoxide," in *Comprehensive Chemical Kinetics,* Bamford and Tipper, Eds., Elsevier Scientific, Amsterdam, p. 1.
10. Lucas, D, Dunn-Rankin, D., Hom, K., and Brown, N.J. (1986), "Ignition by Excimer Laser Photolysis of Ozone," submitted to the *Twenty-First Symposium (Int.) on Combustion,* LBL-20871.

The Interaction of a Laminar Flame with its Self-Generated Flow During Constant Volume Combustion*

D. Dunn-Rankin and R.F. Sawyer

Flame propagation in tubes has been a subject of combustion research for more than a century,[1] and the formation of "tulip" flames during combustion in closed tubes has been recorded for nearly sixty years.[2–7] However, the cause of the tulip flame has eluded researchers. An example of the tulip flame phenomenon is shown in Fig. 1. The photograph is a sequence of frames extracted from a high-speed schlieren movie of a stoichiometric methane/air flame propagating in a closed rectangular duct (38 mm × 38 mm × 155 mm). The flame is initiated by a point igniter near one endwall of the combustion vessel. The tulip flame phenomenon is relatively insensitive to tube cross-section geometry, combustible mixture composition, and ignition source geometry.[7] Detailed descriptions of the development of tulip flames for many different experimental conditions are in the references mentioned above.

ACCOMPLISHMENTS DURING FY 1985

Historically, the tulip flame phenomenon has been attributed to a flame/pressure wave interaction,[3] or a flame instability.[8] Recently, however, the authors have used laser Doppler anemometry (LDA) to explore the possible role of combustion generated flow in tulip flame formation.[9] The present study extends the earlier exploratory work by providing a complete mapping of the flow field during the "tulip" formation. LDA measurements of the fluid velocity near the flame front suggest a fluid mechanical explanation for the formation of tulip flames.

The experimental apparatus (Fig. 2) consists of a laser Doppler anemometer, a high-speed schlieren cinematographic system, a closed combustion vessel, a spark ignition source, a gas mixing device, and a data-logging computer. A detailed description of the experimental apparatus and methodology can be found in an earlier report.[10]

The time history of the experimentally determined vector velocity field during the flame propagation is shown in Figs. 3a and b. The vectors with a dot at their origin represent negative velocity. The

*This work was supported by the Assistant Secretary for Conservation and Renewable Energy, Office of Energy Utilization Research of the U.S. Department of Energy under Contract No. DE-AC03-76SF00098.

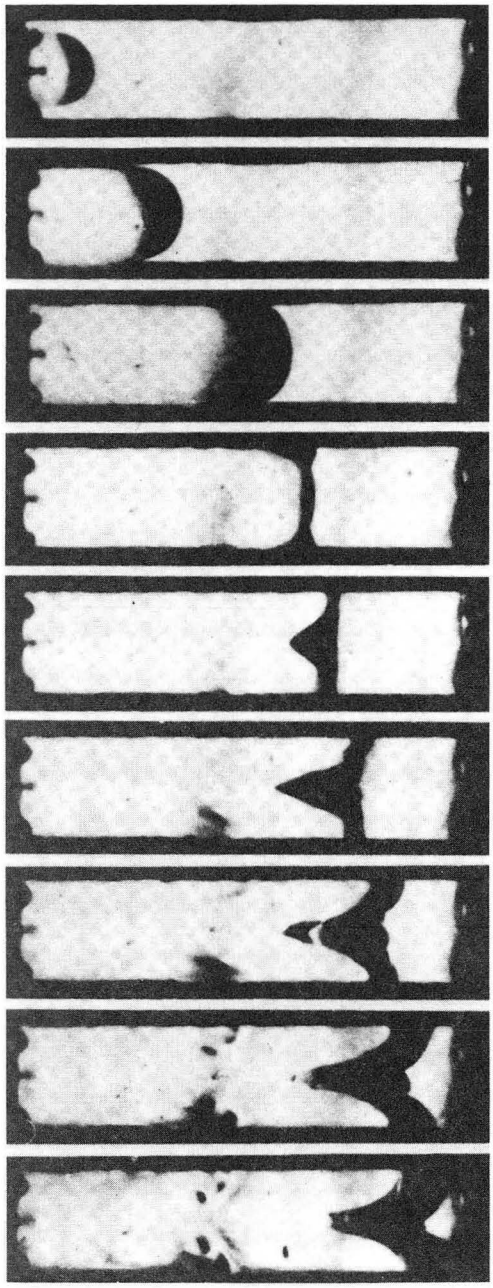

Figure 1. An example of the "tulip" flame formation. Stoichiometric methane/air flame initiated by a spark. Square cross-section vessel (38 mm × 38 mm × 155 mm). (XBB 866-4892)

flow field is assumed to have cylindrical symmetry except in the corners of the chamber. Individual frames from a high-speed schlieren movie of the flame propagation indicate the flame shape and location, and the solid line in the vector plots represents the flame location determined from LDA data rate reduction.

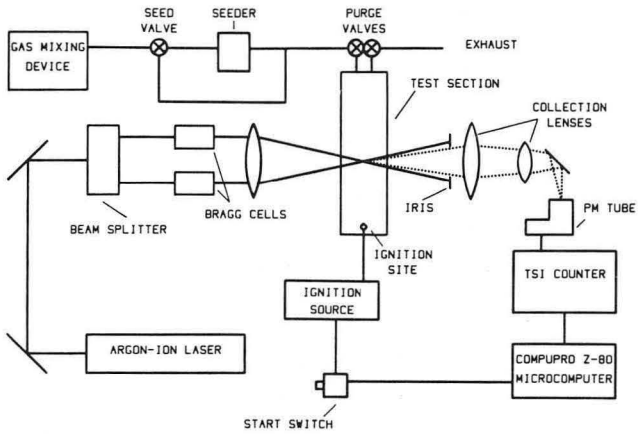

Figure 2. Schematic of experimental apparatus. (XBL 866-2379)

While the flame is convex toward the unburned gas ($t < 15$ ms), the entire flow field is positive. However, by the time the flame flattens ($t = 20$ ms), the burned gas flow field is entirely negative. At the same time, the unburned gas velocity has dropped to a very small, almost constant value. Previous studies have indicated that the decrease in unburned gas velocity is due primarily to a decrease in flame area.[10] The reversal of the direction of the burned gas motion and the decrease in unburned gas velocity occur very rapidly, which suggests that the "tulip" transition is a very rapid process. As the "tulip" continues to grow ($t > 25$ ms), a stagnation region develops in the burned gas behind the vertex of the tulip cusp. Furthermore, a small reverse flow appears in the unburned gas just within the confines of the tulip. This flow pattern and the tulip flame shape persist for the remainder of the combustion process, which indicates that the tulip configuration is a relatively stable flame shape in closed tube combustion.

PLANNED ACTIVITIES FOR FY 1986

Experimental observations will be compared with a theoretical model to identify and confirm the processes which control the flame folding process. The significance of combustion generated flow in engines will be investigated.

REFERENCES

1. Mallard, E. and LeChatlier, H. (1883), "Recherches Experimentales et Theoriques sur la Combustion des Melanges Gazeux Explosifs," *Annales Des Mines 8,* Series 4, p. 274 (in French).

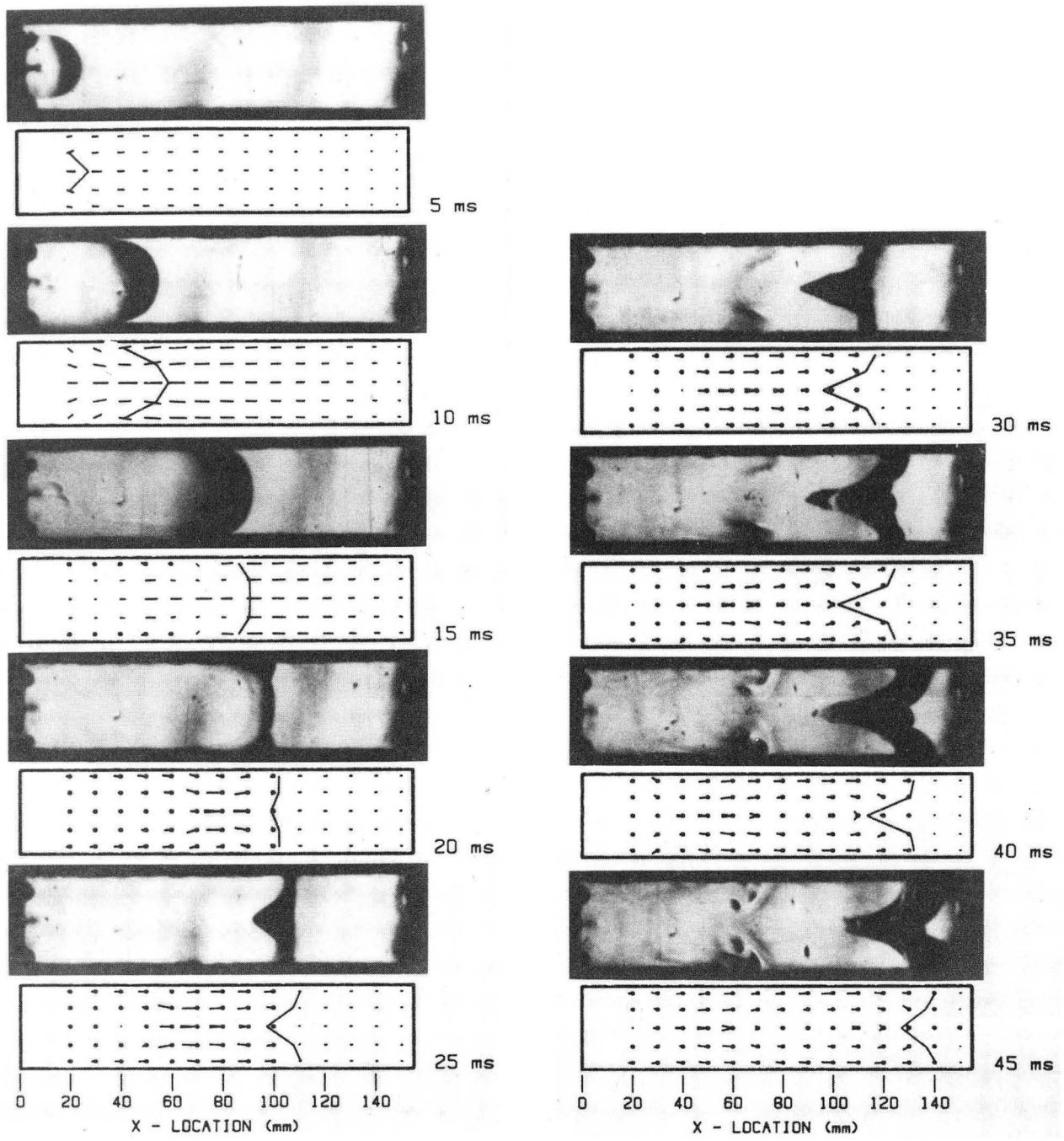

Figure 3. (a) Vector velocity field and flame shape during constant volume combustion. (b) Vector velocity field and flame shape during constant volume combustion. Stoichiometric methane/air flame. |(a) XBB 856-4521, (b) XBB 856-4522|

2. Ellis, O.C. de C. (1928), "Flame Movement in Gaseous Explosive Mixtures (Part 7)," *Fuel; a journal of fuel science 7,* p. 502.
3. Guenoche, H. (1964), "Flame Propagation in Tubes and Closed Vessels," in *Non-Steady Flame Propagation,* G.H. Markstein, Ed., Pergamon Press, New York.
4. Smith, O.I. (1977), "Lean Limit Combustion in an Expanding Chamber," LBL-6851; Ph.D. Thesis, College of Engineering, University of California, Berkeley.
5. Steinert, W.J., Dunn-Rankin, D., and Sawyer, R.F. (1982), "Influence of Chamber Length and Equivalence Ratio on Flame Propagation in a Constant Volume Duct," Western States Section/The Combustion Institute Paper No. 82-52; LBL-14965.
6. Wakai, K. and Shimizu, S. (1984), "Behavior of the Flame in a Closed Chamber," *Proceedings of JSME, 840-14* (October), p. 87 (In Japanese).
7. Dunn-Rankin, D. (1985), "The Interaction Between a Laminar Flame and Its Self-Generated Flow," LBL-19582; Ph.D. Thesis, College of Engineering, University of California, Berkeley.
8. Strehlow, R.A. (1984), *Combustion Fundmentals,* McGraw Hill, New York.
9. Dunn-Rankin, D., Cheng, R.K., and Sawyer, R.F. (1984), "LDA Study of Non-Steady Flame Propagation in a Constant Volume Duct," presented at the Second International Symposium on Applications of Laser Doppler Anemometry to Fluid Mechanics, July 2–4, Lisbon, Portugal; LBL-18150.
10. Dunn-Rankin, D. and Sawyer, R.F. (1985), "LDA Study of the Unburned Gas Motion Induced by Non-Steady Flame Propagation in a Constant Volume Duct," submitted to Joint Western-Central States Section/The Combustion Institute meeting, March 21–23, San Antonio, Texas. In preparation.

Compression Ignition of Coal Slurry Fuels*

D.D. Brehob and R.F. Sawyer

Most of the work on coal-fired diesel engines before 1945 was conducted by German industry using coal dust; see the review by Soehngen.[1] However, since that time most coal fueled diesel research and development has used coal slurries: various percentages of coal in oil, water, methanol, ethanol, or mixtures of the liquid carriers. The existing fuel storage and transportation infrastructure for diesel engines is designed for liquids. Thus, conversion to slurry usage would present fewer difficulties compared to pulverized coal. Coal slurries compared to dust give advantages in the areas of fuel handling, safety, and fuel injection control and reliability, with slight cost disadvantages and an ignitability disadvantage for coal/water slurry only. Coal slurried with water, methanol, and diesel No. 2 are the test fuels for this study. The slurries are evaluated using a 900 rpm, direct injection, square piston engine simulator (Fig. 1) operating for one combustion cycle per experiment.

A comprehensive summary of published work on diesel engine combustion of coal slurries is contained in the thesis by Brehob,[2] which extends an earlier review by Caton and Rosegay.[3] The engine tests described provide valuable information concerning engine modifications to enhance slurry combustion and to improve engine and injection system performance with slurries. The constant volume bomb studies of Siebers and Dyer[4] and the computer model studies of Bell and Caton[5] provide more fundamental information on coal slurry combustion under diesel engine conditions. Detailed information about the ignition characteristics of coal slurries under compression ignition conditions is not available currently. The objectives of this study are: 1) to establish engine conditions required for slurry combustion, and 2) to determine ignition delay characteristics of the three coal slurries tested.

*This work was supported by the Assistant Secretary for Conservation and Renewable Energy, Office of Advanced Energy Conversion Systems, Heat Engines Program of the U.S. Department of Energy under Contract No. DE-AC03-76SF00098.

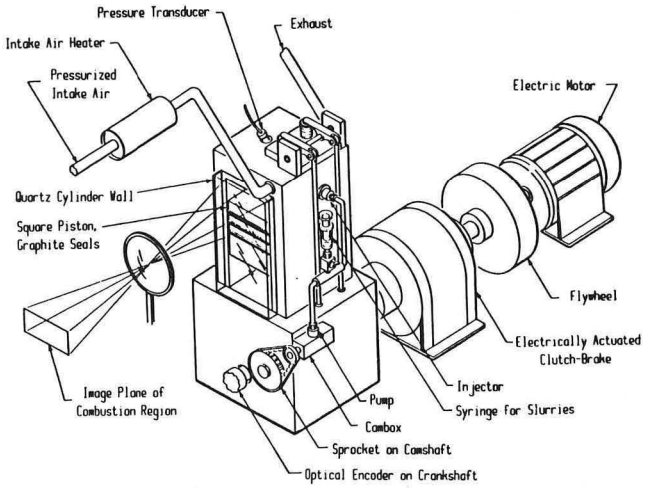

Figure 1. Square piston engine simulator. (XBL 8412-5422A)

ACCOMPLISHMENTS DURING FY 1985

Conditions for Ignition of Fuels

The longest ignition delays measured in the square piston engine simulator at 900 rpm are less than 10 msec (54 CAD) (crank angle degree). For injection at about 20° BTDC (before top dead center), ignition occurs as late as 35° ATDC (after top dead center). After this CAD, the lower temperatures and pressures from expansion do not permit substantial chemical activity. Ignition at 35° ATDC is not of practical significance; it does, however, provide information concerning the ignition characteristics of the fuels.

Neither pressure rise nor light emission is observed when injecting coal/water slurry into the maximum temperature and pressure conditions attainable in the square piston engine simulator in the current configuration: i.e., up to 22:1 CR (compression ratio), 150°C block temperature, and 250°C inlet temperature at IVC (intake valve closing). Thus, coal/water slurry does not compression ignite when injected into air at up to 1150 K and 52 atm in the nearly 10 msec available.

Henein and Elias[6] discuss using inlet air preheated to extend the cetane scale. Following the approach of Henein and Elias, to evaluate diesel No. 2, methanol, coal/oil, and coal/methanol slurries, the inlet air temperature is increased at constant injection timing until ignition is obtained. The measured minimum temperatures required for combustion at 16:1 CR (approximately 30 atm pressure for the injection timing of 20° BTDC) are:

Fuel	Temperature at IVC (K)	Temperature at injection (K)
Diesel No. 2	320	675
Coal/diesel	325	685
Methanol	450	825
Coal/methanol	360	725

The temperatures above are approximate due to the uncertainties in measurement and the unrepeatable nature of ignition near the limiting temperature.

The temperatures for coal/diesel ignition are nearly the same as those for diesel No. 2. Coal/methanol and methanol fuels both require higher temperatures than diesel fuel for ignition as expected due to the low cetane number of methanol. However, coal/methanol ignites at temperatures well below those required for neat methanol.

The autoignition of coal/methanol slurry at lower temperatures than neat methanol is due to either the coal or the additive package in the slurry. As mentioned above, coal addition to the liquid carrier increases the viscosity dramatically, causing the injected fuel droplets to be larger than with neat liquid fuel as shown in Fig. 2. Thus, any physical

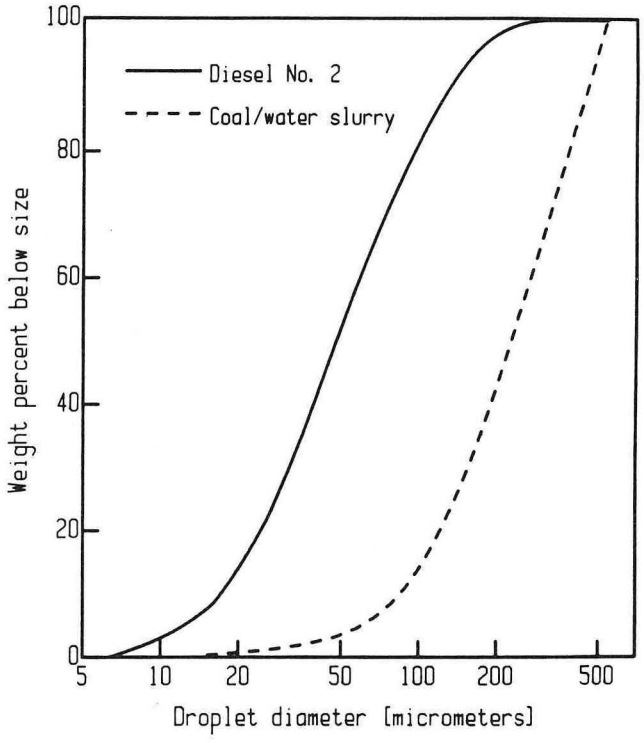

Figure 2. Fuel droplet size distributions for diesel No. 2 and coal/water slurry, from Nelson, *et al.*[7] (XBL 866-2377)

effect of the coal on the autoignition is most probably detrimental.

To investigate any chemical effects that the presence of coal might have on ignition, the volatile fraction must be characterized. Thurgood and Smoot[8] summarize data from 24 experiments in which the gaseous coal pyrolysis products are measured. Twenty of the reported experiments are conducted at rapid heating rates, i.e., greater than 10^4 K/sec. The products of devolatilization depend on coal type, heating rate, final temperature, and other factors. But average values of the components are: 3% CO_2, 15% CO, 53% H_2, 14% CH_4, 10% C_2H_6, and 5% of other C_2 molecules. The final temperatures of the coal in these experiments is 1000 K or higher. The fuel at the periphery of the spray cone injected into the square piston engine simulator experiences very high heating rates: on the order of 10^5 K/sec. However, when the coal/methanol is injected into 725 K air, the final fuel droplet temperature is below the maximum 800 K of the gas. This is significantly below the 1000 K reported by Thurgood and Smoot. Kimber and Gray[9] report that at 1050 K final temperature and a reaction time of 70 msec, less than 25% of the coal's volatile matter is removed. Therefore, it is unlikely that enough combustible gas is devolatilized during the approximately 5 msec before ignition. The more plausible explanation for the autoignition characteristics of coal/methanol is that the additive package contains chemicals that ignite more readily than methanol.

Ignition Delay

The end of the ignition delay is measured in two ways: emission of light from combustion and pressure rise compared to the motoring trace. The amount of light emitted from methanol combustion is much less than that emitted from the other fuels. To obtain adequate sensitivity from the photodiode, the gain is raised by a factor of five for methanol tests. At this high gain with engine block heating, the photodetector senses the infrared radiation from warm combustion chamber surfaces, giving erroneous ignition readings. Thus, only the pressure rise determination at start of combustion is used for methanol.

The diesel No. 2, methanol, coal/oil slurry, and coal/methanol slurry pressure delay results are shown in Fig. 3. Luminosity delay measurements are shown in Fig. 4 for the above fuels except for methanol. The following differences are significant at the 90% confidence level:

1) Coal/diesel has a lower activation temperature than diesel No. 2, coal/methanol, and

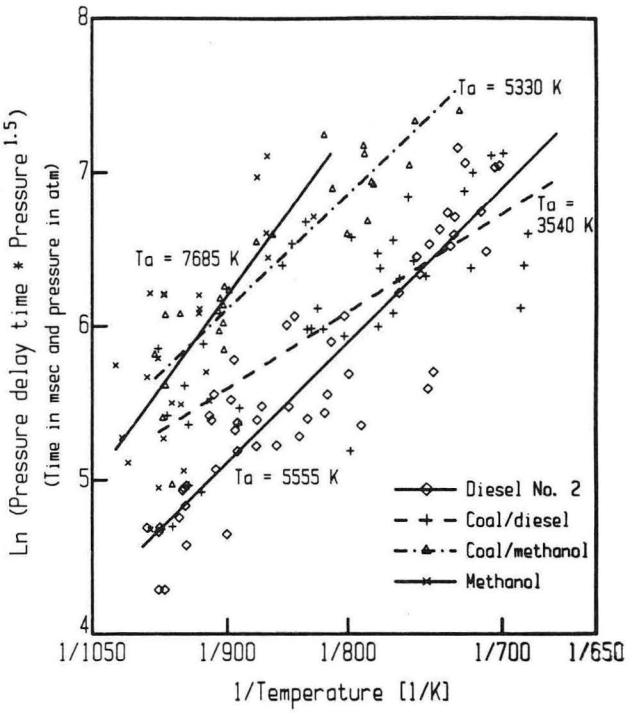

Figure 3. Temperature dependence of pressure defined ignition delay with pressure dependence to the 1.5 power for diesel No. 2, coal/diesel slurry, methanol, and coal/methanol slurry fuels in the square piston engine simulator. (XBL 866-2375)

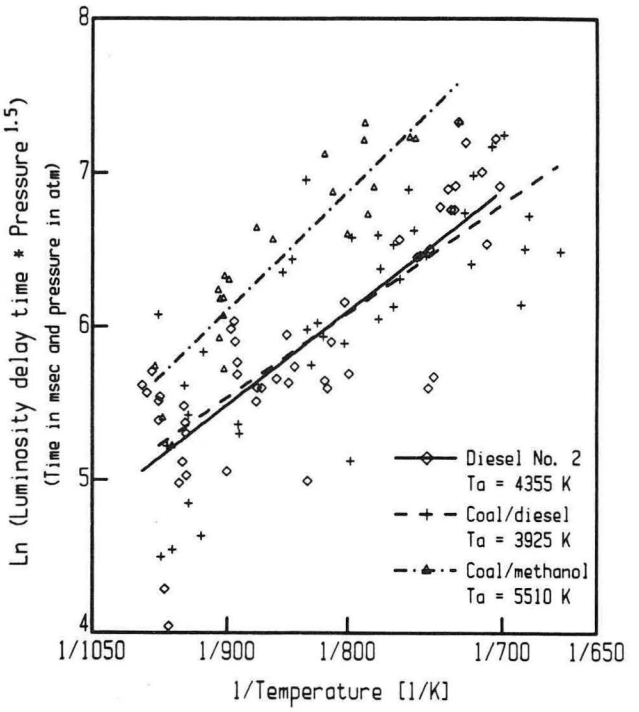

Figure 4. Temperature dependence of luminosity defined delay period with pressure dependence to the 1.5 power for diesel No. 2, coal/diesel slurry, and coal/methanol slurry in the square piston engine simulator. (XBL 866-2376)

methanol fuels by the pressure delay measurement.

2) Coal/diesel slurry has a lower activation temperature than coal/methanol when considering the luminosity delay.

No differences between the luminosity delay and pressure delay results are found within the measurement precision of these tests.

In both the luminosity and pressure delay analyses, the activation temperature for the coal slurry is lower than the neat fuel alone. The ignition delay interval is comprised of overlapping physical and chemical periods. El Wakil, *et al.*[10] present calculated physical delay times for a 20 micrometer decane droplet. They also report that physical delay times are proportional to the droplet diameter to the 1.75 power. From their findings, Fig. 5 is constructed. From Fig. 2, 10% of the mass of diesel fuel droplets is contained in droplets of less than 20 micrometers in diameter. In contrast, 10% of the mass of coal/oil droplets is found in 100 micrometers drop size or less. The physical delay for 20 micrometer droplets is almost negligible throughout the temperature range. However, at 100 micrometers, the physical delay interval is a sizable portion of the total delay period. Temperature plays a lesser role in determining the physical delay period than droplet diameter. Therefore, the lower T_a of coal/oil and coal/methanol slurry compared to the neat fuels may be due to a relatively long physical delay interval which is less sensitive to temperature than the chemical delay.

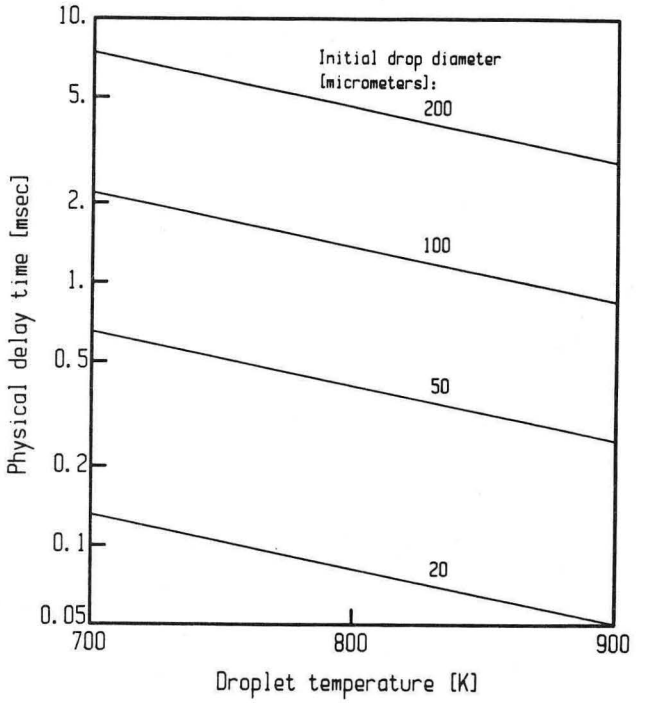

Figure 5. Physical delay time for decane droplets at varying droplet temperatures with drop diameter as a parameter. (Data taken from Fig. 7 of paper by El Wakil, *et al.*[10]). (XBL 866-2378)

Conclusions

1. Coal/methanol slurry ignites at significantly lower inlet temperatures than neat methanol: 360 K versus 450 K.
2. Coal/water slurry does not compression ignite at the conditions attainable in the square piston engine simulator.
3. Methanol compression ignition combustion emits low levels of light, making accurate luminosity delay measurements difficult.
4. The activation temperatures for the test fuels are:

Fuel	T_a (Lum) (K)	T_a (Pres) (K)
Diesel No. 2	4360	5560
Coal/diesel	3925	3540
Methanol	7685	—
Coal/methanol	5510	5330

   The activation temperature for coal/diesel is lower than diesel and coal/methanol based on the pressure delay at the 90% confidence level.
5. The pressure and luminosity delay intervals are not different within the precision of the measurements in the square piston engine simulator.

PLANNED ACTIVITIES FOR FY 1986

This research has concluded and no further activities are planned.

REFERENCES

1. Soehngen, E.E. (1976), *Development of Coal-Burning Diesel Engines in Germany,* U.S. ERDA Report FE/WAPO/3387-1.

2. Brehob, D.D. (1985), *Compression Ignition Characteristics of Coal Slurries,* Ph.D. Thesis, University of California, Berkeley.
3. Caton, J.A. and Rosegay, K.H. (1983), "A Review and Comparison of Reciprocating Engine Operation Using Solid Fuels," SAE Paper 831362.
4. Siebers, D.L. and Dyer, T.M. (1985), "The Autoignition and Combustion of Coal-Water Slurry under Simulated Diesel Engine Conditions," ASME Paper 85-DGP-15.
5. Bell, S.R. and Caton, J.A. (1985), "Analytical Evaluations of Ignition Options for a Coal/Water Slurry Fueled Engine," Fall Meeting of the American Flame Research Committee, Livermore, CA, October 1985.
6. Henein, N.A. and Elias, N.Y. (1978), *SAE Transactions 87,* p. 2470.
7. Nelson, L.P., Seeker, W.R., and Zimperman, R.A. (1985), "The Atomization, Ignition, and Combustion Characteristics of Coal Slurry Fuels in Medium-Speed Diesel Engines," Paper 3-1A, presented at the Joint Technical Meeting of the Central and Western States Sections of the Combustion Institute, San Antonio, Texas, May, 1985.
8. Thurgood, J.R. and Smoot, L.D. (1979), *Pulverized-Coal Combustion and Gasification,* L.D. Smoot and D.T. Pratt, Eds., Plenum Press, p. 169.
9. Kimber, G.M. and Gray, M.D. (1967), *Combustion and Flame 11,* p. 260.
10. El Wakil, M.M., Myers, P.S., and Uyehara, O.A. (1956), *SAE Transactions 64,* p. 713.

Controlled Combustion*

N.J. Brown, J.A. Cavolowsky, C.F. Edwards, K. Hom, D. Lucas, A.K. Oppenheim, T.E. Parker, D.A. Rotman, R.F. Sawyer, and H.E. Stewart

The main purpose of the program is to acquire knowledge of the chemical and physical process that govern the evolution of exothermic energy in combustion systems and the effects of its deposition in the reacting medium. Basic problems one faces in this connection and the methodology adopted for their solution were described in the FY 1982 annual report.[1] The concepts put forth there were formulated comprehensively in a treatise on the Dynamic Features of Combustion published recently in the *Philosophical Transactions of the Royal Society.*[2] In current studies, particular emphasis was placed on further development of the molecular-beam mass-spectrometer technique in the measurement of the temperature profile with the concomitant life history of selected radicals as an indicator of the role they play in the initiation of the combustion process—a preamble to revealing their action in the control mechanism. In parallel to this effort, we continued our studies, carried out primarily by numerical analysis, of the fluid mechanical phenomena of turbulent flow under the influence of the exothermic energy deposition in the field.

ACCOMPLISHMENTS DURING FY 1985

Advances made last year pertain to the following three phases of our program:

1. Molecular beam sampling of plasma jets,
2. Shock tube and laser imaging apparatus,
3. Numerical analysis of the aero-thermo-chemico-dynamic features of combustion fields.

Progress made in each of them is reported here.

Molecular Beam Spectrometry

Possible effects of interaction between the plume and the sampling cone were investigated using laser schlieren photography.[3] According to our observations, in early stages the presence of the cone has negligible effect, and the plume front is not slowed by its presence in the field. At later times, when the front has advanced well past the cone, significant differences were quite evident. However, they were located primarily in the portion of the plume past the cone, whereas the sampled gas did not appear to be disturbed by the deflection of the plume occurring downstream of the sampling tip.

Temperatures in the plume were measured by means of a time-of-flight (TOF) technique we developed and verified previously.[4] Maximum tem-

*This work was supported by the Office of Energy Research, Basic Energy Science, Engineering, and Geosciences Division of the U.S. Department of Energy under Contract No. DE-AC03-76SF00098 and by the National Science Foundation under Grant CPE-8115163.

perature as high as 50,000 K was recorded 2 mm from the igniter, dropping to 2900 K at 4 mm and 1670 K at 8 mm.

Using continuous sampling, concentration of N atoms in the plume was measured as a function of time and distance from the igniter. Atom signals were averaged, normalized, and converted to mole fractions using ionization cross sections available in the literature. These results, displayed here in Fig. 1, represent the first direct measurement of radical species in a pulsed plasma jet igniter. As it was thus established, at the shortest separation distance of 2 mm the maximum concentration reached a maximum of 5%. Thereafter peak values dropped rapidly and smoothly to the practically undetectable level at a distance of about 14 mm. The measurements were found to be in reasonable agreement with equilibrium values computed for the temperature profile we established earlier by the TOF technique.

Concomitantly with these experiments, we carried out an exploratory investigation of the mechanism of plasma ignition by schlieren photography, using our square-piston engine simulator,[5] and completed a thermo-chemical analysis that revealed the influence of a quasi-equilibrium radical pool in the course of a thermal ignition process.[6]

Shock Tube

The experimental spray ignition studies at conditions encountered in an adiabatic diesel engine, reported last year,[7] were handicapped by a severely restricted optical accessibility afforded by the apparatus we used that consisted of a stainless steel vessel located in a high temperature furnace. In order to ameliorate the situation, a 40-ft. long, 5-in. I.D. shock tube was designed and fabricated. Its installation in our laboratory is nearing completion. Displayed in Fig. 2 is the driver section with the diaphragm system and the control console in front. Fig. 3 shows the driven section, while the test section is presented in Fig. 4. Compressed air to be maintained by design in the latter for at least 20 milliseconds should be at a pressure of up to 25 atmospheres within a temperature range of 600 to 900 K.

The program of studies to be carried out by the use of this apparatus consists, in turn, of high speed schlieren photography, quantitative holography, and laser-induced fluorescence imagery.

Numerical Analysis

Following the publication of studies reported in the FY 1984 annual report,[8–11] a concentrated effort was made by the Principal Investigator to bring to focus advances in the knowledge on turbulent combustion achieved as a consequence of their contribution. The result was presented in the plenary lecture at the Tenth International Colloquium on Dynamics of Explosions and Reactive Systems held in Berkeley on August 3–9, 1985.[12] In a nutshell, this can be expressed in terms of the following ten conjectures:

1. At Reynolds numbers encountered in most combustion chambers, the turbulent flow field is dominated by a large scale vortex structure.

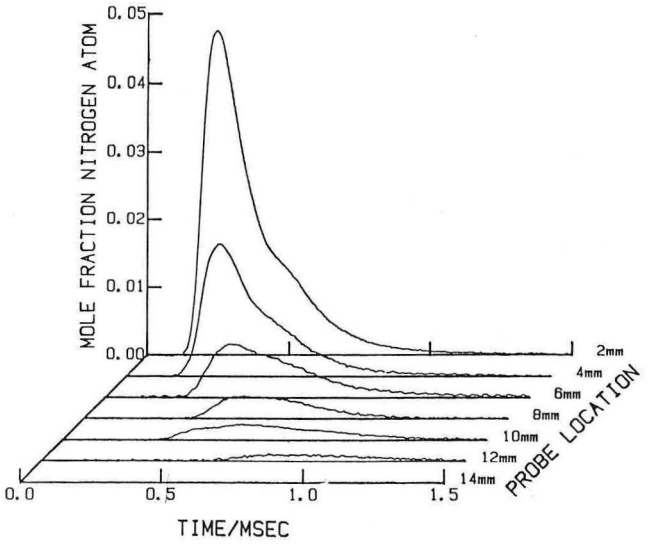

Figure 1. Nitrogen atom concentration as a function of time and distance from the injector tip. (XBL-862-673)

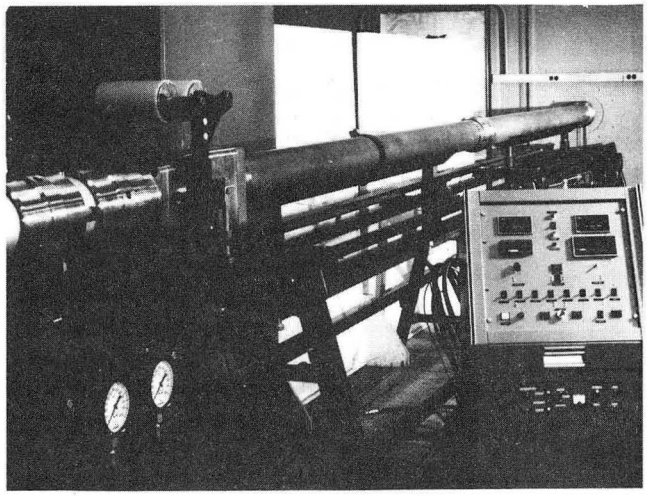

Figure 2. Shock tube driver section. (XBB 862-1156)

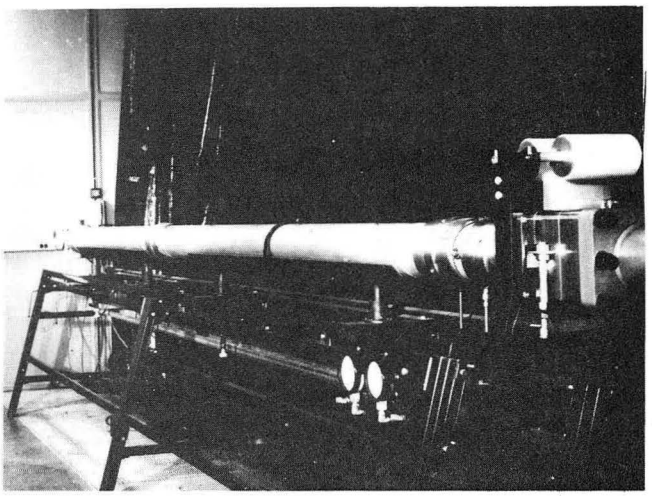

Figure 3. Shock tube driver section. (XBB 862-1157)

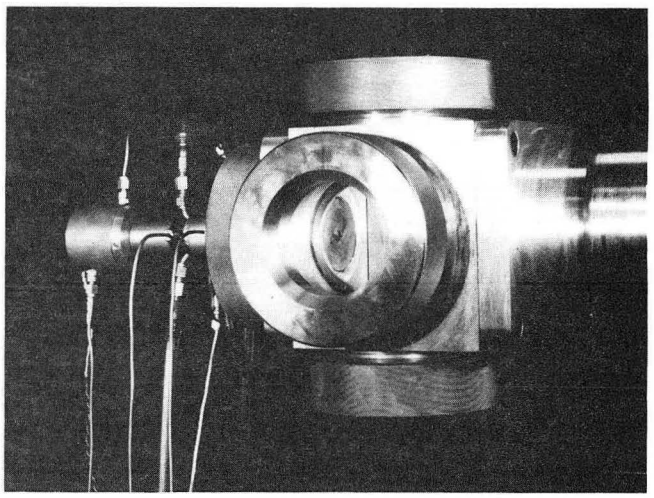

Figure 4. Shock tube test section. (XBB 862-1158)

2. In contrast to a laminar flame, turbulent flame front tends to be established along the particle path rather than across it.
3. Turbulent flame front is an interface—a contact boundary between the unburnt mixture and burnt gases incarcerated in the recirculation zone of a vortex, forming thus effectively its contour.
4. In general the flow field of the fresh mixture remains irrotational, whereas that of the burnt or burning gas is essentially rotational.
5. Although diffusion and reaction across the interface may be enhanced by local turbulence, the time of contact between unburnt and burnt gases is generally too short to attain steady state.
6. As a consequence, the interface forming the flame at the contour of a vortex encounters its subsequent neighbor before a diffusion-reaction wave can be fully developed, so that the process is completed within the recirculation zone.
7. Principal ports of entry for the unburnt mixture into the burnt gas regime are at the cusps between vortex contours.
8. Combustion is enhanced by both effects, the shortened contact time and the prolonged residence time, the former reducing diffusional losses while the latter enhances the progress of reaction.
9. Turbulent flow and combustion fields were treated at their threshold with inviscid flow, in direct contrast to the conventional approach concerned primarily with the intersection between laminar and turbulent flow regimes.
10. Our method of attack is of particular relevance to the technological aspects, while the conventional approach is of a more academic nature.

Of primary significance to the major purpose of our research program is the means we developed for ushering aerodynamics into the enclosure of a combustion chamber. A paper describing this achievement in the simplest possible case has been offered for presentation at the forthcoming Symposium (International) on Combustion to be held in Munich.[13] It concerns of highly idealized case of flame distortion, or stretch, taking place in the course of its propagation in a closed duct as a consequence of the flow field it created—the first time the controlling influence of a flow field generated by the combustion process in an enclosure has been revealed.

PLANNED ACTIVITIES FOR FY 1986

Continue measurements of concentration histories of chemical species involved in ignition of hydrocarbon-oxidizer mixtures and the concomitant temperature profiles by molecular beam mass spectroscopy.

Enhance the photographic study of the generation and formation of plasma jets by the use of the laser-powered high-speed schlieren system.

Develop further the numerical analysis of the aero-thermo-chemical-dynamic processes of combustion in enclosures with particular attention to those modeling conditions in internal combustion engines.

REFERENCES

1. Brown, N.J., *et al.* (1983), "Controlled Combustion," *Energy and Environment Division Annual Report*, FY 1982, LBL-15298, p. 4.
2. Oppenheim, A.K. (1985), "Dynamic Features of Combustion," *Phil. Trans. R. Soc. Lond. A 315*, p. 471.
3. Cavolowsky, J.A., Edwards, C.F., Oppenheim, A.K., and Lucas, D. (1986), "Pulsed Plasma Jet Igniters: Molecular Beam Measurements," *Combustion Science and Technology*, in press.
4. Lucas, D., Peterson, R., Brown, N.J., and Oppenheim, A.K. (1984), "Molecular Beam Mass Spectrometer Sampling of Flash-Ignited Combustion," *Twentieth Symposium (International) on Combustion*, The Combustion Institute, p. 1205.
5. Edwards, C.F., Stewart, H.E., and Oppenheim, A.K. (1985), "A Photographic Study of Plasma Ignition Systems," SAE Paper 850077, 10 pp.
6. Creighton, T.R. and Oppenheim, A.K. (1986), "Role of Radical Pool in Combustion," 10th International Colloquium on Dynamics of Explosives and Reactive Systems, *Progress of Astronautics and Aeronautics*, in press.
7. Parker, T.E., Forsha, M.D., Stewart, H.E., Hom, K., Sawyer, R.F., and Oppenheim, A.K. (1985), "Induction Period for Ignition of Fuel Sprays at High Temperatures and Pressures," SAE Paper 50087, 11 pp.
8. Brown, N.J., *et al.* (1985), "Controlled Combustion," *Applied Science Division Annual Report, FY 1984*, LBL-18754, p. 4.98.
9. Hsiao, C.-C., Ghoniem, A.F., Chorin, A.J., and Oppenheim, A.K. (1984), "Numerical Simulation of a Turbulent Flame Stabilized Behind a Rearward-Facing Step," *Twentieth Symposium (International) on Combustion*, The Combustion Institute, p. 495.
10. Ghoniem, A.F., Chen, D.-Y., and Oppenheim, A.K. (1984), "Formation and Inflammation of a Turbulent Jet," *AIAA J. 24*, p. 224.
11. Hsiao, C.-C., Ghoniem, A.F., and Oppenheim, A.K. (1986), "Numerical Modeling of Aerodynamic Features in Premixed Turbulent Combustion," N.A.S.A. Report, in press.
12. Oppenheim, A.K. (1986), "The Beauty of Combustion Fields and Their Aero-Thermo-Dynamic Significance," 10th International Colloquium on Dynamics of Explosions and Reactive Systems, *Progress in Astronautics and Aeronautics*, in press.
13. Rotman, D.A. and Oppenheim, A.K. (1986), "Aerothermodynamic Properties of Stretched Flames in Enclosures," to be presented at the 21st Symposium (International) on Combustion, Munich, August 3–8.

Reaction of Nitric Oxide with Ferrous Cysteine in Aqueous Solutions*

M.D. Tu and S.G. Chang

Japanese have developed a few flue gas simultaneous desulfurization and denitrification processes in the 70s and have shown that these wet processes are very efficient in SO_2 and NO_x removal (more than 85% for NO_x and 95% for SO_2). However, these wet processes have not reached the commercial stage yet because they are uncompetitive economically, according to cost evaluations.[1]

The most promising type of wet process developed so far is based on the addition of ferrous chelates in scrubbing liquors to enhance the absorption of NO by forming nitrosyl ferrous chelates in aqueous solutions. The nitrosyl ferrous chelates can then react with dissolved SO_2 to produce N_2, N_2O, dithionate, sulfate, and various N-S compounds using the type of chelates patented by the Japanese such as EDTA and NTA, while some ferrous chelates are oxidized by residual O_2 in flue gas and by intermediates produced in the system to ferric chelates, which are inactive. Therefore, this type of process requires regeneration of scrubbing liquors by removing dithionate, sulfate, and N-S compounds from the solutions and reduction of ferric chelates back to ferrous chelates.

ACCOMPLISHMENTS DURING FY 1985

We have recently developed new additives for combined removal of SO_2 and NO_x from flue gas.[2] The new additives include ferrous cysteine, alkalis, and borate. Employment of these new additives creates different and simpler scrubber chemistry compared to Japanese processes using ferrous chelates such as Fe^{2+}(EDTA). The production of dithionate and nitrogen-sulfur compounds can be suppressed or avoided by using these new additives. Ferric ions formed can be reduced by cysteine back to ferrous ions.

The reaction of ferrous cysteine with NO can behave differently depending on the molar ratio of cysteine to ferrous ion, $n_{cysteine}/n_{Fe}^{2+}$, and the pH of the solutions. We have performed experiments to determine the absorption capacity of NO in aqueous solutions containing ferrous cysteine complexes using a bench-scale gas absorber. Also, we have characterized the solid precipitates by means of a FTIR spectroscopy and elemental analysis, and gaseous products by a mass spectrometry.

Figure 1 shows the effect of pH on the absorption of NO when the reaction temperature is 55°C and $n_{cysteine}/n_{Fe}^{2+}$ is 4. The amount of NO absorbed per mole of Fe^{2+}, n_{NO}/n_{Fe}^{2+}, and per mole of cysteine, $n_{NO}/n_{cysteine}$, increases from 0.5 to 2.7 and 0.12 to 0.70, respectively, as the pH of the solution increases from 6 to 8. The n_{NO}/n_{Fe}^{2+} and $n_{NO}/n_{cysteine}$ remain unchanged between pH 8 and 10. The effects of $n_{cysteine}/n_{Fe}^{2+}$ on n_{NO}/n_{Fe}^{2+} and $n_{NO}/n_{cysteine}$ at pH 7 and 8 and 55°C are shown in Fig. 2. The $n_{NO}/n_{cysteine}$ decreases steadily from 0.57 to 0.24 as $n_{cysteine}/n_{Fe}^{2+}$ increases from 2 to 6 at pH 7. When pH is at 8, $n_{NO}/n_{cysteine}$ increases from 0.39 to 0.7 as $n_{cysteine}/n_{Fe}^{2+}$ increases from 2 to 4 and then gradually decreases to 0.64 at $n_{cysteine}/n_{Fe}^{2+}$ of 6. This same behavior was observed for n_{NO}/n_{Fe}^{2+} in solutions at pH 7. The n_{NO}/n_{Fe}^{2+} reaches the maximum value of 1.5 at $n_{cysteine}/n_{Fe}^{2+}$ of 4 and decreases slightly with increasing $n_{cysteine}/n_{Fe}^{2+}$ ratio. However, at pH 8, n_{NO}/n_{Fe}^{2+} increases monotonously from 0.78 to 3.82 as $n_{cysteine}/n_{Fe}^{2+}$ increases from 2 to 6.

Varying the pH of the solution and the ratio of cysteine to Fe^{2+} not only affects the amount of NO absorbed but also changes the nature of the reaction products. Figure 3 shows the IR spectra of the precipitates obtained from the reaction of Fe^{2+} + 4 cysteine with NO at 55°C and different pHs. Also shown in Fig. 3 are the IR spectra of solid cysteine and cystine for comparison. It is obvious from these IR results that the nature of the solid is very different when the pH of solutions is changed from 7 to 10. The IR spectrum of precipitates at pH 7 shows several bands at 350(sh), 515(m), 920(w), 990(w), 1140(sh), 1255(m), 1265(m), 1310(m), 1430(m), and 1775(s) cm^{-1} in addition to all the bands of cystine. The band at 1775 cm^{-1} can be attributed to the M-NO stretching ν_{M-NO}. The relative intensity of this band decreases for solid precipitates obtained at pH 7.5, where the only other bands observed are those of cystine. The IR spectrum of solids at pH 8 shows different features than those at pH 7 and 7.5. The 1775 cm^{-1} ν_{M-NO} band disappears, neither does

*This work was supported by the Assistant Secretary for Fossil Energy, Office of Coal Utilization Systems, U.S. Department of Energy under Contract No. DE-AC03-76SF00098 through the Pittsburgh Energy Technology Center, Pittsburgh, PA.

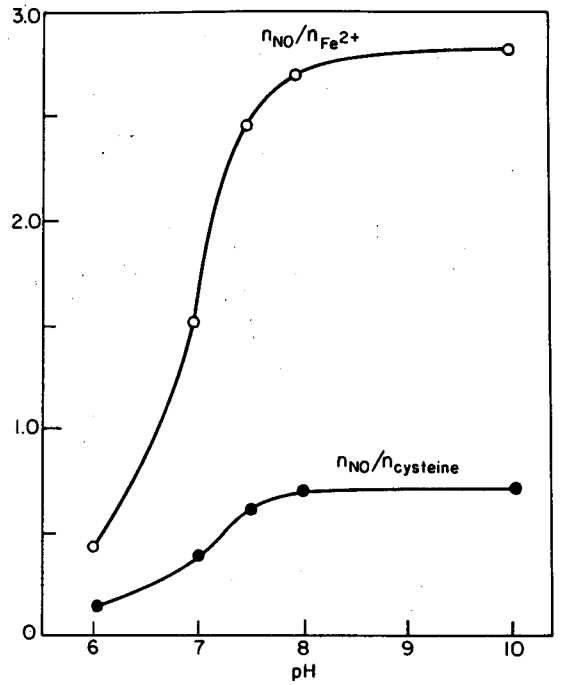

Figure 1. The effect of pH on the absorption of NO in aqueous solutions containing ferrous cysteine, with molar ratio of cysteine to ferrous ion of 4 and at 55°C. (XBL 863-7581)

those bands due to cystine, as observed in solids obtained at pH 7 and 7.5. However, the absence of the cystine bending bands, δ_s-NH_3^+ (1490 cm^{-1}), δ_{as}-NH_3^+ (1580 and 1620 cm^{-1}), and the stretching band, ν—-NH_3^+ (3030 cm^{-1}); and the presence of ν_s-NH_2 (3280 cm^{-1}) and ν_{as}-NH_2 (3350 cm^{-1} and 3370 cm^{-1}) indicate the bonding of the cystine amino group to the ferrous ion. The IR spectrum of solids at pH 10 resembles that of $Fe(OH)_2$ and/or $Fe(OH)_3$. The complete assignments of IR bands are in progress. The IR results are in good agreement with results of elemental analysis. Table 1 shows the n_{NO}/n_{Fe}^{2+} and $n_{cysteine}/n_{Fe}^{2+}$, obtained from elemental analysis, in the precipitates of reactions at pH 7 and 8 and 55°C. The solids at pH 7 contain two moles of NO per each mole of Fe^{2+} found, whereas, the solids at pH 8 does not contain NO at all.

The influence of $n_{cysteine}/n_{Fe}^{2+}$ on the nature of precipitates produced were studied. Figure 4 is the IR spectra of solids obtained at pH 7 and 55 °C. A strong band at 1775 cm^{-1} was observed for all ratio of $n_{cysteine}/n_{Fe}^{2+}$. Additional bands at 515, 990, 1255, 1265, 1310, and 1430 cm^{-1} appear for solids obtained when the ratio of $n_{cysteine}/n_{Fe}^{2+}$ is more than 3. Figure 5 shows IR spectra of the precipitates collected from the reaction at pH 8 and 55°C. There is no NO complex in the reaction products as evident from the absence of a band at 1775 cm^{-1}. Notice the increase in the intensity of the bands at 550, 849,

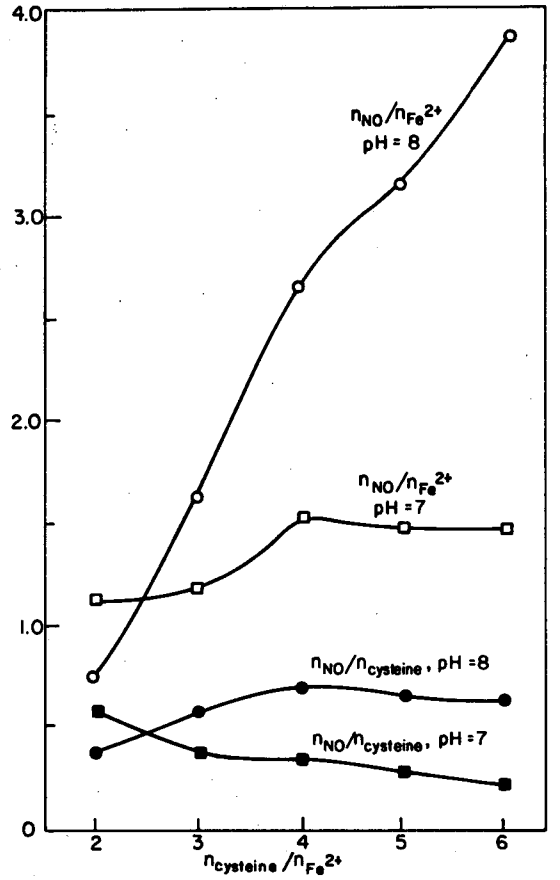

Figure 2. The effect of molar ratio of cysteine to ferrous ion on the absorption of NO in solutions at pH 7 and 8 and 55°C. (XBL 863-7582)

1125, 1300, 1340 cm^{-1}, as the $n_{cysteine}/n_{Fe}^{2+}$ increases from 2 to 6. Additional bands at 775 and 1470 cm^{-1} were observed for solids obtained when the ratio of $n_{cysteine}/n_{Fe}^{2+}$ were 4, 5 and 6; and two more bands at 455 and 870 cm^{-1} when the ratio is 5 and 6.

When the solid sample containing M-NO was subjected to heating (~ 155°C) or vacuum ($\leqslant 10^{-2}$ torr), NO would be released. Figure 6 shows the IR spectra of solids after heating at 155°C for 2 and 7 hours. Part of the NO was released after heating the solid sample for 2 hours, and all the NO had disappeared after heating for 7 hours. Analysis of the gaseous species evolved after heating showed mostly NO with a trace of N_2O. This again confirms that absorbed NO is present in the solid precipitates.

PLANNED ACTIVITIES FOR FY 1986

We will study the kinetics and mechanisms of the reaction of ferrous cysteine with NO and characterize the species produced in solid, liquid, and gas phases in order to make a mass balance for the reaction.

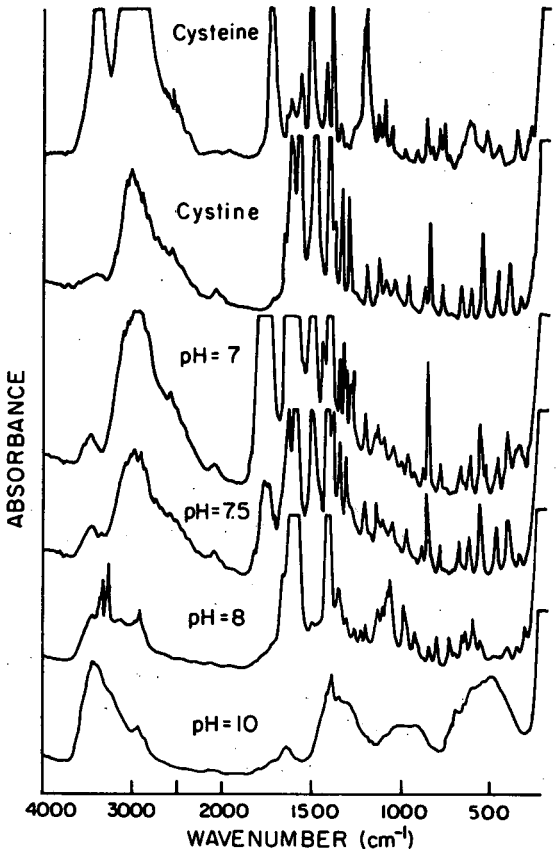

Figure 3. Infrared spectra of cysteine, cystine, and solid products of reaction Fe^{2+} + 4 cystine + NO at different pHs and 55°C. (XBL 863-7583)

Table 1. Chemical composition of the solid reaction products at pH 7 and 8 and 55°C.

$n_{cysteine}/n_{Fe}^{2+}$		2	3	4	5	6
pH 7	$\frac{n_{NO}}{n_{Fe}^{2+}}$	1.95	1.9	2.2	2.1	1.92
	$\frac{n_{cysteine}}{n_{Fe}^{2+}}$	3.0	2.0	2.0	4.3	2.0
pH 8	$\frac{n_{NO}}{n_{Fe}^{2+}}$	0	0	0	0	0
	$\frac{n_{cysteine}}{n_{Fe}^{2+}}$	1.73	2.07	2.14	2.83	3.42

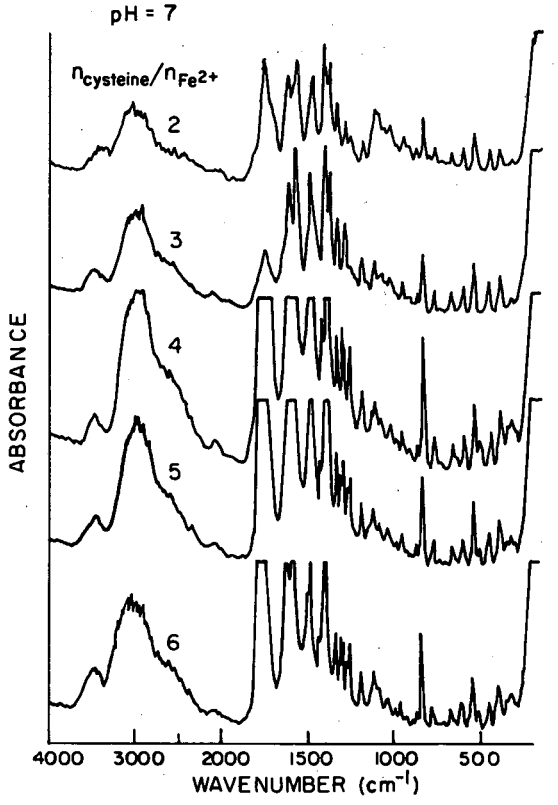

Figure 4. Infrared spectra of solid products from reactions of NO with ferrous cystine, with various molar ratio of cystine to ferrous ion at pH 7 and 55°C. (XBL 863-7584)

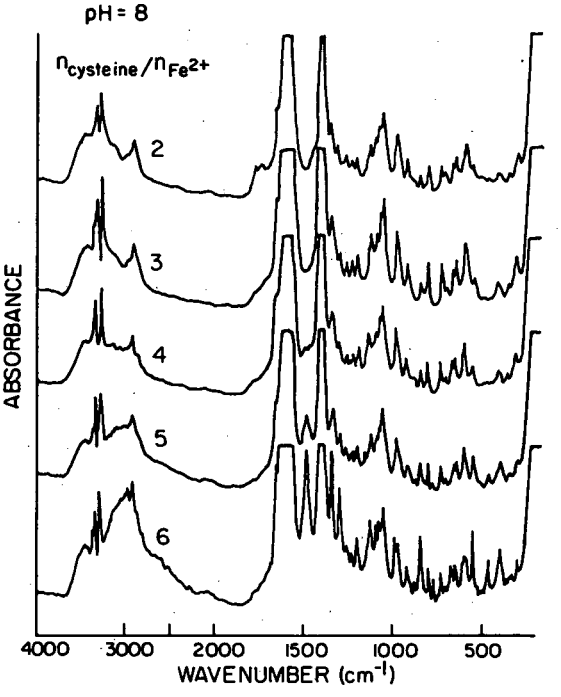

Figure 5. Infrared spectra of solid products from reaction of NO with ferrous cysteine, with various molar ratio of cystine to ferrous ion and at pH 8 and 55°C. (XBL 863-7585)

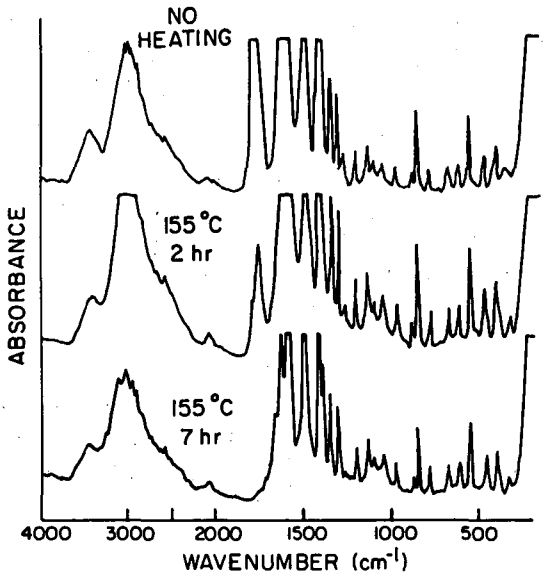

Figure 6. Infrared spectra showing the thermal stability (at 155°C) of solid products obtained from reaction Fe^{2+} + 4 cystine + NO at pH 7 and 55°C. (XBL 863-7586)

REFERENCES

1. Chang, S.G. (1986), "Technical Analyses of a Wet Process for Flue Gas Simultaneous Desulfurization and Denitrification," LBL-18835, to be published in *ACS Symposium Series.*
2. Chang, S.G. and Griffiths, E. (1986), "A Process for Combined Removal of SO_2 and NO_x from Flue Gas," LBL Patent Case No. IB-612.

Kinetics and Thermodynamics of the Reaction Between Cystine and Hydrogen Sulfide Ion*

D.K. Liu and S.G. Chang

We have recently discovered that a mixture of ferrous salts, cysteine, and alkalis (such as lime, limestone, trona, or sodium hydroxide) can be employed as additives in both wet and spray-drying systems to enhance removal efficiency of NO_x and SO_2 from flue gas. The employment of these additives creates different and simpler scrubber chemistry, compared to ferrous chelates such as Fe(II)EDTA or Fe(II)NTA used in several patented Japanese processes. Cysteine can coordinate to ferrous ion to form ferrous-cysteine complex which can efficiently bind and react with NO to form cystinatodinitrosyliron(II) salts. The cystinatodinitrosyliron(II) salt has low solubility and precipitates from neutral pH solutions. It can undergo thermal decomposition at $\geq$ 100°C to release NO and produce cystine, which is a dimer of cysteine. Also, cysteine can be oxidized to cystine in aqueous solutions by residual oxygen in flue gas. This oxidation is catalyzed by the presence of transition metal ions such as ferrous ion. Therefore, a cost-effective process to reduce cystine to cysteine for recycling in the scrubber system is very desirable. There are several methods available for reduction of naturally occurring amino acid cystine to cysteine. These methods include electro- and chemical reductions with sodium in liquid ammonia or zinc in HCl. However, these existing methods require the consumption of electric energy or relatively expensive chemical reagents and may not be cost-effective for large scale preparation in flue gas clean-up industry.

*This work was supported by the Assistant Secretary for Fossil Energy, Office of Coal Utilization Systems, U.S. Department of Energy under Contract No. DE-AC03-76SF00098 through the Pittsburgh Energy Technology Center, Pittsburgh, PA.

ACCOMPLISHMENTS DURING FY 1985

We have demonstrated that cystine (CySSCy) can be efficiently converted to cysteine (CySH) with HS^-/HSO_3^{-} under appropriate conditions.[1] Since little is known about the the kinetics and thermodynamics of the reaction of cystine with hydrogen sulfide ion, we decided to undertake a study of the following equilibria:

$$CySSCy + HS^- \underset{k_{-1}}{\overset{k_1}{\rightleftharpoons}} CySH + CySS^- \quad (1)$$

$$CySS^- + HS^- \underset{k_{-2}}{\overset{k_2}{\rightleftharpoons}} CySH + S_2^{=} \quad (2)$$

The results described here concern mainly with the first of these two reactions.

Equilibrium Constants

The equilibrium concentrations of cystine (CySSCy), cysteine (CySH), and thiacysteine ($CySS^-$) were determined quantitatively by an amino acid analyzer.[1] Assuming no competing reactions besides (1) and (2), we can then calculate the concentrations of HS^- and $S_2^=$ by mass balance. By keeping [CySSCy] = 2 mM and varying the concentrations of HS^-, we have obtained $K_1 = 0.30 \pm 0.06$ and $K_2 = 0.20 \pm 0.04$ at pH = 10 and 25°C.

Rate Constants

We have isolated the first equilibrium from the second in our determination of k_1 and k_{-1}. Our results below show this approximation to be justified.

In opposing reactions of second order represented by the following equation:

$$A + B \underset{k_{-1}}{\overset{k_1}{\rightleftharpoons}} C + D \qquad (3)$$

the rate of product formation (or the rate of disappearance of starting materials) has been shown[2] to be

$$\frac{dx}{dt} = \alpha + \beta x + \gamma x^2 \qquad (4)$$

where $\alpha = k_1 A_o B_o$, $\beta = -k_1(A_o + B_o)$ and $\gamma = k_1 - k_{-1}$, if only A and B are present at the beginning of the reaction. Integrating we get

$$\int \frac{dx}{\alpha + \beta x + \gamma x^2} = \int dt \qquad (5)$$

There are more than one solution to this integral, depending on the relative values of k_1 and k_{-1}. For $k_1 < k_{-1}$ (which is this case), the solution is[3]

$$\tanh^{-1} \frac{2\gamma x + \beta}{q^{1/2}} = \frac{-q^{1/2}}{2} t + \Theta \qquad (6)$$

where $q = \beta^2 - 4\alpha\gamma$ and $\Theta = \tanh^{-1} \beta/q^{1/2}$ at $t = 0$ and $x = 0$. Therefore from the known starting concentrations of CySSCy and HS^-, the amount of cystine reacted at any given time (x) and the equilibrium constant K_1, we can obtain k_1 and k_{-1} from the following version of equation (6):

$$-\tanh^{-1}(ax - b) = ck_{-1}t - d \qquad (7)$$

where $a = 2\gamma/q^{1/2}$, $b = -\beta/q^{1/2}$, $c = q^{1/2}/2k_{-1}$, and $d = -\Theta$. By plotting $-\tanh^{-1}(ax-b)$ versus t, we can obtain k_{-1} from slope/c and k_1 from $0.30 \times k_{-1}$.

Figure 1 shows plots of equation (7) at different concentrations of HS^-. The fact that all the data fitted well as straight lines suggests that (i) the reactions first order with respect to both CySSCy and HS^-, i.e., $R_f = k_1[CySSCy]\,[HS^-]$ and (ii) the first equilibrium can be separated from the second in the determination of k_1 and k_{-1}. From these plots we obtain $k_1 = 1.4 \pm 0.2\ M^{-1}\ min^{-1}$ and $k_{-1} = 4.6 \pm 0.6\ M^{-1}\ min^{-1}$ at pH = 10, $\mu = 0.16$ M and 25°C.

Temperature Dependence

The reaction between CySSCy and HS^- was studied at 25°C, 30°C, 35°C, and 40°C and the results are shown in Fig. 2a. By plotting log k_1 versus $1/T^0$ (Arrhenius plot), Fig. 2b, one obtains $E^* = 15.9$ kcal/mol.

Ionic Strength Dependence

The ionic strength (μ) dependence of the above reaction was also examined. Higher μ than 0.16 M was achieved by addition of NaCl whereas in the case of $\mu = 0.01$ M, the solution was not buffered by borate and the pH was adjusted to 10 by dropwise

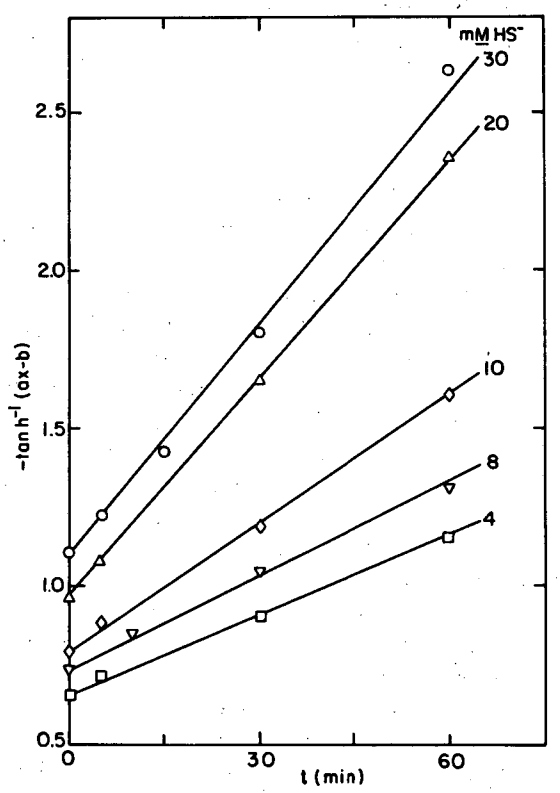

Figure 1. Dependence of the rate of reaction between CySSCy and HS^- on $[HS^-]$. All measurements were made at $T^0 = 25$°C, pH = 10, and $\mu = 0.16$ M. (XBL 863-7519)

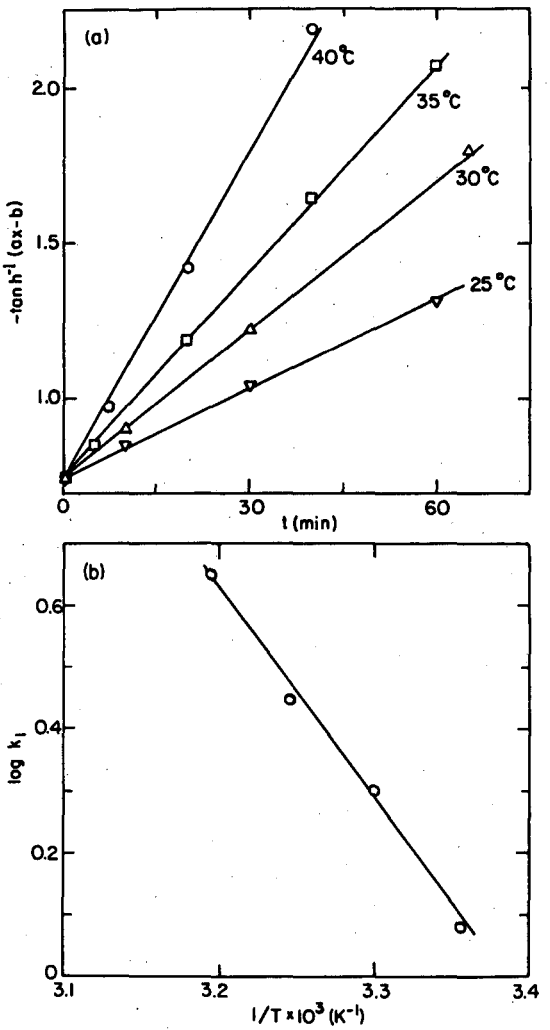

Figure 2. Temperature dependence of the rate of reaction between CySSCy and HS^-: (a) plot of $-\tanh^{-1}(ax-b)$ vs. t at different temperatures, pH = 10 and μ = 0.16 M; (b) plot of log k_1 vs. $1/T^0$ (Arrhenius plot) with slope = −3.47. (XBL 863-7521)

addition of 1N NaOH. The results are shown in Fig. 3a. Since in H_2O at 25°C

$$\log(k_1/k_1^0) = 1.02 z_A z_B \mu^{1/2} \qquad (8)$$

a plot of log k_1 versus 1.02 $\mu^{1/2}$ (in the low ionic strength regime as demanded by the Debye-Hückel model) should yield a slope of $z_A z_B$ and an intercept of k_1^0, the rate constant k_1 at infinite dilution. Such a plot is shown in Fig. 3b, from which we obtain k_1^0 = 0.18 M^{-1} min^{-1} and $z_A z_B$ = 2.0. The later result suggests that CySSCy reacts as a dianion.

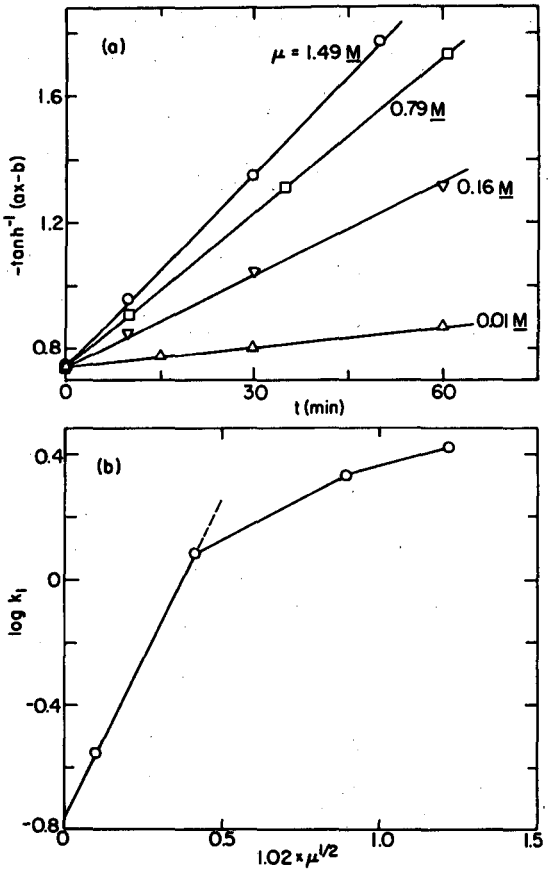

Figure 3. Ionic strength dependence of the rate of reaction between CySSCy and HS^-: (a) plot of $-\tanh^{-1}(ax-b)$ vs. t at different μ's, T^0 = 55°C and pH = 10; (b) plot of log k_1 vs. 1.02 $\mu^{1/2}$ with initial slope = 2.0. (XBL 863-7520)

PLANNED ACTIVITIES FOR FY 1986

Future work includes the pH dependence studies of this reaction and the study of kinetics and thermodynamics of reactions between $CySS^-$ and HS^- (Eq. 2) and between $CySSO_3^-$ and HS^-. The purpose of these studies is to obtain an optimum condition for the production of cysteine from cystine.

REFERENCES

1. Chang, S.G. and Liu, D.K. (1986), "A Process for Production of Cysteine from Cystine," LBL patent case no. IB-638, U.S. patent pending.
2. Benson, S.W. (1960), *The Foundations of Chemical Kinetics,* McGraw-Hill, Chap. 3.
3. *CRC Standard Mathematical Tables* (1968), 16th Edition, S.M. Selby, Ed., CRC Press.

Kinetics of the Reaction of Nitric Oxide with Sulfite and Bisulfite Ions in Aqueous Solution*

D. Littlejohn, K.Y. Hu, and S.G. Chang

There have been several studies[1-4] of the reaction of nitric oxide with dissolved sulfur dioxide, but there is disagreement about the kinetics of the system. An early study was done by Terres and Lichti,[1] who observed the decrease in pressure of nitric oxide in the presence of K_2SO_3, $KHSO_3$, and SO_2 H_2O. They were unable to obtain rate constants, but decided that a $(ONSO_3)^{2-}$ intermediate was involved and that the reaction between nitric oxide and bisulfite ion was first order in both species. Nunes and Powell[2] investigated the reaction of NO with SO_3^{2-} at pH 13–14 by observing the decrease in pressure of NO over the sulfite solution in a well-stirred reactor. The rate expression they obtained consisted of a sulfite dependent term and a sulfite independent term. Takeuchi, *et al.*[3] observed the loss of nitric oxide diluted with nitrogen after it either flowed over a sulfite solution surface or was bubbled through a sulfite solution. They found the reaction had second order dependence on nitric oxide and zero order dependence on sulfite concentration. Their results indicated the reaction was very fast. Martin, *et al.*[4] used a stopped-flow system to observe the reaction between dissolved nitric oxide and dissolved sulfur dioxide at pH $\leq$ 3 by monitoring SO_2 H_2O at 280 mm. They found that the reaction was very slow and could only obtain an upper limit for the rate. In view of the disagreement of these studies, we decided to investigate the reaction system in an attempt to remove the ambiguity associated with it.

ACCOMPLISHMENTS DURING FY 1985

To avoid difficulties with the diffusion rate of nitric oxide influencing the observed rate or reaction, we decided to monitor the reaction of sulfite and bisulfite ions with dissolved nitric oxide rather than nitric oxide gas. A continuous-flow rapid-mixing system which could also be used in the stopped-flow mode was used for the experiments. Both tanks for the reactant solutions were filled with water and degassed by passing argon through them. Nitric oxide was then passed through one of the tanks until the solution was saturated. A lower flow of nitric oxide was passed through the solution during the experiments. The sulfite and/or bisulfite solution was prepared by weighing out reagent grade sodium sulfite and/or sodium metabisulfite. The pH of the solutions was adjusted by the addition of sodium hydroxide or hydrochloric acid, if necessary. After preparation, the two solutions were passed through flowmeters and a mixer and then into either a 1 cm or 5 cm pathlength UV cell. The cell was located in a temperature-controlled compartment in a Cary 219 spectrophotometer. The pH of the mixed solution was monitored with an in-line pH probe downstream of the cell.

Ackermann and Powell[5] found that the only product of the reaction of NO with SO_3^{2-} was N-nitrosohydroxylamine-N-sulfonate (NHAS), which has a strong UV absorption. NHAS was monitored in the wavelength range between 258 nm and 300 nm, where absorptions by other species would not interfere. The reaction was studied in two ways. In continuous-flow measurements, the flow rates of the reactants were stabilized and a spectrum of the reaction mixture was taken from 350 nm to 230 nm. In stopped-flow measurements, the flow rates of the reactants were stabilized and one wavelength where NHAS alone absorbed was monitored. The flow of the reactants was stopped abruptly and the change in NHAS concentration *vs* time was monitored. The results of the experiments at high pH conditions were analyzed to obtain a rate constant for NO + SO_3^{2-}. This rate constant was then used to correct low and intermediate pH experiments to obtain the rate constant for NO + HSO_3^-. The hydrolysis rate for NHAS was obtained from the stopped-flow experiments at low pH, and this was used to correct the low pH experiments for loss of the reaction product.

From the experiments in which the nitric oxide concentration was varied at constant sulfite concentration, it was found that the rate for NHAS production had first order dependence on nitric oxide concentration. Similarly, in experiments where SO_3^{2-} and HSO_3^- were varied with constant NO concentration, it was found that the rate for NHAS production had first order dependence on both SO_3^{2-} and HSO_3^-.

The pH of the mixed solution was varied from 4 to 10.5 to observe what influence the pH had on the rate. A plot of log k *vs* pH is shown in Fig. 1, where k is defined as

$$k = \frac{d[NHAS]/dt}{[NO]([HSO_3^-] + [SO_3^{2-}])}.$$

*This work was supported by the Assistant Secretary for Fossil Energy, Office of Coal Utilization Systems, U.S. Department of Energy under Contract No. DE-AC03-76SF00098 through the Pittsburgh Energy Technology Center, Pittsburgh, PA.

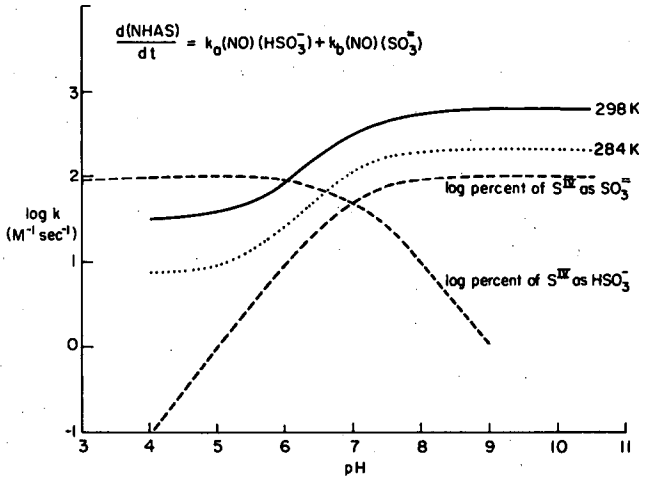

Figure 1. The pH dependence of the observed rate constant. (XBL 853-5938)

Also plotted as dashed lines are log percent of the total S(IV) oxide as HSO_3^- and SO_3^{2-}. The experimental curves indicate that both sulfite and bisulfite ions react with NO. If the reaction occurred only between SO_3^{2-} and NO, the experimentally obtained curve would be expected to follow the dashed line for SO_3^{2-}, rather than leveling out at lower pHs.

We also studied the temperature dependence of the reaction by putting the reactant tanks in a thermostatted bath, passing the reactant solutions through a second thermostatted bath just prior to mixing and regulating the temperature of the sample compartment. The curve of log k *vs* pH at 284 K is also shown in Fig. 1. Only the reaction of NO with SO_3^{2-} was studied at 323 K because of problems with the development of bubbles in the mixed solution which created unpredictable changes in the liquid volume between the mixer and the cell. The formation of the product can be expressed as

$$\frac{d[NHAS]}{dt} = k_a[NO][HSO_3^-] + k_b[NO][SO_3^{2-}].$$

The values for k_a and k_b are listed in Table 1. These values are plotted as log k *vs* 1/T in Fig. 2. For NO + SO_3^{2-}, a pre-exponential term of $A = 3.2 \times 10^{10}$ M^{-1} sec^{-1}, and an activation energy of $E_\alpha = 10.6$ kcal/mole are obtained where $k = Ae^{-E_a/RT}$. For NO + HSO_3^-, a pre-exponential term of 2.6×10^{14} M^{-1} sec^{-1} and an activation energy of 17.6 kcal/mole are obtained.

Table 1.

	k_a (M^{-1} sec^{-1})	k_b (M^{-1} sec^{-1})
284 K	7.5 ± 2	220 ± 35
298 K	32 ± 10	620 ± 100
323 K	–	2000 ± 500

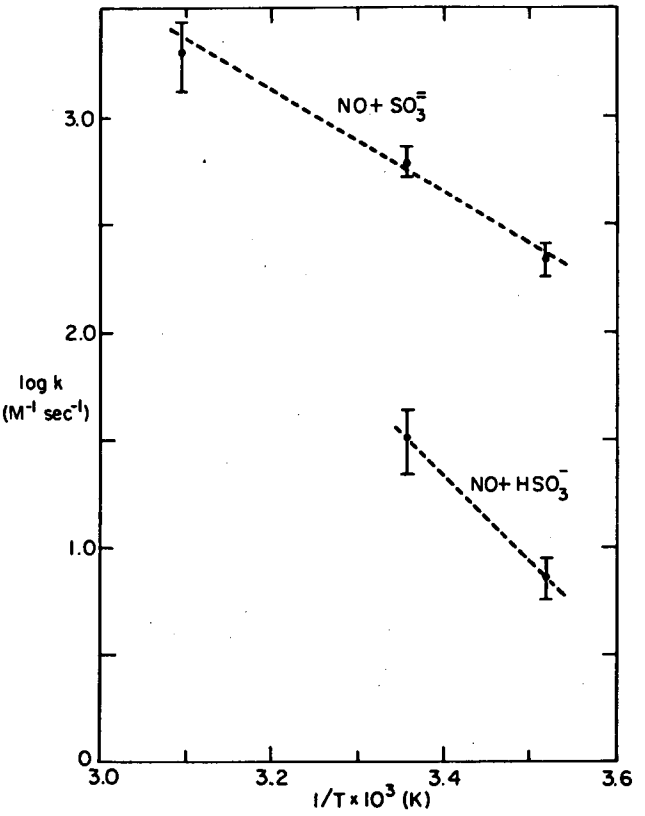

Figure 2. Arrhenius plot for NO + SO_3^{2-} and NO + HSO_3^-. (XBL 857-6393)

It was necessary to correct runs done at low pH for the hydrolysis of the NHAS product. Stopped-flow experiments were done at low pH conditions, and the NHAS concentration was monitored. The decaying absorbance curves obtained from these experiments were used to determine the hydrolysis rate constant for NHAS as a function of pH. Short intervals of the decay curve were used to calculate values of the rate constant. These values were averaged to obtain the hydrolysis rate constant. This is shown in Fig. 3, along with results obtained at higher pH conditions by Ackermann[6] and Seel and Winkler.[7] The latter used EDTA to bind any trace amounts of metal ions present in solution and obtained a lower hydrolysis rate constant than the former, suggesting the hydrolysis may be catalyzed by metal ions.

The first order dependence of the rate on both NO and SO_3^{2-}/HSO_3^- indicates the formation of an intermediate which rapidly reacts with a second NO to form the NHAS product. This is in agreement with what Terres and Lichti[1] and Nunes and Powell[2]

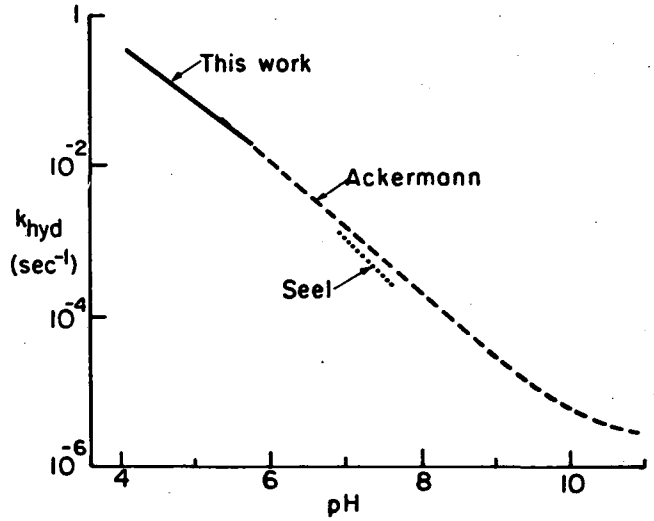

Figure 3. The pH dependence of the NHAS hydrolysis rate. (XBL 857-6394)

have observed. The following reaction scheme can explain our observations:

$$NO_{aq} + SO_3^{2-} \rightarrow (ONSO_3)^{2-}, \quad (1)$$

$$NO_{aq} + (ONSO_3)^{2-} \rightarrow {}^{-}ON(NO)SO_3^{-}, \quad (2)$$

$${}^{-}ON(NO)SO_3^{-} \xrightarrow{H^+} N_2O + SO_4^{2-}. \quad (3)$$

The reaction scheme also applies to HSO_3^-. Nunes and Powell's work with the reaction of NO with SO_3^{2-} and $SnCl_2$ in the presence of Cu(I) led them to believe that NO exists in two forms in aqueous solution, which they refer to as dissolved NO and hydrolyzed NO. They indicate that the dissolved form reacts more slowly than the hydrolyzed form. They propose the following reaction scheme for NO + SO_3^{2-}:

$$NO(gas) = NO(dissolved), \quad (4)$$

$$NO(dissolved) = NO(hydrolyzed), \quad (5)$$

$$NO(dissolved) + SO_3^{2-} \rightarrow (ONSO_3)^{2-}, \quad (6)$$

$$NO(hydrolyzed) + SO_3^{2-} \rightarrow (ONSO_3)^{2-}, \quad (7)$$

$$NO(unspecified) + (ONSO_3)^{2-} \rightarrow {}^{-}ON(NO)SO_3^{-}. \quad (8)$$

For the reaction of dissolved NO with SO_3^{2-} (reaction (6)), Nunes and Powell obtained $-d[NO]/dt = \frac{1}{2} d[NHAS]/dt = 0.45[NO][SO_3^{2-}]$ sec^{-1}, which is about three orders of magnitude slower than the rate we have obtained. From their temperature dependence, we calculate a pre-exponential term of 4.9×10^5 M^{-1} sec^{-1} and an activation energy of 8.2 kcal/mole for reaction (6). The activation energy is fairly close to the value we have obtained for reaction (2), 10.6 kcal/mole. They estimated that the rate constant for conversion of dissolved NO to hydrolyzed NO was about 0.14 sec^{-1} at 298 K.

Using the above rate constants, we modeled the stopped-flow experiments done with NO + SO_3^{2-} at 25°C in an attempt to determine if our results could validate their hypothesis that there are two forms of NO in solution. Since the hydrolyzed NO would react more quickly than the dissolved NO, the rate of NHAS formation should slow down as the hydrolyzed NO is consumed in a stopped-flow experiment. From the comparison of the calculations and the observed NHAS curves, we estimate that K_{eq} = [NO (hydrolyzed)]/[NO (dissolved)] is at least 10. There is considerable uncertainty in this value.

The only way we can reconcile their results with ours is to propose that the dissolution process for NO involves an intermediate which is formed directly from the gas phase and has a rate constant on the order of 0.1 sec^{-1} to form dissolved NO in aqueous solution. Without more information on the dissolution process, it is difficult to speculate about the chemistry associated with it.

PLANNED ACTIVITIES FOR FY 1986

The continuous-flow/stopped-flow apparatus used in this work is well-suited for studying rapid reactions in solution. Aqueous reactions involving dissolved nitrogen oxides and sulfur oxides may be studied in the future. A Raman spectrometer could be used as a detector instead of a UV-visible spectrometer. This would permit simultaneous observation of a number of species in the flowing solution.

REFERENCES

1. Terres, E. and Lichti, H. (1934), "Kinetische Untersuchung uber die Einwirkung von Stickoxyd auf Alkalisulfit, Alkalaibisulfit und schwelflige Saure in wahriger Losung," *Angew. Chem. 47*, p. 511.

2. Nunes, T.L. and Powell, R.E. (1970), "Kinetics of the Reaction of Nitric Oxide with Sulfite," *Inorg. Chem. 9*, p. 1916.
3. Takeuchi, H., Ando, M., and Kizawa, N. (1977), "Absorption of Nitrogen Oxides in Aqueous Sodium Sulfite and Bisulfite Solutions," *I & EC Process Des. & Dev. 16*, p. 303.
4. Martin, L.R., Damschen, D.E., and Judeikis, H.S. (1981), "The Reactions of Nitrogen Oxides with SO_2 in Aqueous Aerosols," *Atmos. Environ. 15*, p. 191.
5. Ackermann, M.N., Powell, R.E. (1967) "Air Oxidation of Hydroxylamine-N-Sulfonate," *Inorg. Chem. 6*, p. 1718.
6. Ackermann, M.N. (1966), "Alkaline Hydrolysis and Oxidation of Hydrolylamine-N-Sulfonate Ion," Ph.D. Thesis, University of California, Berkeley.
7. Seel, F. and Winkler, R. (1963), "Kinetik des saurekatalysierten Zerfalls des Nitrosohydroxylaminsulfonat-Ions," *Z. Naturforsch. 18a*, p. 155.

The Kinetics of Acid Hydrolysis of Nitridotrisulfate Ion*

David Littlejohn, Abigail R. Wizansky, and S.G. Chang

A number of nitrogen sulfonates are produced by reactions between bisulfite ions and nitrite ion in aqueous solution.[1] Thus, their chemistry is of interest in studies of aqueous aerosols in polluted air and in wet flue gas scrubbing systems. Some of the chemistry is shown in Fig. 1. While the hydrolysis reactions of hydroxyimidodisulfate (HIDS) and imidodisulfate (IDS) have been studied,[2,3] those of nitridotrisulfate (NTS) and hydroxylsulfamate (HSA) have not been thoroughly investigated. Sisler and Audrieth[4] observed the hydrolysis of NTS:

$$NTS + H^+ \rightarrow IDS + HSO_4^- . \quad (1)$$

They found that it occurred much more quickly than the hydrolysis of IDS. No quantitative information was obtained.

ACCOMPLISHMENTS DURING FY 1985

We have studied the hydrolysis of NTS over a temperature range of 283 K to 333 K, a pH range of 4 to 7, and an ionic strength range of 0.05 to 1.0. The potassium salt of NTS was prepared by the method of Sisler and Audrieth,[4] and the purity was checked by Raman spectroscopy and ion chromatography. Experiments were done by dissolving the NTS salt in a slightly alkaline solution and then mixing with a acidic buffer solution to initiate hydrolysis. Buffers used included acetate, oxalate, phosphate, phthalate, malonate, and succinate solutions. Sodium chloride was used to adjust the ionic strength of the solutions. The hydrolysis was monitored by measuring the concentrations of the reaction products, IDS and SO_4^{2-}, by ion chromatography.[5] The products could not be measured simultaneously. Sulfate was usually monitored because ion chromatographic detection of SO_4^{2-} is linear over a wider concentration range than IDS.

The dependence of the rate of the hydrolysis reaction on the concentrations of NTS and H^+ was checked. Using buffers to maintain the solutions at pH 5, runs were made in which the NTS concentration was varied from 10^{-3} M to 10^{-2} M. A plot of $\log_{10}$ [NTS] *vs* $\log_{10}$ (rate) is shown in Fig. 2. The slope for the line is 1.07 ± 0.10, indicating first-

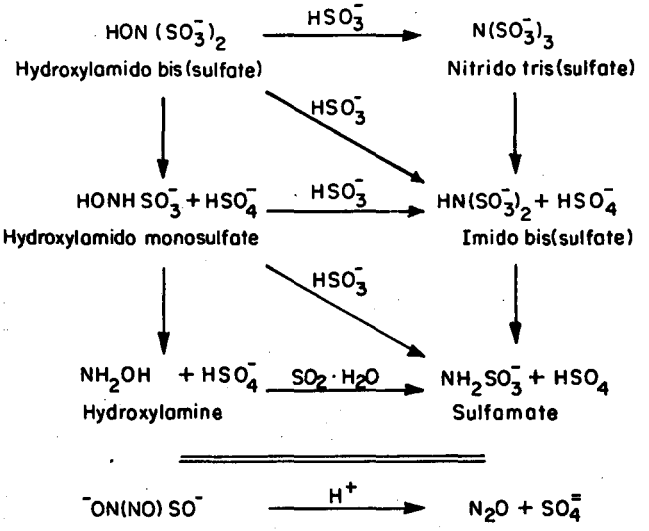

Figure 1. Reactions involving nitrogen sulfonates. (XBL 854-6046)

*This work was supported by the Assistant Secretary for Fossil Energy, Office of Coal Utilization Systems, U.S. Department of Energy under Contract No. DE-AC03-76SF00098 through the Pittsburgh Energy Technology Center, Pittsburgh, PA.

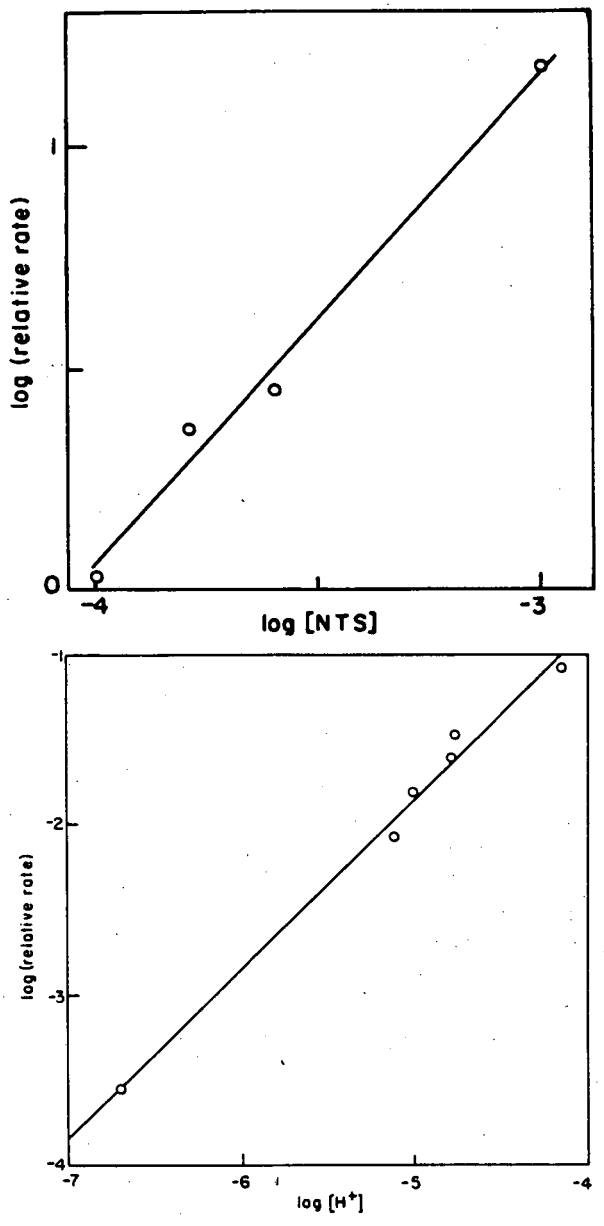

Figure 2. Rate dependence on $[H^+]$ and [NTS]. (XBL 863-1165)

order dependence on NTS concentration. The hydrogen ion dependence was done with solutions of 2.5×10^{-3} M NTS at pH 4 to 7. A plot of $\log_{10}$ (rate) *vs* pH is shown in Fig. 2. The slope of the line is 0.92 ± 0.09, indicating the hydrolysis reaction also has first-order dependence on H^+.

The temperature dependence of the hydrolysis reaction was studied by immersing the reaction mixtures in controlled-temperature water baths. The reaction was studied at 283 K, 298 K, 313 K, and 333 K. The rate constant was calculated using the expression

$$-\frac{d(NTS)}{dt} = k(H^+)(NTS).$$

Most runs were done with initial NTS concentrations of 2.5×10^{-3} M and ionic strengths of μ = 0.05. The rate constants obtained at these conditions are:

T =	283 K	k = 3.03 ± 0.17	$M^{-1}\,sec^{-1}$
	298 K	k = 12.7 ± 2.0	
	313 K	k = 70 ± 18	
	333 K	k = 227 ± 12.	

An Arrhenius plot of these values is shown on Fig. 3. If the rate constant is expressed as $k = A \exp(-Ea/RT)$ where R is the gas constant and T is the absolute temperature, then values of $A = 1.5 \pm 0.7 \times 10^{13}$ $L\,mol^{-1}\,sec^{-1}$ and E_a = 16.5 ± .3 kcal/mole. Both the pre-exponential factor and the activation energy are similar to those of the acid-catalyzed HIDS hydrolysis.[1]

The effect of ionic strength on the hydrolysis reaction was investigated by adding sodium chloride and/or changing the buffer concentration. The ionic strength was varied from μ = 0.08 to μ = 1.0. All runs were done with an NTS concentration of 2.5×10^{-3} M. All of these runs were done in the pH range of 4.8 to 5.2. A plot of log k *vs* $\mu^{1/2}$ is shown in Fig. 4. The slope of the plot should be equal to the product of charges of the reacting ions.[6] The slope of this plot is about −1, suggesting that it is the 1− form of NTS reacting with H+ to form IDS. The ionization constants for NTS are not known. It is estimated the pK_as are fairly low.[4]

Solutions of NTS in the range of pH 8 to 10 exhibit little or no deterioration over a period of

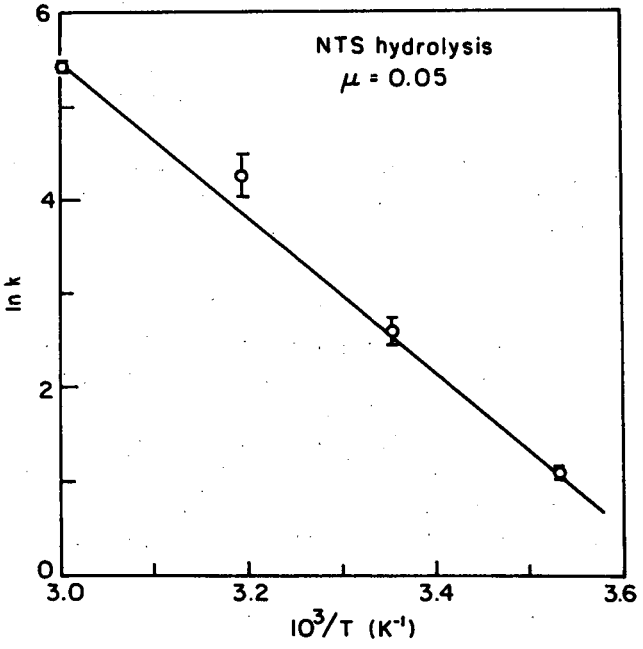

Figure 3. Arrhenius plot for the hydrolysis of NTS. (XBL 863-7576)

many days. This indicates that the uncatalyzed hydrolysis reaction is insignificant compared to the acid-catalyzed reaction.

PLANNED ACTIVITIES FOR FY 1986

Another of the nitrogen sulfonates shown in Fig. 1, HSA, is known to hydrolyze in acidic solutions, and its hydrolysis kinetics have not been studied. The method used to study the hydrolysis of NTS should readily lend itself to the study of the hydrolysis of HSA. We plan to study this reaction in FY 1986.

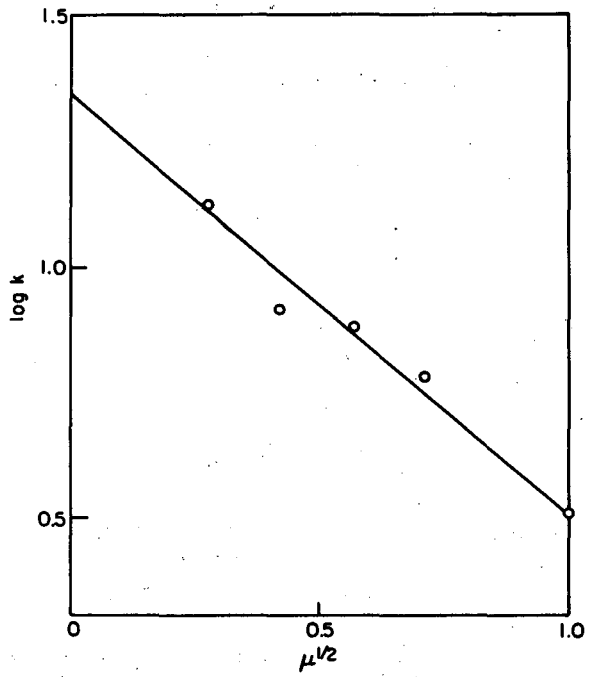

Figure 4. Ionic strength dependence of the hydrolysis of NTS. (XBL 863-7575)

REFERENCES

1. Chang, S.G., Littlejohn, D., and Lin, N.H. (1982), "Kinetics of Reactions is a Wet Flue Gas Simultaneous Desulfurization and Denitrification System," in *Flue Gas Desulfurization*, ACS Symposium Series No. 188, American Chemical Society, Washington, D.C., p. 127.
2. Naiditch, S. and Yost, D.M. (1941), "The Rate and Mechanism of the Hydrolysis of Hydroxylamine Disulfonate Ion," *J. Am. Chem. Soc. 63*, p. 2123.
3. Doyle, G.J. and Davidson, N. (1949), "The Kinetics of the Acid-Catalyzed Hydrolysis of Amine Disulfonate Ion; The Third Ionization Constant of Amine Disulfonic Acid," *J. Am. Chem. Soc. 71*, p. 3491.
4. Sisler, H. and Audrieth, L.F. (1938), "Potassium Nitrilosulfonate," *J. Am. Chem. Soc. 60*, p. 1947.
5. Littlejohn, D. and Chang, S.G. (1986), *Determination of Nitrogen-Sulfur Compounds by Ion Chromatography" Anal. Chem. 58*, p. 158.
6. Olson, A.R. and Simonson, T.R. (1949), "Rates of Ionic Reactions in Aqueous Solutions," *J. Chem. Phys. 17*, p. 1167.

Determination of Nitrogen-Sulfur Compounds by Ion Chromatography*

D. Littlejohn and S.G. Chang

A number of nitrogen-sulfur compounds can form in aqueous solutions of nitrogen oxyanions and sulfur oxyanions.[1,2] Conditions suitable for their formation exist in wet flue gas scrubbers and aqueous aerosols in polluted air. The nitrogen sulfonates of interest include hydroxyimidodisulfate (HIDS), hydroxysulfamate (HSA), nitridotrisulfate (NTS), imidodisulfate (IDS), and N-nitroso-hydroxylamine-N-sulfonate (NHAS).

Three techniques have been previously described for the determination of some of these compounds. The gravimetric and iodometric technique developed by Sato, *et al.*[3] requires a series of treatments of a sample to obtain the amounts of HIDS, NTS, and IDS present. They gave no method for HSA or NHAS determination. Oblath[4] used a method where HIDS was oxidized to nitrosodisulfonate ($ON(SO_3^-)_2$), and colorimetry was done to determine nitrosodisulfonate. This technique also involves a number of steps. Raman spectrometry permits simultaneous determination of all of the compounds listed above and requires a very small sample volume.[5] It eliminates the need for extensive manipulation of the sample. The major limitation of Raman spectrometry is lack of sensitivity. Samples with low concentrations (0.001–0.01 M) of the compounds of interest require very long data aquisition times. Determination of these compounds by ion chromatography has been found to combine high sensitivity and rapid measurement times.

*This work was supported by the Assistant Secretary for Fossil Energy, Office of Coal Utilization Systems, U.S. Department of Energy under Contract No. DE-AC03-76SF00098 through the Pittsburgh Energy Technology Center, Pittsburgh, PA.

ACCOMPLISHMENTS DURING FY 1985

A Dionex 2010i ion chromatograph equipped with a Dionex AG4 guard column, a Dionex AS4 anion separation column, and a Dionex anion fiber suppressor was used in the determinations. For determination of HSA and sulfamate, 1.5 mM bicarbonate eluent was used with a flow rate of 2.0 mL/min at a pressure of 700–800 psi. For determination of HIDS, IDS, and NHAS, the AG4 column alone was used as the separation column with 12 mM or 18 mM carbonate eluents. The flow rate was 1.5 mL/min at a pressure of 200–300 psi. A 50 μL sample loop volume was used. For conductivity suppression, 0.025 N H_2SO_4 was used with a flow rate of 2.5–3.5 mL/min for the 1.5 mM eluent and a flow rate of 5–7 mL/min for the 12 mM and 18 mM eluents.

The NTS and IDS for standard solutions were synthesized by the procedure given by Sisler and Audrieth.[6] HIDS was prepared by the method of Rollefson and Oldershaw.[7] HSA was prepared by the method given by Oblath.[4] The potassium salts of the above compounds were stored in a vacuum desiccator at 5°C until solutions were needed. Solutions of these compounds were treated with sufficient concentrated NaOH to make the solutions alkaline. NHAS solutions were prepared on a vacuum line just prior to use, following the method of Nunes and Powell.[8]

An ion chromatogram of a mixture of IDS, HIDS, and NHAS is shown in the bottom half of Fig. 1. The chromatogram was recorded on the 10 μS scale. The peak present at $\Delta t \approx 1$ min is due to sulfate impurity. An ion chromatogram of a mixture of sulfamate and HSA is shown in the top half of Fig. 1. This chromatogram was also recorded on the 10 μS scale.

It was not possible to make determinations of NTS with the column used in these studies because it is very strongly retained on the column. In the alkaline conditions of carbonate and bicarbonate eluents, NTS has a 3− charge. HSA and sulfamate have 1− charges and will pass through the 5 cm guard column and 25 cm separation column in a few minutes using a low concentration eluent. IDS, HIDS, and NHAS have 2− charges and require a high concentration eluent to pass through the 5 cm guard column alone in a few minutes.

To transport a compound with a 3− charge through a column with this type of ion exchange resin in a reasonable time would require an excessively high eluent concentration. A resin that would work well with NTS would be unlikely to separate the other compounds. It may be possible to analyze

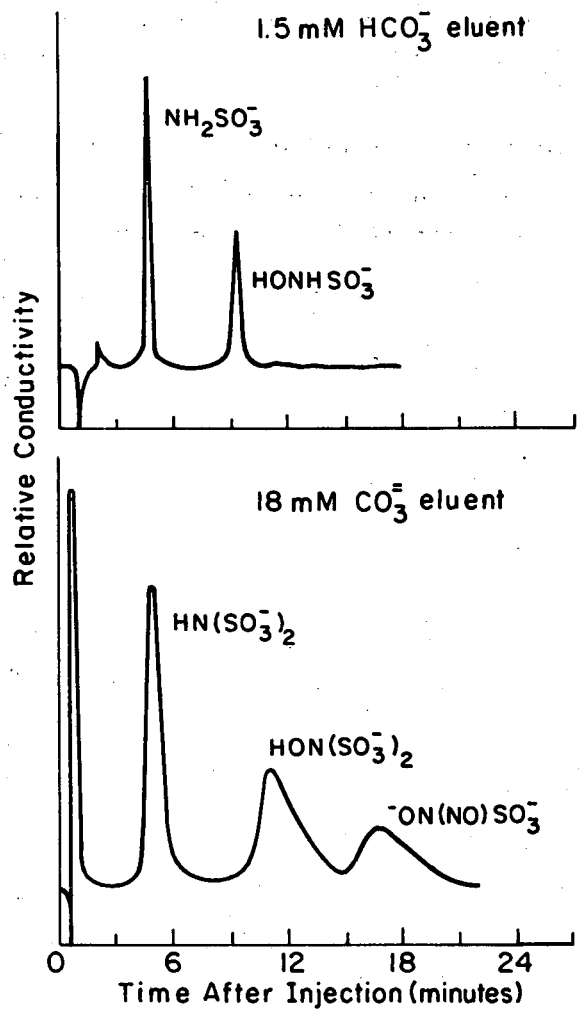

Figure 1. (Top) Ion chromatogram of sulfamate and hydroxysulfamate. (Bottom) Ion chromatogram of imidodisulfate, hydroxyimidodisulfate, and N-nitrosohydroxylamine-N-sulfonate. (XBL 854-6043)

NTS by using a column with a more hydrophobic resin or by MPIC (Mobile Phase Ion Chromatography).

These compounds can hydrolyze in aqueous solutions under acidic conditions. Generally, they are stable in alkaline solutions, although NHAS and HSA are susceptible to attack by oxygen.[9] There is considerable variation in the rates of hydrolysis for these compounds. For a given pH and nitrogen sulfonate concentration, the relative hydrolysis rates, in increasing order, are: HSA, IDS, HIDS, NTS, and NHAS. Since NTS hydrolyzes much more easily than IDS, it can be converted into IDS for measurement by ion chromatography. A sample can be run on the ion chromatograph to determine IDS, acidified to pH 2–3 and allowed to stand 5–10 minutes, and run again to measure the increase in IDS concentration. Tests done with standard solutions indi-

cate this is a quantitative method. The hydrolysis of IDS is sufficiently slow under these conditions that it does not affect the results.[10]

It was found that determinations of nitrogen-sulfur compounds in samples were best done by comparison with standard solutions. Ion chromatograms of dilutions of freshly prepared alkaline solutions of the compounds were run either prior to or following chromatograms of solutions containing unknown amounts of the compounds. This minimized the influence of variations in the ion chromatograph operating parameters. The linearity of the ion chromatograph's response to the compounds was checked by measuring the peak heights obtained from a range of sample concentrations. The highest concentrations injected were 1×10^{-3} M. Figure 2 shows a plot of peak height *vs* concentration for HSA and sulfamate. Both HSA and sulfamate significantly deviate from linearity above 2×10^{-4} M. The peaks become broader and shorter than what would be expected from extrapolation of the peak heights obtained at lower concentration. Figure 3 shows a plot of peak height *vs* concentration for IDS, HIDS, and NHAS. IDS deviated from linear response above 2×10^{-4} M concentration, while HIDS, and NHAS exhibited good linearity up to 6×10^{-4} M concentration. All compounds exhibited broadening of the peaks at the highest concentrations

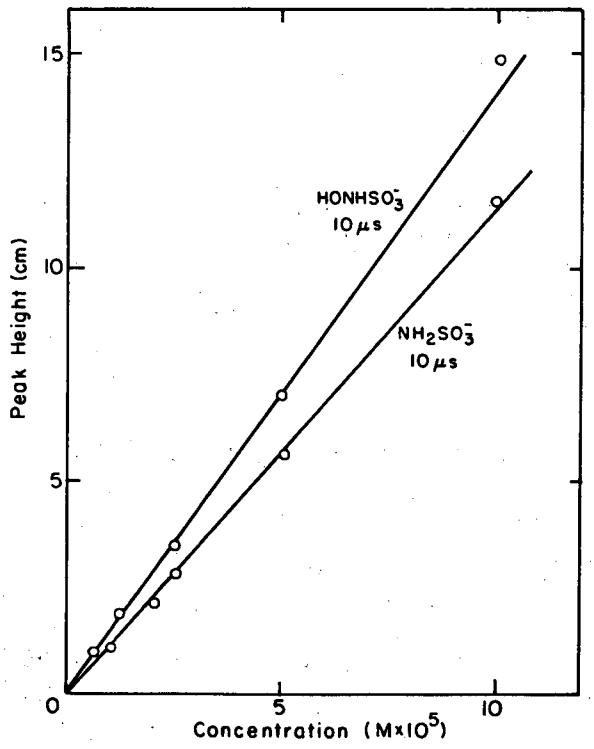

Figure 2. Calibration curve for sulfamate and hydroxysulfamate. (XBL 854-6044)

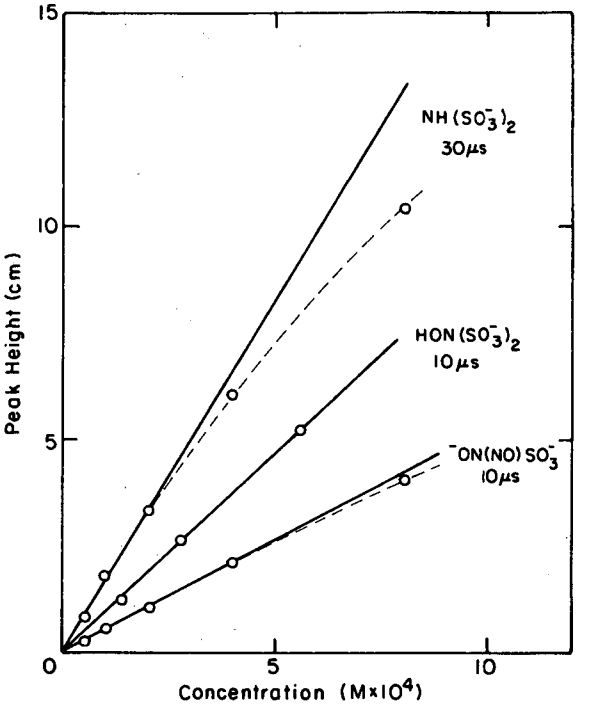

Figure 3. Calibration curve for imidodisulfate, hydroxyimidodisulfate, and N-nitrosohydroxylamine-N-sulfonate. (XBL 854-6045)

tested. Also, when the AG4 column alone was used, reduction in the compounds' retention time was noted at high concentrations ($\sim 1 \times 10^{-3}$ M).

Detection limits for the compounds were obtained where the detection limit was defined as the concentration that generated a peak with a height twice that of the background noise. The detection limits obtained are as follows: HSA : 0.5×10^{-6} M, sulfamate : 0.6×10^{-6} M, IDS : 1.4×10^{-6} M, HIDS : 7.4×10^{-6} M, NHAS : 12×10^{-6} M. As the retention time of a compound increases, the peak broadens and decreases in height. Thus, it is advantageous to have as short a retention time as possible within the limitations of obtaining separation between the peaks of chromatogram.

A number of flue gas scrubbing liquors have been analyzed by the method discussed above. Table 1 lists the range of concentrations observed for seven anions found in several scrubbing liquor samples from typical closed-loop lime-limestone scrubbers. The samples were in the pH range of 6 to 8.5. No HSA was found in the samples, presumably because oxidation would occur rapidly enough to eliminate it from the samples before analysis.

PLANNED ACTIVITIES FOR FY 1986

There are a number of other nitrogen-sulfur compounds that have similar structure to those stu-

Table 1.

Anion	Range of Concentration
Cl^-	$3.0 - 3.6 \times 10^{-2}$ M
NO_3^-	$1.8 - 4.2 \times 10^{-3}$ M
SO_4^-	$3.2 - 4.2 \times 10^{-2}$ M
$S_2O_3^-$	$0 - 3.2 \times 10^{-3}$ M
IDS	$0.7 - 3.3 \times 10^{-3}$ M
HIDS	$0.3 - 0.8 \times 10^{-3}$ M
NTS	$0 - 1.3 \times 10^{-3}$ M

died. Ion chromatography may be a suitable technique to study these compounds also. We plan to attempt to detect some of these compounds by ion chromatography.

REFERENCES

1. Oblath, S.B., Markowitz, S.S., Novakov, T., and Chang, S.G. (1982), "Kinetics of the Initial Reaction of Nitrite Ion in Bisulfite Solutions," *J. Phys. Chem. 86*, p. 4853.
2. Chang, S.G., Littlejohn, D., and Lin, N.H. (1982), "Kinetics of Reactions in a Wet Flue Gas Simultaneous Desulfurization and Denitrification System," *ACS Symp. Ser. No. 188*, American Chemical Society, Washington, DC.
3. Sato, T., Matani, S., and Okabe, T. (1979), "Oxidation of Sodium Sulfite with Nitrogen Dioxide," *ACS/CSJ Chemical Congress*, Honolulu, HI.
4. Oblath, S.B. (1981), "Kinetics of the Reduction of Nitrite Ion by Sulfur Dioxide in Aqueous Solution," Ph.D. Thesis, University of California, Berkeley.
5. Littlejohn, D. and Chang, S.G. (1984), "Identification of Species in a Wet Flue Gas Desulfurization and Denitrification System by Laser Raman Spectroscopy," *Environ. Sci. Tech. 18* p. 305.
6. Sisler, H. and Audrieth, L.F. (1938), "Potassium Nitrilosulfonate," *J. Am. Chem. Soc. 60* p. 1947.
7. Rollefson, G.K. and Oldershaw, C.F. (1932), "The Reduction of Nitrites to Hydroxylamine by Sulfites," *J. Am. Chem. Soc. 54*, p. 977.
8. Nunes, T.L. and Powell, R.E. (1970), "Kinetics of the Reaction of Nitric Oxide with Sulfite," *Inorg. Chem. 9*, p. 1917.
9. Ackermann, M.N. and Powell, R.E. (1967), "Air Oxidation of Hydroxylamine-N-Sulfonate," *Inorg. Chem. 6*, p. 1718.
10. Doyle, G.J. and Davidson, N. (1949), "The Kinetics of the Acid-Catalyzed Hydrolysis of Amine Disulfonate Ion; The Third Ionization Constant of Amine Disulfonic Acid," *J. Am. Chem. Soc. 71*, p. 3491.

Investigation of the Reaction of Oxygen with Bisulfite Ion in Aqueous Solutions Using a High-Pressure Stopped-Flow Technique*

D. Littlejohn, K.Y. Hu, and S.G. Chang

The oxidation of aqueous bisulfite ion by molecular oxygen has been under investigation for many years, and the reaction process is still poorly understood,[1-3] although it is known the main products are SO_4^{2-} and H^+:

$$O_2 + 2HSO_3^- \rightarrow 2SO_4^{2-} + 2H^+$$

*This work was supported by the Electric Power Research Institute, Palo Alto, CA, through the U.S. Department of Energy under Contract No. DE-AC03-76SF00098.

The reaction is very important in wet flue-gas desulfurization processes. It would be highly desirable to be able to control the reaction in wet scrubbing systems so that the degree of oxidation is no larger than that desired. Trace concentrations of transition metal ions have been reported to significantly affect the rate of oxidation, as well as the reaction products.

ACCOMPLISHMENTS DURING FY 1985

We have investigated the reaction by using a high-pressure, rapid-mixing flow system in conjunction with a laser Raman spectrometer. Use of higher-than-atmospheric pressures raises the dissolved oxygen concentration to where it can be more readily observed by Raman spectroscopy. Besides dissolved oxygen, use of Raman spectroscopy permits observation of all important species in the reaction system: HSO_3^-, SO_4^{2-}, SO_2H_2O, HSO_4^-, and $S_2O_6^{2-}$. ClO_4^- is added to the reaction mixture as a

reference ion so that quantitative measurements can be made. The positions of the Raman peaks of these compounds and their relative strengths are listed in Table 1. The hydrogen ion concentration can be obtained from the concentrations of HSO_3^- and SO_2H_2O and the equilibrium between them:

$$SO_2H_2O = HSO_3^- + H^+ \quad K_1 = 0.0139 \text{ M}$$

(Ref. 4)

In addition to this equilibrium, there are several others in this system that are important. They are:

$$HSO_4^- = SO_4^{2-} + H^+ \quad K_2 = 0.0103 \text{ M}$$

(Ref. 1)

$$2HSO_3^- = S_2O_5^{2-} + H_2O \quad K_3 = 0.088 \text{ M}$$

(Ref. 5)

$$HSO_3^- = SO_3^{2-} + H^+ \quad K_4 = 1 \times 10^{-7} \text{ M}$$

(Ref. 6)

$$SO_2\,(g) = SO_2\ H_2O \quad H_1 = 1.5 \text{ M atm}^{-1}$$

(Ref. 7)

$$O_2\,(g) = O_2\,(aq) \quad H_2 = 1.25 \times 10^{-3} \text{ M atm}^{-1}$$

(Ref. 7)

These equilibria are used in determining the concentrations of these species in the reaction system.

A number of experiments have been done with dissolved oxygen concentrations ranging from 8×10^{-3} to 4×10^{-2} M (after mixing) and bisulfite concentrations ranging from 0.06 to 0.4 M (after mixing). The pH of the solution immediately after mixing is in the range of 3.5 to 4. The experiments are performed by obtaining a stable flow of the reactants and abruptly stopping the flow while monitoring one compound with the Raman spectrometer. The behavior of the compounds is observed for a period of time after the flow is stopped. The process is repeated until all species have been observed. The reacted solution is scanned with the Raman spectrometer to determine the concentrations of the compounds present at the end of reaction.

Table 1.

Compound	Raman Peak	R.S.E.[a]
$S_2O_5^{2-}$	235 cm^{-1}	0.15
$S_2O_6^{2-}$	710	0.47
ClO_4^-	934	1.06
SO_4^{2-}	981	1.00
HSO_3^-	1023	0.12
	1055	0.16
HSO_4^-	1050	0.050
X	~ 1090	~ 0.5
$S_2O_6^{2-}$	1092	1.48
SO_2H_2O	1152	0.94
O_2	1550	0.38

[a]R.S.E. (Relative Scattering Efficiency) = $\frac{\text{compound peak height/compound molarity}}{981\ cm^{-1}\ SO_4^{2-}\ \text{peak height}/SO_4^{2-}\ \text{molarity}}$

Metal ions can be added to the reactant solutions to observe their effect on the reaction system. To date, runs have been made with Fe(II) and Mn(II) added to the bisulfite solution.

Most of the experiments done have involved conditions where the bisulfite concentration is in excess of the oxygen concentration. Initial $[O_2]$ to $[HSO_3^-]$ ratios have ranged from 0.02 to 0.4. The results we have obtained allow us to divide the experiments into two groups: those where all the oxygen is consumed very shortly after mixing and those where some oxygen exists for a longer time (on the order of 50 seconds or more). The boundary between the two conditions occurs at $[O_2]$:$[HSO_3^-]$ of about 0.07. Results obtained within each group tend to be similar. The cause of this apparent bimodal behavior is under investigation.

A rapid initial drop in oxygen concentration was observed in almost all the experiments done. A concurrent drop in the bisulfite concentration was also seen. The stoichiometry of the rapidly reacting O_2 to HSO_3^- was about 1 to 2, the same as that for the oxidation reaction.

The curves of concentration *vs* time for O_2, HSO_3^-, $SO_2\ H_2O$, and $(SO_4^{2-} + HSO_4^-)$ obtained from the experiments can be used to develop mass balances for sulfur and oxygen for the experimental runs. The oxygen mass balance using $[O_2] + 2 \times [(SO_4^{2-} + HSO_4^-)]$ shows a dip shortly after the flow is stopped with a gradual return to the original level. The sulfur mass balance using $[HSO_3^-] + [SO_2\ H_2O] + [(SO_4^{2-} + HSO_4^-)]$ shows a similar dip after the flow is stopped. These are shown in Fig. 1 for run 39. These curves are indicative of an intermediate formed from bisulfite and oxygen and decaying into sulfate and hydrogen ion.

While attempting to observe dithionate ion, $S_2O_6^{2-}$, at 1092 cm^{-1}, a curve was obtained that was similar to that which would be expected of the intermediate suggested by the mass balance plots for oxygen and sulfur. Checking nearby wavenumber positions indicated that the signal maximum was at ~ 1090 cm^{-1}, rather than at 1092 cm^{-1}, the $S_2O_6^{2-}$ maximum. The curve for the intermediate is shown in Fig. 2 for run 39, which had conditions where all

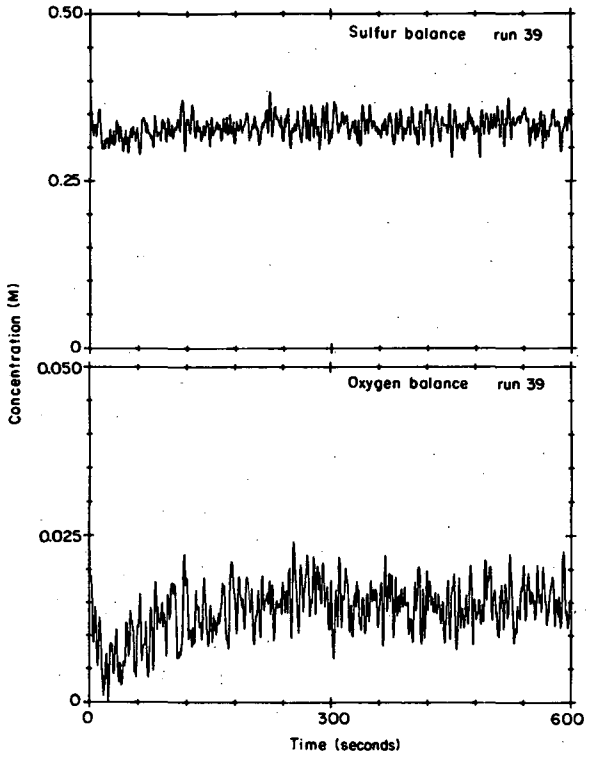

Figure 1. Upper curve—sum of the concentrations of sulfur-containing species in the reaction system *vs* time. Lower curve—sum of concentrations of oxygen-containing species in the reaction system *vs* time. (XBL 863-7579)

of the oxygen was consumed rapidly. By adjusting the height of the curve to flatten the oxygen and sulfur mass balance curves when added to them, the relative scattering efficiency for the intermediate can be estimated to be 0.5. It is listed in Table 1 as "X." The decay rate of the intermediate after its maximum agrees well with the formation rate of (SO_4^{2-} + HSO_4^-), as would be expected. The maximum concentration of the intermediate is reached approximately 10 to 30 seconds after the flow is stopped in the experiments.

PLANNED ACTIVITIES FOR FY 1986

The formation of the observed intermediate, either from the reactants or another intermediate, should show some dependence on reactant concentrations and trace amounts of metal ions. Because of the limited signal-to-noise ratio for the data we can obtain by stopped-flow techniques, it is difficult to calculate quantitative results for the decay of O_2 and HSO_3^- and the growth of the 1090 cm^{-1} intermediate on a short time scale. This is the information needed to deduce the oxygen and bisulfite ion dependence on the reaction rate and needed to observe the possible catalytic effects of metal ions. Also, doing mass balance measurements for sulfur and oxygen

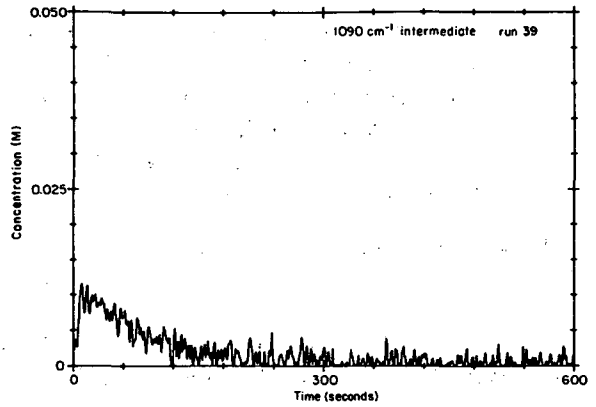

Figure 2. Plot of the 1090 cm^{-1} signal *vs* time. Concentration was calculated assuming one O_2 is equivalent to one intermediate molecule. (XBL 863-7580)

on a short time scale would indicate whether there is another intermediate coupling the reactants to the 1090 cm^{-1} intermediate.

This problem can be overcome by doing continuous flow experiments that would permit long-term observation of the reacting solution at a given time after mixing. The time delay between mixing and observation can be varied by changing the flow rate and the volume between the mixer and the observation cell. We plan to begin such experiments in the near future.

REFERENCES

1. Huss, A., Lim, P.K., and Eckert, C.A. (1982), "Oxidation of Aqueous Sulfur Dioxide. 1. Homogeneous Manganese (II) and Iron (II) Catalysis at Low pH," *J. Phys. Chem. 86*, p. 4224.
2. Huss, A., Lim, P.K., and Eckert, C.A. (1982), "Oxidation of Aqueous Sulfur Dioxide. 2. High-Pressure Studies and Proposed Reaction Mechanisms," *J. Phys. Chem. 86*, p. 4229.
3. Lim, P.K., Huss, A., and Eckert, C.A. (1982), "Oxidation of Aqueous Sulfur Dioxide. 3. The Effects of Chelating Agents and Phenolic Antioxidants," *J.Phys. Chem. 86*, p. 4233.
4. Huss, A. and Eckert, C.A. (1977), "Equilibria and Ion Activities of Sulfur Dioxide Solutions," *J. Phys. Chem. 81*, p. 2268.
5. Connick, R.E., Tam, T.M., and von Deuster, E. (1982), "Equilibrium Constant for the Dimerization of Bisulfite Ion to Form $S_2O_5^{2-}$," *Inorg. Chem. 21*, p. 103.
6. Rhee, J.S. and Dasgupta, P.K. (1985), "The Second Dissociation Constant of SO_2H_2O," *J. Phys. Chem. 89*, p. 1799.
7. *Lange's Handbook of Chemistry* (1973), John A. Dean, Ed., 11th edition, p. 10–5.

TOXICOLOGY STUDIES OF BIOLOGICAL SYSTEMS

Asymmetry of the Inner Mitochondrial Membrane*

R.J. Mehlhorn, J. Maguire, J. Lang, and L. Packer

Mitochondria are often referred to as the "powerhouses" of aerobic cells, because they are the sites within the cells where oxidative metabolism converts foodstuffs to energy-rich adenosine triphosphate (ATP), which is the common currency for energy-consuming reactions in the cell. This project is seeking to determine how the asymmetric structure of the inner mitochondrial membrane is related to energy conversion of respiratory substrates to ion gradients and ATP synthesis. The release of free radical molecules from the membrane, a process that promotes oxidative damage and may contribute to mammalian aging, is also being studied. Our approach uses nitroxide spin probes to specifically probe aqueous and membrane domains, and the basic electron spin resonance (ESR) methodology is being validated in a variety of membrane systems. We have developed ESR procedures for specifically observing spin probes inside of cells and membrane vesicles, including treatment of cells or membrane vesicles with impermeable paramagnetic ion complexes to eradicate the ESR signal of probes in the external aqueous phase. Transmembrane concentrations gradients of hydrophobic ions sensitive to electrical potentials, or of weak acids and amines sensitive to pH gradients, are measured by comparing ESR signals prior and subsequent to treatment with the paramagnetic complexes and related to electrochemical gradients. The intracellular environment can also be studied selectively by the use of spin labeled pH-responsive groups or hydrophobic ions, which can be induced to accumulate inside cells or membrane vesicles by imposing electrochemical potentials. These studies of bioenergetics phenomena have thus enabled us to elaborate procedures for selectively probing internal and external environments of membrane enclosed domains. This has set the stage for studying free radical production and reactions in each of these environments. Irreversible loss of the nitroxide spectrum is related to reactions with biological free radicals. Supportive evidence for free radical formation is being sought with the complementary ESR technique of spin trapping, and this approach is applied to the detection of free radicals in several biological systems. We are also using low temperature electron paramagenetic resonance (EPR) to study the structure of purified mitochondrial electron transport complex II and the mechanism of its production of superoxide radicals.

*This work was supported by the National Institutes of Health (AG-04818) through the U.S. Department of Energy under Contract No. DE-AC03-76SF00098.

ACCOMPLISHMENTS DURING FY 1985

Free Radical Studies

ESR schemes for free radical detection: A procedure for detecting free radical species in biological environments has been described.[1] The method consists of monitoring the loss of ESR signal in a free radical-generating environment such as the respiring mitochondrial membrane and characterizing the reaction products, primarily by chromatographic methods. The significance of this assay is that it allows for the detection of free radical reactions within the membrane interior. We have noted that the lipid spin probes which are deeply imbedded in the mitochondrial membrane, e.g., the stearic acid nitroxides, suffer a very slow spin signal loss relative to aqueous spin probes unless free radical processes are inititated within the membrane and thus they are especially effective for the detection of free radical reactions in these domains. On the other hand, the occurrence of free radical processes in the aqueous mitochondrial regions is amenable to study with conventional nitrone spin traps, although the resulting adducts are so unstable that they do not accumulate significantly and therefore require high concentrations of spin trapping agents to elicit an ESR-detectable signal.

Review of the free radical theory of aging: We have reviewed the status of the free radical theory of aging.[2] The purpose of writing this review was two-fold: (1) to compile the data which appear to support or contradict the theory and (2) to identify research directions that are most likely to make a significant impact on aging research. One specific objective in producing this review was to identify critical research areas that can benefit from our ESR approach for free radical detection. Although the free radical theory of aging was proposed several decades ago the involvement of radicals in the aging

process remains obscure. A diagram encompassing current understanding of free radical processes in mammals and indicating how such radicals might contribute to aging is shown in Fig. 1.

Considerable progress has been made in detecting oxygen free radicals in biological environments, and such radicals are now known to be generated during a variety of metabolic processes. The failure to achieve substantial lifespan extensions with antioxidants casts doubt on the validity of the theory as originally formulated. Further doubts about the theory arise from studies with cultured cell aging models, which fail to exhibit an expected sensitivity

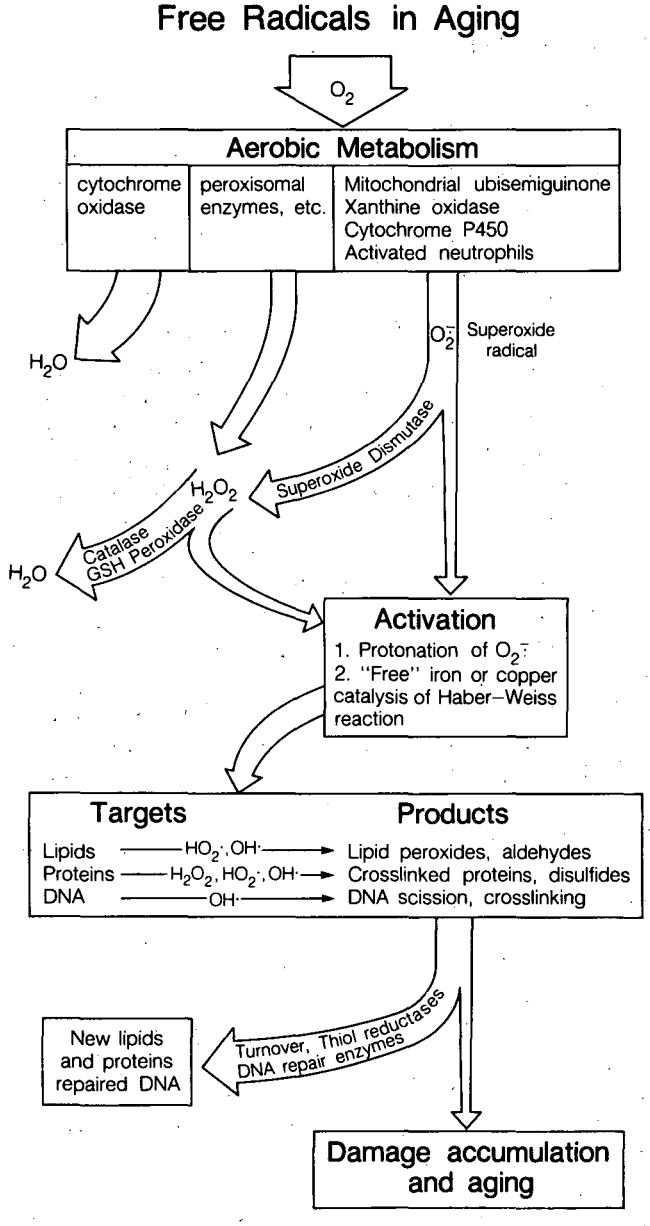

Figure 1. Scheme of free radical reactions in aerobic cells and how they contribute to aging. GSH refers to glutathione. (XBL 855-8893)

to the oxygen concentration in their growth environments. Only one nutritional manipulation, caloric restriction, is known to exert substantial life-extending effects; however its relationship to free radicals has not been resolved. Thus, present knowledge does not argue for a predominant role of free radicals in aging. However, compelling evidence exists for the involvement of free radicals in life-shortening diseases, including autoimmunity, cancer, atherosclerosis, and Parkinson's disease. Further studies of the effects of normally-occurring free radicals are warranted; quantitative data on damage associated with these species may reveal that previous analyses failed to identify critical cellular targets.

Free radical production during the metabolism of diethylstilbestrol: We have found that horseradish peroxidase or prostaglandin H synthase (PGS)-catalyzed oxidation of diethylstibestrol (DES) in the presence of the spin trap 5,5-dimethyl-1-pyrroline-N-oxide (DMPO) caused the generation of an ESR signal indicative of a free radical intermediate (a_N = 14.9 G, a_H = 18.3 G).[3,4] The identity of the trapped radical could not be identified on the basis of published hyperfine coupling constants but the observation that horseradish peroxidasecatalyzed oxidation of 1-naphthol produced an identical ESR signal suggests that the radical was either a phenoxy or phenoxy-derived radical. During horseradish peroxidase-catalyzed oxidation of diethylstilbestrol in the presence of glutathione the thiol reduced the diethylstibestrol radical to generate a thiyl radical, as shown by a thiol-dependent oxygen uptake during horseradish peroxidase-catalyzed oxidation of diethylstilbestrol and the observation of an ESR signal consistent with DMPO-glutathionyl radical adduct formation. A DES analog devoid of free hydroxyl groups, namely diethylstilbestrol dipropionate, did not produce an ESR signal above control levels during horseradish peroxidase-catalyzed metabolism in the presence of 5,5-dimethyl-pyrroline-N-oxide. We concluded that free radicals are formed during peroxidatic metabolism of diethylstilbestrol and must be considered as possible determinants of the genotoxic activity of this compound.

Metal and metalloid interactions with membranes: A review of how trace metals and metalloids in the environment may exert destructive biological effects has been written.[5] In part this work was motivated by a recognition that transition metal ions like copper and iron may play a critical role in promoting metabolically initiated free radical chains by participating in a Fenton reaction. The interaction of metal(loid)s with membranes can be particularly significant. To the extent that membranes prevent the entry of these species into cells, they will inhibit

damaging effects. However, many interactions with membranes can result in direct damage, or, more seriously, can lead to an amplification of toxicity. Direct damage can include structural alteration such as a disruption of vital lipid-protein associations or introduction of new surface charges. More substantial damage can occur when metals or metalloids act catalytically to impair membrane function, e.g., by providing ion conductance pathways or by promoting free radical reactions which may cause massive oxidation of membrane lipids. Recognition of factors involved in the interaction of metal(loid) compounds with membranes is useful for predicting toxic effects of such compounds in biological environments.

Studies of free radical generation and oxidative damage in mitochondria: We have discussed evidence, including data from our laboratory, that oxygen radicals derived from mitochondria play a major role in cellular damage.[6] In this paper we described detection schemes for mitochondrial radicals, which are being developed with ESR spin probe techniques, and which are designed to elucidate the pathways of oxidative damage. We also considered the activities of mitochondrial electron transport and isolated electron transport complexes in superoxide radical generation, transition metal catalysis of free radical formation and evidence for the formation of thiyl radicals, and their possible involvement in oxidative damage. We concluded with a comprehensive hypothesis for the production and fate of mitochondrial oxygen radicals.

Mutagenicity of nitroxide free radicals: We have found that stable nitroxides increase the number of revertants in the Salmonella typhimurium tester strain, TA 104.[7] (The Salmonella mutagenesis assay system is widely used for detecting potential carcinogens.) The observed mutagenicity was more pronounced with the piperidine nitroxide Tempol, than with the pyrrolidine nitroxide PCAOL. Mutagenicity was dramatically increased in the presence of a superoxide radical generating system, xanthine oxidase/hypoxanthine. The nitroxide mutagenicity was suppressed in TA 104 cells that contained the regulon against oxidative stress, OxyR, suggesting that the mutagenic effect is due to an oxidation mechanism that occurs frequently in aerobic cells. A plausible mechanism of mutagenesis was suggested to be the thiol oxidation product sulfenyl hydroperoxide. The enhancement of the nitroxide mutagenicity by exogenous xanthine oxidase appears to rule out a significant role for a direct attack of the nitroxide on DNA radicals in the mutagenic effect.

Superoxide production by an isolated mitochondrial electron transport complex: We have obtained data that purified mitochondrial electron transport complex II generates superoxide radicals in the absence of ubiquinone.[8] Although the rate of superoxide radical production is about 2% of the rate seen with the enzyme when the artificial dye phenazine methosulfate is used as an electron acceptor, our measurement of a finite rate contradicts earlier literature reports that this complex does not produce superoxide.

Bioenergetics Studies

ESR probe studies of transmembrane proton movements: Procedures for using nitroxide spin probes to kinetically study proton gradients have been described.[9] Membrane proton pumps, like bacteriorhodopsin, generate electrochemical potentials that can be measured with a combination of probes responsive to transmembrane electrical and pH gradients. We described how nitroxide spin probes are employed to study permeability of halobacterial envelope vesicle and erythrocyte membranes to spin labeled weakly polar molecules, ions, amines, and weak acids. Weakly polar spin probes with fewer than two hydrogen bonding residues permeate most membranes too rapidly to measure with available stop-flow ESR techniques (half-time for uptake less than 100 msec). One of these nitroxides, 4-oxo-2,2,6,6-tetramethyl piperidine-N-oxyl (TEMPONE), has been used to measure volume changes in many envelope and cell preparations and permeates at least one cell (the red cell) appreciably more rapidly than water does. The permeability of amine and carboxyl spin labels is also high when the probes are predominantly in their uncharged states. However, under typical physiological conditions where these species exist predominantly in their charged forms, the permeabilities of these probes may be imposing rate limitations on measurements of proton fluxes. This limitation can be overcome by working with nitroxides whose pK_a's are similar to those of the membrane suspensions under study. Hydrophobic spin-labeled cations with point but not delocalized charge centers enter halobacterial envelope vesicles in response to light-induced transmembrane electrical potentials. However, in no case that we have examined is the permeability of permanently charged cationic nitroxides fast enough to respond to electrical membrane energization phenomena in the sub-second time domain. Amphiphilic cationic spin probes, which are analogues of the widely-used cationic detergent cetyl-trimethyl ammonium bromide (CTAB), bind extensively to the halobacterial membrane yet do not partition into non-polar organic solvents, and thus would not be considered

to be hydrophobic ions. These amphiphiles exhibit significant rates of membrane permeation but do not accumulate in response to electrical potentials, suggesting that they diffuse across the membrane in conjunction with anions. We have emphasized that ion pairing may well occur with many other membrane-binding probes and must be controlled for accurate and meaningful measurements of proton gradients.

ESR studies of light-dependent volume changes in cell envelope vesicles from Halobacterium halobium: The measurement of volume changes can provide information about solute fluxes, including ionic currents, across biological membranes. This potential application of the ESR technique was developed in illuminated cell envelope vesicles from *H. halobium,* an experimental system that has proven to be a useful model system for perfecting several ESR assays of bioenergetics parameters.[10] We demonstrated light-driven swelling in vesicles containing halorhodopsin (a proposed inward-directed chloride pump) and shrinking in vesicles containing bacteriorhodopsin, (an outward-directed proton pump which functions in these vesicles in combination with a proton/sodium antiporter). Swelling of the halorhodopsin vesicles was not inhibited by uncouplers or by gramicidin, whereas shrinking of the bacteriorhodopsin vesicles was inhibited by these ionophores. Vesicles from a strain which contains both pigments, R1, showed relatively small volume changes with illumination. This study established procedures for using the ESR volume measurement technique for obtaining fundamental insights into mechanisms of ion pumping across energy-transducing membranes.

Surface potential measurements of mitochondrial membranes: Measurements of the surface potential of the inner mitochondrial membrane using electron paramagnetic probes have been described.[11] The first stage of this research consisted of characterizing the permeability of our nitroxide probes used for these measurements. It had been suggested by other workers that the Cat_n probes used for such studies were too permeable to be useful for surface potential work. We have found that the probes do indeed cross the inner mitochondrial membrane at an appreciable rate at room temperature, but that rapid mixing procedures can be used to overcome this difficulty. The problem of probe reduction and destruction was discussed, and kinetic analysis of the decrease of ESR signal intensity, inferred from double integration of the spectra, was used to correct for this phenomenon. Data were presented on the permeability of the mitochondrial membrane to cationic, amphiphilic spin probes designated Cat_n. The uptake of these probes was compared to that of a freely permeable phosphonium ion probe. The repartitioning of the Cat_n probes upon energization of mitochondria with ATP was interpreted in terms of a decrease of about 15 millivolts in the surface potential of the inner mitochondrial membrane upon energization. Conflicting interpretations of spin probe data about mitochondrial surface potentials in the literature were also reviewed, and misinterpretations of data were identified.

PLANNED ACTIVITIES FOR FY 1986

Evidence will be sought for the hypothesis that biological oxidative damage associated with normal aerobic metabolism is due primarily to mitochondrial superoxide free radicals in a process that involves thiols and transition metal ions. This hypothesis provides an explanation for the marginal effects of antioxidants in retarding aging rates, without discarding the primary concept of the "free radical theory of aging," i.e., that metabolically generated free radicals cause aging. To test the postulate that mitochondrial superoxide plays a predominant role in cell damage, superoxide production of several subcellular fractions will be compared. Mitochondrial superoxide production will be quantitated within and outside of the mitochondria, thus defining the effect of the asymmetric structure of the membrane on superoxide production. Data on the membrane sidedness of superoxide release and on non-mitochondrial sources will provide valuable data about the relative contributions of the extramitochondrial and intramitochondrial compartments to the total cellular superoxide burden. Lipid peroxidation will be compared with thiol oxidation to estimate how these two potentially major targets of superoxide radicals are affected by superoxide released from mitochondria. Electron spin resonance tools for the detection and characterization of free radical species will play an integral part in the studies; they will be supported by HPLC analyses of oxidation products, including thiol and lipid derivatives. The animal model will consist of controlled age groups of Fischer 344 rats.

REFERENCES AND BIBLIOGRAPHY

1. Mehlhorn, R.J. and Packer, L. (1984), "ESR Spin Destruction Methods for Radical Detection," *Methods Enzymol. 105,* p. 215.
2. Mehlhorn, R.J. and Cole, G. (1985), "The Free Radical Theory of Aging: A Critical Review," *Adv. Free Radical Biology & Medicine 1,* p. 165.
3. Ross, D., Mehlhorn, R.J., Moldeus, P., and Smith, M. (1986), "Metabolism of Diethylstilbestrol by Horseradish Peroxidase and Prostaglandin Synthase: Generation of Free Radicals

and Their Interaction with Glutathione," *J. Biol. Chem. 260,* p. 16210.

4. Ross, D., Mehlhorn, R.J., Moldeus, P., and Smith, M.T. (1986), "Metabolism of Diethylstilbestrol by Horseradish Peroxidase and Prostaglandin Synthase Evidence for a Free Radical Intermediate," in *Proceedings of the 3rd International Symposium on Biological Reactive Intermediates,* R. Snyder, Ed, Plenum Press, in press.
5. Mehlhorn, R.J. (1986), "The Interaction of Metals and Metalloids with Biomembranes," to be published as a Dahlem Workshop Book, Springer Verlag, in press.
6. Mehlhorn, R.J., Maguire, J.J., Hartzog, G., and Packer, L. (1986), "Oxygen Radicals and Cancer: Free Radical Generation and Oxidative Damage in Mitochondria," in *Biomembranes in Cancer Cells,* T. Galeotti, A. Cittadini, G. Neri, and S. Papa, Eds, Elsevier Science, Amsterdam, p. 223.
7. Sies, H. and Mehlhorn, R.J. (1986), "Mutagenicity of Nitroxide Free Radicals," submitted to *Arch. Biochem. Biophys.*
8. Maguire, J.J., Mehlhorn, R.J., Akrell, B.A.C., and Packer, L. (1986), "Superoxide Production by Mitochondrial Complex II," submitted to *Arch. Biochem. Biophys.*
9. Mehlhorn, R.J., *et al.* (1986), "Measurement of Transmembrane Proton Movements with Nitroxide Spin Probes," *Methods Enzymol.,* in press.
10. Mehlhorn, R.J., Schobert, B. Packer, L., and Lanyi, J. (1985), "ESR Studies of Light-Dependent Volume Changes in Cell Envelope Vesicles from Halobacterium Halobium," *Biochim. Biophys. Acta. 809,* p. 66.
11. Hartzog, G., Mehlhorn, R.J., and Packer, L. (1986), "A Reevaluation of Mitochondrial Surface Potentials," in *Ion Interactions in Energy Transport Systems,* S. Papa, G. Papageorgiou, and J. Barker, Eds, Plenum Press, in press.

Ackrell, B.A.C., Maguire, J.J., Dallman, P., and Kearney, E.B. (1984), "Effect of Iron Deficiency on Succinate and NADH-Ubiquinone Oxidoreductases in Skeletal Muscle Mitochondria," *J. Biol. Chem. 259,* p. 10053

Ackrell, B.A.C., Cochran, B., Larson, K., Maguire, J.J., and Kearney, E.B. (1985), "Lack of Assembly of Succinate and NADH-Ubiquinone Oxidoreductases in Iron-Deficient Rat Skeletal Muscle Mitochondria," in *Flavins and Flavoproteins,* R.C. Bray, P.C. Engel, and S.G. Mayhew, Eds, Walter de Gruyter, Berlin, N.Y., in press.

Ball, M.C., Mehlhorn, R.J., Terry, N., and Packer, L., (1985), "Electron Spin Resonance Studies of Ionic Permeability Properties of Thylakoid Membranes of Beta Vulgaris and Avicennia Germinans," *Plant Physiol. 78,* p. 1.

Hederstedt, L., Maguire, J.J., Waring, A.J., and Ohnishi, A.J. (1985), "Characterization by EPR and Studies on Subunit Location and Assembly of the Iron-Sulfur Clusters of Bacillus Subtilis Succinate Dehydrogenase," *J. Biol. Chem. 260,* p. 5554.

Lomax, T.L. and Mehlhorn, R.J. (1986), "Determination of Plant Membrane Vesicle Volume and pH Gradient Using Electron Spin Resonance Spectroscopy," *Biochim. Biophys. Acta. 821,* p. 106.

Lomax, T.L., Mehlhorn, R.J., and Briggs, W.R. (1985), "Quantitation of [^{14}C] IAA Uptake by Plant Membrane Vesicles Using ESR Volume and ΔpH Determinations," *Proc. Natl. Acad. Sci. USA. 82,* p. 6541.

Maguire, J.J., *et al.* (1986), "Electron Paramagnetic Resonance Studies of Succinate Dehydrogenase II. Evidence for Detection of the Tetranuclear Cluster S-2 in Succinate Ubiquinone Reductase and Reconstitutively Active Enzyme," *J. Biol. Chem. 260,* p. 10909.

Melandri B.A., Mehlhorn, R.J., and Packer, L. (1984), "Light-Induced Proton Gradients and Internal Volumes in Chromatophores of Rhodospeudomonas Sphaeroides," *Arch. Biochem. Biophys. 235,* p. 95.

Packer, L. and Mehlorn, R.J. (1986), "Modification and Spin Labeling Studies of Membrane Bioenergetics," in *Recent Advances in Biological Membrane Studies: Structure and Biogenesis, Oxidations and Energetics,* L. Packer. Ed, in press.

Poole, R.J., Mehlorn, R.J., and Packer, L. (1985), "A Study of Transport in Tonoplast Vesicles Using Spin-Labelled Probes," in *Biochemistry and Function of Vacuolar Adenosine-Triphosphatase in Fungi and Plants,* B.P. Martin, Ed, p. 114.

Impacts of Large Extraterrestrial Bodies and Mass Extinctions*

F. Asaro, Helen V. Michel, W. Alvarez, and L.W. Alvarez

Studies of the extinction of species and the ages of craters in the last 250 million years (MY) have suggested they each have a periodicity of 26–28 MY. Extraterrestrial causes have been hypothesized for these effects, and the best developed theory suggests that a companion star to our Sun, nicknamed Nemesis, orbits the Sun with the same period. Other hypotheses of the source of the perturbation of the comet cloud are a planet X orbiting the Sun and the periodic movement of the solar system through the Galactic center. At the time of Nemesis' closest approach, comets from the outer fringes of the solar system are injected into the inner part and a small number of these can impact on the Earth. The more energetic impacts would raise a huge dust cloud that contained the vaporized comet debris. This cloud would be distributed all around the Earth and settle in a few months. Evidence for the impacts would appear world wide as single or multiple Ir and other geochemical anomalies and be repeated about every 26–28 MY. Such evidence for single impacts has been amply demonstrated for the 66 MY old Cretaceous-Tertiary boundary,[1] and to a lesser extent for the 39 MY old horizon in the terminal Eocene.[2] One exciting ramification is that multiple impacts during a comet shower could produce what appear to be gradual (10^5) year extinctions.

The purpose of this project is test the validity of the Nemesis and other models for the periodic extinctions of species by a detailed stratigraphic study for iridium and other geochemical or mineralogical anomalies in rock strata associated with minor and mass extinctions. To accomplish these studies it is necessary to test many thousands of samples, and previous techniques are inadequate.

*This work was supported by the Director, Office of Energy Research, Office of Basic Energy Sciences, Engineering and Geosciences Division of the U.S. Department of Energy under Contract No. DE-AC03-76SF00098 and the National Aeronautics and Space Administration Ames Research Center under Contract No. A-71683B. Support was also received from the Murdock Charitable Trust.

As a byproduct of this effort we would also determine the usefulness of Ir and other geochemical anomalies (associated with bolide impacts) as time markers by finding: a) What mineral phases or fossil forms are likely to contain the above anomalies in marine and non-marine environments, b) How far and in what direction are the above anomalies likely to migrate from the position of initial deposition (and thus influence the validity of a geochemical anomaly horizon as a high-precision worldwide time marker), and c) How likely are the above anomalies to disappear from the sedimentary record.

As another byproduct we would attempt to determine and demonstrate the usefulness of each geochemical anomaly horizon as a worldwide time marker.

ACCOMPLISHMENTS DURING FY 1985

An Iridium Coincidence Spectrometer, which can measure by neutron activation analysis (without any chemical separation) iridium contents of rocks 500 times faster than was previously possible without labor-intensive chemical separations, has been built and tested. It is 100 times faster than analyses previously made by us at LBL which involved high volume carrier-free radiochemical separations, and it is 10 to 100 times cheaper to operate than the cost of analyses elsewhere which necessitates rather complete radiochemical separations of iridium.

The spectrometer is very reliable in that interference corrections from irradiated elements other than iridium are nearly negligible. Also the possibility of contamination due to the use of iridium carrier in chemical separations is eliminated.

To register an iridium event, the spectrometer requires that two nuclear gamma-rays characteristic of the isotope ^{192}Ir be detected nearly simultaneously (i.e., in coincidence) in two Ge solid state crystals. Two other isotopes, ^{46}Sc and ^{60}Co, each have two high energy gamma rays in coincidence, which can scatter out of the Ge crystals and leave residues of energy which would appear to be coincident gamma-rays of ^{192}Ir. Two large tanks of mineral-oil-based scintillator completely surround the germanium detectors, detect the scattered radiations, and veto nearly all of the unwanted coincidences seen by the germanium. The resulting background from irradiated rock samples which count 40,000

counts per second in each germanium detector is only 2–3 coincidences per hour. Although this background is usually not significant, it is always measured and considered.

The sensitivity of the spectrometer at the 95% confidence level for rock samples of the type we normally expect to measure is 50 parts-per-trillion of iridium in a 7 min count. This performance is possible through the cooperation of the staff of the University of Missouri Research Reactor Facility in Columbia, Missouri.

About 5000 samples have been collected for a detailed search for geochemical anomalies related to impacts with particular emphasis on rocks 90–95 MY old from the Italian Apennine mountains and the Western interior United States. This level has many extinctions and corresponds to the next older extinction horizon (in the predicted ~27 MY cycle) before the 39 and 66 MY old horizons where worldwide iridium anomalies have already been detected.

The iridium anomaly in ~39 MY old rock strata has now been seen in a deep sea core taken from near New Zealand. This is the most southerly region that this anomaly has been seen, and it confirms its worldwide distribution.

PLANNED ACTIVITIES FOR FY 1986

Detailed studies will be made of the 250 MY old Permian-Triassic boundary in China[3] in collaboration with Chinese scientists. Studies of this boundary in India will be made with Canadian scientists. This boundary is of particular interest because the largest mass extinction known in the geological record took place in that time region. Eighty to ninety percent of the good rock sections from that time are in China with a few others in Russia, Iran, and India.

Detailed studies of the fine structure of iridium anomalies at extinction horizons will be made to determine if there are indications of clustering of comet impacts on the Earth.

REFERENCES

1. Michel, H.V., Asaro, F., Alvarez, W., and Alvarez, L.W. (1985), "Elemental Profile of Iridium and Other Elements Near the Cretaceous-Tertiary Boundary in Hole 577B," Deep Sea Drilling Project Initial Report DSDP Vol. 86, p. 533.
2. Alvarez, W., Asaro, F., Michel, H.V., and Alvarez, W. (1982), "Iridium Anomaly Approximately Synchronous with Terminal Eocene Extinctions," *Science 216*, p. 8.
3. Asaro, F., *et al.* (1985), "Geochemical Study of the Permian-Triassic Boundary in the Meishan, Tangshan and Watchapo Mountain Sections in the People's Republic of China," in Abstracts with Program, Conference on Rare Events in Geology, Gwatt, Switzerland, May 20–22, 1985.

Studies of Source of Lithic Artifacts and Trade Routes by Elemental Analysis*

F.H. Stross, F. Asaro, and H.V. Michel

X-ray fluorescence analyses (XRF) and neutron activation analyses (NAA) were used in studies to determine patterns of distribution of artifacts made from obsidian. The studies were carried out in collaboration with the academic institutions who funded the projects.

*This work was supported by the University of Texas, San Antonio, and the University of Colorado, Boulder, and by the U.S. Department of Energy under Contract No. DE-AC03-76SF00098.

ACCOMPLISHMENTS DURING FY 1985

Wild Cane Cay Project

This project was carried out in collaboration with Heather McKillop from the University of California at Santa Barbara and was jointly funded by the Social Sciences and Humanities Research Council of Canada and U.C., Santa Barbara, with Ms. McKillop as the principal investigator. It is to study the role of coastal areas in the development of prehistoric, complex societies. Specifically, Wild Cane Cay, an island off the mouth of the Deep River in southern Belize, was chosen for study as an example of coastal commerce in Maya territory during Classic and Postclassic periods (ca 4th century A.D. to the Conquest).

One hundred obsidian artifacts were studied. They were mostly scrapers or knives, including

bifaces and stemmed blades, and also cores (residual rock from the manufacture of blades from boulders).

Preliminary analysis of the artifacts by XRF indicated that 78 specimens came from deposits related to the volcano Ixtepeque; 17 specimens matched the important El Chayal source, farther to the west-(northwest), and one specimen matched the "representative Rio Pixcaya" composition, a large deposit yet farther west. All these sources are located in the highlands of Guatemala, southwest of Wild Cane Cay. Three specimens came from one source of unknown location, which was designated "Source Z." One specimen was unassigned. The four specimens last mentioned bear a general resemblance to Guatemala Highland obsidian patterns, but do not closely match any of those known to us. The results are presented in Table 1. All of the source assignments are considered to be tentative until they are confirmed by NAA on selected samples.

It is of interest that an earlier study,[1] made in collaboration with Professor N. Hammond (Rutgers University), involved 23 obsidian artifacts from Wild Cane Cay, of which 19 came from Ixtepeque and four from El Chayal, a proportion very similar to that found for the present, larger sampling by McKillop.

Belize River Trade Project

This study of artifacts from Belize (formerly British Honduras in Central America) has been carried out in collaboration with Dr. Anabel Ford from the University of California, Santa Barbara. Procurement sources for obsidian artifacts found in the inhabited Peten area, dating from the first millenium A.D., during the period of Mayan florescence shifted from the western to the eastern obsidian sources in the Guatemala Highlands. The habitations were

Table 1. Preliminary XRF Results on Wild Cane Cay Obsidian Samples (McKillop, *et al.*, unpublished data) Site 32/179-1.

No. of Samples	Ba (ppm)[a]	Zr (ppm)[b]	Rb/Zr	Sr/Zr
		Matching Ixtepeque Source		
78	1034 ± 46	176 ± 7	.58 ± .02	.90 ± .02
Reference[b]	1030 ± 27	175 ± 2	.57 ± .01	.90 ± .02
		Matching El Chayal Source		
17	923 ± 48	119 ± 4	1.30 ± .07	1.31 ± .03
Reference[b]	915 ± 24	117 ± 3	1.24 ± .04	1.29 ± .04
		Matching Rio Pixcaya Source		
1	1010 ± 22	117 ± 1	.96 ± .01	1.65 ± .01
Reference[b]	1105 ± 32	115 ± 3	1.01 ± .05	1.65 ± .06
		Unknown Source Z		
3	909 ± 52	99 ± 3	1.62 ± .05	1.49 ± .02
		Unassigned Artifact (Sample 8143-Y)		
1	966 ± 30	139 ± 4	1.37 ± .06	1.47 ± .06

[a]Errors are root-mean-square deviations for groups and estimated counting errors for single samples.

[b]Reference source data are from Asaro, *et al., Am. Antiquity 43*, 436 (1978); Stross *et al., Am. Antiquity 48*, 323 (1983); and Asaro, *et al.*, unpublished data.

directly or indirectly connected with the important center of Tikal, centrally located in the vast jungle area of the Peten, and the changes in obsidian procurement are of significance because they presumably reflect political events such as changes in the power structures, trade monopolies, military actions, and migrations. A manuscript was prepared for publication.

Other studies of the Belize River region (Colha, Pulltrouser Swamp, Cerros) carried out in collaboration with Professor Tom Hester of the University of Texas of San Antonio have also shown that most of the obsidian originated from the Guatemalan Highlands. These studies in Belize are significantly changing certain aspects of Mayan history, both in very early times (before the beginning of the Christian era) and in the post-classic (after the tenth century A.D.) to and including the Conquest.

PLANNED ACTIVITIES FOR FY 1986

Belize River Trade Project

Several continuing studies are concerned with the movement of obsidian raw material and artifacts between the Peten area—specifically the centers of Tikal and Yaxha—and Moho Cay, a small island at the mouth of the Belize River, which apparently was used as a trans-shipment point between coastal and inland trade for a long time. The Belize River itself was used in the shipment as far inland as it was navigable or convenient, probably to a point near the present-day Benque Viejo (site of Xunantunich) at the Guatemala-Belize border; the goods were then carried overland to or from points west in the Peten.

The area of the presumed portage point, including the site of el Pilar, has been excavated by BRASS (the Belize River Archaeological Settlement Survey, organized by the University of California, Santa Barbara), and a relatively high density of obsidian artifacts has been observed here. Analysis of these artifacts leading to the determination of the sources of obsidian, coupled with dating of the strata in which they were found, is expected to shed light on the important features of trade in that region.

Colossi of Memnon Project

Analytical studies of the Colossi of Memnon, well-known quartzite monuments located in the Plain of Thebes in Upper Egypt, have revealed[2] that the Roman reconstruction of the northern statue, and consequently the prior damage to the monument, had been far more extensive than hitherto supposed and included the entire rear portion of the pedestal of the statue. Speculation on how the damage had been brought about included the setting of great fires around the monuments, to spall and weaken the stone.

The technique of thermoluminescence (TL) is capable of measuring the length of time elapsed since certain materials, including clay and quartzite, were last subjected to temperatures exceeding ca 500°C. It has been possible to engage the collaboration of a team of French scholars expert in the application of TL to quartzite (including Professor M. Schvoerer, pioneer in this technique) for performing some measurements on Colossi samples available to us. By this study it may be possible to determine if great fires were indeed set around the Colossi in historic times. This would provide information on how, and possibly by whom, the defacement observed today (and already in Roman times) had been brought about, and thus reveal some highly relevant background relating to hitherto unknown history involving these monuments.

REFERENCES

1. Stross, F.H., *et al.* (1978), "Mayan Obsidian: Source Correlation for Southern Belize Artifacts," *Archaeometry 20*(1), p. 89.
2. Bowman, H., *et al.* (1984), "The Northern Colossus of Memnon: New Slants," *Archaeometry 26*(2), p. 218.

LAWRENCE BERKELEY LABORATORY
TECHNICAL INFORMATION DEPARTMENT
UNIVERSITY OF CALIFORNIA
BERKELEY, CALIFORNIA 94720